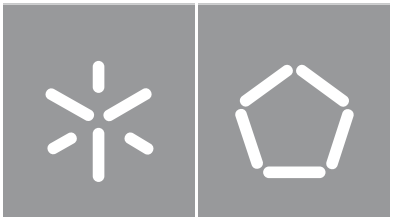
Universidade do Minho
Escola de Engenharia

Wagner de Campos Galuppo

Computational Modelling and Optimisation of the Extrusion Blow Moulding Process

December 2024

Computational Modelling and Optimisation of the Extrusion Blow Moulding Process
Wagner de Campos Galuppo
UMinho | 2024



Universidade do Minho
Escola de Engenharia

Wagner de Campos Galuppo

Computational Modelling and Optimisation of the Extrusion Blow Moulding Process

Philosophy Doctorate Thesis in
Polymers and Composites Engineering

Work accomplished under the supervision of
Professor João Miguel de Amorim Novais da Costa Nóbrega

December 2024

Direitos de autor e condições de utilização do trabalho por terceiros

Este é um trabalho académico que pode ser utilizado por terceiros desde que respeitadas as regras e boas práticas internacionalmente aceites, no que concerne aos direitos de autor e direitos conexos.

Assim, o presente trabalho pode ser utilizado nos termos previstos na licença abaixo indicada.

Caso o utilizador necessite de permissão para poder fazer um uso do trabalho em condições não previstas no licenciamento indicado, deverá contactar o autor, através do RepositóriUM da Universidade do Minho.

Licença concedida aos utilizadores deste trabalho:



Atribuição CC
BY
https://creativecommons.org/licenses/by/4.0/

Acknowledgements

I would like to express my deepest gratitude to my parents, Ana Maria de Campos and Sergio Prado Galuppo Filho, who have provided unwavering support throughout my life. Although my father was with me for nearly thirteen years, the invaluable lessons he imparted remain with me always. My mother for the efforts she made for my well-being. The lessons they taught me about integrity and trustworthiness have had a priceless impact on me. My heartfelt thanks also go to my siblings, Fernando Furlanetto Galuppo and Lia Raquel de Campos Galuppo, for their constant encouragement and support. I greatly appreciate all the attention, support, care and motivation given by my dear Fernanda Maria Follmann. I extend my sincere thanks to my entire family on both sides for their support in helping me overcome the challenges.

To my friends who stood by me, I am grateful. Michel Massih, Isabella C. Bisco, Julia Deliza, Filipi Cury, Thiago Cantusio, Rodrigo Gianfrancesco, Michel Moriale, Felipe Scott, Pedro Bisco, Felipe Klein, Gustavo de Almeida and others who have been accompanying me in life. My friends from UDESC, University of Calgary, ITA, and University of Minho—Luis Amorim, Raquel Santos, Mariana Silva, Ana Pereira, Ricardo Ribeiro, Glenn Van Otten, João Manuel Lopes, Giulia Infurna, Davy Fonseca, Sophia Piacenza, Iran Segundo, Domingos Machado, José Camargo, Antonio de Andrade, Ylan Ádlin, Alberto Campuzano, Tiago Mota, José Amadeu Tasqi, Milene Viana, Nathalia Hammes, Natália Homem, Alexandre Rocha, Eduardo Oliveira, Casimiro Ferreira and many more—are also greatly appreciated.

I am especially grateful to my Ph.D. supervisor, Prof. João Miguel de Amorim Novais da Costa Nóbrega, for his guidance and unwavering support in overcoming challenges. I am thankful for his initiatives, resiliency, persistence and encouragement, during moments of frustration with unresolved questions. I greatly appreciate his willingness to share his knowledge and for standing by me at every stage of my candidacy since our friendship began in 2017. I am also grateful to my previous mentors, Professors Luiz V. O. Dalla Valentina, Craig T. Johansen, Paulo Sergio B. Zdanski, Marcelo José S. de Lemos, for their dedication to my development as an engineer and scientist. Special thanks to Prof. José Luís C. M. Alves for assisting with the validation of hyperelastic models and to Dr. Davide Nocita, who generously offered to take the raw material and characterise it, thereby helping with the fitting of the material that was hindering an accurate extrusion simulation.

My thanks to colleagues and staff at the Department of Polymers and Composites at the University of Minho, especially João Romero, Ricardo Costa, Bruno Ramôa for their friendship and for sharing their expertise with me in programming and assisting with several things, also to Mohammadreza Aali for his friendship and support throughout several experimental characterisation runs. Thanks to the staff at Logoplaste, especially Francisco Alves, Shreena Glory, and Pedro Santana. Finally, to the European Union and the Portuguese Foundation for Science and Technology (FCT) for funding this research with the Ph.D. grant 2020.08395.BD.

Statement of integrity

I hereby declare having conducted this academic work with integrity. I confirm that I have not used plagiarism or any form of undue use of information or falsification of results along the process leading to its elaboration.

I further declare that I have fully acknowledged the Code of Ethical Conduct of the University of Minho.

University of Minho, 30th September 2024

Name: Wagner de Campos Galuppo

Signature: _____

Abstract

Computational Modelling and Optimisation of the Extrusion Blow Moulding Process

The Extrusion Blow Moulding (EBM) process is one of the most widely used methods for producing hollow thermoplastic containers. The development of advanced computational tools to simulate EBM primary phases is a straightforward way for improving process efficiency, reducing production costs, and understanding the complex behaviours of the materials involved. This research aims to create this numerical framework, improve material usage efficiency, reduce waste, and adjust process control variables, aiming for more sustainable manufacturing. The open-source computational library OpenFOAM® was chosen to be used and create new libraries and enhance existing ones, enabling the simulation of the key stages of the EBM process, namely the parison extrusion, mould clamping and parison inflation. The implemented tools were designed to be flexible and in the future allow the creation of an integrated modelling code, covering all process, to overcome the limitations of the currently available proprietary simulation software.

Viscoelastic and hyperelastic material models were incorporated to simulate the different phases of the process, improving the numerical predictions of polymer rheology during its processing. The finite area class and method were utilised to simulate deformable membranes and employed in the mould clamping and inflation phases. Additionally, multi-phase flow modelling was employed to simulate the extrusion phase, where a new solver with an advanced method for capturing the interface between the polymer and air was deployed. The geometry of a real extrusion tool was analysed to evaluate thickness distribution and the impact of support air in assisting with the extrudate formation.

Another significant contribution of this work is the development of an automated optimisation methodology for thickness distribution, enhancing material usage efficiency, particularly in the packaging sector. This tool promotes digital manufacturing and integrates Industry 4.0 concepts, facilitating further improvements in EBM production systems. The method aims for precise control over the extrudate thickness along its length, analogous to real process control variables, minimising deviations between the obtained and desired values for the final product.

The models were validated through analytical and experimental methods, demonstrating that the simulated results closely aligned with reference data. Accurate simulation predictions offer valuable insights for decision-makers, underscoring the potential of the implemented numerical tools to enhance the efficiency of the EBM process. Overall, this research advances the understanding of EBM processes and offers a powerful tool for both industry and academia, contributing to the continuous transformation towards more sustainable and efficient manufacturing practices.

Keywords: Extrusion Blow Moulding, Numerical Simulation, Optimisation, Viscoelasticity, Hyperelasticity

Resumo

Modelação Computacional e Optimização do Processo de Moldação por Extrusão-Sopro

O processo de Moldação por Extrusão e Sopro (MES) é um dos métodos mais utilizados para a produção de recipientes ocos com materiais termoplásticos. O desenvolvimento de ferramentas computacionais avançadas para simular suas principais fases é uma forma expedita para melhorar sua eficiência, reduzir custos de produção e compreender a reologia complexa dos materiais envolvidos. Esta pesquisa visa criar esta ferramenta, melhorar a eficiência do uso de material, reduzir desperdícios e ajustar variáveis de controlo do processo e uma manufatura mais sustentável. Utilizou-se da biblioteca computacional de código aberto OpenFOAM® para criar novas bibliotecas e melhorar algumas das já existentes, de modo a simular principais fases da MES. As ferramentas concebidas são flexíveis, e superam as limitações existentes nos softwares de simulação comerciais da MES. Assim, os códigos podem ser ampliados e personalizados para atender às necessidades da indústria e academia.

Modelos de materiais viscoelásticos e hiperelásticos melhoraram as previsões numéricas dos comportamentos dos termoplásticos durante o seu processamento. A classe e o método de área finitas foram utilizados para simular membranas deformáveis, sendo aplicados às fases de fecho do molde e insuflação. Adicionalmente, a modelação de escoamentos multifásicos, assim como um novo código com um método avançado de captura da localização da interface, foram empregues nas simulações da fase de extrusão. A geometria de uma ferramenta de extrusão real foi analisada para avaliar a distribuição de espessuras resultante e o impacto do ar de suporte na formação do extrudido.

Outra contribuição relevante foi o desenvolvimento de uma metodologia automatizada de otimização da distribuição de espessuras, melhorando a eficiência da utilização de material, no setor das embalagens. Esta ferramenta promove a manufatura digital e incorpora conceitos da Indústria 4.0, levando melhorias nos sistemas de produção com o MES. O método visa o controlo sobre as espessuras do extrudido ao longo do seu comprimento, análogo às variáveis de controlo do processo real, minimizando as diferenças entre os valores obtidos e os valores desejados para o produto final.

Os modelos foram validados por métodos analíticos e experimentais, nos quais os resultados simulados apresentaram valores e distribuição similares aos dados de referência. As previsões das simulações fornecem informações valiosas para a tomada de decisões, destacando o potencial das ferramentas numéricas implementadas para melhorar a eficiência do processo MES. Este trabalho de investigação apresenta contribuições efetivas para a compreensão dos processos baseados em MES, e oferece uma ferramenta poderosa tanto para a indústria como para a academia, contribuindo para a transformação contínua rumo a práticas de manufatura mais sustentáveis e eficientes.

Palavras-chave: Moldação por Extrusão e Sopro, Simulação Numérica, Otimização, Viscoelasticidade, Hiperelasticidade

Publications and Communications

The following publications were prepared, submitted, and published in peer-reviewed international journals based on the present work.

- W. d. C. Galuppo, P. Santana, F. Alves, and J.M. Nóbrega, Extending the finite area method for enhanced simulation of deformable Membranes and its application to extrusion blow moulding, Thin-Walled Structures. Volume 203 (2024) 112–184, DOI: https://doi.org/10.1016/j.tws.2024.112184.
- W. d. C. Galuppo, P. Santana, F. Alves, and J.M. Nóbrega, A Computational Framework for Optimising Extrusion Blow Moulding: Enhancing Material Efficiency and Reducing Waste for Industry 4.0, submitted for publication.
- W. d. C. Galuppo, D. Nocita, P. Santana, F. Alves, and J.M. Nóbrega, Extrusion Blow Moulding Process: Numerical Simulations for the Parison Extrusion Phase, in preparation (2024).
- A. Gaspar-Cunha P. Costa W. d. C. Galuppo, J.M. Nóbrega, F. Duarte, and L. Costa, Multi-Objective Optimization of Plastics Thermoforming, Mathematics. Volume 9, no. 15: 1760, (2022). DOI: https://doi.org/10.3390/math9151760

The following were published in the relevant international industrial journal based on the present work.

- F. Alves, W. d. C. Galuppo, P. Santana, N. Bento, J.M. Nóbrega, and B. Machado, A smarter process. Experimental Assessment tools, Computational Methods for EBM. (2023) website: http://digitaledition.plasticsmachinerymagazine.com/publication/?m=54208&i=800468&p=14&ver=html5.

The following works were presented in international conferences based on the present work.

- W. d. C. Galuppo, J. Romero, F. Alves, B. Machado, and J.M. Nóbrega, Thickness Distribution Optimization For Blow Moulded Parts, 17th OpenFOAM Workshop, Cambridge, Jul 2022.
- W. d. C. Galuppo, F. Alves, P. Santana, and J.M. Nóbrega, Optimising Thickness Distribution in Membrane Inflation Processes for Industrial Applications, 4TH FOAM@IBERIA MEETING, Santander, September 2022.
- W. d. C. Galuppo, F. Alves, P. Santana, and J.M. Nóbrega, Assessing Different Formulations to Simulate Membrane Inflation Processes, 18th OpenFOAM Workshop, Genoa, Jul 2023.

- W. d. C. Galuppo, F. Alves, P. Santana, and J.M. Nóbrega, Comparing Simulation Approaches for Modelling Membrane Inflation Phenomena, Polymer Process Innovation PPI, Guimarães, September 2023.
- W. d. C. Galuppo, F. Alves, P. Santana, and J.M. Nóbrega, Parison Programming Optimization in Extrusion Blow Moulding, FOAM@IBERIA23, Guimarães, November 2023.
- J.M. Nóbrega, Computational rheology et al. with OpenFOAM® computational library, 18th International Congress on Rheology, Rio de Janeiro, Dec 2020.
- F. Alves, W. d. C. Galuppo, P. Santana, N. Bento, B. Machado, and J.M. Nóbrega, Extrusion Blow Moulding Simulator: a Novel Approach to Support the Digital Transformation of the Packaging Industry, XXI Congresso da Sociedade Portuguesa de Materiais – MATERIAIS 2023, Guimarães, April 2023.
- J.M. Nóbrega, F. Alves, P. Santana, N. Bento, and B. Machado, Extrusion Blow Molding Simulator: Towards the Digital Transformation of the Packaging Industry, 38th International Conference of the Polymer Processing Society (PPS), St.Gallen, May 2023.
- F. Alves, W. d. C. Galuppo, P. Santana, N. Bento, B. Machado, and J.M. Nóbrega, Extrusion Blow Moulding Simulator: Towards the Digital Transformation of The Packaging Industry, FOAM@IBERIA23, Guimarães, November 2023.

Table of contents

Chapter 1 – Introduction 1

1.1 Extrusion Blow Moulding 2

1.2 State-of-the-art 4

1.2.1 Extrusion Die parameters 4

1.2.2 Sag and Swell 5

1.2.3 Extrusion Blow Moulding Simulation 6

1.2.4 Extrusion Blow Moulding Software 7

1.3 Motivation 8

1.4 Objectives 10

1.5 Thesis Structure 12

References 12

Chapter 2 – Extending the finite area method for enhanced simulation of deformable membranes and its application to extrusion blow moulding 21

Abstract 21

2.1 Introduction 22

2.2 Theoretical Formulation 24

2.2.1 Material Description 25

2.2.2 Mathematical Model 27

2.2.3 Membrane Formulation 30

2.2.4 Constitutive Models 32

2.2.5 Contact Model 37

2.3 Evaluation Examples 37

2.3.1 Material Characterisation 38

2.3.2 Spherical Balloon 38

2.3.3 Conceptual Mould 40

2.3.4 Real Bottle 43

2.4 Results and Discussions 44
2.4.1 Spherical Balloon 44
2.4.2 Conceptual Mould 47
2.4.3 Real Bottle 49
2.5 Conclusions 56
References 57
Chapter 3 – A computational framework for optimising extrusion blow moulding: Enhancing material efficiency and reducing waste for industry 4.0 61
Abstract 61
3.1 Introduction 62
3.2 Mathematical Modelling and Methods 65
3.2.1 Parison Programming 65
3.2.2 Parison Grouping 66
3.2.3 Optimisation Methodology 68
3.3 Case Studies 70
3.3.1 Cylindrical Bottle with Constant Target Thickness 71
3.3.2 Cylindrical bottle with variable target thickness 72
3.3.3 Oval-shaped bottle with variable target thickness 73
3.4 Results and Discussion 76
3.4.1 Cylindrical bottle with constant target thickness 77
3.4.2 Cylindrical bottle with variable target thickness 82
3.4.3 Oval-shaped bottle with variable target thickness 91
3.5 Conclusion 95
References 97
Chapter 4 – Extrusion Blow Moulding Process: Numerical Simulations of the Parison Extrusion Phase 103
Abstract 103
4.1 Introduction 104
4.2 Mathematical Modelling 106
4.2.1 Governing Equations 107

4.2.2 Constitutive Model 108
4.2.3 Two phase flow 111
4.2.4 Computational framework 114
4.2.5 Parison Cut 114
4.3 Materials and Methods 115
4.3.1 Extrusion Die Design 115
4.3.2 Extrusion Process Setup 117
4.3.3 Material and Rheological Characterisation 117
4.4 Evaluation Cases 120
4.4.1 Mesh Sensitivity Analysis 121
4.4.2 Algebraic and Geometric VoF Methods 123
4.4.3 Experimental Assessment 123
4.5 Results Analysis and Discussion 124
4.5.1 Mesh Sensitivity Analysis 124
4.5.2 Algebraic and Geometric Volume-of-Fluid (VoF) Methods 130
4.5.3 Experimental Assessment 131
4.6 Conclusion 133
References 135
Chapter 5 – Conclusion 142
5.1 Summary of Key Findings 142
5.2 Contributions to the Field 143
5.3 Future Research Directions 144
5.4 Final Remarks 145

List of figures

Figure 1.1: Schematic illustration of the EBM process main phases. 3

Figure 1.2: Schematic illustration of the extrusion die and terminologies. 5

Figure 1.3: Illustration of the sag and swell competing effects in the extrudate 6

Figure 1.4: Global Plastics production. 9

Figure 2.1: Configurations for two instants of a body by a Lagrangian description of motion. . . 25

Figure 2.2: Parison geometry and membrane cells discretisation. 33

Figure 2.3: Experimental data collected from uniaxial elongational tests at different rates (points) and the corresponding two-parameter Mooney-Rivlin model fitting (line). 38

Figure 2.4: Discretised spherical balloon. 39

Figure 2.5: Conceptual moulds used for the experimental measurements. 41

Figure 2.6: Experimental measurements of parison and digitalisation processing. 42

Figure 2.7: Moulds used to produce the bottle. 44

Figure 2.8: Several views of the real bottle produced by the EBM process and digitalised via X-ray microtomography. 44

Figure 2.9: Setup for the numerical simulation for the mould clamping and inflation phases in the EBM process. 45

Figure 2.10: Inflation pressure as a function of stretch for the spherical balloon with the imposed deformation. 46

Figure 2.11: Inflation pressure by stretches for the spherical balloon with the imposed internal pressure. 47

Figure 2.12: Frontal view analysis for the conceptual mould. 48

Figure 2.13: Experimental and numerical profiles for the parison at the end of mould clamping phase. 50

Figure 2.14: Thickness map of all views for the final inflated parison. 52

Figure 2.15: Profiles for the thickness distributions in two cross-sections. 53

Figure 2.16: Profiles for the thickness distributions in other two cross-sections. 54

Figure 2.17: Measurement verification for the thickness profile of plane YZ at the welding edge region. 55

Figure 3.1: Parison programming technique example. 66

Figure 3.2: Example of parison's cells grouping and its initial thickness definitions. 67

Figure 3.3: Example of target thickness definition for the inflated parison. 68

Figure 3.4: Schematic representation of the automatic optimisation process, outlining the iterative adjustment of parison thickness. 70

Figure 3.5: Meshes with four levels of refinements considered in the optimisation study. 72

Figure 3.6: Mould dimensions and relative positioning with the extruded parison (dimensions in millimetres). 72

Figure 3.7: Schematic of the final part with the defined non-uniform target thickness profile and corresponding optimisation regions. 73

Figure 3.8: Definitions of regions for the optimisation study and lengths dimensions in millimetres for the real bottle. 74

Figure 3.9: Definitions of regions for the optimisation study, and the black line is the final thickness profile for the experimental bottle obtained with a constant die gap opening. 75

Figure 3.10: Parison optimisation groups definition, alongside with their relative position and lengths (dimensions in mm). 76

Figure 3.11: Parison optimisation groups and thickness map obtained with mesh M3, before mould clamping. 78

Figure 3.12: Parison optimisation groups and thickness map obtained with mesh M3, post-inflation. 79

Figure 3.13: Variation of initial thickness profiles during the optimisation process across all simulated cases with coarser meshes. 80

Figure 3.14: Variation of initial thickness profiles during the optimisation process across all simulated cases with finer meshes. 81

Figure 3.15: Lines taken from the bottle and their corresponding indices to analyse the final thickness profiles. 82

Figure 3.16: Final thickness profile evolution during the optimisation process for the simulated cases runs 1 to 5 and 10 using coarser meshes. 83

Figure 3.17: Final thickness profile evolution during the optimisation process for the simulated cases runs 1 to 5 and 10 using finer meshes. 84

Figure 3.18: Variation of defined thicknesses in optimisation, at axial groups midpoints, through the optimisation process for all simulated cases with coarser meshes. 85

Figure 3.19: Variation of defined thicknesses in optimisation, at axial groups midpoints, through the optimisation process for all simulated cases with finer meshes 86

Figure 3.20: Evolution of the parison initial thickness profiles along the optimisation process for all cases with coarser meshes. 87

Figure 3.21: Evolution of the parison initial thickness profiles along the optimisation process all cases with finer meshes. 88

Figure 3.22: Evolution of the bottle thickness profiles along the optimisation process for all cases with coarser meshes. 89

Figure 3.23: Evolution of the bottle thickness profiles along the optimisation process for all cases with finer meshes. 90

Figure 3.24: Colour map of distinct fields of the inflated parison. 91

Figure 3.25: Thickness distributions for the two optimisation techniques addressed 92

Figure 3.26: Comparison of initial and final thickness profiles between multi-mesh and single-mesh (M4) optimisation processes. 93

Figure 3.27: Final thickness maps for the oval-shaped bottle case study. 94

Figure 3.28: Final thickness profiles for the oval-shaped bottle case study. 95

Figure 3.29: Real parison geometry dimensions measurements, obtained via constant die gap opening and via programmed parison technique. 96

Figure 4.1: Illustrative representation of the phase indication, α, for a two-phase flow, solved by the Volume of Fluid method. 112

Figure 4.2: Extruded parison immediately before, and after cut. The illustration is with regard a full 360 degrees revolution parison, along with the phase fraction, field used to perform the cut. 115

Figure 4.3: Extrusion geometry design with defined parameters. 116

Figure 4.4: Results obtained on the frequency sweep tests of the HDPE 5502 at processing temperature of $200\ ^{\circ}\mathrm{C}$. 118

Figure 4.5: PTT 8 modes constitutive model fitting with HDPE 5502 rheological data at processing temperature of $200\ ^{\circ}\mathrm{C}$. 119

Figure 4.6: Naming used to distinguish the domain boundary regions used in the extrusion phase simulations. 120

Figure 4.7: Mesh refinements for all the meshes. 122

Figure 4.8: Mesh refinements effects in the phase fraction α field. 125

Figure 4.9: Mesh refinements effects in interface position between the two phases. 126

Figure 4.10: Mesh refinements effects in pressure field for the air phase fraction. 126

Figure 4.11: Mesh refinements effects in polymeric extra-stress tensor field for the mixture fraction. 127

Figure 4.12: Mesh refinements effects in the polymeric extra-stress of mixture fraction, a) location of the centroids of the last cells in the channel and b) polymeric extra-stress variations in the the dimensionless length through the channel width. 128

Figure 4.13: Mesh refinements effects in the phase fraction interface position, a) Location for the cutting plane used to take the profiles, b) Phase fraction full profile for all meshes refinement in the cut plane, and c) Phase fraction profile at the transition location between the air and polymer phases. 129

Figure 4.14: Comparison of the AVoF and GVoF methods for representing the interface of the phase fraction field. 130

Figure 4.15: Comparison of the phase fraction (α) field between AVoF and GVoF methods for meshes M3, M4, and M5. 131

Figure 4.16: Comparison of interface positioning for the full parison extruded in a long chamber and the parison from M3 using a shorter chamber. 132

Figure 4.17: Interface location for different support air velocity conditions in the mandrel. a) Full geometry, b) zoomed-in view of the die gap, c) zoomed-in view of the outlet. 133

Figure 4.18: Measurements for the parison: a) thickness distribution and b) diameter swell. . . 134

CHAPTER 1 Introduction

Blow moulding is a manufacturing process applied for the production of hollow plastic parts through the inflation of a heated plastic tube, commonly designated by parison, in extrusion blow moulding, or preform, in injection blow moulding. Likewise in various other industrial processes, it involves the application of heat and forces to convert raw material into a final desired shape, also aiming at achieving specific final properties. Normally, the parison or preform is subjected to blown forces until it conforms to the desired final shape, which is often dictated by a mould cavity, where its walls constrains the parison as it undergoes touching it during the blowing process [1–3]. The process of blow moulding is, in general, classified and distinguished by three main techniques, as outlined below:

- Extrusion Blow Moulding: The produced parison is obtained via the extrusion process, and then inflated within a mould cavity [4].

- Injection Blow Moulding: The parison is produced in the form of a preform using the injection moulding process. Subsequently, this preform is preheated and then inflated within a second mould to produce the final part [5, 6].

- Injection Stretch Blow Moulding: This process is similar to injection blow moulding, but during the inflation phase of the parison within a second mould, a shaft pushes the bottom part of the preform downstream, stretching it while applying blowing pressure, simultaneously [7, 8].

Among these methods, extrusion blow moulding has been chosen as the main focus of this research due to various factors, which will be discussed in the following sections of this chapter.

The remaining of this chapter covers the introduction of the Extrusion Blow Moulding (EBM) process, explaining its importance and emphasising its significance in the current global manufacturing landscape. Subsequently, there is the state-of-the-art section providing the concepts of the EBM along with the simulation context. Following, there is a section dedicated to present and discuss the motivation trailing this work, followed by the section of its objectives. Finally, Section 1.5 provides an overview of the structure of the remaining chapters of this thesis.

1.1 Extrusion Blow Moulding

The Extrusion Blow Moulding (EBM) stands out among the aforementioned blow moulding processes, as a manufacturing process for its versatility and usage in the plastics industry, and its ability in producing a broad application spectrum with hollow parts dimensions ranging from millimetres to metres [7, 9]. It is capable of manufacturing small containers in the millimetres scale, up to large as chemical toilets, double wall, and industrial components, such as 20,000 litters super-large water tank [2]. Moreover, the capability to handle much more complex final geometries such as bottle with handle, and even a plastic tool box with the detailed slots to dispose and attach the tool can be produced via EBM, while the others are not capable of [10]. Although less pressure-intensive compared to injection moulding, this technique plays a vital role in the production of durable and precisely shaped plastic products [8]. The versatility of EBM makes it a preferred choice in various applications, particularly in the packaging industry, where its efficiency and the high quality of the products it produces are valued and required [2, 3].

The EBM is a cyclic process that encompasses distinct phases, which are depicted in Figure 1.1 and are described as follows:

- Parison Extrusion (Phase I): The process cycle starts by melting the plastic material, with the use of an extruder, and pushing the resultant molten plastic through tooling set formed by a mandrel and die. These tooling set, usually annular, shapes the molten into a tube-like structure, commonly designated by parison. During this phase the air can be blown in the internal part of the parison to support its shape, i.e. to avoid the tube collapsing. In addition, sometimes, the bottom part of the parison can be closed, a technique known as pinch-off, while small quantity of air is blow to enlarge the parison shape during this phase. A noteworthy aspect of this phase is the possible use of a sophisticated technique, known as programmed parison, that allows for precise modification of the extruded thickness, resulting in a non-uniform distribution of thickness along the parison length [9, 10].

- Mould Clamping (Phase II): The parison is subsequently clamped into a mould. It often involves leaving a single opening, typically at the top, to facilitate the next phase procedures. Also, it is common to cut the parison with a hot wire during this processing phase. At the end of this phase, the closed moulds moves carrying the clamped parison to another place and continue with the next phase, while the parison keeps being continuously extruded. [1–3]

- Inflation (Phase III): During this phase, compressed air is blown by a nozzle into the inner cavity of the parison through the opening left at the previous phase. This action results in a substantial increase in pressure on the inner surface of the parison. The pressure difference between the inner and outer parison surfaces creates a resultant force that deforms the parison and gradually expands it to conform to the mould cavity in which it is confined, thus shaping it into its desired final form. Air-vents air are placed in strategical locations to avoid entrapped air

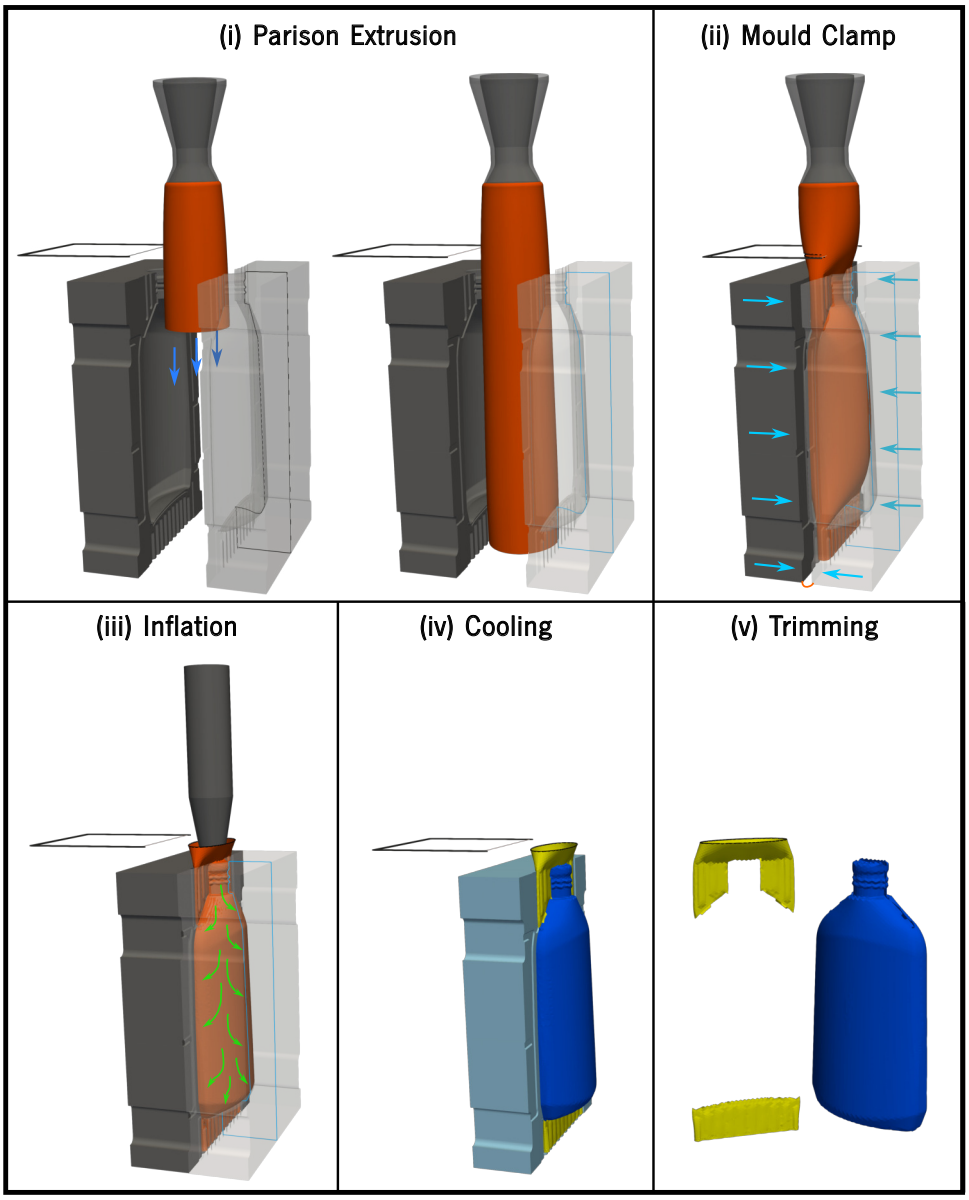


Figure 1.1: Schematic illustration of the EBM process main phases.

bubbles to interfere the parison from displacing and touching the moulds surface, conforming to the desired final shape. Additionally, when producing bottles, it is common that, during its displacement, the nozzle used to blow the air mechanically compress the polymer melt between the nozzle outer surface and the mould, near the top region of the bottle, where the bottle neck is formed. These mechanical compressions ensure proper capturing of all the intricate details that cannot be achieved just by air blowing. [1–3]

- Cooling (Phase IV): Once the parison gets in contact with the mould walls, the cooling process begins, mainly driven by the lower mould temperature. The mould temperature is controlled via internal cooling circuits, usually by water, to extract the heat, which is transferred from the hot parison to the mould by conduction. The primary goal is to solidify the molten plastic as quickly as possible, as it is during this phase that the final shape and properties are definitively

established [9, 10].

- Trimming and Ejection (Phase V): Once the polymer reaches the appropriate stiffness, the mould opens, and the solidified part is ejected. Excess plastic, known as flash, is then trimmed away, concluding the processing cycle [9, 10].

Slight variations of these phases can be found, such as intermittent extrusion, the use of a knife to parison cut instead of hot wire, although the descriptions provided are the most commonly applied in the context of the EBM process [4, 9, 10]. These phases collectively determine the quality and physical characteristics of the final product, making them crucial focal points for both practical application and theoretical modelling. Phases I to IV are of outstanding importance in shaping the final properties of the manufactured part. Therefore, these phases hold exceptional significance when considering numerical modelling for the process computational simulations.

1.2 State-of-the-art

1.2.1 Extrusion Die parameters

The extrusion die is utilised to extrude the parison and consists of metal components, typically made of steel, with one serving as a mandrel (inner component) and the other known as a bush (outer component). These components are schematically illustrated in Figure 1.2 a). The molten polymer is forced through the annular channel formed by the cavity between these two components. In service, the mandrel and bush can be adjusted in terms of their relative positioning, with the mandrel moving up and down within the bush as indicated by the arrows in Figure 1.2 a), a feature designated by parison programming.

In terms of design, dies are categorised based on the angle at which they are set to extrude the parison. These designs are to reach appropriated diameters for the extruded parison, increasing and decreasing it from the main diameter of the extruder. The three most common die shapes used in the EBM process are straight, diverging, and converging. These three types can be seen in Figure 1.2 a), and Figure 1.2 b) illustrates how they can be characterised in terms of angle [10–12].

Another important aspect concerns the positioning of the mandrel and bush, where the lowest plane of the mandrel can be either below or above the lowest plane of the bush. This positioning determines the die gap size, referred to as Δr_{gap} in Figure 1.2 c). Lastly, the die contraction ratio (r^*_{CR}) parameter measures the extent of channel contraction that the polymer will undergo in the extrusion die flow channel. This ratio is given by dividing the radius variation at middle region of the extrusion channel (Δr_{mid}) by the die gap thickness (Δr_{gap}), i.e., $r^*_{\text{CR}} = \Delta r_{\text{mid}} / \Delta r_{\text{gap}}$, as shown in Figure 1.2 c) [10–12].

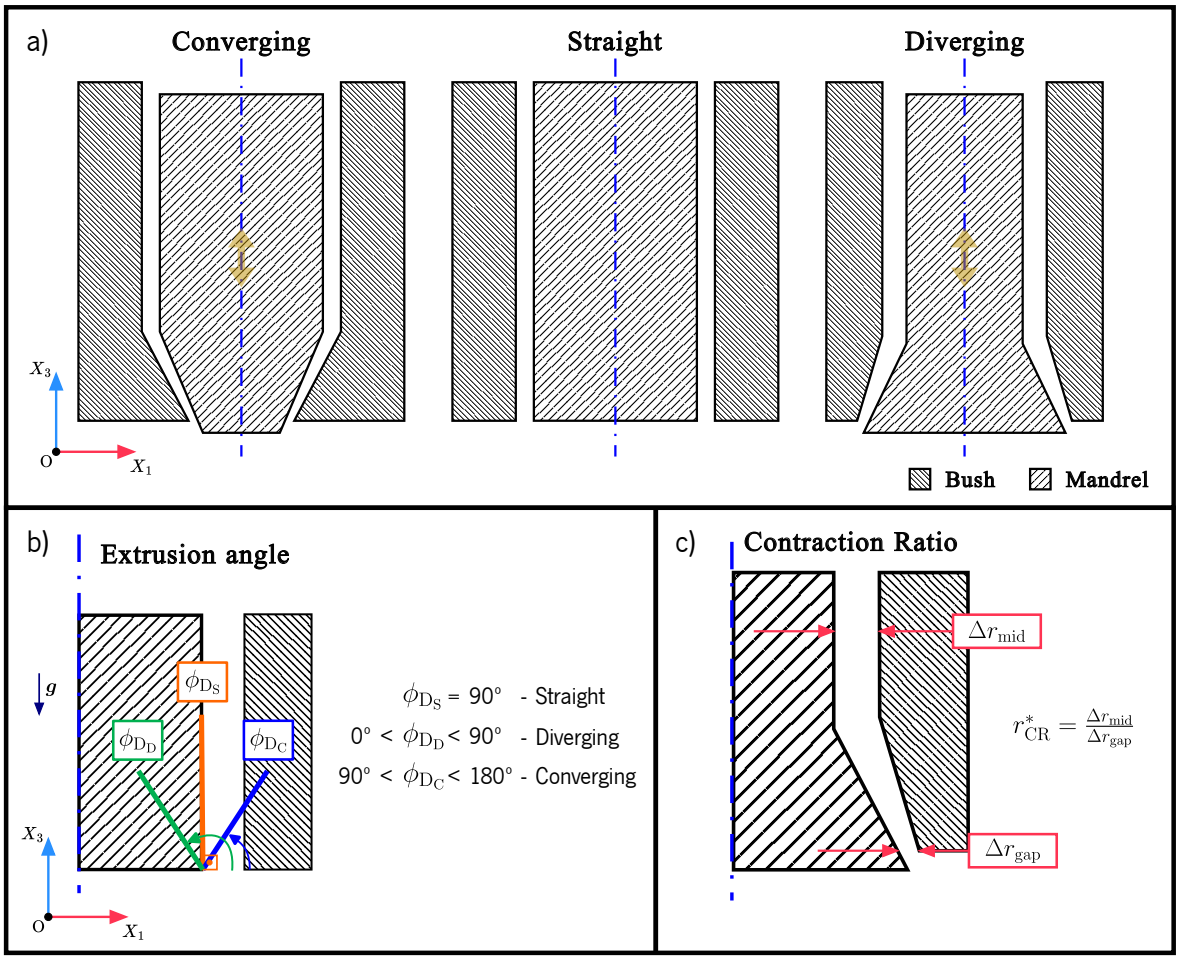


Figure 1.2: a) Examples of all three classified types. b) Angle measurement ranges for each type. c) Definition of die contraction ratio. (adapted from Garcia-Rejon et al. [13])

1.2.2 Sag and Swell

The polymer melt exhibits viscoelastic behaviour, combining the characteristics of both viscous and elastic materials. This behaviour significantly influences the material swell as it exits the die [11, 14]. Die swell refers to the expansion of the molten material perpendicular to the flow streamlines at the die exit, as shown in Figure 1.3 a). The material swell, after exiting the die lip, is attributed to two distinct phenomena: the transformation of the polymer melt velocity profile, from quasi-parabolic, inside the die at flow channel, to flat, after the leaving the confined flow, and the relaxation of the polymer molecules, which are deformed inside the flow channel [1, 11, 14]. The phenomenon called as diameter swell is of particular interest on the EBM process, since it promotes changes on the parison geometry and dimensions. The diameter swell is usually quantified by the ratio of the parison outer diameter divided by the bush (or die) outer diameter, as follows: [15–18]:

$$d^*_{\text{swell}} = \frac{d_{\text{parison}}}{d_{\text{die}}}, \tag{1.1}$$

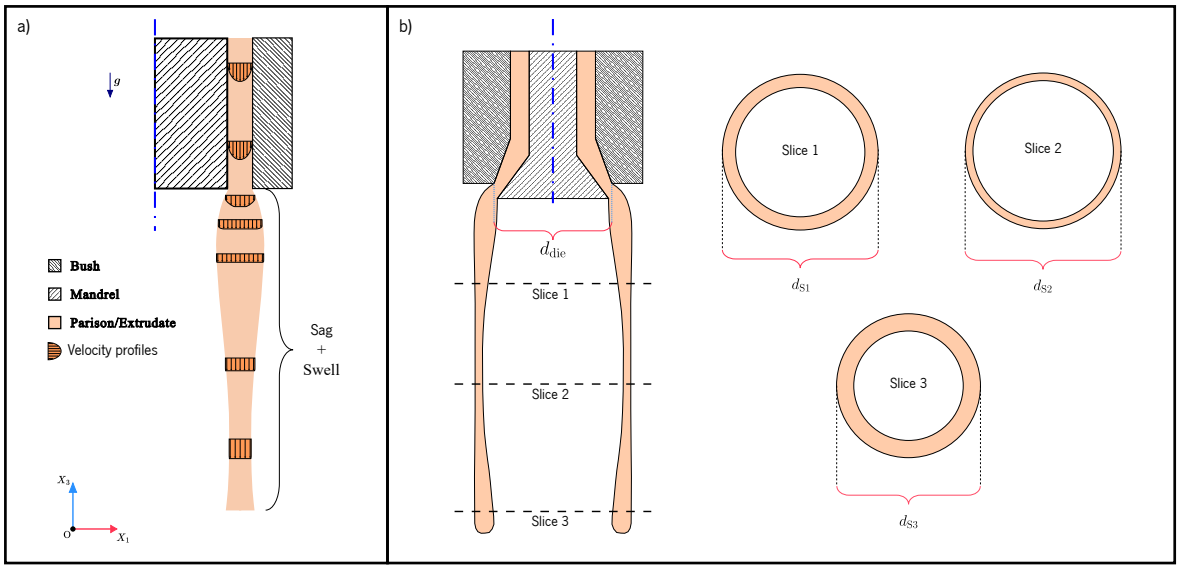


Figure 1.3: Illustration of the sag and swell competing effects in the extrudate: a) Representation in a simplified cross-sectional view showing velocity profiles and the deformation effects; b) Detailed depiction of parison geometry, highlighting diameter changes across different slices (Slice 1, Slice 2, and Slice 3) due to sag and swell phenomena

where d^*_{swell} is the extrudate diameter swell, d_{die} is the die diameter measured at the bush, and d_{parison} is the parison external diameter, e.g. the diameters d_{S1}, d_{S2} and d_{S3} of Figure 1.3 b) [19].

Another significant phenomenon is the sag effect, which is observed in the extrudate that has already exited the extrusion die flow channel. As the molten material is extruded, both its quantity and weight increase, causing the lower regions of the parison to stretch the upper regions due to the influence of gravity. The stretching effect is directly influenced by the extrusion temperature and the polymer melt rheological properties, and lead to a significantly thinner extrudate, as illustrated in Figure 1.3 a) [11, 20–22].

The study of the swell and sag phenomena is relevant for EBM because they have a direct impact on the final geometry of the parison.

1.2.3 Extrusion Blow Moulding Simulation

Early efforts to simulate the extrusion phase in Extrusion Blow Moulding (EBM) began with Dealy and Orbey [12], who developed a lumped-parameter model to predict parison length and shape, though it inaccurately accounted for sag and swell. Subsequent studies, such as those by Garcia-Rejon et al. [13], explored the influence of die design on parison swell, with findings highlighting how die geometry and material properties affect thickness and diameter swell. Tanoue et al. [23, 24] expanded on these concepts by predicting various swell types using the Giesekus model. Later contributions, including those by Huang et al. and Tang et al. [25], focused on refining viscoelastic models like K-BKZ and Phan–Thien–Tanner (PTT) for more accurate industrial-scale predictions, emphasising the need

for material-specific parameters and advanced numerical methods to model material swell phenomena under different die configurations.

Due to the similarities between the clamping and inflation phases of EBM and the forming phase of thermoforming, simulation research works in both areas overlaps, particularly regarding simulation and material processing [26–28]. Khayat et al. [29] pioneered modelling efforts by simulating fluid flow within a cavity using a membrane model, representing the parison's inflation and addressing back pressure effects. Debbaut et al. [30] compared experimental data with numerical predictions for blow-moulded parts, noting minor discrepancies due to factors like parison shape and temperature. Nam et al. [31] explored free-inflation in thermoforming, emphasising the importance of accounting for initial temperature distribution, especially for thicker sheets. Marckmann et al. [32] developed a computational model for EBM and thermoforming, integrating adaptive mesh refinement and achieving notable accuracy when comparing numerical and experimental results, though they recommended refining constitutive models to include temperature effects.

In what concerns the simulation of the entire EBM process, Laroche et al. [33] provided a comprehensive study about a fuel tank, covering parison formation, inflation, solidification, and warpage. It used an integral viscoelastic model to calculate the parison sag, a semi-empirical equation for swell, and a non-isothermal viscoelastic model for inflation, noting that temperature variations during extrusion significantly impact inflation behaviour. Warpage and residual stress were modelled with a linear viscoelastic solid model, and the simulations largely matched experimental data, though some deviations were noted. Tanifuji et al. [34] extended this work by using a Lagrangian Eulerian (LE) FEM with automatic re-meshing to simulate the competing effects of swell and drawdown during parison formation. While their method showed good agreement with experiments, some discrepancies were attributed to limitations in the LE formulation, including issues with boundary conditions and artificial viscosity. Both studies focused on axisymmetric parisons, though real-world applications often use non-axisymmetric designs [30, 35].

1.2.4 Extrusion Blow Moulding Software

In order to simulate the EBM process, there are three distinct options available as proprietary simulation software: BlowSim, B-Sim [36], and Polyflow [37]. BlowSim and B-Sim originated from a research project in Canada [38, 39] and have become the most widely used software in the EBM industry, with B-Sim being particularly relevant [36]. However, these software options do not consider the parison extrusion phase in the simulation process, which significantly limits the capability for an integrated optimisation method [40]. Consequently, obtaining a parison with the desired characteristics suggested by the simulation software often requires a trial-and-error process, and in some cases, may not even be achievable.

During its early development at the Université Catholique de Louvain (Belgium), Polyflow was the only software available in the market for simulating various polymer processing techniques using

viscoelastic models [37]. However, after its acquisition by Fluent in 1997, and subsequently by Ansys in 2006, the rate of development for Polyflow significantly decreased. Although Polyflow allows the simulation of the extrusion, mould clamp, and inflation phases separately for EBM process simulation, it does not provide alternatives for linking the results of these different phases. As a result, the integrated process optimisation capability of Polyflow is substantially limited.

1.3 Motivation

The demand for plastics and their production have experienced exponential growth over the past seven decades, as illustrated in Figure 1.4 a). The packaging industrial sector emerges as the primary consumer of plastics from this exponential growth, where it have been consistently following this trend as schematically presented in Figure 1.4 b).

Among various industries, the packaging sector accounts for nearly one third of total plastic usage, while the construction sector comprises approximately one sixth [41]. The blow moulding sector is projected to grow annually by 5% up to 2030 [9, 43]. Furthermore, 40% of the high-density polyethylene (HDPE) production in the United States, approximating 5.8 million tons, was consumed by the EBM process [9]. Such significant material usage underscores the importance of studying the EBM process for efficiency and sustainability purposes.

Efforts are currently underway to enhance industrial process efficiency, optimising material usage, and minimising waste generation through recycling and direct improved resources' utilisation such as material, and indirect such as energy and transportation [44–46]. This has prompted the need to improve process efficiency in the packaging sector in order to promote responsible material usage and waste reduction, ultimately working towards the critical goal of reducing plastic consumption [44–49]. These endeavours are expected to yield significant environmental, social and economic benefits, particularly in a society grappling with the challenge of reducing plastic consumption [50, 51].

Numerical Simulations have seen an increasing application and utilisation across diverse industries and fields in the last decades, providing valuable insights to guide processes design, products development, performance improvements, and manufacturing optimisations. Mathematical modelling and numerical simulations are also valuable frameworks and instruments for predicting potential failures and performance issues, previously to the actual implementation of the process, or to manufacture the real final product or device [52–60].

The advent of computers and its digital transformation is permeating various industrial sectors [61–65]. Following three significant industrial revolutions, the current stage is now transitioning into its fourth revolution, widely recognised as Industry 4.0 [66–69]. This new era is distinguished by enhanced automation, sophisticated data exchanges in manufacturing technologies, and the introduction of several novel concepts such as cyber-physical systems, the Internet of Things (IoT),

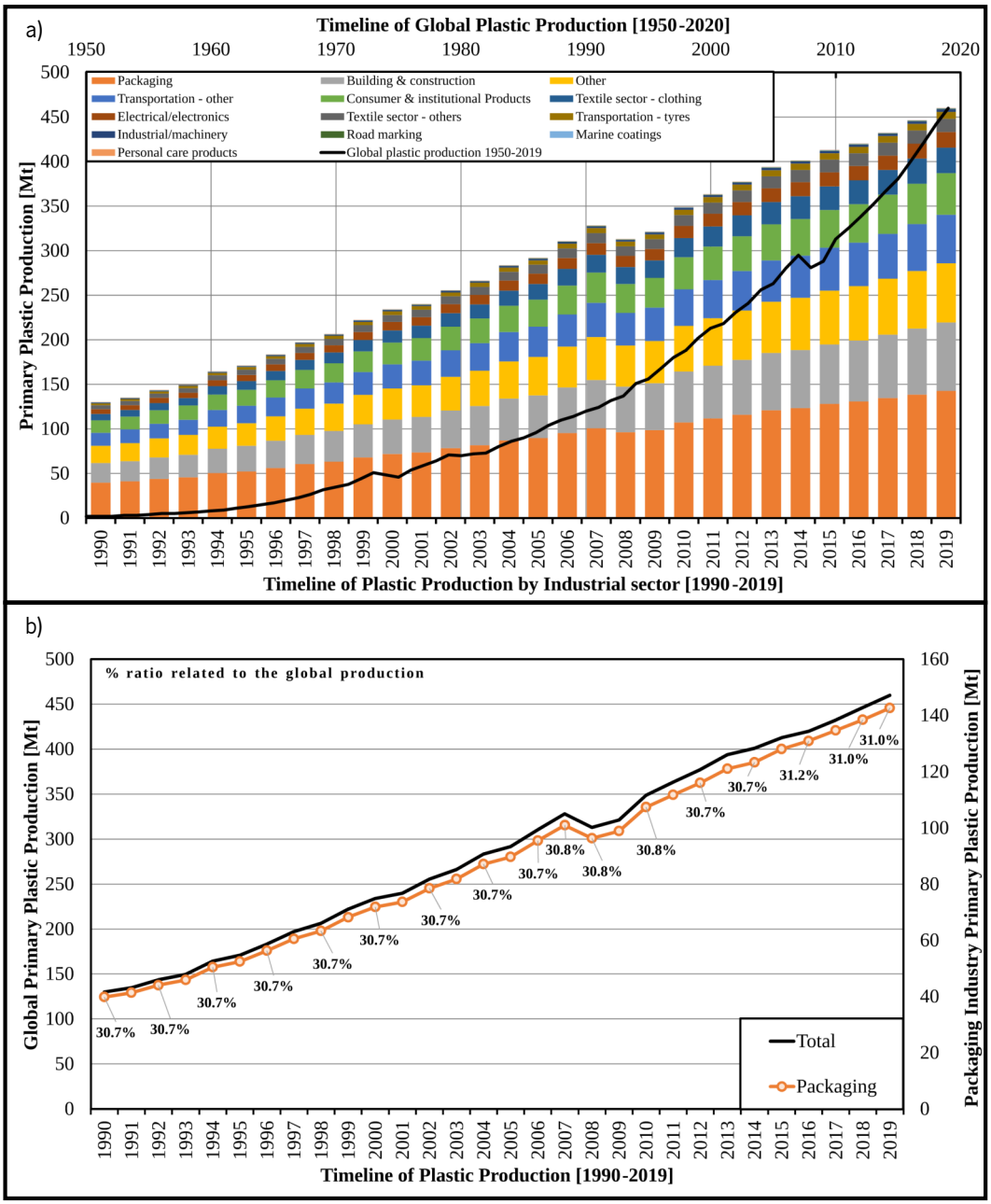


Figure 1.4: a) The global primary plastics production from 1950 to 2019 and by industrial sector from 1990 to 2019, b) Timeline between 1990 and 2019 of all primary plastic production along with the packaging industry [41, 42].

cloud computing, cognitive computing, digital twins, and digital manufacturing [70–76]. The primary objectives of Industry 4.0 includes elevating productivity, flexibility, and efficiency, alongside minimising resource consumption to facilitate more tailored product manufacture [74, 77, 78]. The enduring success of Industry 4.0 is predicated on the widespread integration of these modern technologies across diverse industrial sectors [74, 79].

Numerical simulations are indispensable for the digital transformation of the industry, serving as a crucial component within this broader context. Therefore, modernising manufacturing practices

such as the digital manufacturing [80, 81].

Optimising resources consumption, particularly in material use, is imperative for sustainable manufacturing [82–84]. Various optimisation strategies—such as topology, shape, size, and material optimisation—have been widely explored to achieve the best possible outcomes in terms of performance, strength, weight, cost, and sustainability. These approaches aim to balance efficiency with reduced environmental impact, ensuring that manufacturing processes contribute to a more sustainable industrial perspective. [85–88]. The material distribution optimisation within the EBM process is a field that remains active due to its impact on sustainability and the quest to minimise plastic usage in manufactured parts [89–92].

1.4 Objectives

The main objective of the present work is to develop a computational framework for conducting numerical simulations of the phases of the EBM process. This framework aims to address the limitations of existing tools and enhanced modelling capabilities for a more accurate simulation of EBM phases.

In proprietary simulation software, such as those discussed in Section 1.2.4, users are restricted from modifying the source code, which limits the ability to adapt the software to specific modelling requirements. This restriction presents a significant obstacle when attempting to improve accuracy or extend functionality. To overcome these limitations, users may develop their own custom codes or contribute to open-source computational libraries.

Open-source platforms provide access to their source code, allowing for utilisation, examination, and modification, thereby fostering collaboration and the advancement of simulation technologies. A notable alternative that emerges in the context of open-source platforms is OpenFOAM ® [93], an extensible computational library capable of solving multi-physics problems and performing parallel computing. OpenFOAM ® has achieved widespread usage within both academic and industrial communities globally. It is capable to solve fluid dynamics problems [94–97] as well as solid mechanics-related problems [98–101]. OpenFOAM ® proves to be a particularly feasible tool for customisation. Given its capabilities and the identified limitations of currently available options, it has been selected as the preferred platform for this work. The existing classes in OpenFOAM ® can be utilised and extended with the necessary complementary capabilities to simulate the EBM process. Furthermore, the intrinsic parallelisation capability of the OpenFOAM ® computational library will facilitate the simulation of complex scenarios within a reasonable timeframe.

This PhD project is part of a broader initiative aimed at developing an interconnected model of the various stages involved in the EBM process, with a focus on the extrusion, mould-clamping, and inflation phases. One of the secondary objectives is the precise modelling of the extrusion phase using efficient approaches. Specifically, the goal is to accurately predict the geometry of the extruded

parison while incorporating a strategy to simulate the cutting process of the parison.

In the context of modelling the mould-clamping and inflation stages, multiple methodologies will be implemented and evaluated to identify the most effective approach. A membrane-based formulation is anticipated, as it provides accurate modelling for a wide range of products manufactured via EBM. However, various approaches such as cell-centred or vertex-centred, as well as dynamic or quasi-static methods with explicit method, will be explored. The aim is to determine the approach that offers the best balance between numerical stability and result accuracy.

Given the distinct nature of the extrusion, mould-clamping, and inflation phases, unique modelling strategies are anticipated for each phases; thus, a suitable connection between these phases should be devised and implemented.

As mentioned in Section 1.2.1, during extrusion the local thickness of the parison can be adjusted. A secondary objective of this research is to develop an automated method for specifying the thickness distribution along the length of the parison. This approach will ensure that the desired thickness distribution is achieved in the final product.

By integrating these modelling strategies, this research will not only enhance our understanding of the EBM process but also improve accuracy in predicting product outcomes, ultimately contributing to the optimisation of industrial EBM techniques.

Based on the above, this work aims to address several shortcomings in existing codes, particularly concerning the optimisation of parison thickness distribution and the interconnection of different phases. From a numerical perspective, the study intends to introduce innovative advancements, including the simulation of parison formation through extrusion, with the capability to model both the polymer and the air commonly used to assist the parison shape during its extrusion, thereby employing a multiphase flow approach. Additionally, the study will provide capabilities for numerical simulation of the clamping and inflation phases, where significant nonlinearities are anticipated due to large deformations, contact, and material behaviour. Finally, an environment will be established to automate the optimisation of the EBM process control variables, aiming to achieve or approximate results that align with the desired final criteria for the final product, such as material distribution. It is expected that the developed computational framework will yield more accurate results compared to current codes and address some of the industry's most pressing needs, including the simulation of general parisons, waste reduction, and improved thickness distribution for final parts produced via the EBM process.

The principal outcome of this research is expected to be the promotion of computational modelling tools as a support for design tasks within the extrusion blow moulding industry, which plays a significant role in the plastic packaging sector. These advancements are expected to enhance process efficiency, resulting in material and waste savings, with considerable societal and economic impacts at a time when reducing plastic consumption is crucial.

1.5 Thesis Structure

The remainder of this thesis is organised into four chapters, three of which are based on published papers and manuscripts that are in preparation for publication, all stemming from the work developed during this research.

In Chapter 2, a shell membrane formulation is proposed and implemented using the OpenFOAM ® computational library's finite area class. The implementation is initially validated against an analytical solution and subsequently extended to experimental verification, where the simulated results are compared with data obtained from experimental measurements.

Chapter 3 presents the development of a computational framework designed specifically for optimising parts produced through EBM processes. This framework builds upon the developments presented in Chapter 2 to perform simulations. The control variables, discretised to mirror the real process, are adjusted with a focus on enhancing the effectiveness of integrating EBM processes into Industry 4.0 and optimising material distribution in EBM-produced parts. The framework's efficacy is evaluated through simulated test cases, as well as an experimental comparison between non-optimised and optimised bottle production.

Chapter 4 focuses on simulating the extrusion phase of the EBM process and investigating its influence on parison formation. This phase employs RheoTool (version 5.0) [102], an open-source toolbox based on OpenFOAM ® that utilises the finite volume method to simulate complex fluid flows of Generalised Newtonian Fluids (GNF) and viscoelastic fluids. Additionally, a newly developed solver that employs a geometric method for capturing the interface is introduced to enhance the accuracy of the final results. The results are evaluated from multiple perspectives, including a comparison with experimental measurements.

Finally, the concluding chapter of this thesis discusses the overall findings of the research, reflecting on the proposed objectives. It also outlines potential directions for future work.

References

[1] John Goff, Tony Whelan, and Don DeLaney. The dynisco extrusion processors handbook. Edition, 2:284, 2000.

[2] MO Ghafur, B Koziey, and J Vlachopoulos. Simulation of thermoforming and blowmolding—theory and experiments. Rheological Fundamentals of Polymer Processing, pages 321–383, 1995.

[3] Luis F Ramos-De Valle. Principles of polymer processing. Handbook of Polymer Synthesis, Characterization, and Processing, pages 451–461, 2013.

[4] Samuel L Belcher. Practical Extrusion Blow Molding, volume 54. CRC Press, 1999.

[5] Samuel L Belcher. Practical guide to injection blow molding, volume 71. CRC Press, 2007.

[6] Benoit Cosson, Luc Chevalier, and Gilles Régnier. Simulation of the stretch blow moulding process: from the modelling of the microstructure evolution to the end-use elastic properties of polyethylene terephthalate bottles. International Journal of Material Forming, 5:39–53, 2012.

[7] G. H. Menary, C. W. Tan, M. Picard, N. Billon, C. G. Armstrong, and E. M. A. Harkin-Jones. Numerical Simulation of Injection Stretch Blow Moulding: Comparison with Experimental Free Blow Trials. AIP Conference Proceedings, 907(1):939–944, 04 2007.

[8] Ottmar Brandau. 1 - a short history of stretch blow molding. In Ottmar Brandau, editor, Stretch Blow Molding (Second Edition), Plastics Design Library, pages 1–4. William Andrew Publishing, Oxford, second edition edition, 2012.

[9] Samuel L. Belcher. 13 - blow molding. In Myer Kutz, editor, Applied Plastics Engineering Handbook (Second Edition), Plastics Design Library, pages 265–289. William Andrew Publishing, Moscow, Ohio, second edition edition, 2017.

[10] Michael Thielen. Extrusion Blow Molding. Carl Hanser Verlag GmbH & Company KG, 2021.

[11] John Vlachopoulos and Nickolas D Polychronopoulos. Understanding rheology and technology of polymer extrusion, 2019.

[12] JM Dealy and Nese Orbey. A model for parison behavior in the extrusion blow molding process. AIChE journal, 31(5):807–811, 1985.

[13] A Garcia-Rejon, R.W DiRaddo, and M.E Ryan. Effect of die geometry and flow characteristics on viscoelastic annular swell. Journal of Non-Newtonian Fluid Mechanics, 60(2):107–128, 1995.

[14] F.A. Morrison. Understanding Rheology. Raymond F. Boyer Library Collection. Oxford University Press, 2001.

[15] Z. Tadmor and C.G. Gogos. Principles of Polymer Processing. Wiley, 2013.

[16] Christian Hopmann and Walter Michaeli. 5 - monoextrusion dies for thermoplastics. In Christian Hopmann and Walter Michaeli, editors, Extrusion Dies for Plastics and Rubber (Fourth Edition), pages 167–288. Hanser, fourth edition edition, 2016.

[17] R. Ahmed, R.F. Liang, and M.R. Mackley. The experimental observation and numerical prediction of planar entry flow and die swell for molten polyethylenes. Journal of Non-Newtonian Fluid Mechanics, 59(2):129–153, 1995.

[18] Milivoje Kostic and Louis Reifschneider. Design of extrusion dies. Encyclopedia of Chemical Processing, 01 2006.

[19] Alan H. Wagner and Dilhan M. Kalyon. Parison formation and inflation behavior of polyamide-6 during extrusion blow molding. Polymer Engineering & Science, 36(14):1897–1906, 1996.

[20] D.V. Boger and K. Walters. Rheological Phenomena in Focus. Contributions to Economic Analysis. Elsevier Science, 1993.

[21] Chris Rauwendaal. Understanding Extrusion. Hanser Publications, 3 edition, November 2018.

[22] H.F. Giles, E.M. Mount, and J.R. Wagner. Extrusion: The Definitive Processing Guide and Handbook. Plastics Design Library. Elsevier Science, 2004.

[23] Shuichi Tanoue, Yoshifumi Kuwano, Toshihisa Kajiwara, Kazumori Funatsu, Kousuke Terada, and Masashi Yamabe. Numerical simulation of blow molding—viscoelastic flow analysis of parison formation. Polymer Engineering & Science, 35(19):1546–1554, 1995.

[24] Shuichi Tanoue, Toshihisa Kajiwara, Kazumori Funatsu, Kousuke Terada, and Masashi Yamabe. Numerical simulation of blow molding—prediction of parison diameter and thickness distributions in the parison formation process. Polymer Engineering & Science, 36(15):2008–2017, 1996.

[25] Han-Xiong Huang, Yan-Sheng Miao, and Dong Li. Numerical prediction and experimental validation of viscoelastic annular swell. Advances in Polymer Technology, 25(4):259–269, 2006.

[26] James L Throne. Understanding thermoforming. Hanser Gardner Publications Cincinnati, OH, 2008.

[27] Peter W. Klein. Fundamentals of Plastics Thermoforming. Springer International Publishing, 2009.

[28] Syed Ali Ashter. Thermoforming of Single and Multilayer Laminates. William Andrew Publishing, 2014.

[29] Roger E Khayat and Paul Raducanu. A coupled boundary/finite-element approach for the three-dimensional simulation of air venting in blow molding and thermoforming. International journal for numerical methods in engineering, 43(1):151–174, 1998.

[30] Benoît Debbaut, Olivier Homerin, and Noor Jivraj. A comparison between experiments and predictions for the blow molding of an industrial part. Polymer Engineering & Science, 39(9):1812–1822, 1999.

[31] Gi Joon Nam, Jae Wook Lee, and Kyung Hyun Ahn. Three-dimensional simulation of thermoforming process and its comparison with experiments. Polymer Engineering & Science, 40(10):2232–2240, 2000.

[32] Gilles Marckmann, Erwan Verron, and Bernard Peseux. Finite element analysis of blow molding and thermoforming using a dynamic explicit procedure. Polymer Engineering & Science, 41(3):426–439, 2001.

[33] D. Laroche, K. K. Kabanemi, L. Pecora, and R. W. Diraddo. Integrated numerical modeling of the blow molding process. Polymer Engineering & Science, 39(7):1223–1233, 1999.

[34] Shin-Ichiro Tanifuji, Tsuyoshi Kikuchi, Jun-Ichi Takimoto, and Kiyohito Koyama. Overall numerical simulation of extrusion blow molding process. Polymer Engineering & Science, 40(8):1878–1893, 2000.

[35] Kit L. Yam, editor. The Wiley Encyclopedia of Packaging Technology. John Wiley & Sons, Hoboken, NJ, 3rd edition, 2009.

[36] Accuform. B-SIM. Accuform, Jetelova 582, Czech Republic, 2018.

[37] ANSYS Inc. Polyflow. ANSYS Inc., Canonsburg, PA, 1995. Software.

[38] K Kouba, O Bartos, and J Vlachopoulos. Computer simulation of thermoforming in complex shapes. Polymer Engineering & Science, 32(10):699–704, 1992.

[39] K Kouba and J Vlachopoulos. Modeling of thermoforming and blow molding. In Theoretical and Applied Rheology, pages 374–376. Elsevier, 1992.

[40] Han-Xiong Huang, Jiong-Cheng Li, Dong Li, and Geng-Qun Huang. New strategies for predicting parison dimensions in extrusion blow molding. Polymer-Plastics Technology and Engineering, 50(13):1329–1337, 2011.

[41] Roland Geyer, Jenna R. Jambeck, and Kara Lavender Law. Production, use, and fate of all plastics ever made. Science Advances, 3:e1700782, 2017.

[42] Organisation for Economic Co-operation and Development (OECD). Plastics use by application. https://stats.oecd.org/viewhtml.aspx?datasetcode=PLASTIC_USE_10&lang=en, 2023. Accessed: 2023-Nov-25.

[43] Market Research Future. Blow molding plastics market size, growth and analysis report 2030. https://www.marketresearchfuture.com/reports/blow-molding-plastics-market-4718, 2021. Accessed: [16/Feb/2024].

[44] The facts 2020. https://plasticseurope.org/knowledge-hub/plastics-the-facts-2020/, 2021. Accessed: 2023-Nov-25.

[45] The facts 2021. https://plasticseurope.org/knowledge-hub/plastics-the-facts-2021/, 2022. Accessed: 2023-Nov-25.

[46] The facts 2022. https://plasticseurope.org/knowledge-hub/plastics-the-facts-2022/, 2023. Accessed: 2023-Nov-25.

[47] The circular economy for plastics – a european analysis 2024. https://plasticseurope.org/knowledge-hub/the-circular-economy-for-plastics-a-european-analysis-2024/, 2024. Accessed: 2024-Aug-09.

[48] Johann Schweighofer Harald Pilz and Evelin Kletzer. The contribution of plastic products to resource efficiency. https://www.teppfa.eu/wp-content/uploads/HSEGUAFinalreportplasticsressourceefficiencyupdateJan2005.pdf, 2005.

[49] European Commission. Single-use plastics. https://environment.ec.europa.eu/topics/plastics/single-use-plastics_en, 2021. Accessed: 2024-02-15.

[50] Harald Pilz, Johann Schweighofer, and Evelin Kletzer. The contribution of plastic products to resource efficiency. https://www.teppfa.eu/wp-content/uploads/HSEGUAFinalreportplasticsressourceefficiencyupdateJan2005.pdf, 2005. Accessed: 2023-Nov-26.

[51] Jeniffer Rankin. European parliament votes to ban single-use plastics. The Guardian, 27, 2019.

[52] Ajeesh S S and S Arul Jayachandran. Computation of shear buckling stress of thin-walled sections using constrained spline finite strip method. Thin-Walled Structures, page 111813, 2024.

[53] Lang Li, Fusen Jia, Lu Liu, Runpei Yu, Qiancheng Zhang, and Lei Li. Response of aluminium honeycomb sandwich panels under combined shock and impact loading: Experimental and numerical investigations. Thin-Walled Structures, 193:111256, 2023.

[54] Erik Burman, Miguel A. Fernández, Stefan Frei, and Fannie M. Gerosa. A mechanically consistent model for fluid–structure interactions with contact including seepage. Computer Methods in Applied Mechanics and Engineering, 392:114637, 2022.

[55] Pedro Veiga Rodrigues, Bruno Ramoa, Ana Vera Machado, Philip Cardiff, and João Miguel Nóbrega. Assessing the compressive and impact behavior of plastic safety toe caps through computational modelling. Polymers, 13(24), 2021.

[56] Felipe Klein Fiorentin, Bernardo Oliveira, João Pereira, José Correia, Abilio De Jesus, and Filippo Berto. Fatigue behavior of metallic components obtained by topology optimization for additive manufacturing. Frattura ed Integrità Strutturale, 15:119–135, 12 2020.

[57] S. Chahardoli and A. Alavi Nia. Investigation of mechanical behavior of energy absorbers in expansion and folding modes under axial quasi-static loading in both experimental and numerical methods. Thin-Walled Structures, 120:319–332, 2017.

[58] Peter Nørtoft and Jens Gravesen. Isogeometric shape optimization in fluid mechanics. Structural and Multidisciplinary Optimization, 48:909–925, 2013.

[59] B.W. Schafer, Z. Li, and C.D. Moen. Computational modeling of cold-formed steel. Thin-Walled Structures, 48(10):752–762, 2010. Coupled Instabilities in Metal Structures CIMS 2008.

[60] Marcelo Assato and Marcelo J. S. de Lemos. Turbulent flow in wavy channels simulated with nonlinear models and a new implicit formulation. Numerical Heat Transfer, Part A: Applications, 56(4):301–324, 2009.

[61] Eberhard Blümel. Global challenges and innovative technologies geared toward new markets: Prospects for virtual and augmented reality. Procedia Computer Science, 25:4–13, 2013. 2013 International Conference on Virtual and Augmented Reality in Education.

[62] Henning Kagermann. Change Through Digitization—Value Creation in the Age of Industry 4.0, pages 23–45. Springer Fachmedien Wiesbaden, Wiesbaden, 2015.

[63] Achim Walter, Robert Finger, Robert Huber, and Nina Buchmann. Smart farming is key to developing sustainable agriculture. Proceedings of the National Academy of Sciences, 114(24):6148–6150, 2017.

[64] David Reinsel-John Gantz-John Rydning, John Reinsel, and John Gantz. The digitization of the world from edge to core. Framingham: International Data Corporation, 16:1–28, 2018.

[65] Morteza Ghobakhloo. Industry 4.0, digitization, and opportunities for sustainability. Journal of Cleaner Production, 252:119869, 2020.

[66] Lorenzo Ardito, Antonio Messeni Petruzzelli, Umberto Panniello, and Achille Claudio Garavelli. Towards industry 4.0. Business Process Management Journal, 25(2):323–346, Jan 2019.

[67] Jan Ola Strandhagen Sven-Vegard Buer and Felix T. S. Chan. The link between industry 4.0 and lean manufacturing: mapping current research and establishing a research agenda. International Journal of Production Research, 56(8):2924–2940, 2018.

[68] Lucas Santos Dalenogare, Guilherme Brittes Benitez, Néstor Fabián Ayala, and Alejandro Germán Frank. The expected contribution of industry 4.0 technologies for industrial performance. International Journal of Production Economics, 204:383–394, 2018.

[69] Adam Schroeder, Brian Trease, and Alessandro Arsie. Balancing robot swarm cost and interference effects by varying robot quantity and size. Swarm Intelligence, 13(1):1–19, Mar 2019.

[70] Wing B. Lee, Benny C.F. Cheung, and Siu K. Kwok. Digital Manufacturing and RFID-Based Automation, pages 859–879. Springer Berlin Heidelberg, Berlin, Heidelberg, 2009.

[71] Radhakisan Baheti and Helen Gill. Cyber-physical systems. The impact of control technology, 12(1):161–166, 2011.

[72] Dharmendra S Modha, Rajagopal Ananthanarayanan, Steven K Esser, Anthony Ndirango, Anthony J Sherbondy, and Raghavendra Singh. Cognitive computing. Communications of the ACM, 54(8):62–71, 2011.

[73] Javaid Butt. Exploring the interrelationship between additive manufacturing and industry 4.0. Designs, 4(2), 2020.

[74] Ahmad Barari, Marcos Tsuzuki, Yuval Cohen, and Marco Macchi. Editorial: intelligent manufacturing systems towards industry 4.0 era. Journal of Intelligent Manufacturing, 32(7):1793–1796, Oct 2021.

[75] Andrew Kusiak. Smart Manufacturing, pages 973–985. Springer International Publishing, Cham, 2023.

[76] Ahmed Awouda, Emiliano Traini, Giulia Bruno, and Paolo Chiabert. Iot-based framework for digital twins in the industry 5.0 era. Sensors, 24(2), 2024.

[77] Andreja Rojko. Industry 4.0 concept: Background and overview. International Journal of Interactive Mobile Technologies (iJIM), 11(5):pp. 77–90, Jul. 2017.

[78] Judit Nagy, Judit Oláh, Edina Erdei, Domician Máté, and József Popp. The role and impact of industry 4.0 and the internet of things on the business strategy of the value chain—the case of hungary. Sustainability, 10(10), 2018.

[79] Eric L. Xu Li Da Xu and Ling Li. Industry 4.0: state of the art and future trends. International Journal of Production Research, 56(8):2941–2962, 2018.

[80] Blaž Rodič. Industry 4.0 and the new simulation modelling paradigm. Organizacija, 50(3):193–207, 2017.

[81] William de Paula Ferreira, Fabiano Armellini, and Luis Antonio De Santa-Eulalia. Simulation in industry 4.0: A state-of-the-art review. Computers & Industrial Engineering, 149:106868, 2020.

[82] A.D. Jayal, F. Badurdeen, O.W. Dillon, and I.S. Jawahir. Sustainable manufacturing: Modeling and optimization challenges at the product, process and system levels. CIRP Journal of Manufacturing Science and Technology, 2(3):144–152, 2010. Sustainable Development of Manufacturing Systems.

[83] Zhongfei Zhang, Ting Qu, Kuo Zhao, Kai Zhang, Yongheng Zhang, Lei Liu, Jun Wang, and George Q. Huang. Optimization model and strategy for dynamic material distribution scheduling based on digital twin: A step towards sustainable manufacturing. Sustainability, 15(23), 2023.

[84] Rohit Agrawal, Abhijit Majumdar, Anil Kumar, and Sunil Luthra. Integration of artificial intelligence in sustainable manufacturing: current status and future opportunities. Operations Management Research, 16(4):1720–1741, Dec 2023.

[85] M.F. Ashby. Overview no. 92: Materials and shape. Acta Metallurgica et Materialia, 39(6):1025–1039, 1991.

[86] Martin Philip Bendsoe and Ole Sigmund. Topology optimization. Springer, Berlin, Germany, 2 edition, July 2011.

[87] Javier Vera-Sorroche, Adrian Kelly, Elaine Brown, Phil Coates, Nayeem Karnachi, Eileen Harkin-Jones, Kang Li, and Jing Deng. Thermal optimisation of polymer extrusion using in-process monitoring techniques. Applied Thermal Engineering, 53(2):405–413, 2013. Includes Special Issue: PRO-TEM Special Issue.

[88] Jiyoung Jung, Kundo Park, Byungjin Cho, Jinkyoo Park, and Seunghwa Ryu. Optimization of injection molding process using multi-objective bayesian optimization and constrained generative inverse design networks. Journal of Intelligent Manufacturing, 34(8):3623–3636, Dec 2023.

[89] Renê S. Pinto, Hugo M. Silva, Fernando M. Duarte, João P. Nunes, and António Gaspar-Cunha. Neuroevolutionary Multiobjective Optimization of Injection Stretch Blow Molding Process in the Blowing Phase, pages 307–318. Springer International Publishing, Cham, 2021.

[90] António Gaspar-Cunha, José A. Covas, and Janusz Sikora. Optimization of polymer processing: A review (part i—extrusion). Materials, 15(1), 2022.

[91] António Gaspar-Cunha, José A. Covas, and Janusz Sikora. Optimization of polymer processing: A review (part ii-molding technologies). Materials, 15(3), 2022.

[92] Erik Steinmetz, Seamus Scanlon, Tyler Schneider, and João Maia. Multi-layer co-extrusion blow molding. International Polymer Processing, 39(2):202–209, 2024.

[93] Openfoam-v2206 - esi group. https://www.openfoam.com/news/main-news/openfoam-v2206, 2022. Accessed: 2024-Jul-13.

[94] Olga Sousa Carneiro, Ananth Rajkumar, Luís Lima Ferrás, Célio Fernandes, Alberto Sacramento, and João Miguel Nóbrega. Computer aided die design: A new open-source methodology. AIP Conference Proceedings, 1843(1):030008, 05 2017.

[95] O. S. Carneiro, A. Rajkumar, C. Fernandes, L. L. Ferrás, F. Habla, and J. M. Nóbrega. Development and experimental assessment of a numerical modelling code to aid the design of profile extrusion cooling tools. AIP Conference Proceedings, 1896(1):120008, 10 2017.

[96] C. Fernandes, M.S.B. Araujo, L.L. Ferrás, and J. Miguel Nóbrega. Improved both sides diffusion (ibsd): A new and straightforward stabilization approach for viscoelastic fluid flows. Journal of Non-Newtonian Fluid Mechanics, 249:63–78, 2017.

[97] C. Fernandes, L.L. Ferrás, M.S. Araujo, and J.M. Nóbrega. Development length in planar channel flows of inelastic non-newtonian fluids. Journal of Non-Newtonian Fluid Mechanics, 255:13–18, 2018.

[98] Zeljko Tukovic and Hrvoje Jasak. Updated lagrangian finite volume solver for large deformation dynamic response of elastic body. Transactions of FAMENA, 31:55, 01 2007.

[99] Philip Cardiff. Development of the Finite Volume Method for Hip Joint Stress Analysis. PhD thesis, University College Dublin, 2012.

[100] P. Cardiff, A. Karač, and A. Ivanković. A large strain finite volume method for orthotropic bodies with general material orientations. Computer Methods in Applied Mechanics and Engineering, 268:318–335, 2014.

[101] P. Cardiff, Ž. Tuković, P. De Jaeger, M. Clancy, and A. Ivanković. A lagrangian cell-centred finite volume method for metal forming simulation. International Journal for Numerical Methods in Engineering, 109(13):1777–1803, 2017.

[102] Manuel A. Alves Francisco Pimenta. GitHub Repository - fppimenta/rheoTool: Toolbox to simulate GNF and viscoelastic fluid flows in OpenFOAM® - version 5.0. https://github.com/fppimenta/rheoTool, 2022. [Accessed 09-08-2024].

CHAPTER 2

Extending the finite area method for enhanced simulation of deformable membranes and its application to extrusion blow moulding

Abstract: This paper investigates the mechanics of the Extrusion Blow Moulding (EBM) process, focusing on the clamp and inflation phases. The simulation framework employed in this study has been developed using OpenFOAM ® and extended the available Finite Area Method with a vertex-centred approach. This cutting-edge developments integrated a corotational formulation with a quasi-static approximation. The computational code and algorithm are verified and validated through comparisons between analytical solutions, experimental measurements and simulation results, ensuring the accuracy and reliability of the proposed approach. The implemented code is verified by checking fundamental principles of hyperelastic materials behaviour, demonstrated through equibiaxial deformation of spherical balloons. The use of neo-Hookean and Mooney-Rivlin material models provides crucial insights into material responses under different inflation conditions. The studies begin employing a conceptual mould within the EBM process that allows examining the effects of mould clamping on parison deformation. Then the study extends to analysing a real bottle manufactured via EBM, employing Stereolithography (STL) digitisation and thickness mapping to quantify the material distribution. The simulation results closely replicates experimental observations, capturing the inherent non-linearity of these process stages, including large deformations and displacements, hyperelasticity and parison-mould contacts. This interdisciplinary research enhances understanding of the EBM process phases and analogous processes, providing valuable insights for plastic manufacturing. It improves the design process for meeting specific requirements and offers guidelines to avoid potential failures. The findings underscore the importance of such studies in advancing sustainable and efficient plastic manufacturing practices, with applications ranging from inflatable structures to EBM processes.

Keywords: Finite strain theory, Membrane formulation, Hyperelasticity, Finite Area Method, Extrusion Blow Moulding

This chapter was adapted from W. d. C. Galuppo, P. Santana, F. Alves, and J.M. Nóbrega, Extending the finite area method for enhanced simulation of deformable membranes and its application to extrusion blow moulding, Thin-Walled Structures. Volume 203 (2024) 112–184, DOI: https://doi.org/10.1016/j.tws.2024.112184

2.1 Introduction

The significance, context, and motivation for simulating the Extrusion Blow Moulding (EBM) process, as discussed in Chapter 1, underscored that Phases I to IV are of outstanding importance in shaping the final properties of the manufactured part. Therefore, these phases hold exceptional significance when considering numerical modelling for the process simulation. From those, this work covers Phases II and III, of the envisaged developments that aim to simulate all the relevant EBM process phases.

Due to the similarity of the two processes, the state-of-the-art presented hereafter, covers not only work on the mould clamping and inflation phases of the EBM process, but also developments related to the forming phase of the thermoforming process. Furthermore, it is worth noting that these processes share similarities, not only in their simulation aspects but also with regard to materials used for processing, as highlighted by prior studies [1–3].

The pioneering work found was conducted by Khayat et al. [4], which primarily focused on modelling the forming phase in the thermoforming and EBM processes. A simplified assumption was made to solve the fluid (air) behaviour within a cavity, considering it as a three-dimensional potential flow driven by the displacement of an isotropic homogeneous membrane. This membrane was discretised to represent the parison of arbitrary shape, with confined air between parison moulds released through strategically positioned vents. The mechanical behaviour of the membrane considered a hyperelastic Mooney-Rivlin material model. The study covered an investigation into the inflation of a square-shaped container and explored custom positioning strategies for the air vents. Furthermore, the back pressure effects on the membrane's trajectories were rigorously addressed. When considering scenarios where the pressure inside the membrane remains constant or follows a time-dependent preset function, their model accounted for the resulting pressure variations across both time and location on the membrane's surface.

Followed by the previous study, the investigation conducted by Debbaut et al. [5] involved the comparison of experimental results with numerical predictions. This research focused on an industrial blow-moulded part featuring a complex geometrical shape of a bottle with a handle. The governing equations describing the motion of the body were represented using a Lagrangian approach, moreover they employed a membrane-based modelling approach. Simulations were carried out under isothermal conditions, utilising the viscoelastic Kaye–Bernstein-Kearsley-Zapas (K-BKZ) constitutive model. While the study reported minor discrepancies between experimental data and numerical predictions at specific locations, these deviations were attributed to factors such as the initial parison shape and thickness, sagging effects, temperature influence, and potential slippage.

In the study by Nam et al. [6], simulations of the thermoforming process were conducted both by utilising a three-dimensional solid element analysis and also a membrane approximation. The investigation focused on the free inflation of a rectangular sheet, employing a hyperelastic material

model. They performed two distinct analyses, which exhibited consistent behaviour for sheets with lower thicknesses, but deviated as the sheet thicknesses were increased. To measure the proximity of results, the dimensionless parameter $l^* = (W/H)$ was introduced, where W represents the sheet width and H denotes its thickness. The findings of the study revealed that non-isothermal analysis yielded numerical results more closely aligned with the experimental data, where at the extremities of the sheet is noticed the largest differences with the highest difference of 17%, but the overall profile is similar for the parts thermoformed without plug assistance. Additionally, accounting for the initial temperature distribution across the sheet emerged as a crucial factor for achieving more reliable simulations of the thermoforming process. It was noticed that when opting for the membrane approximation over the shell, a closer alignment between results of these two approaches were verified, particularly for cases where the parameter l^* exceeded 100.

Marckmann et al. [7], reported the development of a computational code for simulating the EBM and thermoforming of thermoplastic hollow parts. Their approach considered the principle of Virtual Work associated with a hybrid (Eulerian–Lagrangian) method, accounting for inertia effects. The parison material was assumed isothermal, nonlinear hyperelastic Mooney-Rivlin constitutive model, and with the membrane approach. The interaction between the parison and the mould was modelled as perfectly sticky. Moreover, the study implemented adaptive mesh refinement techniques, significantly enhancing performance, particularly for capturing fine details near the corners. The research presented results from four simulation cases that illustrated the benefits achieved with the improvements made. To validate the developed tools, numerical results were rigorously compared with both experimental data and numerical data obtained in existing literature. The accuracy of the simulations was notably commendable for both blow-moulding and thermoforming processes. Identified areas for potential improvement included refining constitutive models, particularly by considering the influence of temperature.

There are several applications where thin structures with membrane formulations and membrane shell are used in real and simulations [8–18]. The work of Danielson [8] on explicit methods using lumped-mass for simulating solids contact problems presented an interesting formulation of lumped-mass explicit analysis, where inertial, contact and internal forces are used to describe the mechanical behaviour of thin structures like shell membranes. This work associated with the content published in the work of Cardiff [19] enlightened the developments of this research group for these approaches, where the parison is approximated to a thin structure as a shell membrane like, and deformed using the predominant action forces, like weight, pressure, etc., instead of using just internal, inertial and contact forces as was done in Danielson [8].

In this study, an innovative computational framework is developed to numerically simulate the clamp and inflation phases of the EBM process. The work performed, allows for evaluating the effectiveness of employing a lumped-mass explicit method that incorporates a novel artificially damped velocity scheme as a computational framework for simulating the deformation of finite strain membrane structures. The approach utilises a novel corotational formulation with a quasi-static

approximation to increase the calculations stability. Additionally, the Finite Area Method for discretising the overall fields available in the OpenFOAM ® computational library finite area class, which is face-centred [20], is modified to a vertex-centred arrangement, as it is more suitable for the adopted quasi-static approximation. This new arrangement utilises non-overlapping cells centred at the vertices of the finite area mesh [19] to evaluate mass, force, and displacement fields. The material behaviour is modelled using neo-Hookean and Mooney-Rivlin hyperelastic constitutive models, assuming isothermal and adiabatic conditions.

This paper is organised as follows: Section 2.2 introduces the theoretical background, covering the material description and the mathematical model, as well as the details of the implemented numerical algorithm. It also focuses on the discretisation of membranes within the context of finite strain theory, alongside the constitutive models and contact condition. Section 2.3 presents the evaluation examples, beginning with a simplified geometrical configuration that facilitates the analytical validation, and two additional complex cases studied both experimental and numerically. In Section 2.4, the results obtained on the simulations of those evaluation cases are analysed, and the numerical results compared with the analytical and experimental data, for validation purposes. The paper concludes in Section 2.5 that synthesises the findings and implications of this research.

2.2 Theoretical Formulation

This work considers the matter at a macroscopic length-scale level to its analysis as stated by the continuum mechanics field. Furthermore, this document adheres to the nomenclature used in continuum mechanics [21, 22], using capital letters and small letters to represent material and spatial descriptions, respectively. It is pertinent to note that, in certain contexts for convenience, the subscript zero ($_0$) is used to designate a material description, following the same approach of the following books [21, 22]. A particle denoted as X is an element of a body $\mathcal{B}$, expressed as $X \in \mathcal{B}$. A body $\mathcal{B}$ itself is defined by a set of such particles, i.e., $\mathcal{B} = \{{}^1X, {}^2X, {}^3X, \ldots, {}^nX\}$, where each particle is distributed in space and time. The spatial region occupied by the body $\mathcal{B}$ at any given time defines its configuration, denoted as κ. This body, at time $t = 0$, occupies its initial configuration, frequently referred to as Base or undeformed configuration κ_0, in which a particle X occupies position $\mathbf{X}$ in the Euclidean space, referred to a reference frame of right-handed system in material coordinates. When the continuum experience external actions, e.g. external forces, it responds by changing its geometric shape into a new configuration state at time t, designated by κ_t. The particles' distribution for the body at this state is designated by current configuration, or deformed configuration. At this time, the particle X changes its original position $\mathbf{X}$ to a new position $\mathbf{x}$ in the deformed configuration, as illustrated in Figure 2.1. The mathematical description for these configurations of a deformable body can follow two approaches: the well known Material/Lagrangian description and the Spacial/Eulerian description. The present study follows the Material description formulation associated with the finite strain theory, due to the intrinsic geometrical nonlinearities for simulating the EBM mould clamping and inflation

phases, where large displacements, large rotations and large strains, and material nonlinearities are considered with respect to EBM processing materials and their inherent condition during these phases.

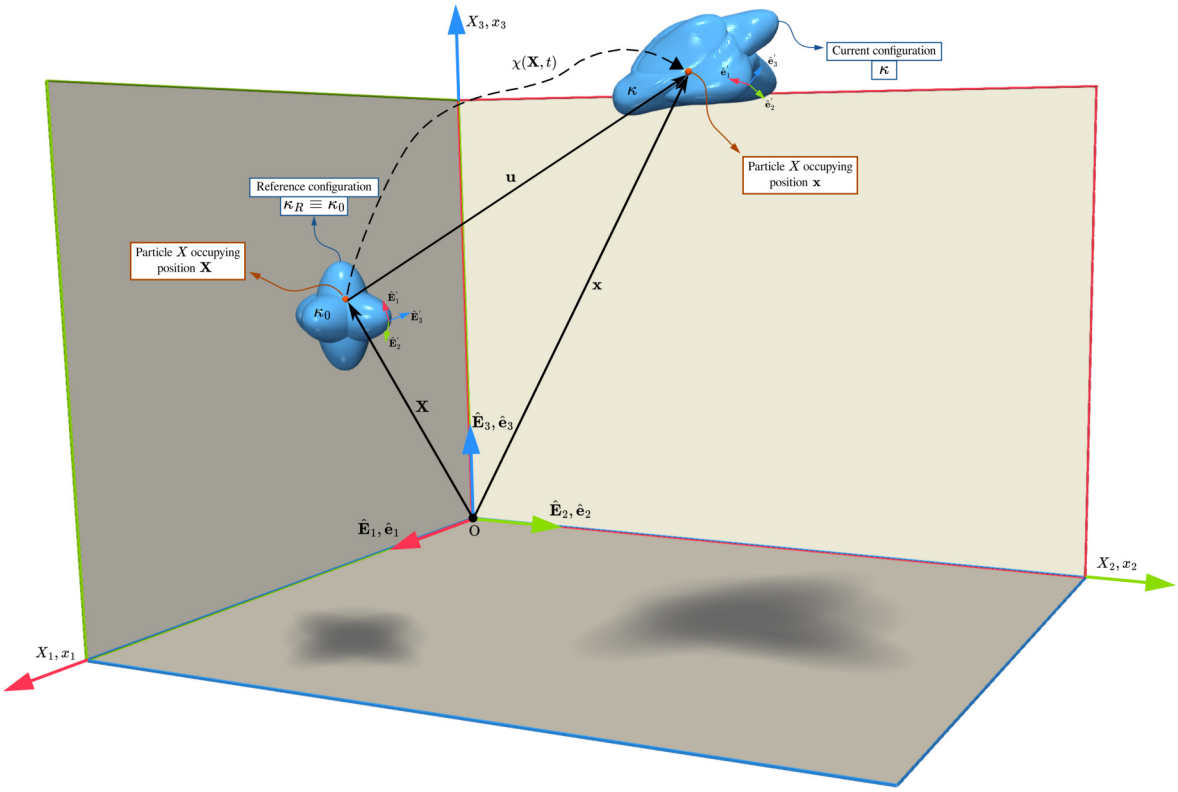


Figure 2.1: Configurations for two instants of a body by a Lagrangian description of motion.

2.2.1 Material Description

The motion of a body describes how each point moves from its position in the reference configuration κ_R to its current position. This reference can be the initial body configuration, which is usually an undeformed / stress-free state referred as $\kappa_R \equiv \kappa_0$. On the other hand, it can also be related to any known intermediate state of its configuration. This gives the rise to two distinguishable approaches to formulate the discrete equations, the Updated Lagrangian approach, and the Total Lagrangian approach. The former updates the reference κ_R to a previous known state, and the latter uses the original configuration at time $t = 0$ as a reference configuration $\kappa_R \equiv \kappa_0$. The Total Lagrangian was the chosen option to be used for discretising the governing equations. Thus, the current configuration is related to the reference body in its initial configuration, as described by:

$$\mathbf{x} = \chi(\mathbf{X}, t) \quad , \quad \mathbf{X} = \chi(\mathbf{X}, 0), \tag{2.1}$$

and a generic variable φ of the body in a configuration is given by:

$$\varphi = \varphi(\mathbf{x}(\mathbf{X},t),t) = \varphi(\mathbf{X},t), \tag{2.2}$$

where χ is the mapping function/deformation mapping function for the body from its reference configuration to a given instant current configuration at time t. This function depends on time and a referential body configuration, for instance at time $t = 0$, i.e. $\kappa_0(\mathcal{B}) = \chi(\mathbf{X},0) = \mathbf{X}$. Thus, the motion is the mapping between the reference and current configurations. The displacement is a vector $\mathbf{u}$ formed by connecting the particle positions from their reference configuration $\mathbf{X}$ to their current configuration $\mathbf{x}$, as follows:

$$\mathbf{u} = \mathbf{x} - \mathbf{X} \;\;,\;\; \mathbf{u}(\mathbf{X},t) = \mathbf{x}(\mathbf{X},t) - \mathbf{X}. \tag{2.3}$$

When all the deformed configuration particles are connected to their reference configuration the displacement field is found, and the relative displacements sensed by the continuum is its deformation, which is the key field for determining stresses, strengths, fatigues, and more. The continuum mechanics fundamental field that relates the body from its reference and deformed configurations to strains is called the deformation gradient $\mathbf{F}$, and is used to dissociate rigid body translation and rotation from deformations, which is the main parameter to be associated with stresses. This principal key for the mathematical modelling is covered in the next chapter. The deformation gradient is a tensor related to two-point material from reference to current configuration, thus it has its basis in both configurations, and is better visualised in index notation as follows:

$$\mathbf{F}(\mathbf{X},t) = F_{i,J}\hat{\mathbf{e}}_i\hat{\mathbf{E}}_J \;\;,\;\; F_{i,J} = \frac{\partial x_i}{\partial X_J} = \begin{bmatrix} \frac{\partial x_1}{\partial X_1} & \frac{\partial x_1}{\partial X_2} & \frac{\partial x_1}{\partial X_3} \\ \frac{\partial x_2}{\partial X_1} & \frac{\partial x_2}{\partial X_2} & \frac{\partial x_2}{\partial X_3} \\ \frac{\partial x_3}{\partial X_1} & \frac{\partial x_3}{\partial X_2} & \frac{\partial x_3}{\partial X_3} \end{bmatrix}. \tag{2.4}$$

where $\hat{\mathbf{e}}_i$ and $\hat{\mathbf{E}}_J$ are the unit orthonormal base vectors, presented in Figure 2.1, for the spatial coordinates (Current Configuration) and material coordinates (Reference Configuration) directions, respectively. Furthermore, a local coordinate system using $\hat{\mathbf{e}}'_i$ and $\hat{\mathbf{E}}'_J$, presented in Figure 2.1 and also as unit orthonormal base vectors, follows the same material and spacial orientations as the previous Global Coordinate system used as the basis of the deformation gradient tensor. There is a linear transformation between these local and global coordinate system that transforms one into the other and vice-versa with the inverse of the transformation matrix.

By isolating $\mathbf{x}$ from Equation (2.3) and replacing in Equation (2.4), the deformation gradient can

be written based on displacements as follows:

$$\mathbf{F} = \frac{\partial}{\partial \mathbf{X}}(\mathbf{X}+\mathbf{u}) = \frac{\partial \mathbf{X}}{\partial \mathbf{X}} + \frac{\partial \mathbf{u}}{\partial \mathbf{X}} = \mathbf{I} + \frac{\partial \mathbf{u}}{\partial \mathbf{X}} = (\mathbf{I} + \nabla_0 \mathbf{u})^T. \tag{2.5}$$

where $\nabla_0 \mathbf{u}$ is the material displacement gradient tensor, material due to the partial derivatives being taken with respect to $\mathbf{X}$ in the material coordinates.

2.2.2 Mathematical Model

The EBM process mould clamping and inflation phases are governed by the continuity (Equation (2.6)) and linear momentum balance (Equation (2.8)) equations. Considering the rapid processing times that these phases undergo, the simulations are simplified to assume isothermal condition, which is in line with previous works covering the same process [5, 7], and all the elastic deformation upon the body due to work is perfectly stored as elastic energy as postulated in Green elastic materials [23], which were successfully assessed in previous works [4–7].

Based on the above, the continuity conservation equation is expressed as follows:

$$\int_{\Omega_0} \rho_0 \mathrm{d}\mathbf{X} = \int_{\Omega} \rho \mathrm{d}\mathbf{x} \;\; , \;\; \mathrm{d}\mathbf{x} = J\mathrm{d}\mathbf{X} \;\; \rightarrow \;\; \int_{\Omega_0} (\rho_0 - J\rho)\mathrm{d}\mathbf{X} = 0. \tag{2.6}$$

where J is the Jacobian of the motion, and it is obtained by calculating the determinant of the deformation gradient tensor $\mathbf{F}$ [21], Ω is the body volume, ρ is its specific mass, and each property taking the subscripts $(\ _0)$ refers to the variable being evaluated at the reference configuration, the ones at current configuration does not take subscripts.

A particular situation happens for the case of polymer materials that are used under EBM processing conditions, in which the predominance of incompressibility is assumed [24], thus the Jacobian is unitary, $J = 1$. Also, many polymers largely deform without changing its volume [24] under this processing conditions typical to EBM, consequently mass and volume are preserved. These conditions correspond to an isochoric deformation, in which $\rho_0 = \rho$.

The second equation that rules the mechanical behaviour for the polymer processed with the EBM process concerns the momentum balances, in which the applied loads can be grouped into surface forces and body forces. The considered predominant surface forces are the forces that arise from the pressure difference between the inner and outer parison surface $\mathbf{f}_p$, the force that takes action within the membrane plane $\mathbf{f}_m$ due to strains and its material stiffness, and the contact forces $\mathbf{f}_c$ after the body being in contact with the mould surface. The body forces taken into account are the inertial resulting force $\mathbf{f}_r$ and the weight of the body, attributed to gravitational acceleration $\mathbf{f}_g$. During

the parison extrusion phase of the EBM process, the weight force vector of the parison is primarily utilized to orient the extrusion direction and aid by straightening the parison. In a quasi-static approach, the solution is reached when the sum of these forces are approximately zero, as stated in

$$\mathbf{f}_p + \mathbf{f}_m + \mathbf{f}_c + \mathbf{f}_g = \mathbf{f}_r \Rightarrow \mathbf{f}_r \approx \mathbf{0}. \tag{2.7}$$

These forces are succinctly described via the linear momentum balance equation that obeys the following expression:

$$\frac{\partial}{\partial t}\int_{\Omega} \rho \mathbf{v} \mathrm{d}\Omega = \oint_{\Gamma} \hat{\mathbf{n}} \cdot \boldsymbol{\sigma}^T \mathrm{d}\Gamma + \int_{\Omega} \rho \mathbf{b} \mathrm{d}\Omega, \tag{2.8}$$

where the left-hand term accounts for inertial forces, the first term in the right-hand respects to surface forces, while the second is related to body forces. Furthermore, $\mathbf{v}$ is the velocity vector, calculated as the time derivative of the displacements $\mathbf{v} = \partial \mathbf{u}/\partial t$, $\hat{\mathbf{n}}$ is the body surface area unity normal vector, $\boldsymbol{\sigma}$ is the Cauchy/True stress tensor, Γ is the body closed surface and this first term from the right-hand side of the Equation (2.8) is obtained from the divergence theorem, and expressed as a closed integral, and, finally, $\mathbf{b}$ is the body force vector per unit mass. Mainly, two approaches are possible for the solution of the previous equations, by following an implicit method or an explicit method. This works uses the latter by a modified version of the leap-frog algorithm [25] that does the integration of the Newton's second law of motion, associated with a lumped mass method. The default algorithm known as kick-drift-kick [25] which is a version of Leap-frog algorithm, also known as velocity Verlet algorithm, is presented in Algorithm 1 [25].

In this work, a modified version of the presented algorithm is considered. The modification is related to the calculation of velocity field corresponding to time step t_{i+1} performed in Equation (2.13). The new calculation is formulated in such a way that an artificial damping factor in inserted to the dynamic response of the explicit algorithm. Since a quasi-static approach is being considered, the intermediate solutions, which include a non-physical damping to increase stability, do not affect the final result, for which a zero net force is achieved. In fact, the solution is considered converged when the force reaches a value lower than a predefined tolerance. Thus, the modification considers a linear variation between the velocity in the time interval t_i and t_{i+1}, as follows:

$$\Delta \mathbf{x} = \int_{t_i}^{t_{i+1}} \mathbf{v}(t) \mathrm{d}t, \quad \text{Assuming a linear variation for: } \mathbf{v}(t) = \alpha(t)\mathbf{v}_{i+1} + (1-\alpha(t))\mathbf{v}_i, \tag{2.14}$$

where,

Algorithm 1 leap-frog algorithm

Step 1) Calculate the resulting force vector for each vertex at time t_i using Equation (2.7).
Step 2) Calculate acceleration of each vertex based on the configuration at time t_i

$$\mathbf{a}_i = f(\mathbf{x}_i) = \frac{1}{m}\sum \mathbf{f}_{r,i} \tag{2.9}$$

Step 3) Calculate velocity at time $t_{i+1/2}$

$$\mathbf{v}_{i+1/2} = \mathbf{v}_i + \mathbf{a}_i \frac{\Delta t}{2} \tag{2.10}$$

Step 4) Calculate the new body position vector at time t_{i+1}

$$\mathbf{x}_{i+1} = \mathbf{x}_i + \mathbf{v}_{i+1/2}\Delta t \tag{2.11}$$

Step 5) Update position vector to this new body configuration and calculate new acceleration vector at time t_{i+1}

$$\mathbf{a}_{i+1} = f(\mathbf{x}_{i+1}) = \frac{1}{m}\sum \mathbf{f}_{i+1} \tag{2.12}$$

Step 6) Calculate velocity at time $t = i + 1$

$$\mathbf{v}_{i+1} = \mathbf{v}_{i+1/2} + \mathbf{a}_{i+1} \frac{\Delta t}{2} \tag{2.13}$$

Step 7) Loop back to the calculation of Step 3

$$\alpha(t) = \frac{t - t_i}{t_{i+1} - t_i} = \frac{t - t_i}{\Delta t}. \tag{2.15}$$

Consequently, $\alpha(t)$ varies linearly between 0 and 1, while t varies between t_i and t_{i+1}. Substituting them in Equation (2.14):

$$\Delta\mathbf{x} = \int_{t_i}^{t_{i+1}} \frac{t - t_i}{\Delta t}\mathbf{v}_{i+1} + \frac{t_{i+1} - t}{\Delta t}\mathbf{v}_i \mathrm{d}t, \tag{2.16}$$

which results in:

$$\mathbf{v}_{i+1} = \frac{2\Delta\mathbf{x}}{\Delta t} - \mathbf{v}_i. \tag{2.17}$$

With this expression, numerical simulations presented instabilities, thus an artificially damped coefficient, that ranges between $0 \leq \zeta < 1$ has been added to the first term of the right-hand side of

Equation (2.17) as follows:

$$\mathbf{v}_{i+1} = \zeta \frac{2\Delta \mathbf{x}}{\delta t} - \mathbf{v}_i. \tag{2.18}$$

Consequently, the kick-drift-kick Leap-frog algorithm is achieved when $\zeta = 1$. This results in a default periodic behaviour, which occurs because of the conservation of the system's energy and the transformation between the different forms of energy involved, namely kinetic and potential. By including a damping coefficient (ζ) between 0 and 1 in the calculation, the oscillatory behavior of the undamped system is dissipated, allowing the forces to reach an equilibrium state. This makes the quasi-static solution possible when $\sum \mathbf{f} \approx \mathbf{0}$.

In the default undamped algorithm, the system oscillates, showing the dynamics of a Periodic Steady State. However, it can quickly diverge when applied to undamped or stiff linear systems due to its inherent numerical instability under certain conditions. The addition of the damping coefficient is one strategy used to mitigate instabilities and reduce the oscillations. It dissipates the energy and errors, promoting stability [26, 27]. As the system approaches a quasi-static state, the convergence criterion for equilibrium is met when the maximum resulting force is less than a defined threshold value. At this point, the configuration is saved, and the external loads are updated to the next step values. This iterative process continues, ensuring that force balance is achieved for each step.

The quasi-static approximation improves calculation stability by ensuring that the system approaches equilibrium at each calculation. This avoids residual oscillations and associated errors that are more prone to occur in dynamic processes. The implemented calculation for the proposed algorithm is schematically presented in Algorithm 2 for the mould clamping phase, and in Algorithm 3 for the inflation phase.

2.2.3 Membrane Formulation

The implemented membrane formulation uses the OpenFOAM ®'s finite area library classes [20] for the parison's discretisation, which is a locally two-dimensional surface, placed in the three-dimensional Euclidean space as a curved surface made up of flat triangles as finite area cells, i.e., each cell has coplanar centroid and vertices. Differently from the originals developments as having fluid phases in the surroundings of interfacial finite area surface [20], here these fluid phases neighbouring the finite area mesh, for instance the blown air during the inflation, are not simulated, and a boundary conditions is applied for that instead. This was the basis for extending the further developments required to simulate the mould clamping and inflation phases from the EBM process.

The Figure 2.2 shows the mesh of a typical parison, generated by the meshing software Gmsh [28], which uses triangular face area cells to discretise the parison surface. The created mesh is then converted to OpenFOAM® mesh format before using it as a finite area mesh. Figure 2.2 also

Algorithm 2 Mould clamping phase

```
Load parison and moulds meshes, fields, boundary conditions and simulation setup.
Initialise incremental displacements list to displace the moulds parts towards closing.
Initialise list of free vertices which are free to move.
while "Moulds not touching each other" do
    Displace the moulds to the new position.
    if "mould hit any free vertices from the parison" then
        Update the hit vertices list.
        Displace the vertices to the touching point at the moulds surface.
    end if
    Calculate for this new configuration all the relevant fields, stresses, strains, thicknesses etc.
    while "maximum resultant force (f_r) ≤ f_convergence" do
        Iterate as Algorithm 1, but taking Equation (2.18) in place of Equation (2.13).
        Displace free vertices to the new configuration and calculate the new resulting force field.
        if "displaced vertices of parison hit the moulds" then
            Remove vertices' IDs from the free vertices to move list.
            Add vertices' IDs to the touched vertices list.
            Displace touched vertices to the touched location in the mould surface.
        end if
    end while
    Save converged configuration and updated fields.
end while
end
```

illustrates a typical vertex (black dots) stencil in the centre of its surrounding finite area cells (translucent purple triangular faces), notice that more vertices are illustrated because the neighbouring finite area cells for the stencil vertex contains its own three vertices each. The implemented discretisation resorts to a vertex-centred explicit method for the governing equations, namely continuity (2.6) and linear momentum balance (2.8) equations, where these finite area mesh cells' vertices are displaced linearly towards the resulting force direction obtained via Equation (2.7), specifically in the Step 4 in Algorithm 1 with Equation (2.11). The finite area cells' edges are the orange lines, and edges' centroids are the smaller purple points. The cells are modelled as constant strain triangles (CST) in a corotational formulation.

To create a corotational formulation, a local coordinate system is constructed and updated as the simulation progresses and the membrane deforms. This is achieved using the coordinate system class available in OpenFOAM® and creating the own local reference frame for each finite area cell.

The local coordinate system for each cell is placed at its centroid, as indicated by the yellow points in Figure 2.2. The local x-axis (red arrows), denoted as $\hat{\mathbf{x}}_l$, is a unit vector that points from the cell centroid towards the first vertex index among the three vertices that make up the cell's vertices list. The local z-axis (blue arrows), denoted as $\hat{\mathbf{z}}_l$, is the unit normal vector of the face, oriented from the higher pressure side to the lower pressure side. Essentially, it points from the internal region towards the external region of the parison surface. The local y-axis (green arrows) is determined by taking the

Algorithm 3 Inflation phase

```
Load closed mould and clamped parison meshes, fields, boundary conditions and simulation
setup.
Create a list containing all the values for the incremental blown pressures.
for "each pressure in the blown pressures list" do
    Update pressure value for each finite area cell
    Calculate the resulting force for all free vertices to move.
    while "maximum resultant force (f_r) ≤ f_convergence" do
        Run Algorithm 1, but taking Equation (2.18) in place of Equation (2.13).
        Displace free vertices to the new positions and calculate the new resulting force field.
        if "displaced vertices of parison hit the mould" then
            Remove vertices' IDs from the free vertices to move list.
            Add vertices' IDs to the touched vertices list.
            Displace touched vertices to the touched location in the mould surface.
            if "free vertices list is empty" then
                Print (MOTIONLESS CONDITION REACHED!)
                Save latest configuration and updated fields.
                end
            end if
        end if
    end while
    Save latest configuration and updated fields.
end for
end
```

cross product of the $\hat{\mathbf{z}}_l$ and $\hat{\mathbf{x}}_l$ vectors, resulting in $\hat{\mathbf{y}}_l = \hat{\mathbf{z}}_l \times \hat{\mathbf{x}}_l$, which is also a unit vector.

The resultant local reference frame is a right-handed orthonormal basis, located on all membrane cells. Furthermore, the fields for stresses, strains, pressures, thicknesses, areas, and volumes are discretised as finite area fields, where these properties are evaluated at the surface faces' centroids.

2.2.4 Constitutive Models

The behaviour of matter in the EBM process is governed by constitutive equations, which provides a mathematical description of material response. Given the extensive existing range of materials and substances, various models have been deployed to represent their behaviour. Among these models, two groups of materials, namely, viscoelastic and hyperelastic are commonly used for describing the inflation and EBM processes materials behaviour [5, 6]. However, these models present different complexities due to the inherent nonlinearities of these materials behaviours. Viscoelastic models are computationally more expensive when compared to the hyperelastic counterparts, but they offer increased accuracy when the relaxation times from the viscoelastic spectrum are sufficiently small in relation to the overall time frame considered for evaluation and observation [29–31].

The mould clamping and inflation phases, among the five mentioned in Section 2.1, are performed within a short time span compared to entire time to perform all these EBM processing

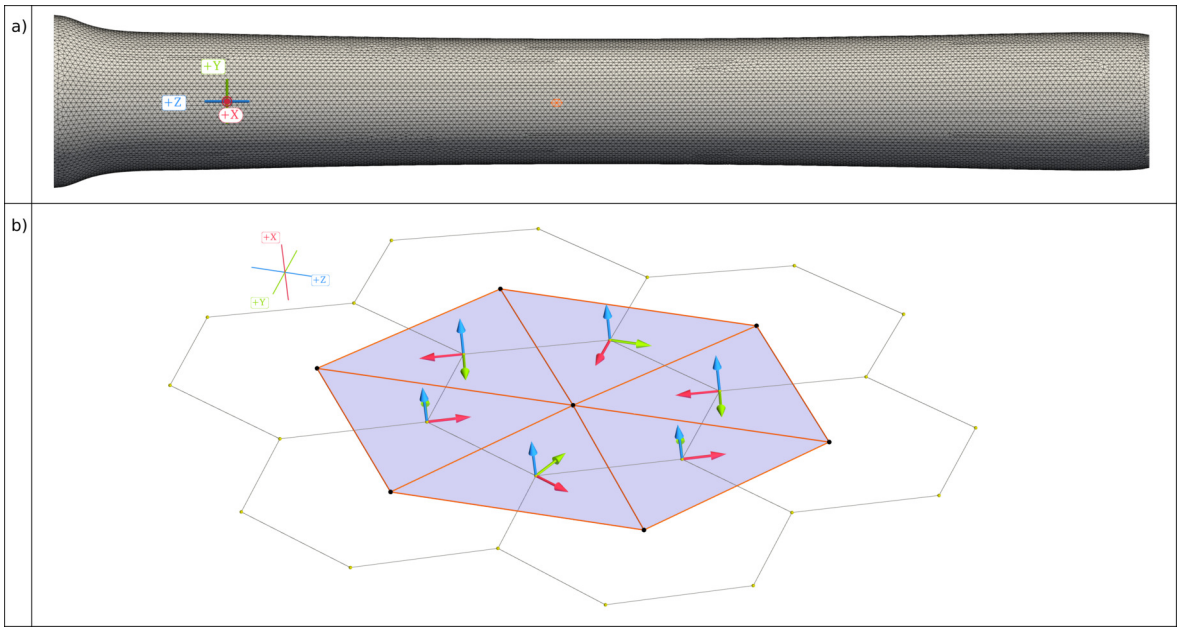


Figure 2.2: Parison geometry and membrane cells discretisation, a) Parison Mesh and b) the stencil for the vertex-centred method.

phases. Considering the relaxation time of the materials under these processing conditions of mould clamping and inflation phases, it is reasonable to assume their behaviour to resemble that of a hyperelastic materials [32]. For constitutive modelling, the Saint Venant-Kirchhoff, neo-Hookean, and Mooney-Rivlin models are considered, progressively, these model increases the complexity and ability to capture the materials nonlinearities.

Hyperelastic materials are characterised by having a load path work independence, i.e., the work done is independent of the deformation path [21–24, 33]. Furthermore, the potential function for the stresses in these models postulates an existing Helmholtz free-energy continuous function ψ, per unit reference volume. This function is referred to as the strain-energy function and is a scalar-valued function of a tensor, which can be calculated based on different strain tensors, e.g. $\mathbf{F}$ the deformation gradient tensor, $\mathbf{C} = \mathbf{F}^T\mathbf{F}$ the right Cauchy–Green deformation tensor, or $\mathbf{E} = (1/2)(\mathbf{F}^T\mathbf{F} - \mathbf{I}) = (1/2)(\mathbf{C} - \mathbf{I})$ the Green-Lagrangian strain tensor [21, 22, 34]. Another commonly used deformation tensor used to obtain the potential function ψ is the left Cauchy-Green deformation tensor, which has a spatial orientation and is obtained as $\mathbf{b} = \mathbf{F}\mathbf{F}^T$. Thus, a stress rises from the derivation of the stored energy potential functions, as follows.

$$\mathbf{S} = 2\frac{\partial \psi(\mathbf{C})}{\partial \mathbf{C}} = \frac{\partial w(\mathbf{E})}{\partial \mathbf{E}}, \tag{2.19}$$

where $\mathbf{S}$ is the Second Piola-Kirchhoff stress tensor [21, 22, 34]. There are different ways to measure stress tensors, and these different stress tensors can be converted into one type or another via the deformation gradient tensor, where the first relation is reached through Nanson's formula [21, 22, 34],

that relates areas in the reference and deformed configurations, and then the first relation is between Cauchy stress $\boldsymbol{\sigma}$ and nominal stress $\mathbf{P}$ tensors, as:

$$\mathbf{P} = J\boldsymbol{\sigma} \cdot \mathbf{F}^{-\mathsf{T}}. \tag{2.20}$$

The Saint Venant–Kirchhoff is the simplest hyperelastic model where large deformations are due to rotations and involves small strains. It models the material behaviour analogous to the way that the linear elastic materials are modelled in the infinitesimal strain theory, but in the finite strain theory it is stated as in Equation (2.21), where $\mathbb{C}$ is the fourth-order tensor of elastic moduli for the Kirchhoff materials [21, 22, 34]. A fourth-order tensor has 81 independent parameters, and due to symmetries for the stress tensor $\mathbf{S}$ and strain tensor $\mathbf{E}$, that rules the linear map, associated with the intrinsic preservation of energy in hyperelasticity leads to this fourth order tensor in being also symmetric [21, 22, 34], then the independent parameters are reduced into 21. Finally, by considering the isotropic behaviour, the independent parameters are reduced into 2 independent parameters, also known as material constants, as follows

$$\mathbf{S} = \mathbb{C} : \mathbf{E} = 2\mu\mathbf{E} + \lambda(tr(\mathbf{E}))\mathbf{I}, \tag{2.21}$$

where the material constants are the shear modulus μ and the Lamé's first parameter λ, which both are also known as Lamé's parameters and have the dimensions of pressure. These constants can be expressed in terms of the Young's modulus E, that has the dimensions of pressure, and the dimensionless Poisson's ratio ν. Notice that the scalar E and the tensor $\mathbf{E}$ represent different quantities.

The relationship between the Lamé's parameters with Young's modulus and Poisson's ratio, associated with the use of a corotational formulation, as described in Section 2.2.3 for plane stress conditions of a membrane, the general constitutive relation from Equation (2.21) can be simplified into the form in an orthonormal basis local coordinate system given by:

$$\mathbf{S} = \mathbb{C} : \mathbf{E} \rightarrow \begin{Bmatrix} S_{11} \\ S_{22} \\ S_{12} \end{Bmatrix} = \begin{bmatrix} \frac{E}{1-\nu^2} & \frac{E\nu}{1-\nu^2} & 0 \\ \frac{E\nu}{1-\nu^2} & \frac{E}{1-\nu^2} & 0 \\ 0 & 0 & \frac{E}{2(1+\nu)} \end{bmatrix} \begin{Bmatrix} E_{11} \\ E_{22} \\ 2E_{12} \end{Bmatrix}, \tag{2.22}$$

where the stresses are obtained by multiplying a compliance matrix with the strains. In the particular situation of the plane stress, the deformation tensors, right Cauchy–Green $\mathbf{C}$, Green-Lagrangian $\mathbf{E}$ and left Cauchy–Green $\mathbf{b}$ can be simplified as follows:

$$\mathbf{C} = \begin{bmatrix} C_{11} & C_{12} & 0 \\ C_{21} & C_{22} & 0 \\ 0 & 0 & C_{33} \end{bmatrix}, \tag{2.23}$$

$$\mathbf{E} = \begin{bmatrix} E_{11} & E_{12} & 0 \\ E_{21} & E_{22} & 0 \\ 0 & 0 & E_{33} \end{bmatrix}, \text{ and} \tag{2.24}$$

$$\mathbf{b} = \begin{bmatrix} b_{11} & b_{12} & 0 \\ b_{21} & b_{22} & 0 \\ 0 & 0 & b_{33} \end{bmatrix}. \tag{2.25}$$

In addition to the previous compliance matrix from Equation (2.22), in order to calculate the deformation in the normal direction of the membrane plane, it is assumed that the material can deform freely in this direction, thus the term E_{33} can be calculated by:

$$E_{33} = \frac{\nu}{E}(S_{11} + S_{22}). \tag{2.26}$$

Equation (2.26) can be further simplified assuming the referred incompressibility, which is considered in this work, as stated in Section 2.2.2. The finite area cells are planar, and their volumes are obtained by multiplying the area by the thickness. With the incompressibility assumption, the cells deforms with an isochoric deformation and the deformation in the third direction from the local coordinate system of a cell, E_{33}, can be obtained with the following relation:

$$\Omega_0 = \Omega \;\Rightarrow\; \Gamma_N\, H = \Gamma_n\, h \;\Rightarrow\; \frac{\Gamma_N}{\Gamma_n} = \frac{h}{H}, \tag{2.27}$$

then

$$C_{33} = (F_{33})^2 = \left(\frac{h}{H}\right)^2 = \left(\frac{\Gamma_N}{\Gamma_n}\right)^2 \text{ and } E_{33} = \frac{1}{2}\left[\left(\frac{h}{H}\right)^2 - 1\right] = \frac{1}{2}\left[\left(\frac{\Gamma_N}{\Gamma_n}\right)^2 - 1\right], \tag{2.28}$$

where Γ_N and Γ_n represent the normal area of the cell membrane in the reference and current

configurations, respectively, and H and h represent the cell thickness in the reference and current configurations, respectively. Taking into account incompressibility, since the areas and thicknesses of the reference configuration and the area of the deformed configuration are known, the thickness of the deformed configuration can be determined by $h = (\Gamma_N H)/\Gamma_n$.

Equation (2.19) can also be simplified for the case of incompressible materials, as follows:

$$\mathbf{S} = 2\frac{\partial \psi(\mathbf{C})}{\partial \mathbf{C}} - pJ\mathbf{C}^{-1}, \tag{2.29}$$

where p denotes the cell internal pressure, an unknown function to be determined by the incompressibility condition.

The neo-Hookean material model extends the linear law of the Saint Venant–Kirchhoff model Equation (2.21), valid for large deformations of large rotations and small strains [34–36]. For the neo-Hookean model the restriction of small strains is dropped, since it is the simplest model for dealing with a limited range of large strains (up to 50%) with good accuracy [37–39]. The strain-energy function ψ for these materials are given in terms of the isochoric part of $\mathbf{C}$, as follows:

$$\psi(\mathbf{C}) = c_{10}(I_{\mathbf{C}} - 3), \tag{2.30}$$

$$\boldsymbol{\sigma} = 2c_{10}\mathbf{b} - p\mathbf{I}, \tag{2.31}$$

where $\mathbf{I}$ is the second-order identity tensor.

The Mooney-Rivlin material model is the most comprehensive model covered in this study. There are several other hyperelastic models such as Polynomial, Ogden, Arruda-Boyce, etc., but the more complex they become the computational costs tends to increase as well. The Mooney-Rivlin material model with two constants was chosen for the present work due to its versatile applicability and because it covers a wide range of deformation with good accuracy (up to 200%) [37–39], which was relevant to numerically model the EBM process mould clamping and inflation phases. In the same way as in the neo-Hookean material, the Mooney-Rivlin postulates its strain-energy function based on the right Cauchy-Green deformation tensor and its invariants. The strain-energy function for this material model is defined as follows:

$$\psi(\mathbf{C}) = c_{10}(I_{\mathbf{C}} - 3) + c_{01}(II_{\mathbf{C}} - 3), \tag{2.32}$$

where $II_{\mathbf{C}} = tr(\mathbf{CC}) = \mathbf{C}:\mathbf{C}$ is the second invariant of the right Cauchy-Green deformation tensor, and $c_{10} = \mu_{10}/2$, $c_{01} = \mu_{01}/2$ are material constants empirically obtained via material characterisation, furthermore the shear modulus is $\mu = \mu_{10} - \mu_{01}$ [24, 40]. The stress calculated by the Mooney-Rivlin material model can also be determined and presented in terms of the Cauchy stress tensor $\boldsymbol{\sigma}$ and the left Cauchy-Green deformation tensor $\mathbf{b}$ as follows:

$$\boldsymbol{\sigma} = 2(c_{10} + c_{01})\mathbf{b} - 2c_{01}\mathbf{b}^2 - \frac{2}{3}(c_{10}I_{\mathbf{C}} + 2c_2 II_{\mathbf{C}})\mathbf{I}. \tag{2.33}$$

2.2.5 Contact Model

There are several contact models available in the literature that can be used, including perfect sticky, penalty method, and frictional contact models, among others. Each model has its own specialities, advantages, and disadvantages, depending on the type of contact and the specific requirements of the simulation analysis [41].

The chosen contact model was the perfectly sticky model that assumes adhesion between the parison and the mould upon contact. This selection is logical because the moulds are kept at a lower temperature than the parison, and their surfaces are usually rough to aid in air escape. This roughness induces a non-slip condition between the parison and the mould upon contact. Therefore, as the moulds move to clamp the parison and the parison deforms due to its stiffness and/or the pressure forces during the inflation process, a mapping is established between the vertices of the cells and the surfaces of the moulds to capture these contact points. The functions hitPoint and hit from the class PointIndexHit in OpenFOAM are employed to manage these intersection points between the membrane and the moulds. When a cell vertex intersects the surface of the mould, it is moved to the point of intersection. In subsequent calculation steps, it moves along with the mould surface.

2.3 Evaluation Examples

In this section, after the material characterisation section, three evaluation examples are included and defined. The first example involves a straightforward evaluation where simulated results are compared with the analytical solution for the purpose of validating the implemented formulation. Then, a second evaluation is an assessment case for the actual EBM process using a conceptual mould, which was conceived to allow the measurement of the parison at the end of the mould clamping phase. Finally, the third and final evaluation corresponds to a case where a real container, manufactured by the EBM process, is studied. This involves comparing results from numerical simulation with experimentally obtained data, after the mould clamping and inflation phases.

2.3.1 Material Characterisation

The material used in the experiments, HDPE 5502, was characterised using uniaxial tests performed at the processing temperature ($T = 190°\mathrm{C}$) with an AR-G2 rheometer with the Sentmanat Extensional Rheometer (SER) platform [42]. The tests were conducted at three different elongational rates, $\dot{\varepsilon} = \{1.8, 2.0, 2.2\}[1/s]$, which represent the rates experienced by the material during the inflation stage. The obtained data were fitted to the two-parameter Mooney-Rivlin hyperelastic model, being the results are presented in Figure 2.3.

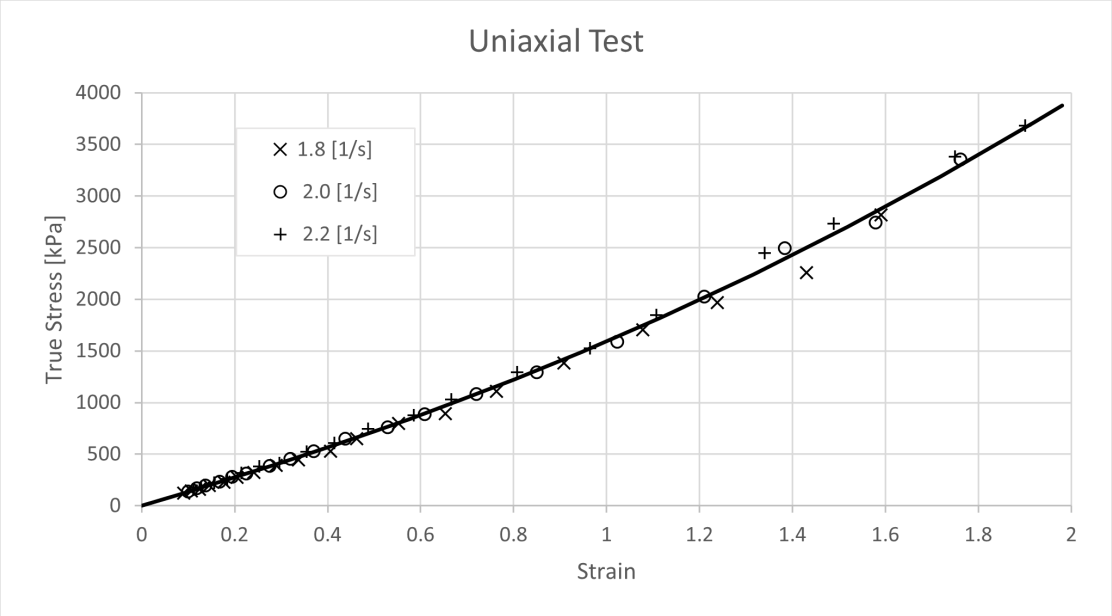


Figure 2.3: Experimental data collected from uniaxial elongational tests at different rates (points) and the corresponding two-parameter Mooney-Rivlin model fitting (line).

The fitting that minimised the quadratic error for the experimental points resulted in the constants $c_{10} = 226.58\,\mathrm{kPa}$ and $c_{01} = 1.01\,\mathrm{kPa}$ for the two-parameter Mooney-Rivlin model, given by Equation 2.33.

2.3.2 Spherical Balloon

Due to its similarities with the physics of the inflation phase in the EBM process, the well-known process of free-inflation of a spherical balloon has been investigated with the developed calculation tools. A reference case has been defined, as stated in Holzapfel [24], by using a sphere with a constant initial dimensionless radius $R^* = R/H = 100$. One can see in Figure 2.4 the discretised finite area mesh for $1/8$ of an entire sphere centred at the origin and placed in the first octant of the three-dimensional Euclidean space. A symmetry boundary condition is defined for each of the Cartesian planes formed by the principal rectangular axis. The mesh has 30 cells per boundary edge and, 1378 triangular cells in total.

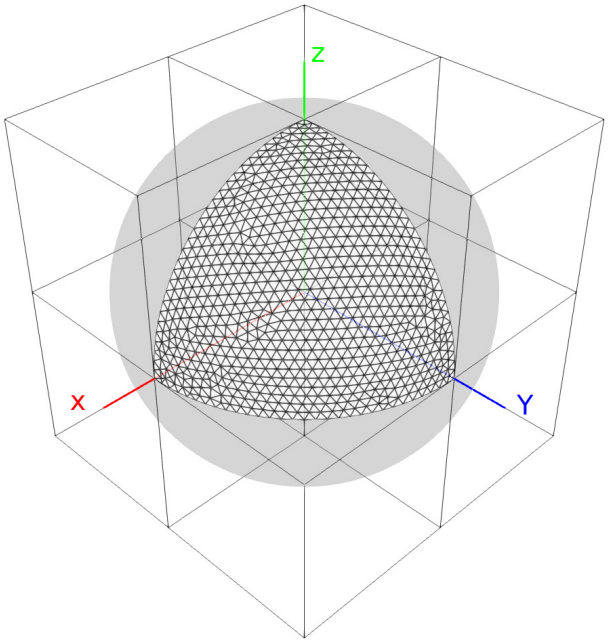


Figure 2.4: Discretised spherical balloon.

When positive pressure is applied to the inside surface of the spherical balloon, it deforms to reach an equilibrium state where the radius increases. This particular geometry chosen allows an analytical solution that equates equilibrium conditions between the internal pressure and the internal forces induced in the membrane due to its stiffness.

Two alternative approaches are analysed. The first involves by imposing a state of deformation on the spherical balloon, in order to calculate the induced stress field. The second approach involves gradually increasing the internal pressure and seeking the equilibrium condition for the resulting forces. The latter resembles the approach implemented numerically for simulating the mould clamping and inflation phases of EBM process.

It is well-established that every direction within the plane of the membrane for a perfect sphere corresponds to a principal direction [24]. Consequently, under the inflation pressure, the sphere undergoes an equibiaxial deformation in the two angular directions of the spherical coordinate system. This leads to the following stretch ratios: $\lambda_\theta = \lambda_\phi = \lambda$ and $\lambda_r = 1/\lambda^2$ [24], where λ_θ and λ_ϕ are the stretches in the angular basis directions and λ_r is in the radial basis direction in the spherical orthonormal coordinate system. The corresponding Cauchy stresses can be expressed in a unified form, as

$$\sigma = \sum_{p=1}^{N} \mu_p (\lambda^{\alpha_p} - \lambda^{-2\alpha_p}), \tag{2.34}$$

which encompasses both hyperelastic material models employed in this work, the neo-Hookean and

Mooney-Rivlin models [24]. Here, μ_p represents the shear moduli, and N is a positive integer determining the number of terms in the strain energy function. With $N = 1$ and $\mu_1 = 2c_1$ Equation (2.34) corresponds to the neo-Hookean material model [24]. For $N = 2$, $\mu_1 = 2c_{10}$ and $\mu_2 = -2c_{01}$ the evolution corresponds to the two term Mooney-Rivlin material model [24].

For the equilibrium condition, the analytical solution for internal pressure is a function of current radius r, thickness h, and stress σ, is given by:

$$p_i = 2\left(\frac{h}{r}\right)\sigma. \tag{2.35}$$

The incompressibility condition implies that $r = R\lambda$ and $h = H/\lambda^2$. By substituting these into Equation (2.35) and incorporating σ from Equation (2.34), the following analytical expression is derived for the inflation pressure:

$$p_i = 2\frac{H}{R}\sum_{p=1}^{N}\mu_p\left(\lambda^{(\alpha_p-3)} - \lambda^{(-2\alpha_p-3)}\right) \tag{2.36}$$

Simplifying Equation (2.36) for the neo-Hookean material model yields:

$$p_i = 4\frac{H}{R}\left[c_1\left(\frac{1}{\lambda} - \frac{1}{\lambda^7}\right)\right], \tag{2.37}$$

while for the Mooney-Rivlin the relation is the following:

$$p_i = 4\frac{H}{R}\left[c_{10}\left(\frac{1}{\lambda} - \frac{1}{\lambda^7}\right) + c_{01}\left(\lambda - \frac{1}{\lambda^7}\right)\right]. \tag{2.38}$$

2.3.3 Conceptual Mould

This evaluation example aims at comparing simulated and experimental results during the clamp phase of the EBM process, which is used to produce a real part. To facilitate the experimental analysis, a conceptual mould was devised to enable visualisation and recording of the parison deformation during the mould clamping phase. The conceptual mould is depicted in Figure 2.5, where one can observe the recording cameras location, the frontal camera on the right mould and the side camera on the left mould (highlighted in orange).

The primary objective of this evaluation is to compare the experimental dimensions of the

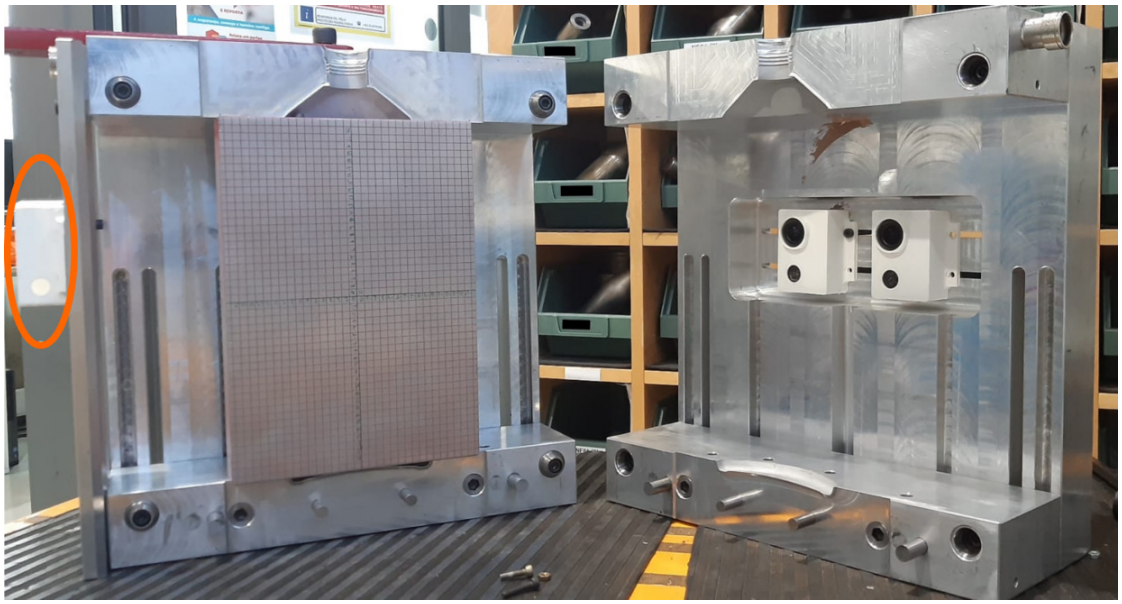


Figure 2.5: Conceptual moulds used for the experimental measurements.

parison's geometry at the final stage of the mould clamping phase with the corresponding numerical results.

The material used to extrude the parison was raw virgin High-Density Polyethylene (HDPE) 5502, provided by TotalEnergies Petrochemicals. This material possesses a specific mass of $\rho = 954\,\mathrm{kg/m^3}$ and a thermal expansion coefficient of $\beta = 1.1 \times 10^{-4}\,\mathrm{K^{-1}}$ [43].

The extrusion tool setup employed a divergent configuration with a constant die gap opening, with a mass flow rate of $\dot{m} = 3.73\,\mathrm{g/s}$, at a processing temperature of $T = 190°\mathrm{C}$. The EBM cycle lasted $20.4\,\mathrm{s}$ per parison cut. Moreover, the moulds' closure took place in $0.33\,\mathrm{s}$ which corresponds just to 1.62% of the cycle time. The parison dimensions, at the beginning of the mould clamping phase, were measured from two viewpoints, front and side, using the above-mentioned cameras. These measurements were essential for generating the discretised initial parison geometry to be used in the calculations.

To determine the parison's dimensions, each viewpoint was approximated to a cylinder with a varying diameter throughout its axial length, ranging from the top to the bottom. Since at a same axial position there are two different values for the diameters, the parison cross-section was approximated by an ellipse. Accordingly, the front diameter regarding the parison's width, i.e., the ellipse's major axis, while the side diameter corresponds to the parison's depth, i.e., the ellipse's minor axis. The methodology used to measure the parison in the reference configuration is depicted in Figure 2.6. This process involved the use of a grid scale (Figure 2.6 a)) and superimposing grid images onto the parison images. This approach was adopted to minimise out-of-focus distortions that can occur in camera-captured images.

The previous measurements approximated the intermediate variation between each measurement plane from the top to the bottom as a quartic function. This function equates the

measured diameter along the Z coordinate, where $Z = 0.0\,\text{mm}$ corresponds to the die gap, and its value increases along the extrusion direction, i.e. the parison length. Since the diameters differ depending on the viewpoint, one quartic function was obtained for each viewpoint, as follows:

$$D(Z)_{front} = -5.048\times10^{-9}Z^4 + 3.762\times10^{-6}Z^3 - 9.461\times10^{-4}Z^2 + 0.138Z + 47.170 \text{ mm, and} \quad (2.39)$$

$$D(Z)_{side} = -1.411\times10^{-8}Z^4 + 8.894\times10^{-6}Z^3 - 2.006\times10^{-3}Z^2 + 0.206Z + 47.170 \text{ mm.} \quad (2.40)$$

The measured values used to obtain the above equations, which were used to create the virtual model, are presented in the graph between the two views of the virtual parisons in Figure 2.6 b). The parison surface was built by using Blender [44], a 3D computer graphics software tool.

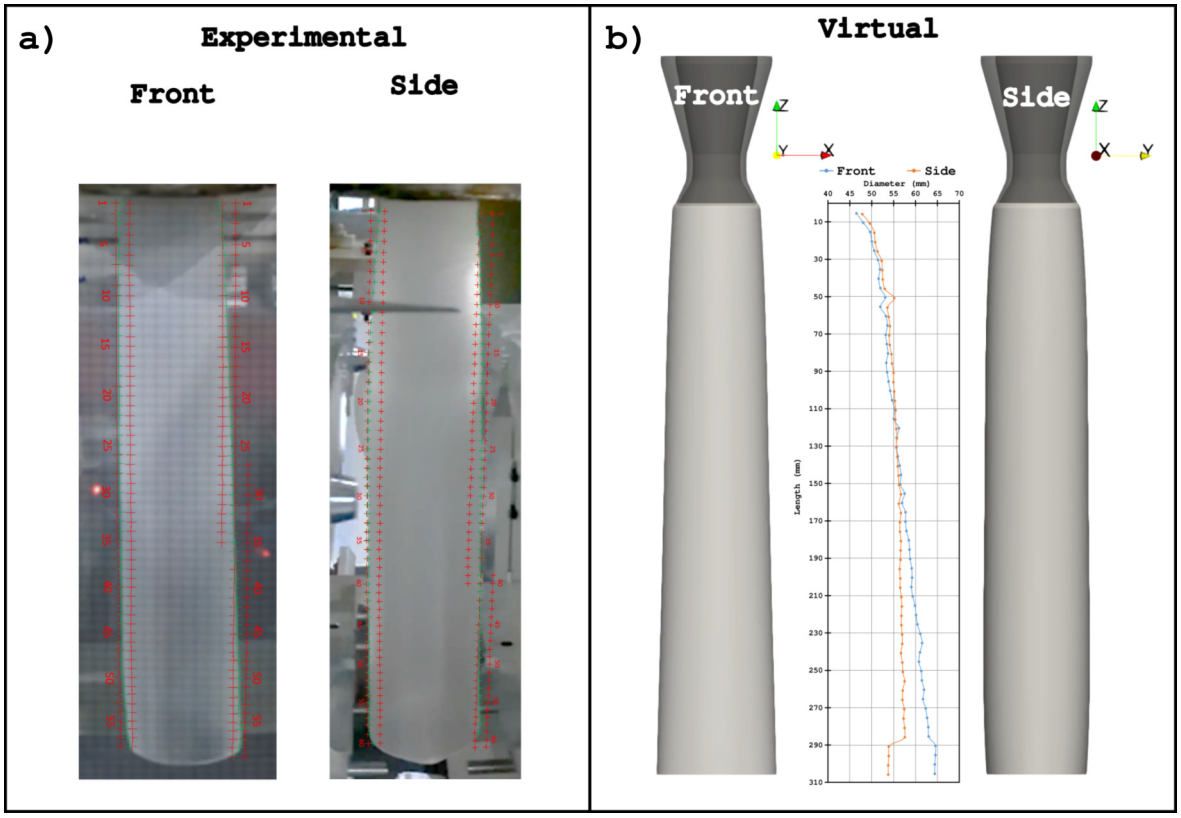


Figure 2.6: Experimental measurements of parison and digitalisation processing, a) Real parison and b) virtual built parison in front and side perspective views.

The initial thickness distribution of the real parison could not be directly measured. Therefore, it was made a simplifying assumption of a constant initial thickness, uniformly distributed throughout

the entire parison length. This thickness distribution was calculated in a way that ensures mass conservation, in addition, due to the incompressibility condition that applies to extruded polymers, volume conservation is also guaranteed. Furthermore, this uniformly distributed approximation was simple but reasonable, considering that the parison was extruded with a constant die gap. However, as the extrusion time increases, a non-uniform thickness distribution may occur due to the viscoelastic response of the material under the extrusion conditions, as well as the effects of drawdown and sagging. Although these differences could be obtained, they were neglected in this work.

For this example, the total weight of the parison, including the flash, i.e. the clamped material, was $m = 76.8\,\mathrm{g}$. Utilising the previously determined specific mass, the volume as $V = 79.45\,\mathrm{cm}^3$. The processing temperature was approximately $153\,\mathrm{K}$ higher than the room temperature $T = 298.15\,\mathrm{K}$, at which the previous measurements were conducted. Assuming negligible variations in the thermal expansion coefficient of Total-5502 within this temperature range, the corrected volume calculated is $V = 81.206\,\mathrm{cm}^3$ for the section of the parison below the knife, which was positioned at $54.0\,\mathrm{mm}$ below the extrusion die gap.

The area of the parison downstream from the knife is $A = 457.68\,\mathrm{cm}^2$. Dividing the total polymer volume by this area, an average uniform thickness for the entire parison of $H = 1.774\,\mathrm{mm}$ is obtained.

2.3.4 Real Bottle

For this last evaluation study, a real part was in fact produced by the EBM process. All the material and process definitions used for manufacturing this part were the same as those covered in Section 2.3.3, likewise the definitions and setups for preparing and build the virtual data to perform the simulation. The difference concerns the moulds' geometry, and the simulation of both phases, i.e., the parison clamping and inflation.

The moulds are depicted in Figure 2.7, together with the computer-aided design (CAD) drawings, left and right sides, respectively. This mould was designed to produce the final part depicted in Figure 2.8.

The produced bottle sample, used to compare with the numerical simulation results, was scanned by using an X-Ray microtomography from the RX Solutions, model Easytom S. The scanned bottle is presented in Figure 2.8 in several perspectives. Moreover, the microtomography allows obtaining the thickness distribution in the entire bottle.

Finally, the virtual setup used to simulate the mould clamping and inflation phases for this assessment evaluation example is presented in Figure 2.9.

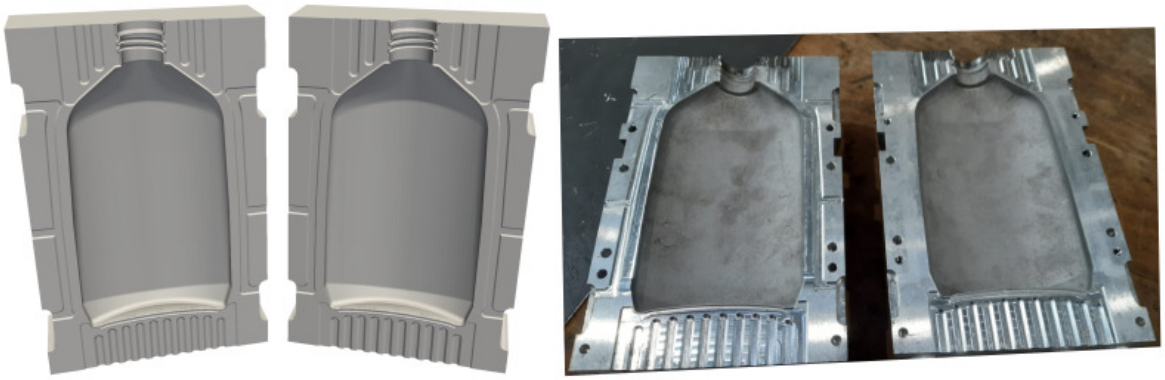


Figure 2.7: Moulds used to produce the bottle.

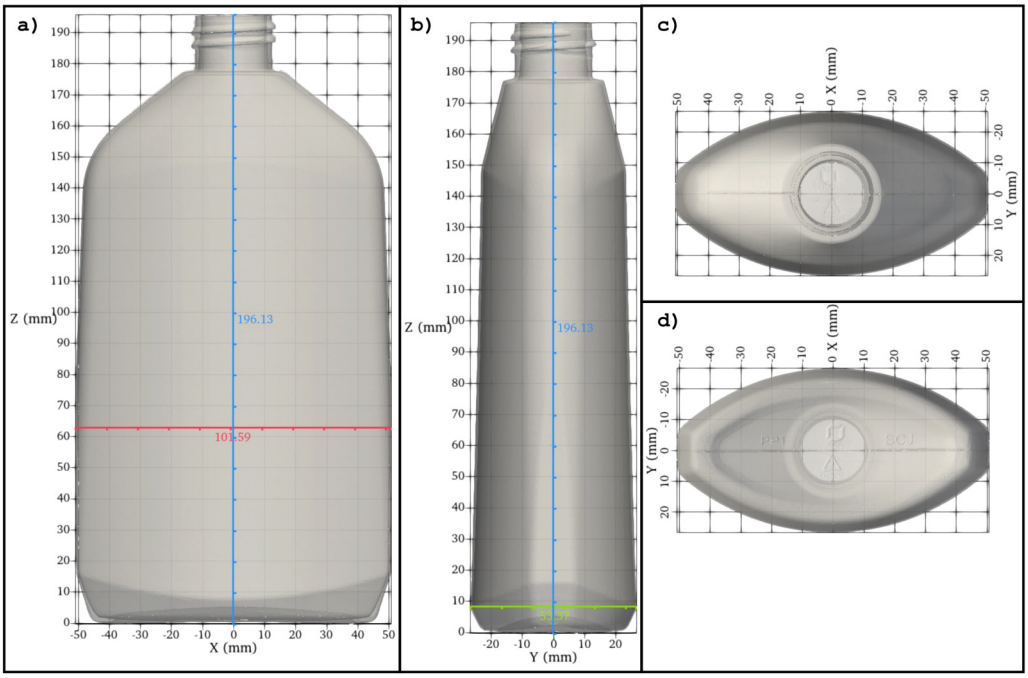


Figure 2.8: Several views of the real bottle produced by the EBM process and digitalised via X-ray microtomography, a) frontal view, b) lateral view, c) top view, and d) bottom view.

2.4 Results and Discussions

In this section, the results of the three cases presented in Section 2.3 are analysed and discussed.

2.4.1 Spherical Balloon

The first simulation involves an imposed state of deformation, whereas the second entails a gradual increase in internal pressure until equilibrium among all the forces is reached.

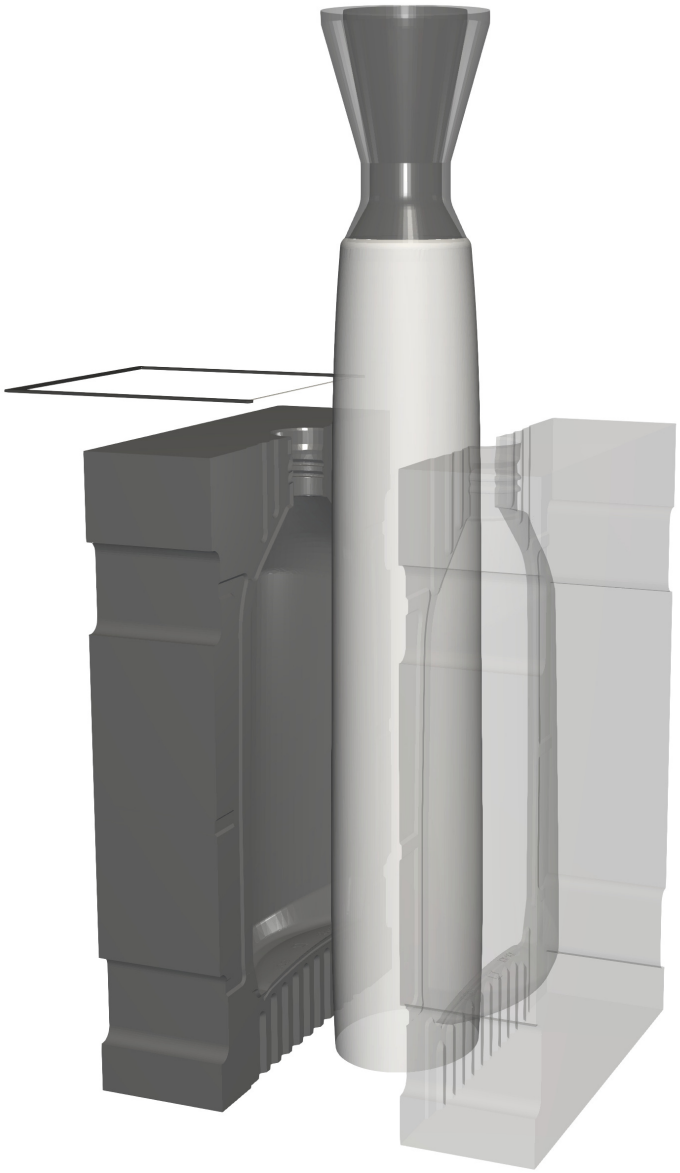


Figure 2.9: Setup for the numerical simulation for the mould clamping and inflation phases in the EBM process.

In the first simulation, the perfect spherical geometry simplifies the analysis of the balloon's deformed state. Specifically, the current configuration of the balloon in spherical coordinates only changes its radius, denoted as $\kappa_t(r,\theta,\phi) = \kappa_0(\lambda R,\Theta,\Phi)$. As the implemented numerical code uses the rectangular coordinate system, a transformation is required to express the imposed deformation in this spherical coordinates. Utilising the transformation identities ($x = r\sin(\theta)\cos(\phi)$, $y = r\sin(\theta)\sin(\phi)$, and $z = r\cos(\theta)$), the imposed state of deformation in rectangular coordinates is given by:

$$\begin{aligned}\kappa_t(x,y,z) &= \kappa_0(\lambda R\sin(\Theta)\cos(\Phi), \lambda R\sin(\Theta)\sin(\Phi), \lambda R\cos(\Theta)) \\ &= \kappa_0(\lambda X, \lambda Y, \lambda Z).\end{aligned} \tag{2.41}$$

The simulations use a constant shear modulus, $\mu = 422.5$ kPa, consistent with Holzapfel [24]. The neo-Hookean material model is defined by a constant $c_1 = 2\mu$, while the Mooney-Rivlin model incorporates constants $c_{10} = 0.4375\mu$ and $c_{01} = 0.0625\mu$ following the material parameters provided in Anand [40].

The evolution of inflation pressure concerning the imposed stretch λ is depicted in Figure 2.10 for both analytical and simulation results. Simulation results were computed using Equation (2.35), with the von Mises stress σ_{vm} calculated by

$$\sigma_{\mathrm{vm}} = \sqrt{\frac{1}{2}\left[(\sigma_{xx}-\sigma_{yy})^2 + (\sigma_{yy}-\sigma_{zz})^2 + (\sigma_{zz}-\sigma_{xx})^2\right] + 3(\sigma_{xy}^2 + \sigma_{yz}^2 + \sigma_{xz}^2)}. \tag{2.42}$$

Using the von-Mises stress in Equation (2.35) is an appropriate choice, obviating the need for complex transformations between coordinate systems. Moreover, it provides an effective measure of stress in the material and is widely employed in solid mechanics analysis. Furthermore, due to the chosen shape of a spherical geometry, the stress state in the spherical coordinate system aligns with the principal stresses, namely, $(\sigma_1 = \sigma_r = 0)$, $(\sigma_2 = \sigma_\theta)$, $(\sigma_3 = \sigma_\phi)$. As a result, $\sigma_{vm}(x,y,z) = \sigma_{vm}(r,\theta,\phi) = \sigma_\theta = \sigma_\phi = \sigma$ as calculated from Equation (2.34).

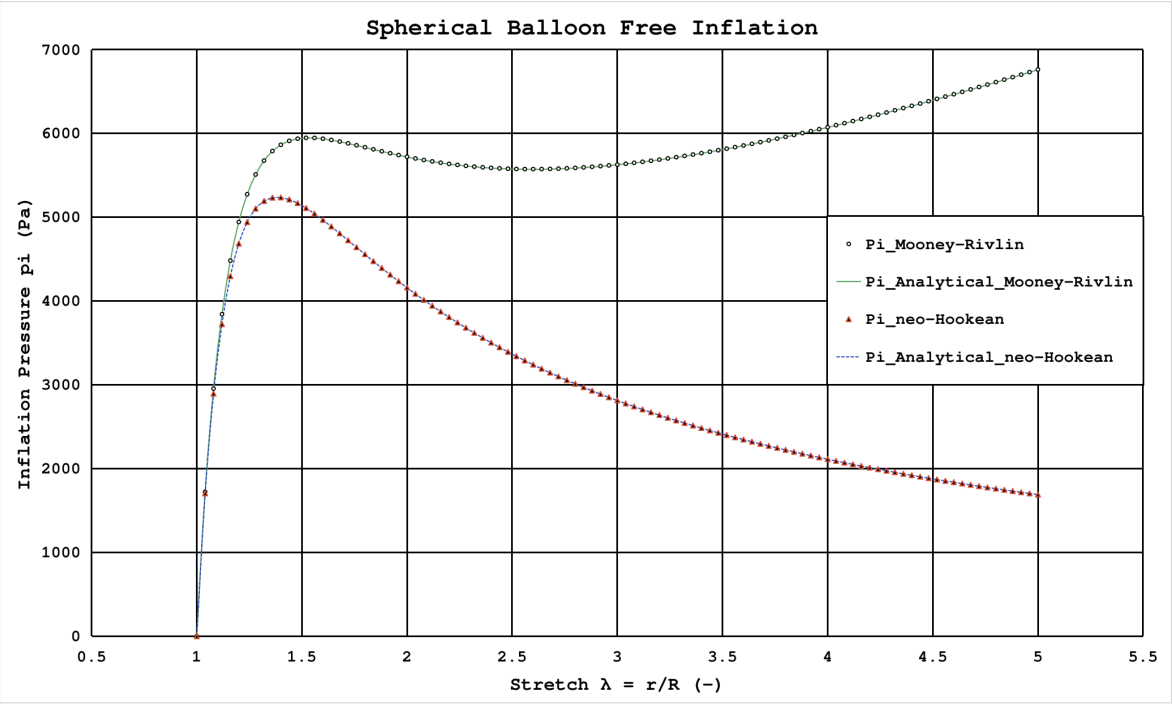


Figure 2.10: Inflation pressure as a function of stretch for the spherical balloon with the imposed deformation.

In the context of the second type of simulation for the stated problem, the discussion is centred on the Mooney-Rivlin material model. This choice was deliberate because this simulation method, characterised by a gradual, step-by-step increase in internal pressure, reveals a distinct behaviour. Specifically, at a stretch value of approximately $\lambda \approx 1.5$, both material models experience a local

maximum pressure. Beyond this point, the material "snaps through" [24], and a new equilibrium position is only attained at $\lambda \approx 3.8$ for the Mooney-Rivlin model just, within the studied range. This phenomenon does not manifest in the case of the neo-Hookean material model. The progression of stretches necessary to reach equilibrium under applied internal pressure is illustrated in Figure 2.11.

The numerical results obtained from the implemented code, in conjunction with the incorporated constitutive models, successfully replicated the real analytical behaviour observed during the free-inflation of the spherical balloon. Given the similarities to the real process, the gradual increase in the internal pressure was chosen as the appropriate method for simulating the inflation phase of the EBM process.

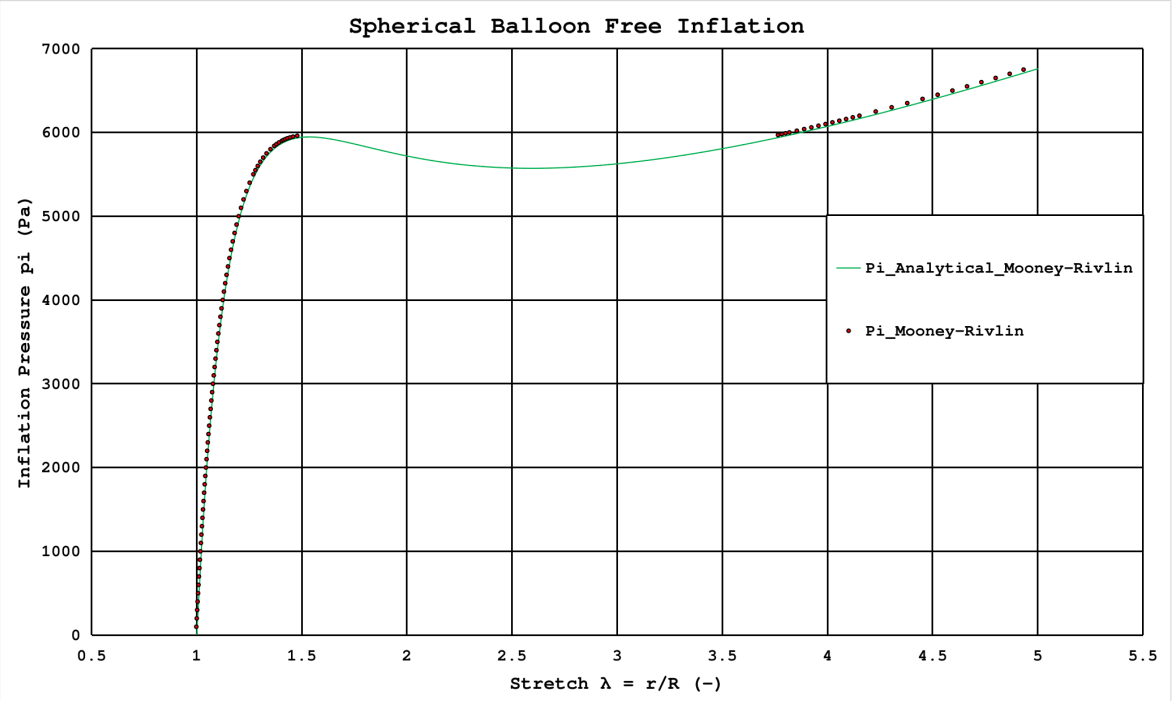


Figure 2.11: Inflation pressure by stretches for the spherical balloon with the imposed internal pressure.

2.4.2 Conceptual Mould

The experimental measurements for the parison followed the approach described in Section 2.3.3. The behaviour of a cylinder or a ring when subjected to transversal compression or tension, due to the material's stiffness, a reaction occurs in an axis perpendicular to the plane direction of applied forces. When under tension/traction the circle becomes ovalised with the major axis aligned with the applied forces, on the other hand, when under compression, the major axis switches to axis perpendicular to the applied forces, as verified in other studies [45]. Accordingly, the analysis in this section is undertaken, encompassing both qualitative and quantitative dimensions, where the just effects of the compression forces induced by the mould closure are responsible for the observed parison deformation.

First, examining the parison dimensions in a frontal view perspective, the experimental data, as shown on the left side of Figure 2.12, revealed that the parison stretched outward in the plane of mould partition plane. This observation is consistent with expectations, as the parison is compressed in the perpendicular direction when the moulds are closed.

Regions of the parison that are not affected by the moulds deform due to the stiffness of the material, although there is less deformation expected in those regions. Furthermore, the stiffer the material of the parison, the more noticeable the displacements are expected to be in the unaffected regions.

Based on the information provided above, it is expected that the mould clamping phase will result in an elliptical cross-section. The axis ratio, which is the ratio of the minor axis to the major axis, decreases as the mould closes. This behaviour was observed in both the experimental images and the numerical simulation results, as shown in Figure 2.12.

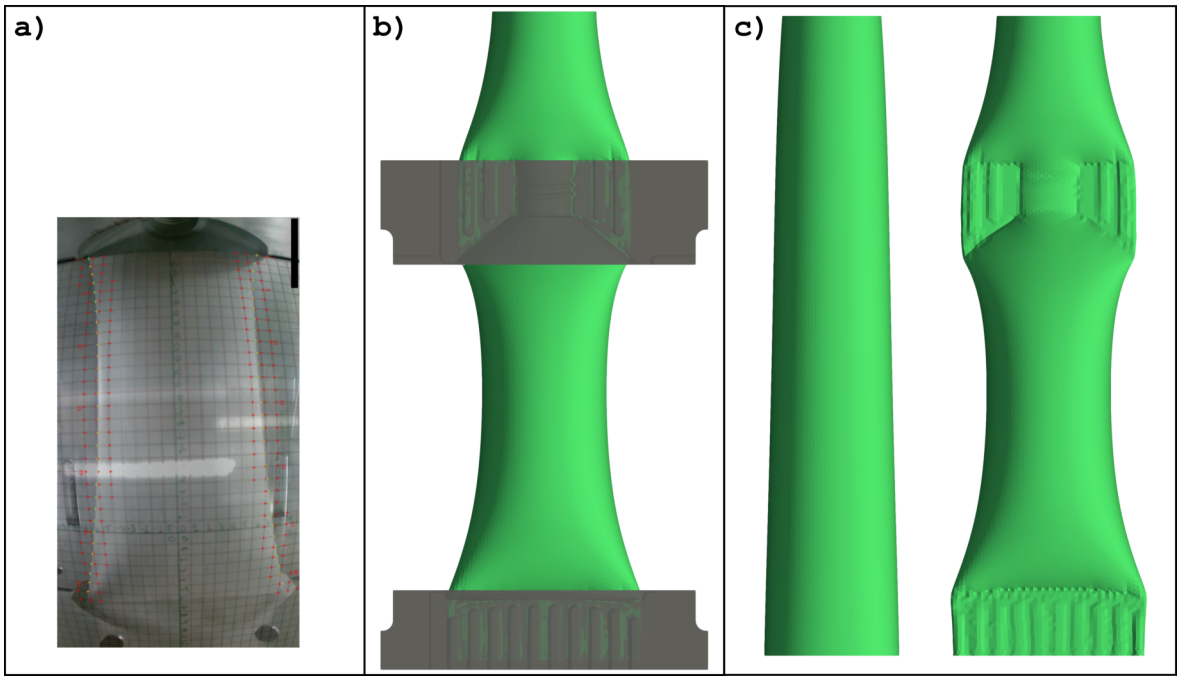


Figure 2.12: Frontal view analysis for the conceptual mould, a) Experimental and b) numerical geometry configurations at the end of mould clamping phase, in c) is the parison before clamping on the left, and after clamp on the right.

These measurements were taken from the uppermost plane adjacent to the bottle neck, extending towards the bottom within the visible portion of the conceptual mould. The length of the position was standardised by dividing the actual length by the total length. This yielded a consistent dimensionless scale known as the Downstream Dimensionless Length, ranging from 0 at the top to 1 at the bottom. The Downstream Dimensionless Length serves as the abscissa axis for Figures 2.13 a) and b).

Comparing the numerical results for the width of the parison's major axis to the corresponding

experimental measurements, in Figure 2.13 a), there is a close correspondence observed along the length of the parison. Notably, the numerical profile exhibits a slightly more convex shape than the experimental one. In contrast, when viewed from the side in Figure 2.13 b), the numerical profile appears slightly larger and more concave compared to the experimental measurements.

Among the variables that could affect these profiles, the most significant factor is the support pressure applied during the mould closure, which occurs simultaneously with the parison cut. These phenomena cause an oscillating pressure evolution and a corresponding alteration in the dimensions of the parison, which are observed as incremental and decremental changes in the camera images. Thus, although the measured and numerical results are not an exact match, this evaluation yields reliable findings that closely approximate real measured data. These results establish a strong basis for further evaluation in more intricate scenarios, especially in the subsequent example, which involve comparing real produced parts with their corresponding simulations.

2.4.3 Real Bottle

In this final evaluation example, the material distribution for a finished part is compared with the results of numerical simulations. The experimental data was digitised by reconstructing the bottle as a Stereolithography (STL) file object, and the thickness was mapped from 3759 measurement points uniformly distributed across the external surface of the bottle. Consequently, the colour map on the part surface, shown in Figure 2.14 a), represents interpolated values between these measured points. This is consistent with the numerical results in which the surface thickness is interpolated from calculated points.

For a qualitative comparison, both the experimental and simulated bottles, viewed from the two principal directions, are juxtaposed in a colour gradient scale map presented in Figure 2.14. The Figure 2.14 a) displays the experimental data, while the simulated data is presented in Figure 2.14 b). It should be noted that the geometries on the left, most side of Figure 2.14, feature spare chords, which are not part of the actual bottle. These spare chords are visually amplified changing its diameter according to its thicknesses. They are presented in a separate bottle positioned alongside, and marked by labelled black lines. Their diameter has been intentionally exaggerated to some extent, yet it varies proportionally with the actual part thickness. The black meridian line, in analogy with the geographic coordinate system (GCS), namely line ML in Figure 2.14, is taken from the prime meridian and anti-meridian lines in the geometry, splitting the geometry in two pieces a west and east halves. This is the longest profile taken in the geometry. Furthermore, following the same analogy as used in GCS, another three latitudinal intersection planes were taken to evaluate the thicknesses profiles, namely lines LQ1, LQ2 and LQ3 as indicated in Figure 2.14, for comparing the results. These latitudinal profiles were taken at $1/4$, $2/4$ and $3/4$ of the bottle total height, going from the bottom to the neck.

In these results, it is evident the overall good agreement between the measured and calculated data. Notably, a thicker region is observed at the central area of the bottle. This thickness increase is

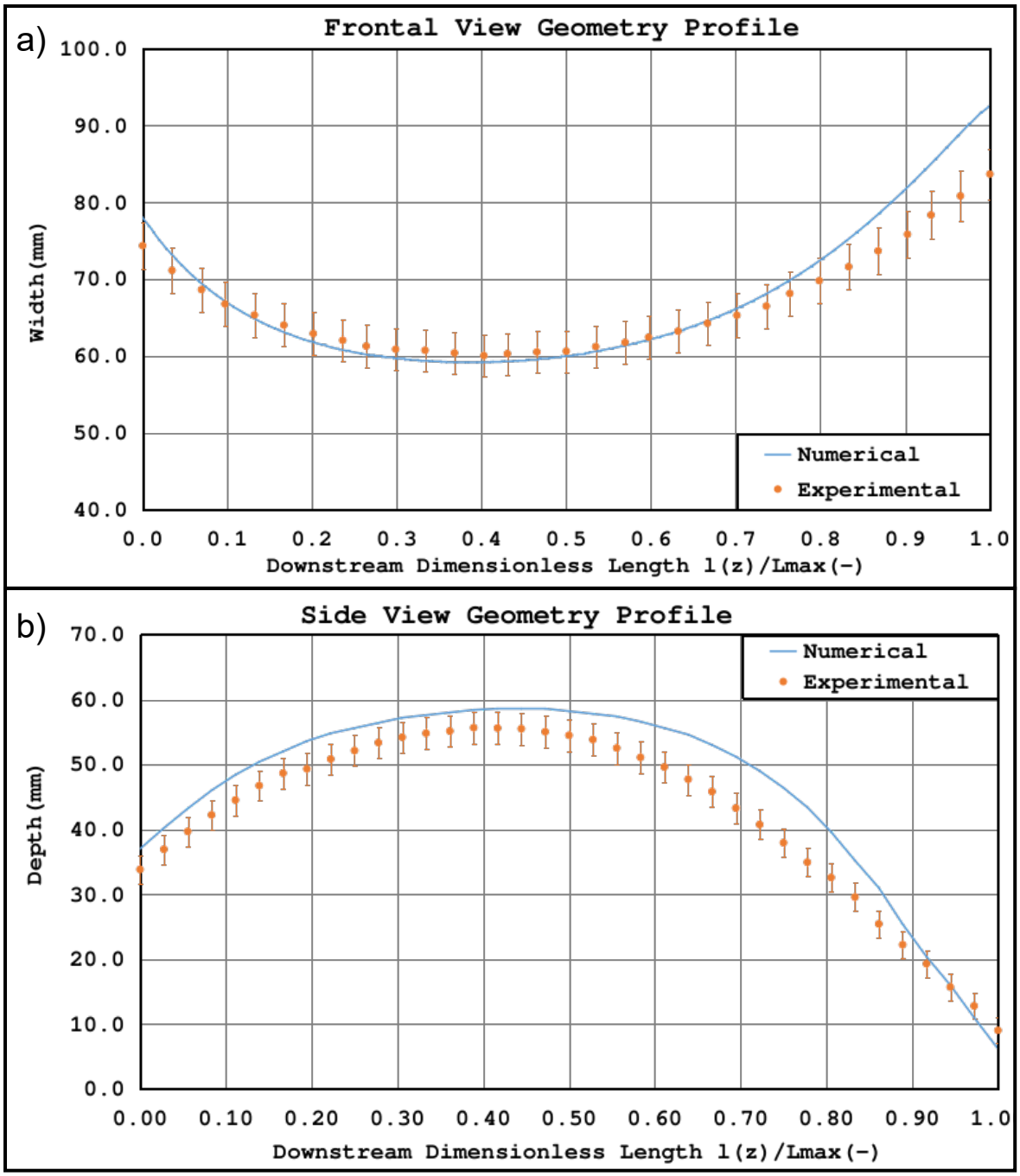


Figure 2.13: Experimental and numerical profiles for the parison at the end of mould clamping phase, a) frontal view and b) side view.

attributed to the proximity between the parison and the mould in this region, which is the first zone to touch the mould at the inflation phase. This causes the thickness to decrease with the distance from this central area. As the parison deforms, it stretches and becomes thinner until touching the moulds.

A distinct thicker region is also noticeable at the partition surface, where the parison surfaces come into contact with each other. This thicker region, a result of the closing process, is commonly referred to as the "welding edge". It plays a crucial role as it provides to the part added thickness enhancing its mechanical strength in this region, which is important during the detachment and

removal of excess plastic, known as flash, from the final part. Moreover, it also serves to prevent failures during service, since weld regions are a region with a decreased mechanical strength and prone to failure. Furthermore, certain areas of maximum thickness are observed at the corners of these welding edges due to the moulds' compression implied in the parison's surfaces during the mould clamping phase. These thicker regions are consistently observed in both the experimental and numerical data.

An almost symmetrical pattern in the thickness distribution map can be observed between the primary rectangular orthonormal planes XY, XZ, and YZ in the numerical results. In contrast, the experimental data exhibits slight variations between the two halves, specifically the meridian and anti-meridian thickness profiles, which is anticipated in the context of real-world scenarios, where perfect symmetry is unlikely to occur. The numerical results lack perfect symmetry due to the mesh not being entirely symmetrical, resulting in the cells being stretched slightly more on one side than the other.

When considering the profiles obtained by the latitudinal intersect planes, i.e., lines LQ1, LQ2 and LQ3, there are no significant differences in thickness distribution map between the halves, but a minor difference becomes apparent when considering the prime meridian bisect plane, line ML of the bottle's height. In this latter case, LM profile, it can be observed, primarily in the thicker region, that this thicker region is slightly wider at LQ1 profile than the LQ2 when compared to the same region, which, in turn, is slightly wider than the region at LQ3 profile. This asymmetry might be attributed to an initial non-uniform thickness distribution in the parison before the mould clamping phase.

As mentioned before, the effects of elapsed time for extrusion and own weight, can result in a non-uniform thickness distribution, despite setting a constant die gap opening during extrusion. Thus, considering this source of thickness deviation in the parison prior to the mould clamping phase, a phenomenon known as "necking" effect, results in a central region with lower thickness than the bottom region. This was not considered, thus was simplified, when discretising the initial thickness field for the virtual parison.

The observed difference in the thickness distribution map between the halves is more prominent when considering the XZ bisect plane. This discrepancy could potentially arise from minor irregularities in the parison, such as slight tortuosity or deviations from perfect straightness in its axial central line at the end of extrusion. These characteristics were simplified and assumed as perfectly straight in the virtual parison reconstruction. This experimental asymmetries resulted in different contact places with the mould, thus the thicker side may come into contact with the moulds earlier, resulting in less stretching when compared to the opposite side.

It is also noticed that the neck region of the bottle, as observed in the experimental measurements, exhibits a significantly greater thickness when compared to the same region in the simulated results. The discrepancy arises from the fact that the simulations do not consider the calibration performed by the blown air nozzle in the real process. This is achieved by repositioning the nozzle to a lower position

and physically compressing the polymer into the mould cavity in this region of the bottle's neck. This operation aims to shape the neck in the final part, particularly with regard to the screw design and intricate details in this region, thus creating a thicker wall in this place. These phenomena were not considered in the numerical model.

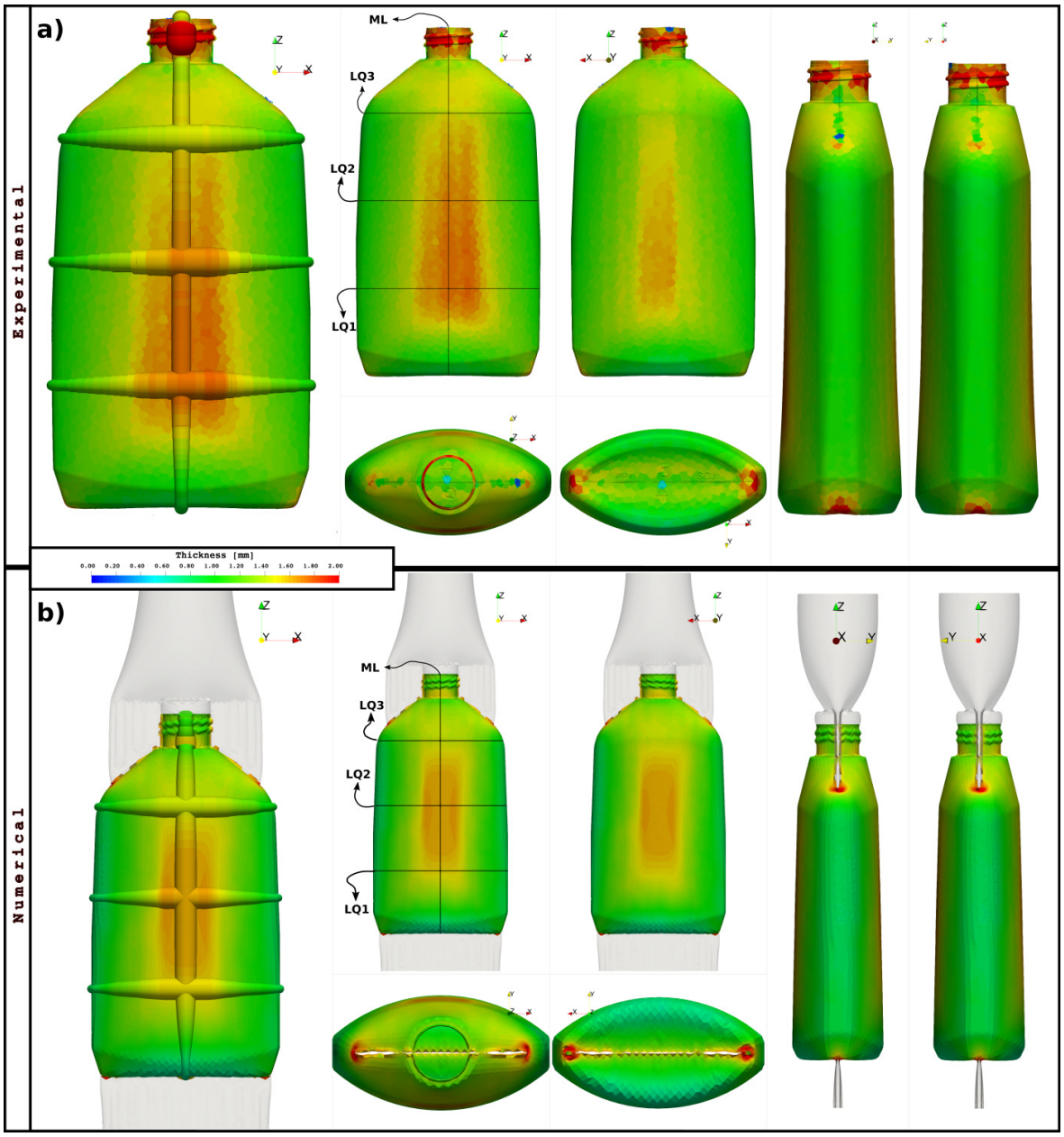


Figure 2.14: Thickness map of all views for the final inflated parison, a) experimental results and b) numerical results.

For a quantitative comparison, the thickness profiles under scrutiny are those corresponding to the positions delineated by the black lines in Figure 2.14. These profiles are classified according to the orthonormal planes on which they are situated, as well as their specific locations along the axes where these planes intersect. The thickness profiles across the four cross-sections are depicted in Figures 2.15 and 2.16.

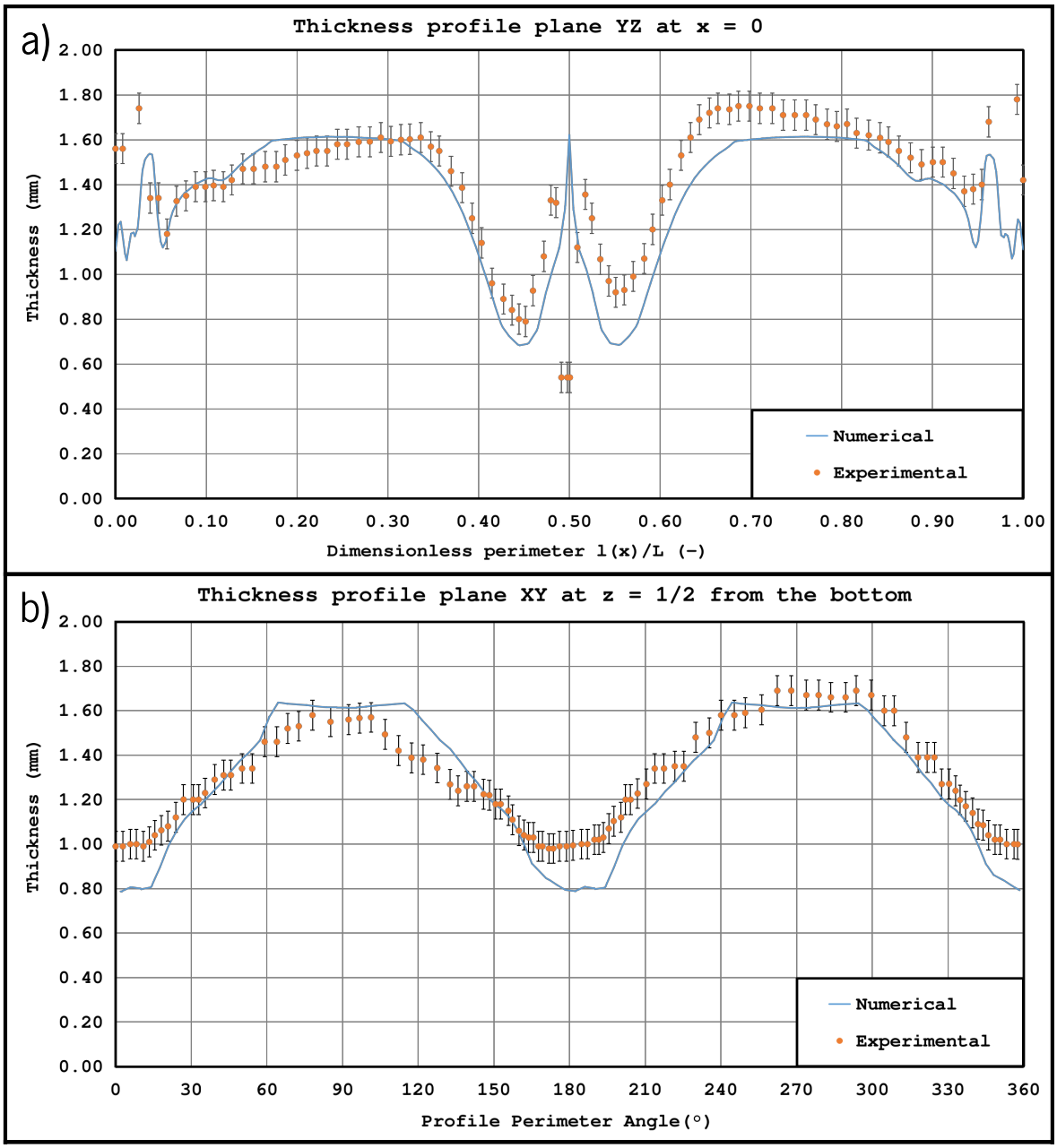


Figure 2.15: Profiles for the thickness distributions in two cross-sections, a) ML cross-section. b) LQ1 cross-section.

The graph, in Figure 2.15 a) illustrates the thickness profile for the line ML of Figure 2.14, along the dimensionless perimeter on the abscissa. This line extends from the anti-meridian (the rear side of the bottle's neck) towards the prime meridian (the front part of the bottle's neck). In Figure 2.15 b), and Figures 2.16 a), and b), the thickness profiles for lines LQ1, LQ2, and LQ3 (see Figure 2.14) are depicted, respectively. In these graphs, the abscissa represents the "Profile Perimeter Angle $(^{o})$", defined as the angle in the XY plane measured counter-clockwise, ranging from 0^{o} to 360^{o}, where 0^{o} is aligned with the $X+$ axis from the rectangular orthonormal basis. It is notable that, in the experimental measurements, the region spanning from 0.0 to 0.5, corresponding to the bottle's rear, is thinner compared to the region between 0.5 and 1.0, representing the front part, which is consistent with the

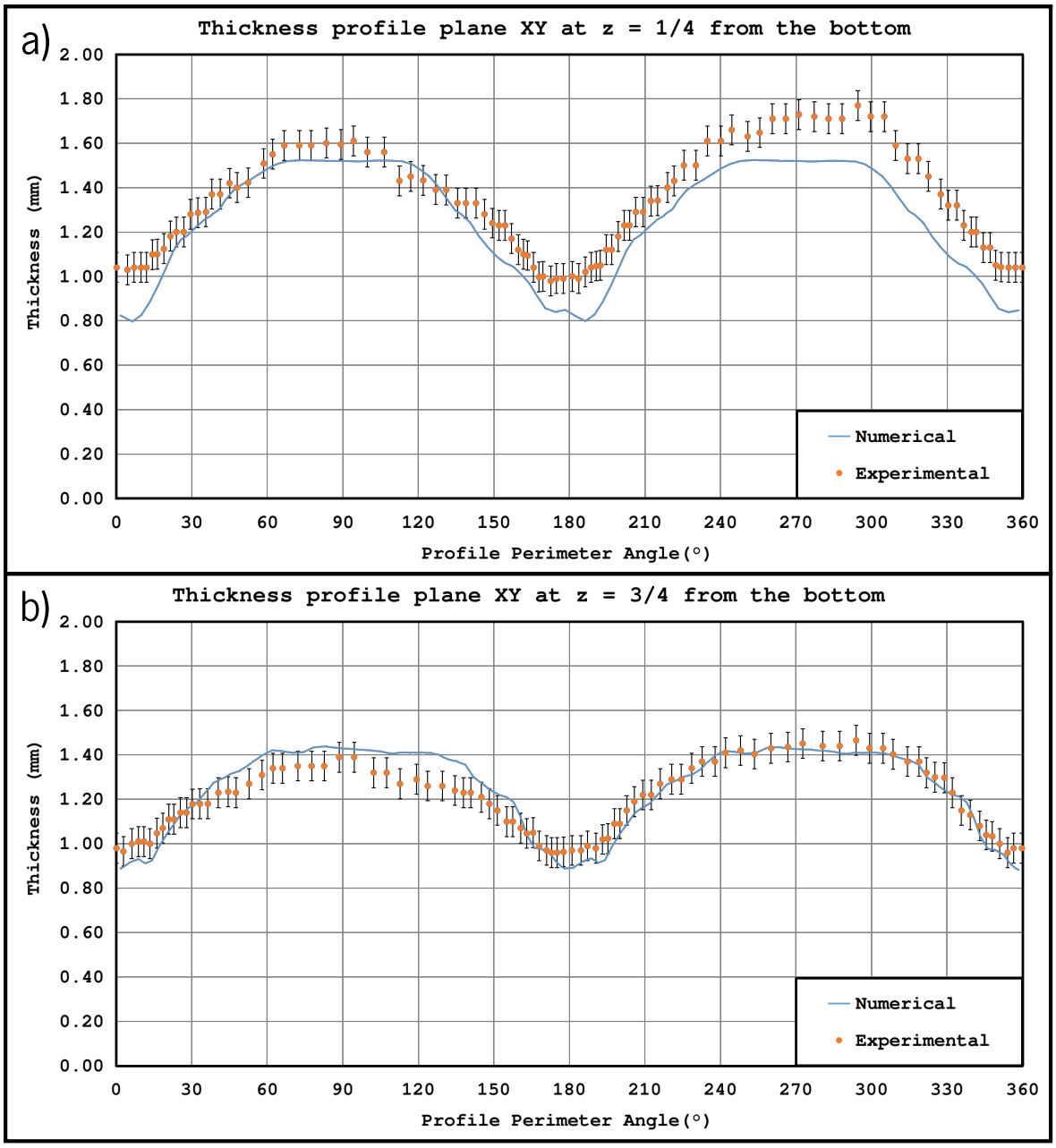


Figure 2.16: Profiles for the thickness distributions in other two cross-sections, a) LQ2 cross-section. b) LQ3 cross-section.

graph shown in Figure 2.15 a).

In both profiles, i.e., meridional and latitudinal cross-section profiles, the thickness experiences a rapid increase around the dimensionless profile value of 0.5. Notably, the welding edge at the bottom of the bottle intersects this profile at the dimensionless perimeter of 0.5. It is a worth mentioning that some measured points in this region exhibited a significant decrease in thickness. Accordingly, detailed measurement verification was conducted in this area, revealing that surface irregularities in this region adversely affected the device's measurements. As a result, the thickness in this region was confirmed to be $1.47 \pm 0.067\,\mathrm{mm}$, which is in good agreement with the numerical results, and

the measurements' uncertainty was provided with the device used for that. Further insights into this verification are available in Figure 2.17, offering both a comprehensive and zoomed-in perspectives views for additional clarity.

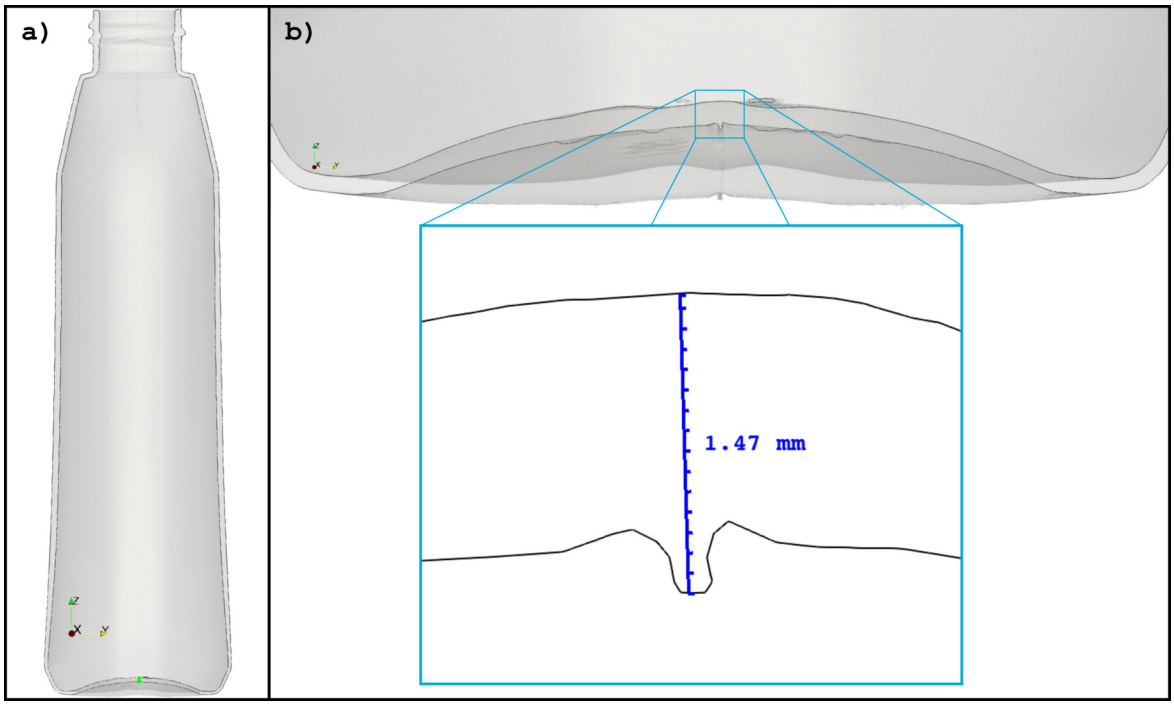


Figure 2.17: Measurement verification for the thickness profile of plane YZ at the welding edge region, a) full bottle slice and b) zoom at the mould partition plane.

The other three plots, i.e., Figure 2.15 b), and Figures 2.16 a) and b), across all profiles from 0^{o} to 180^{o} (the rear side of the bottle), it is evident that the measured thickness is lower than the front side of the profile, i.e., from 180^{o} to 360^{o}, corroborating the asymmetry observed during the qualitative analysis. The concurrence and correspondence between these profiles are in agreement between numerical simulations and measured data, with the profile from Figure 2.16 b) exhibiting the most congruence.

A noteworthy observation is the presence of a plateau region characterised by constant thickness, spanning the angular range from 60^{o} to 120^{o} and from 240^{o} to 300^{o}, in the numerical simulation results. This phenomenon arises because these regions of the parison came into contact with the moulds during the mould clamping phase, resulting in what is commonly referred to as a "frozen zone" within the parison. In experimental processing, it can be noticed a plateau in the same region for the bottle, but it did not afford a capability to assess, capture and validate this phenomenon, nor verified by the same behaviour in their thickness profiles.

2.5 Conclusions

This research work covers the development and assessment of a modelling framework for the complex mechanics of the clamp and inflation phases in the EBM process. This was accomplished by implementing a novel Finite Area Method in the OpenFOAM® computational library. The developed tools incorporate a membrane approach with hyperelastic materials, in a vertex centred arrangement, following a corotational formulation, and adopting a quasi-static approximation. The result is a comprehensive, innovative computational model that can simulate the deformation of membranes, which encompasses the envisaged phases of the EBM process.

The validity and reliability of the developed tools have been thoroughly confirmed through comparisons of the numerical results with analytical solutions and experimental measurements.

The developed framework has been validated through a comprehensive study of a renowned problem in the literature regarding the inflation of a spherical balloon. This study has yielded invaluable insights into the behaviour of hyperelastic materials under different inflation conditions. The obtained results confirm the proper implementation of the code.

Subsequently, the code was first evaluated in the EBM process, with a specific emphasis on the mould clamping phase. For that, a novel conceptual mould was devised and used to collect relevant experimental data that is not accessible with conventional moulds. The good correlations obtained between the numerical results and experimental data demonstrate that the developed simulation framework can accurately capture the most relevant details of the parison deformation induced during the mould clamping phase.

Then, the final validation study involved the production of a real bottle, where the predicted final thickness distribution by the code is compared with experimental data measured using X-Ray microtomography. The collect data is analysed in detail both qualitatively and quantitatively. Again, an excellent match is achieved between the experimental and numerical results, indicating that the developed code can accurately capture the most important aspects of the thickness distribution in a real part.

Based on the results obtained, it can be concluded that the implemented simulation framework is an excellent tool for guiding the design of the EBM process, tools, and parts. In a society that prioritises sustainability and performance in a world dependent on plastic products, this research and development can assist in designing EBM processes to meet specific requirements and predict potential failures in advance. This provides valuable guidance for the continuous evolution of the industry.

References

[1] James L Throne. Understanding thermoforming. Hanser Gardner Publications Cincinnati, OH, 2008.

[2] Peter W. Klein. Fundamentals of Plastics Thermoforming. Springer International Publishing, 2009.

[3] Syed Ali Ashter. Thermoforming of Single and Multilayer Laminates. William Andrew Publishing, 2014.

[4] Roger E Khayat and Paul Raducanu. A coupled boundary/finite-element approach for the three-dimensional simulation of air venting in blow molding and thermoforming. International journal for numerical methods in engineering, 43(1):151–174, 1998.

[5] Benoît Debbaut, Olivier Homerin, and Noor Jivraj. A comparison between experiments and predictions for the blow molding of an industrial part. Polymer Engineering & Science, 39(9):1812–1822, 1999.

[6] Gi Joon Nam, Jae Wook Lee, and Kyung Hyun Ahn. Three-dimensional simulation of thermoforming process and its comparison with experiments. Polymer Engineering & Science, 40(10):2232–2240, 2000.

[7] Gilles Marckmann, Erwan Verron, and Bernard Peseux. Finite element analysis of blow molding and thermoforming using a dynamic explicit procedure. Polymer Engineering & Science, 41(3):426–439, 2001.

[8] Kent T. Danielson. Curved node-to-face contact schemes for higher-order finite elements in lumped-mass explicit methods. Computer Methods in Applied Mechanics and Engineering, 395:115056, 2022.

[9] Gerhard A. Holzapfel, Robert Eberlein, Peter Wriggers, and Hans W. Weizsäcker. Large strain analysis of soft biological membranes: Formulation and finite element analysis. Computer Methods in Applied Mechanics and Engineering, 132(1):45–61, 1996.

[10] Eugenio Oñate and B-H Kröplin. Textile composites and inflatable structures, volume 3. Springer Science & Business Media, 2005.

[11] Shaochen Yang, Bing Zhao, and Wujun Chen. The added mass of a biaxial tensioned membrane in still air. Thin-Walled Structures, 195:111531, 2024.

[12] Qinghua Han, Chao Wu, Mingjie Liu, and Hao Wu. A corotational isogeometric assumed natural strain shell element in updated lagrangian formulation for general geometric nonlinear analysis of thin-walled structures. Thin-Walled Structures, 194:111311, 2024.

[13] Matteo Pelliciari, Stefano Sirotti, Angelo Aloisio, and Angelo Marcello Tarantino. Analytical, numerical and experimental study of the finite inflation of circular membranes. International Journal of Mechanical Sciences, 226:107383, 2022.

[14] R. Zorrilla, R. Rossi, R. Wüchner, and E. Oñate. An embedded finite element framework for the resolution of strongly coupled fluid–structure interaction problems. application to volumetric and membrane-like structures. Computer Methods in Applied Mechanics and Engineering, 368:113179, 2020.

[15] Mariana Remešíková, Marián Šagát, and Peter Novysedlák. Discrete lagrangian algorithm for finding geodesics on triangular meshes. Applied Mathematical Modelling, 76:396–427, 2019.

[16] Yan Yang, Sheng shen Qian, Jing hai Gong, and Guo zhi Qiu. Design method for precise-forming of air-supported structures considering weld seams. Thin-Walled Structures, 145:106397, 2019.

[17] J. Rodriguez, G. Rio, J.M. Cadou, and J. Troufflard. Numerical study of dynamic relaxation with kinetic damping applied to inflatable fabric structures with extensions for 3d solid element and non-linear behavior. Thin-Walled Structures, 49(11):1468–1474, 2011.

[18] E. Verron and G. Marckmann. An axisymmetric b-spline model for the non-linear inflation of rubberlike membranes. Computer Methods in Applied Mechanics and Engineering, 190(46):6271–6289, 2001.

[19] P. Cardiff and I. Demirdžić. Thirty years of the finite volume method for solid mechanics. Archives of Computational Methods in Engineering, 28(5):3721–3780, Aug 2021.

[20] Zeljko Tukovic and Hrvoje Jasak. Simulation of free-rising bubble with soluble surfactant using moving mesh finite volume/area method. In Proceedings of 6th International Conference on CFD in Oil & Gas, Metallurgical and Process Industries, no. CFD08-072, pages 1–11, 2008.

[21] Junuthula Narasimha Reddy. An introduction to continuum mechanics. Cambridge university press, 2013.

[22] Ted Belytschko, Wing Kam Liu, Brian Moran, and Khalil Elkhodary. Nonlinear finite elements for continua and structures. John wiley & sons, 2014.

[23] R.W. Ogden. Non-linear Elastic Deformations. Dover Civil and Mechanical Engineering. Dover Publications, 1997.

[24] G.A. Holzapfel. Nonlinear Solid Mechanics: A Continuum Approach for Engineering. Wiley, 2000.

[25] William C. Swope, Hans C. Andersen, Peter H. Berens, and Kent R. Wilson. A computer simulation method for the calculation of equilibrium constants for the formation of physical clusters of molecules: Application to small water clusters. The Journal of Chemical Physics, 76(1):637–649, 01 1982.

[26] Bengt Fornberg. On the instability of leap-frog and crank-nicolson approximations of a nonlinear partial differential equation. Mathematics of Computation, 27(121):45–57, 1973.

[27] Pini Gurfil and Itzik Klein. Stabilizing the explicit euler integration of stiff and undamped linear systems. Journal of guidance, control, and dynamics, 30(6):1659–1667, 2007.

[28] Christophe Geuzaine and Jean-Francois Remacle. Gmsh. http://gmsh.info/, 2020. Accessed: 2023-Jun-06.

[29] B.L. Koziey, M.O. Ghafur, J. Vlachopoulos, and F.A. Mirza. Chapter 3 Computer simulation of thermoforming, volume 11 of Composite Materials Series. Elsevier, 1997.

[30] A. Weizel, T. Distler, R. Detsch, A.R. Boccaccini, L. Bräuer, F. Paulsen, H. Seitz, and S. Budday. Hyperelastic parameter identification of human articular cartilage and substitute materials. Journal of the Mechanical Behavior of Biomedical Materials, 133:105292, 2022.

[31] Will Zhang, Javiera Jilberto, Gerhard Sommer, Michael S. Sacks, Gerhard A. Holzapfel, and David A. Nordsletten. Simulating hyperelasticity and fractional viscoelasticity in the human heart. Computer Methods in Applied Mechanics and Engineering, 411:116048, 2023.

[32] M. O. Ghafur, B. Koziey, and J. Vlachopoulos. Simulation of Thermoforming and Blowmolding — Theory and Experiments. Springer Netherlands, Dordrecht, 1995.

[33] Simon Wiesheier, Julia Mergheim, and Paul Steinmann. Discrete data-adaptive approximation of hyperelastic energy functions. Computer Methods in Applied Mechanics and Engineering, 416:116366, 2023.

[34] Ellad B. Tadmor, Ronald E. Miller, and Ryan S. Elliott. Numerical solutions: the finite element method. Cambridge University Press, 2011.

[35] Klaus Bernd Sautter, Manuel Meßmer, Tobias Teschemacher, and Kai-Uwe Bletzinger. Limitations of the st. venant–kirchhoff material model in large strain regimes. International Journal of Non-Linear Mechanics, 147:104207, 2022.

[36] Krzysztof Kamil ur, Nasser Firouzi, Timon Rabczuk, and Xiaoying Zhuang. Large deformation of hyperelastic modified timoshenko–ehrenfest beams under different types of loads. Computer Methods in Applied Mechanics and Engineering, 416:116368, 2023.

[37] Beomkeun Kim, Seong Beom Lee, Jayone Lee, Sehyun Cho, Hyungmin Park, Sanghoon Yeom, and Sung Han Park. A comparison among neo-hookean model, mooney-rivlin model, and ogden model for chloroprene rubber. International Journal of Precision Engineering and Manufacturing, 13(5):759–764, May 2012.

[38] S. Rossi, N. Abboud, and G. Scovazzi. Implicit finite incompressible elastodynamics with linear finite elements: A stabilized method in rate form. Computer Methods in Applied Mechanics and Engineering, 311:208–249, 2016.

[39] Yevgen Gorash, Tugrul Comlekci, and Robert Hamilton. Cae-based application for identification and verification of hyperelastic parameters. Proceedings of the Institution of Mechanical Engineers, Part L: Journal of Materials: Design and Applications, 231(7):611–626, 2017.

[40] L. Anand. Moderate deformations in extension-torsion of incompressible isotropic elastic materials. Journal of the Mechanics and Physics of Solids, 34(3):293–304, 1986.

[41] Peter Wriggers and Tod A Laursen. Computational contact mechanics, volume 2. Springer, 2006.

[42] Martin L Sentmanat. Miniature universal testing platform: from extensional melt rheology to solid-state deformation behavior. Rheologica acta, 43(6):657–669, 2004.

[43] Total Energies. Technical datasheet 5502. https://polymers.totalenergies.com/5502, 2022. Accessed: 2023-Jul-18.

[44] Blender Online Community. Blender - a 3D modelling and rendering package. Blender Foundation, Stichting Blender Foundation, Amsterdam, 2018.

[45] M.A. Lillie and J.M. Gosline. Mechanical properties of elastin along the thoracic aorta in the pig. Journal of Biomechanics, 40(10):2214–2221, January 2007.

CHAPTER 3

A computational framework for optimising extrusion blow moulding: Enhancing material efficiency and reducing waste for industry 4.0

Abstract: This study presents a computational framework specifically designed to optimise parts produced through Extrusion Blow Moulding (EBM) processes. By focusing on the crucial phases of the EBM process, namely mould clamping and parison inflation, the framework aims to assist manufacturers in precise material usage control, thereby reducing waste and optimising resources to produce the final parts. The simulation of those phases relies on advanced numerical simulations based on finite strain theory and membrane formulation. The optimisations are carried out iteratively in an automated manner. This optimisation process involves refining the thickness distributions and modifying initial controlling variables to achieve the desired final result that meets the desired specifications. The framework is evaluated through a series of detailed case studies, which include idealised models of cylindrical-like shape bottles and a practical application involving real-world industrial product with a more complex shape format. The latter study comprises an extensive experimental validation. The obtained results demonstrate the developed framework's effectiveness in optimising material distribution, resulting in significant reductions in material waste and improvements in the quality of the final product. Moreover, the proposed framework proves to be a valuable tool for integrating EBM processes into Industry 4.0, offering an extensible and efficient solution for manufacturers aiming to enhance EBM production capabilities, while minimising environmental impact.

Keywords: Extrusion Blow Moulding, Optimisation, Digital Manufacturing, Numerical Simulation

This chapter was adapted from W. d. C. Galuppo, P. Santana, F. Alves, and J.M. Nóbrega, A computational framework for optimising extrusion blow moulding: Enhancing material efficiency and reducing waste for industry 4.0, submitted for publication.

3.1 Introduction

The advent of digital transformation is permeating various industrial sectors [1–5]. Following three significant industrial revolutions, the current stage is now transitioning into its fourth revolution, widely recognised as Industry 4.0 [6–9]. This new era is distinguished by enhanced automation, sophisticated data exchanges in manufacturing technologies, and the introduction of several novel concepts such as cyber-physical systems, the Internet of Things (IoT), cloud computing, cognitive computing, digital twins, and digital manufacturing [10–16]. The primary objectives of Industry 4.0 includes elevating productivity, flexibility, and efficiency, alongside minimising resource consumption to facilitate more tailored product manufacture [14, 17, 18]. The enduring success of Industry 4.0 is predicated on the widespread integration of these modern technologies across diverse industrial sectors [14, 19].

The demand for plastics and their production have experienced exponential growth over the past seven decades, with the industrial sector emerging as the primary consumer. Among various industries, the packaging sector accounts for nearly one third of total plastic usage in the last decade, while the construction sector comprises approximately one sixth [20]. This has prompted the need to improve process efficiency in the packaging sector in order to promote responsible material usage and waste reduction, ultimately working towards the critical goal of reducing plastic consumption [21–25].

Blow moulding, a technique for fabricating hollow plastic parts by inflating a heated plastic tube (parison) within a mould, offers a distinct advantage over injection moulding by necessitating significantly lower pressures. Among the three blow moulding techniques—Extrusion Blow Moulding (EBM), Injection Blow Moulding, and Injection Stretch Blow Moulding—EBM is particularly favoured due to its versatility, e.g. the capability to produce bottles with handles, and broad application spectrum with parts dimensions ranging from millimetres to metres [26–33].

The blow moulding sector is projected to grow annually by 5% up to 2030 [33, 34], furthermore the high-density polyethylene (HDPE) production in the United States approximating 5.8 million tons, had accounted for 40% of its total, consumed by the EBM process [33]. Such significant material usage underscores the importance of studying the EBM process for efficiency and sustainability purposes.

Optimising resource consumption, particularly in material use, is imperative for sustainable manufacturing [35–37]. Various optimisation strategies, such as minimisation and maximisation, topology, shape, size, and material optimisation, have been explored to achieve optimal performance, strength, weight, cost, and sustainability outcomes [38–41]. The material distribution optimisation within the EBM process is a field that remains active due to its impact on sustainability and the quest to minimise plastic usage in manufactured parts [42–45].

The EBM process involves a series of essential steps crucial to ensuring the quality of the final product [33, 46–48]. Among all five key phases - (I) parison extrusion, (II) mould clamping, (III) parison inflation, (IV) part cooling and (V) trimming [48] - the leading four phases play a critical

role in defining the physical characteristics of the final product, underscoring their significance in the numerical modelling and simulation of the EBM technique. Therefore, a particular emphasis on modelling Phases II and III are taken as foundational elements in simulating the EBM process for the digital manufacturing technology and optimisation.

Computational numerical simulations, increasingly utilised across various industries, offer profound insights into designing processes, products development, and manufacturing optimisations. These simulations are indispensable for identifying potential failures and enhancing product performance, playing an essential role within the context of Industry 4.0 transitioning, by modernising manufacturing practices such as the digital manufacturing [49, 50].

Initial investigations into the use of simulations to optimise material distribution in EBM-produced parts can be traced back to Laroche et al. [51]. They conducted a comparison between numerical and experimental results of a blow moulded part, specifically a fuel tank. The objective of the optimisation was to achieve a final part with a uniform thickness distribution and minimal weight. The study revealed that the simulated and experimental data produced similar results in most of the analysed regions. This research demonstrated the potential for rapidly converging to an optimal thickness distribution through an iterative process.

Subsequent studies, carried out by Gauvin et al. [52], have further improved the optimisation of blow-moulded part performance by employing a gradient-based numerical optimisation scheme. This approach utilised finite element simulations to determine optimal process conditions and establish a relationship between part performance and processing conditions. The study employed a two-step sequential optimisation approach to solve the objective function, resulting in enhancements in process efficiency.

Hsu et al. [53] developed a fuzzy optimisation algorithm to optimise material distribution in the EBM process. This method combined engineering heuristics with numerical optimisation techniques, employing fuzzy rules to model the supervision process. Through testing on multiple cases, this approach demonstrated control over the thickness distribution, enabling the achievement of target mechanical properties while minimising weight.

In the same year, Yu et al. [54] presented another study utilising soft computing. They introduced a strategy called fuzzy neural-Taguchi network, with a genetic algorithm (FUNTGA), to minimise the number of simulations required for optimising the blow moulding process. The optimisation focused on improving the final product quality by ensuring a uniform thickness distribution and reducing material usage.

Huang and Huang [55] optimised parison thickness in extrusion blow moulding by utilising a hybrid method that combined finite element method (FEM), artificial neural network (ANN), and genetic algorithm (GA). This approach improved part quality while also reducing material usage by achieving an optimal thickness distribution. Compared to the commonly used trial-and-error approach, their method significantly shortened the part development time, demonstrating its potential for optimisation.

A slightly different but similar process, known as the glass container forming process, was studied and optimised by Groot et al. [56]. They developed a numerical optimisation method to optimise the initial thickness and shape of the preform, with a focus on minimising errors in the glass-air interface to achieve the desired container shape. The method determined optimal initial shapes, resulting in significant improvements in part quality and material usage.

More recently, Denysiuk et al. [57] investigated a methodology for optimising material usage in blow-moulded containers by finding an optimal thickness distribution based on the geometry. The objective is to minimise material usage in blow-moulded containers while maintaining strength, structural integrity, and ensuring compliance with necessary performance requirements. The solution was approximated using neural networks and integrated with finite element analysis. The study emphasised the importance of employing appropriate target strategies linked to evolutionary algorithms to achieve optimisation according to specified conditions.

The referenced studies underscore the substantial potential of computational techniques in optimising EBM processes. Although these studies primarily focus on well-established optimisation methods, they do not extensively explore the specifics of EBM process modelling. Notably, Lagrangian discretisation approaches present significant advantages for modelling the critical phases of the EBM process. These approaches enable precise tracking of the thickness of each computational cell during both the initial and final stages, which facilitates the development of more streamlined and efficient optimisation methods. Additionally, the smooth movement of the mandrel and the resulting continuous parison thickness distribution are essential factors addressed in this research. These elements form the main focus of the present work.

This study is part of a larger project that focuses on the EBM manufacturing process. The goal is to contribute to the integration of this sector into Industry 4.0. Currently, design tasks associated with EBM rely on experimental trial-and-error approaches due to the lack of dedicated computational modelling tools. The success of these inefficient approaches heavily depends on the previous experience of the individuals involved.

The main objective of this particular work is to develop a digital manufacturing framework that automates the optimisation of the material distribution. To address this need, the authors of the present work previously developed a numerical tool based on finite strain theory and membrane formulation [48]. This tool performs numerical simulations of the mould clamping and inflation phases of the EBM process, and demonstrated a strong alignment between its numerical predictions and experimental data. The goal of this work is to expand upon these previous developments by providing an automatic algorithm that enhances the tool's capability to objectively simulate and optimise the final thickness distribution of EBM-produced parts through an iterative process. This implementation will provide the design process with a tool that offers insights to identify and address potential issues, as well as optimise resource utilisation.

The structure of this paper is as follows: Section 3.2 elaborates the theoretical background for

the numerical tool employed to simulate both the clamp and inflation phases, as well as the details on the discretisation process. This section also delves into the parison programming and grouping technique, along with a further view of the developed algorithm used for the automated optimisation. Section 3.3 presents the testing cases used to verify the performance of the proposed algorithm. This includes a simplified geometry and objective, followed by two more complex cases, where the final testing case involves the verification of numerical predictions with a real part produced via EBM process. Section 3.4 showcases the results and discussions derived from the evaluated cases. Lastly, Section 3.5 summarises the findings and concludes the remarks of this study.

3.2 Mathematical Modelling and Methods

In the EBM process, the extrusion starts by transforming gradually the polymer from solid grains into a melt by thermal conduction and viscous shearing between a rotating screw and a barrel. This transformation facilitates the work of transforming this molten plastic into another desired geometry until reaching the final desired shape for the final part. The molten plastic is then pushed through the channel formed by the set of die-mandrel during the Phase I, transforming it into a molten plastic tube like, the parison. Next phases, namely Phase II - Mould clamping and Phase III - Inflating the Parison transforms the produced parison into the final desired geometry. Thus, there is a high dependency between the produced parison in the end of the Phase I with the final part obtained in the end of the Phase III.

The mathematical model, discretisation steps, and calculation algorithm used to simulate these phases of the process are identical to those detailed in Section 2.2.

3.2.1 Parison Programming

Parison programming is a sophisticated technique used during the extrusion Phase I in the EBM process that facilitates the precise modification of the thickness of a circumferential layer at specific moments in time. This method allows obtaining a non-uniform parison thickness distribution along its length. This procedure is essential for meeting specific requirements such as the specified strength with minimum weights, especially for containers designed to withstand internal pressure or heavy loads. This technique involves adjusting the die gap opening, by the relative movement between the mandrel and the die, during parison formation, thus, selectively changing the wall thickness at different locations along the parison's axial length. This level of control is crucial for optimising material efficiency and ensuring product quality.

In Figure 3.1 there is a schematic illustration of the parison programming process. This diagram provides a clear depiction of the die and mandrel, along with the molten plastic inside the die and outside in the parison. The sequence commences at $t = 0s$, with the die fully opened. At the point captured in Figure 3.1 a), the mandrel begins its upward movement, resulting in the narrowing of

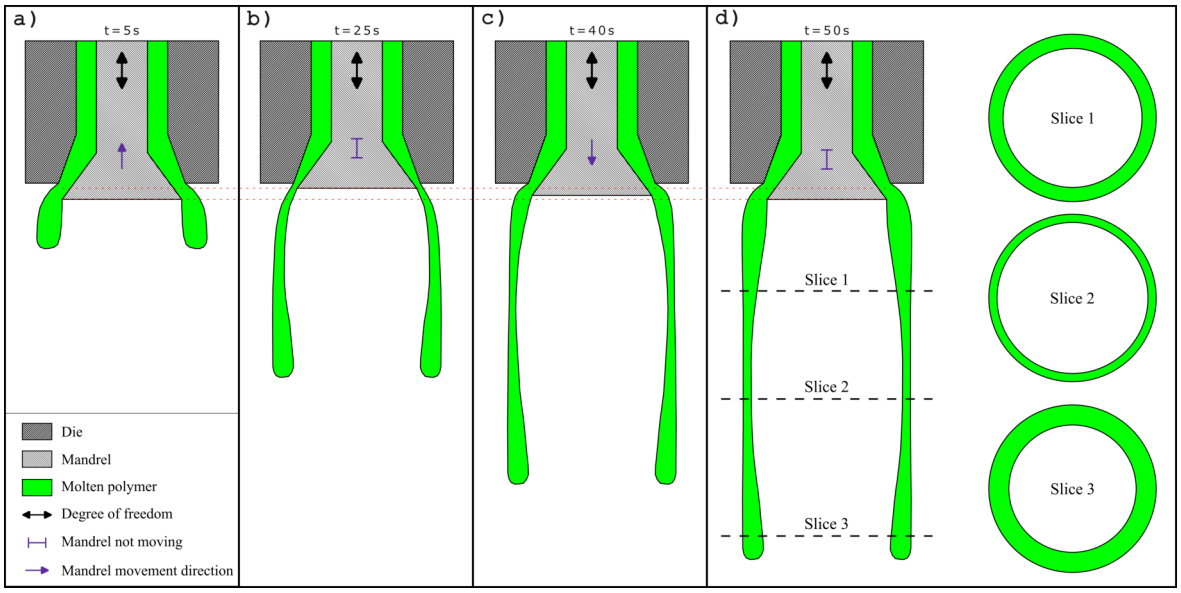


Figure 3.1: Parison programming technique example. a) begins of mandrel's upward movement, b) minimum die gap width, c) descending mandrel near to its lowest position, d) maximum die gap width and fully extruded parison with some latitudinal slices.

the die gap. By $t = 25s$ (as shown in Figure 3.1 b), the mandrel stops ascending at its maximum height, representing the moment of minimum die gap, or minimum parison thickness, before changing direction to descend. Figure 3.1 c) displays the mandrel descending, shortly before it reaches its lowest position at $t = 50s$, as illustrated in Figure 3.1 d), where the mandrel's motion halts. Moreover, Figure 3.1 d) emphasises three distinct latitudinal slices across the parison's length-specifically, Slices 1, 2, and 3—illustrating how the die gap opening influences the production of a parison with a non-uniform thickness distribution, as schematically represented in Figure 3.1 d). The thickness is measured by the distance between the external and internal interfaces of the parison, i.e., the radial difference between the two concentric circles in a layer, in this illustrative case where the die and mandrel are designed as circular concentric profiles, as shown in Figure 3.1 d).

In the real and practical EBM process, this technique involves imposing in the machine the desired die gaps (control points) along the parison extrusion. These defined control points cover the full parison length, from the die outlet to its lowest point. In fact, this lowest point was initially coincident with the cutting plane of the previous cycle, and in the new cycle it corresponds to the lowest parison point. It is worth emphasising that the profile followed by the mandrel movement varies continuously and smoothly as it passes through the predefined die gap, or control, points.

3.2.2 Parison Grouping

As outlined in the previous section, defining control points along the parison extrusion is crucial since it determines the material distribution in the final product. The aim is to establish a set of mandrel locations in order to achieve a desired variable thickness distribution on the extruded parison.

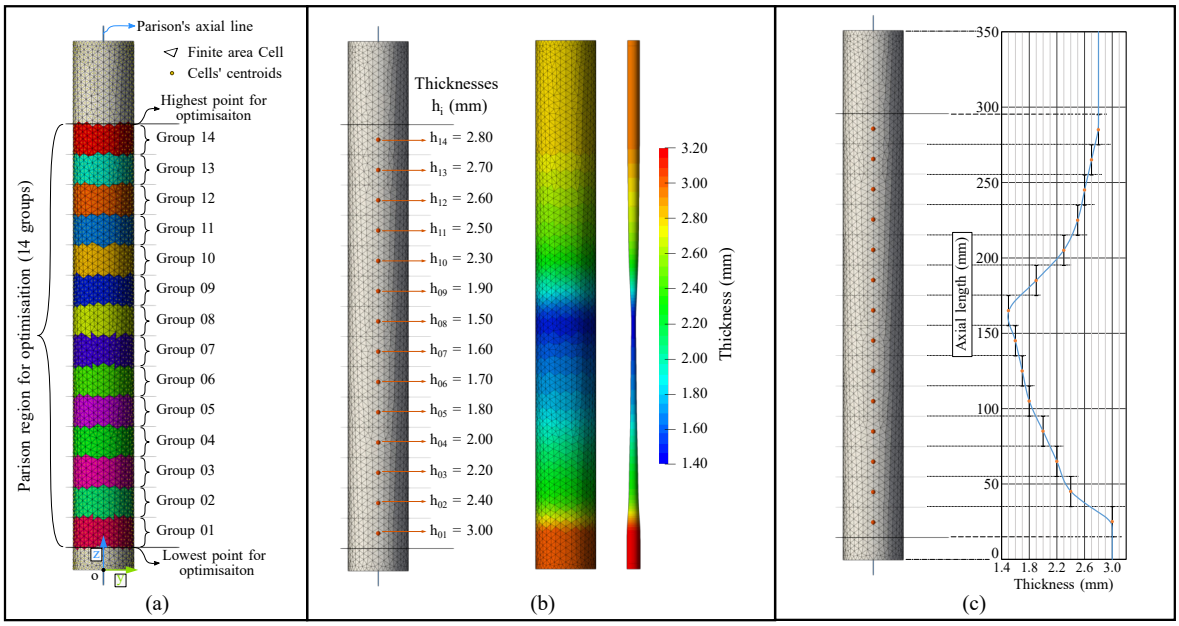


Figure 3.2: Example of parison's cells grouping and its initial thickness definitions: a) Parison optimisation region and optimisation groups definition, b) attribution of initial thicknesses to each optimisation group and c) resulting initial thickness profile attributed for the parison prior to the mould clamping phase.

Parison programming yields in obtaining a non-uniform thickness distribution longitudinally, but it maintains a uniform thickness along its angular direction at the same axial position. Hence, the proposed computational cell grouping approach was conceived to segment the parison into regions, designated by axial layers, that its centroids corresponds to control points at different discrete axial locations, imposed by the mandrel movement.

The envisioned cell grouping process (refer to Figure 3.2 a) starts from the bottom of the parison (the initial extruded section) towards the top (final cut plane section of the parison), which delineates the region of parison that can be optimised. The actual optimised parison segment can cover the total parison length or just a segment of it, as depicted in Figure 3.2 a). The region that is going to be optimised is then divided into a number of layers (mandrel-die gap control points), as illustrated in Figure 3.2 a) for fourteen layers, equally spaced within the optimisation region.

The parison's computational cells are then associated into these groups, based on the location of their centroids. For instance, a cell belongs to a particular group if its centroid falls within the axial range of that group. Despite a cell's area crossing its group boundaries, its classification relies on its centroids location, ensuring accurate thickness control, as the centroid-based discretisation aligns with how variables such as thickness are computed at cell centroids.

In Figure 3.2 a) the illustrated groups are identified and distinct colours are attributed to them just for visualisation purposes. This way each cell receives its respective group index, and corresponding colour, demonstrating a proper classification within the optimisation region's boundaries.

Once groups are established, the next step involves assigning thickness values to all finite area

cells. Each group is assigned a reference discrete location of its corresponding initial thickness (h_0), placed at its axial group midpoint, and indicated by orange dots in Figure 3.2 b). The thickness attributed for the cells, positioned in between two referential midpoints, is calculated by using a spline function, specifically the Catmull-Rom spline interpolation available in OpenFOAM® [64]. This technique attempts to replicate a smooth thickness variation that is encountered in practice when using parison programming. The actual initial thickness (h_0) for each cell is thus determined by using its axial position of its cell's centroid and the corresponding value interpolated resulting from the spline function.

The parison grouping and resulting initial thickness profile attributed to the parison are displayed in Figure 3.2 c). Again, the orange dots represent the midpoint of each group layer, and error bars are indicating the extent of each group. The blue line shows the thickness profile as defined by spline interpolation across the parison's computational cells. The computational cells from the non-optimised regions inherit a constant thickness value from the last adjacent layer within the optimised section.

3.2.3 Optimisation Methodology

The optimisation methodology involves defining a target thickness h_T for the parison as it is at the end of the inflation phase. In order to attain the final product thickness this target thickness must consider the thermal expansion for the material in the range of the processing and environment temperatures. The parison mesh in this final configuration is divided into layers from the bottom to the neck, and each layer can have arbitrary height and a desired target thickness. In Figure 3.3 a), the desired thickness colormap for the parison at the end of parison inflation is illustrated. Similar to the

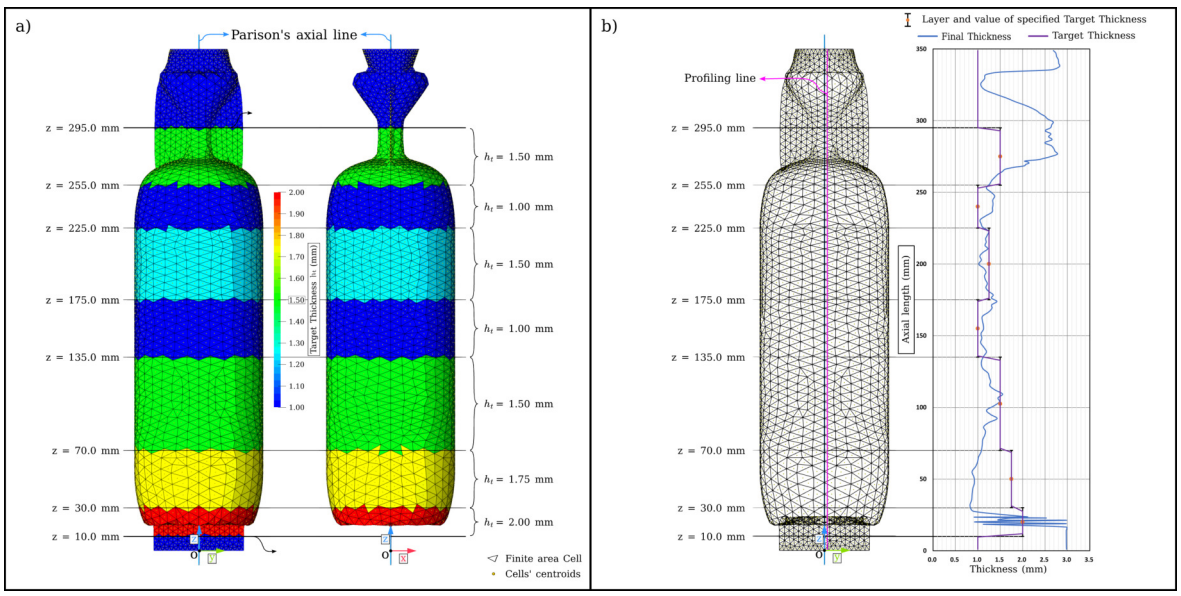


Figure 3.3: Example of target thickness definition for the inflated parison: a) Definition of parison optimisation region and optimisation groups and b) Attribution of thicknesses to optimisation groups, along with Resulting thickness profile for the parison

approach in Section 3.2.2, the target thickness is based on the centroids of cells in their final positions, with each cell within a layer assigned a uniform target thickness, leading to a step-wise profile as seen in Figure 3.3 b), where the final thickness distribution for a hypothetical case is also illustrated.

In regions where the final thickness matches the desired values, corrections may not be necessary. However, for the entire parison, adjustments are often needed to reduce the difference between the target and actual thicknesses. The proposed optimisation algorithm adjusts the initial thickness so that the final inflated parison more closely aligns with the desired thickness distribution. Practicality dictates that the initial thickness distribution for this optimised parison reflects a feasible production via the real EBM process controls. It is possible to correct each individual cell thickness and obtain a final inflated parison with a perfect, or almost perfect, final desired thickness distribution, however this solution is of impractical manufacturing in the real EBM process.

Initially, each cell is assigned a thickness h_0 prior to the start of mould clamping (Phase II). After undergoing deformation and displacement through Phases II and III, each cell's final position $\mathbf{X}_c$ and thickness h_F are calculated. Next, desired target thickness h_T, based on specifications, is assigned to its position at the end of Phase III. Thickness relative deviation δ_h for each cell is computed using the following expression:

$$\delta_h = \frac{h_F - h_T}{h_T}. \tag{3.1}$$

This deviation is then averaged within each optimisation group, producing a group-specific average thickness deviation $\overline{\delta}_h$, calculated by:

$$\overline{\delta}_{hj} = \frac{\sum_{i=1}^{n} \delta_{hj,i} A_{j,i}}{\sum_{i=1}^{n} A_{j,i}}, \tag{3.2}$$

where $\overline{\delta}_{hj}$ is the average thickness deviation for a group (j) of cells, $\delta_{hj,i}$ is the thickness deviation and $A_{j,i}$ is the area of a cell (i).

With these group averages, a new optimised initial thickness $\overline{h}_0$ for each group is calculated:

$${}^{\text{new}}h_{0j} = {}^{\text{old}}h_{0j}\left(1 - \gamma_j \overline{\delta}_{hj}\right), \tag{3.3}$$

where γ_j is the relaxation factor, used for optimising the initial thickness of a group (j), to dampen

larger thicknesses variations.

An important highlight with regard to the proposed optimisation procedure goes to the considered summation process. Just the cells that belong to the final part, i.e. excluding those in the flash area at the end of the mould clamping, are considered for optimisation calculations, to ensure rapid convergence to the desired profile. The optimisation procedure also imposes limitations to prevent unrealistic thickness values: ensuring new thicknesses do not fall outside a predefined range. Moreover, the initial studies performed allowed to conclude that constraining changes between the new optimised value to be within 80% of variation in relation to the original value, which forces a smooth transition, is a good practice.

The process starts with a base case, conducts sequential simulations, adjusting initial thicknesses based on the outcomes of the previous simulation. This algorithm continues through a set of predefined optimisation simulation cases, or until the thickness deviations reach acceptable ranges. Figure 3.4 provides a schematic representation of this iterative process, showcasing how the algorithm refines the initial thickness distribution for manufacturing an optimal part.

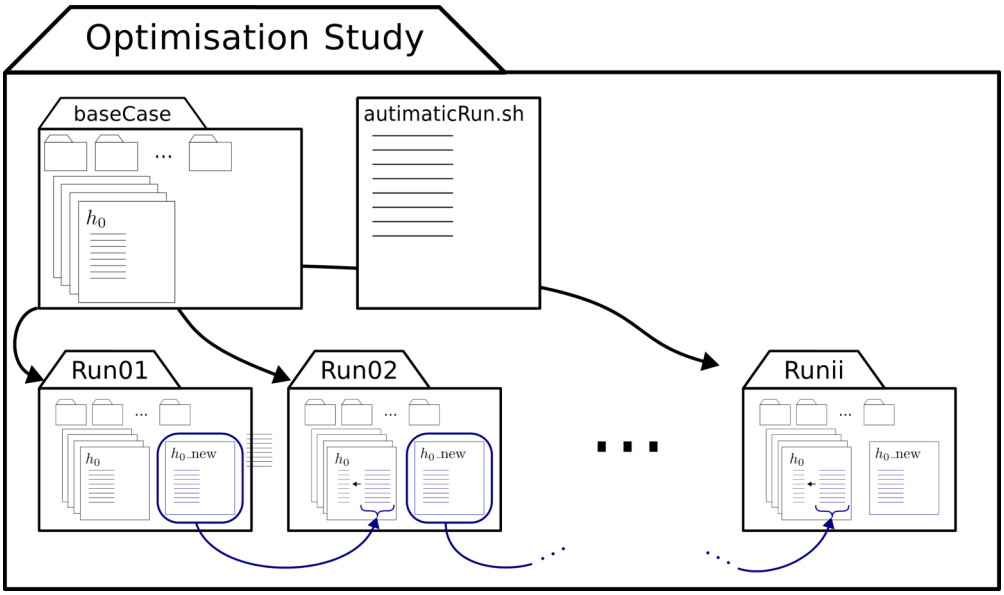


Figure 3.4: Schematic representation of the automatic optimisation process, outlining the iterative adjustment of parison thickness.

3.3 Case Studies

This section presents three distinct case studies to demonstrate the practical application of the developed computational framework in optimising the thickness distribution of parts produced by EBM. The first two case studies focus on cylindrical parisons used to manufacture cylindrical bottles. In ideal conditions, parisons are designed as perfect cylinders, which could be approximated as axisymmetrical shapes. However, during mould clamping due to the induced deformations, mainly motivated by the

regions clamped in the mould, the final bottles lose axisymmetry, resulting in geometries with a double, or a single, or, without any plane of symmetry.

The initial case study examines on how to obtain a thickness distribution as uniform as possible in the final cylindrical bottle. The subsequent case extends this examination to scenarios where a non-uniform thickness distribution is desired in the final product, to meet hypothetical specific design or performance criteria.

The third case study turns the focus from idealised models to the optimisation of a real practical bottle, produced by the EBM process. This case compares the simulation results with actual manufacturing outcomes, providing a direct evaluation of the framework usability and accuracy.

All case studies in this study considered the material properties of raw virgin High-Density Polyethylene (HDPE) 5502, supplied by TotalEnergies SE Petrochemicals. This material was chosen due to its prevalent usage in industrial applications and its detailed analysis in prior studies [48]. The physical and mechanical properties of HDPE 5502, necessary for the simulations, includes a specific mass $\rho = 954\,\mathrm{kg/m^3}$ and a thermal expansion coefficient $\beta = 1.1 \times 10^{-4}\,\mathrm{K^{-1}}$, as detailed in the TotalEnergies report [65]. The material's hyperelastic behaviour of the parison, during mould clamping and inflation phases, is modelled using the two-parameter Mooney-Rivlin model, characterised by constants $c_{10} = 226.58\,\mathrm{kPa}$ and $c_{01} = 1.01\,\mathrm{kPa}$ [48].

3.3.1 Cylindrical Bottle with Constant Target Thickness

This case study explores the optimisation of material distribution in producing a cylindrical bottle with a target uniform thickness. The analysis begins with a parison modelled as an ideal cylinder, characterised by a constant radius of $R = 20.0\,\mathrm{mm}$. While the radius remains unchanged, the thickness distribution along the parison is subject to optimisation. The parison is subdivided into fourteen axial optimisation segments, evenly distributed along its length from $15.0\,\mathrm{mm}$ to $295.0\,\mathrm{mm}$, within a total axial length of $350.0\,\mathrm{mm}$. These parisons and its axial segments are consistent with the one depicted in Figure 3.2 a). Each segment employs a relaxation factor $\gamma_j = 0.5$ across all layers for the optimisation, i.e. every new calculated thickness variation, even those bounded between the limits of 80% of change, are then multiplied by this relaxation factor.

The optimisation process commences with an initial parison thickness h_0 set at $3.0\,\mathrm{mm}$. The goal is to achieve a final bottle characterised by a uniform thickness $h_T = 1.0\,\mathrm{mm}$. The study considers four levels of mesh refinement to ensure accuracy and robustness in the simulation results; these are showcased side by side, with it corresponding metrics, for evaluative comparison in Figure 3.5.

Given the nature of double symmetry in both the parison and the final product, allowed to conduct these simulations using only a quarter of the circular parison perimeter, spanning from $0°$ to $90°$, with the $0°$ position aligned with the mould closure plane.

The simulation process transforms the initial parison into the final desired bottle shape, whose

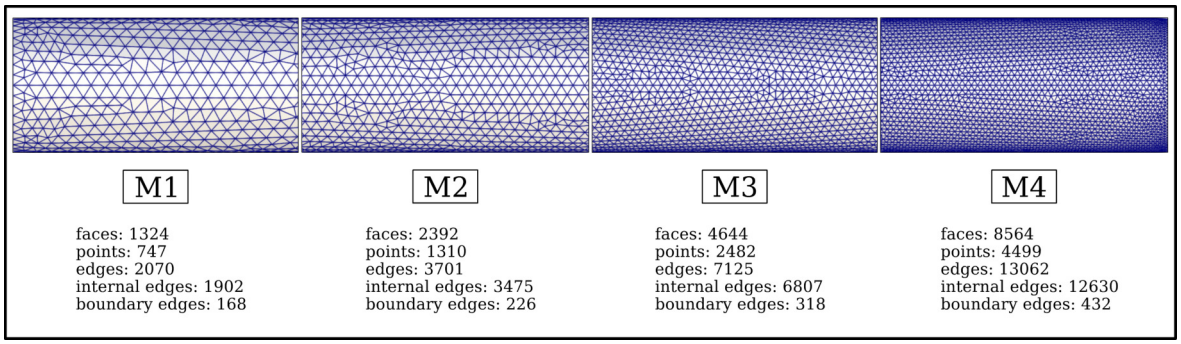


Figure 3.5: Meshes with four levels of refinements considered in the optimisation study.

dimensions and positions are presented in detail in Figure 3.6. In the setup of Figure 3.6, the black line represents the parison's placement within the mould, while the translucent purple indicates the closed mould geometry. The arrangement ensures that the parison and mould are perfectly aligned with concentric axial lines. Notably, the bottle's lid section (excluding the conical region) is positioned downstream, offset by $50.0\,\mathrm{mm}$ from the parison's highest point.

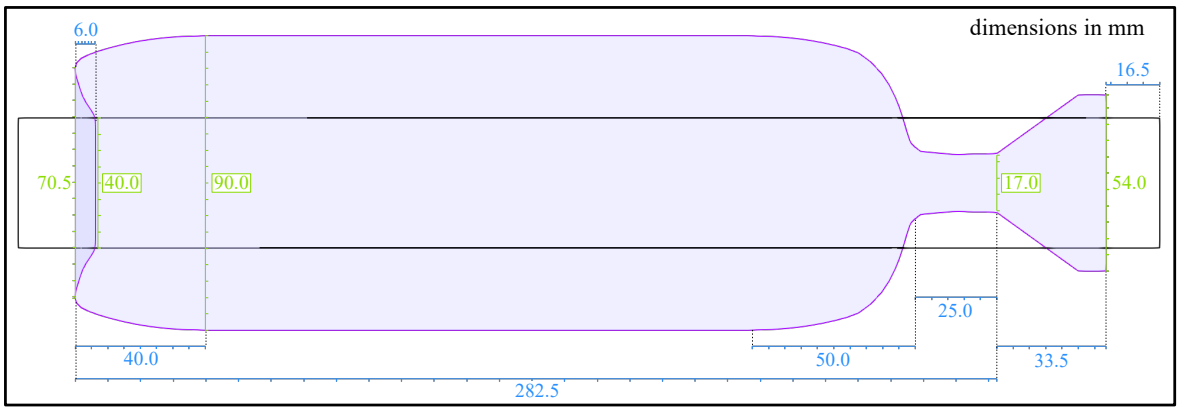


Figure 3.6: Mould dimensions and relative positioning with the extruded parison (dimensions in millimetres).

This analytical segment evaluates the consistency of thickness across different simulation runs within the same mesh refinement level, and assesses variations across the different levels of mesh refinement applied.

3.3.2 Cylindrical bottle with variable target thickness

This subsection extends the analysis from Section 3.3.1, utilising the same cylindrical parison and bottle configuration. However, the focus here switches to the implementation of a variable target thickness in the final product, diverging from the previous case's uniform thickness distribution. The specific target thickness profile aimed for in this case study is depicted in Figure 3.7, highlighting regions with different desired thicknesses to meet varying functional requirements of the final bottle.

For areas not covered by specific target thickness layers, a default thickness, $h_T = 1.5\,\mathrm{mm}$, has been set. This approach mirrors the methodology employed in Section 3.3.1, where the initial

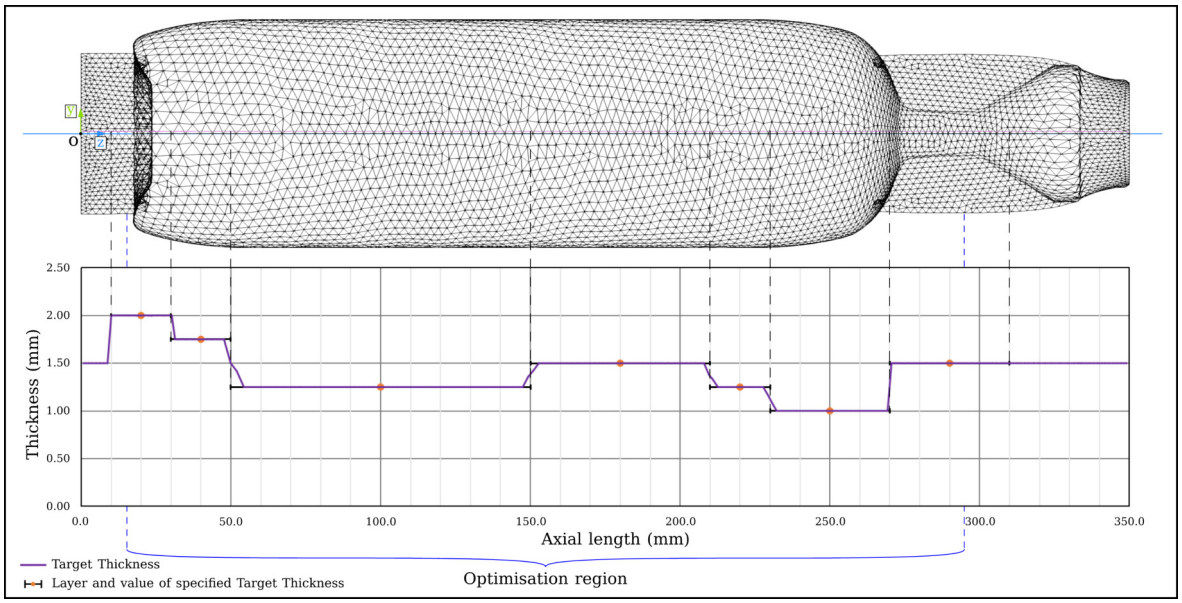


Figure 3.7: Schematic of the final part with the defined non-uniform target thickness profile and corresponding optimisation regions.

thickness of the parison is maintained as $h_0 = 3.0\,\mathrm{mm}$ to initiate the optimisation process. The same optimisation groups and axial ranges previously defined are applied here.

The additional aspect of this case study involves evaluating the optimisation process by starting with a coarser mesh and gradually transitioning to finer meshes as it progresses. This incremental refinement aims to streamline the optimisation trajectory, utilising the outcomes from the coarse mesh simulations to inform and improve subsequent optimisations on the finer meshes.

The strategy aims to strike a balance between computational efficiency and the accuracy necessary for effective material distribution in the final product. This is achieved by initiating the algorithm with two simulations using the M1 mesh, followed by one simulation for each refined mesh, resulting in a total of five simulations for the study.

3.3.3 Oval-shaped bottle with variable target thickness

A final case study involves the optimisation of an oval-shaped bottle that was experimentally produced using the Bekum BM-304SE model. This industrial machine is capable of processing and producing parisons with the programmed parison technique. During this study, the extruded parison obtained during processing, before the mould clamping phase (phase II), was measured and digitally reconstructed using Blender, a 3D computer graphics software [66]. Front and side views were used to measure the parison and create its virtual representation. The technique used in here for the measurements were the same as those utilised and presented in a previous study of [48].

Variations on the shape of the outer surface of the extruded parison are neglected. The considerations taken are that just minor changes occurs when producing it via a constant die gap

or programmed parison technique, therefore, this degree of freedom is not considered for the simulations. Consequently, just the geometry for the parison obtained through a constant die gap opening is considered during the optimisation. The measurements, shape functions and built parison were the same as those presented in [48].

In order to optimise this bottle, the first step is to trace the thickness profile of the final bottle produced without parison programming, i.e. via a constant die gap. This final thickness profile is used to create a new optimised target profile.

As illustrated in Figure 3.8, the inflated parison is divided into three distinct regions: a non-optimised region, a transition region, and an optimised region. The non-optimised region covers the neck of the bottle and a shallow bottom region, which includes its entire base. The transition region allows the gradual movement between the mandrel and die, taking into account the shape variation for the final part. Finally, the optimised region is set to half the final thickness obtained in the bottle produced without programmed parison, aiming to reduce the weight of this region by half and lowering the overall weight of the final part.

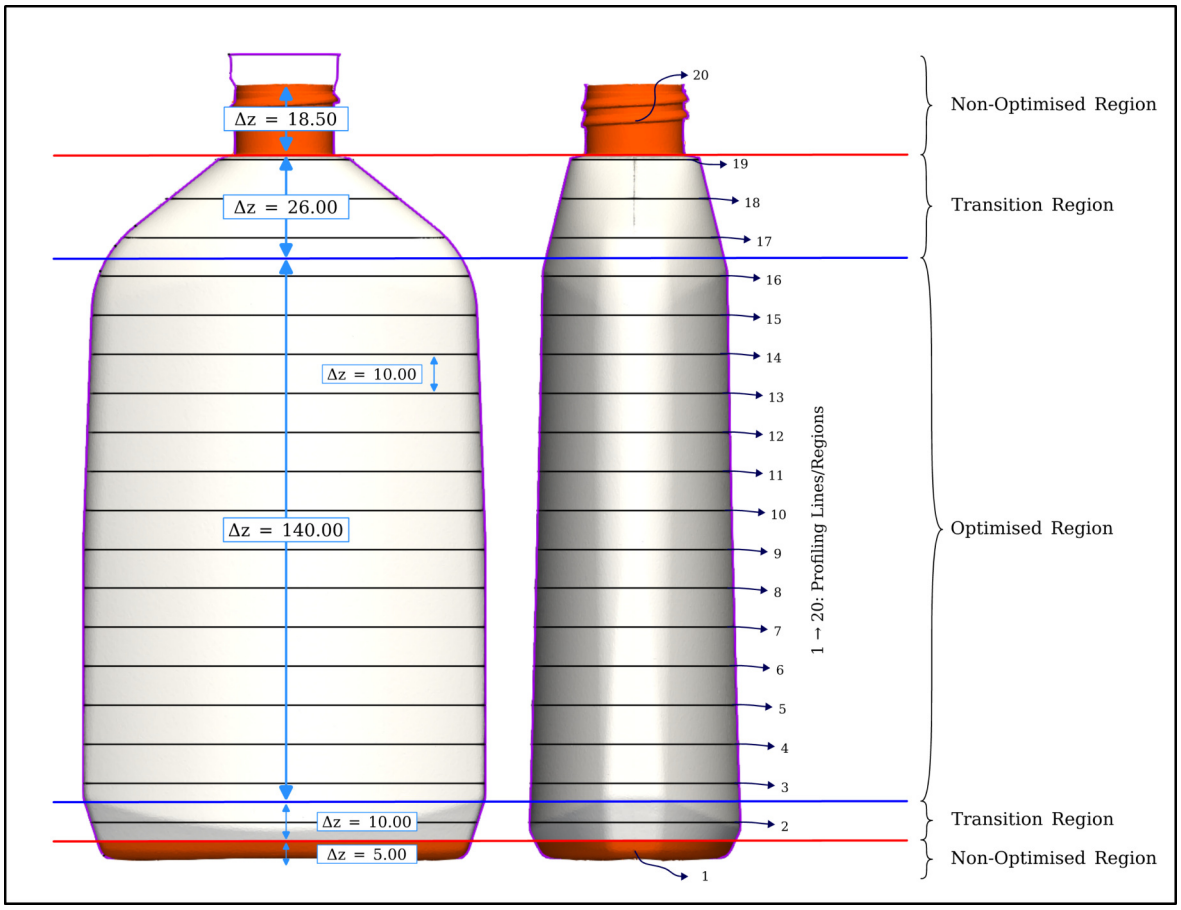


Figure 3.8: Definitions of regions for the optimisation study and lengths dimensions in millimetres for the real bottle.

The black line profile in Figure 3.9 represents the final thickness profile obtained for the manufactured bottle, produced in the actual process without parison programming technique. Each

line/region index in the abscissas corresponds to the index provided in Figure 3.8. The black labels, along with the black line, indicate the average thickness value found for each sampling line/region, while the red bars represent the standard deviations of the thicknesses. The purple line profile represents the desired thickness distribution of the optimised bottle, where each thickness value was calculated using the factors depicted as purple labels linked to the purple line.

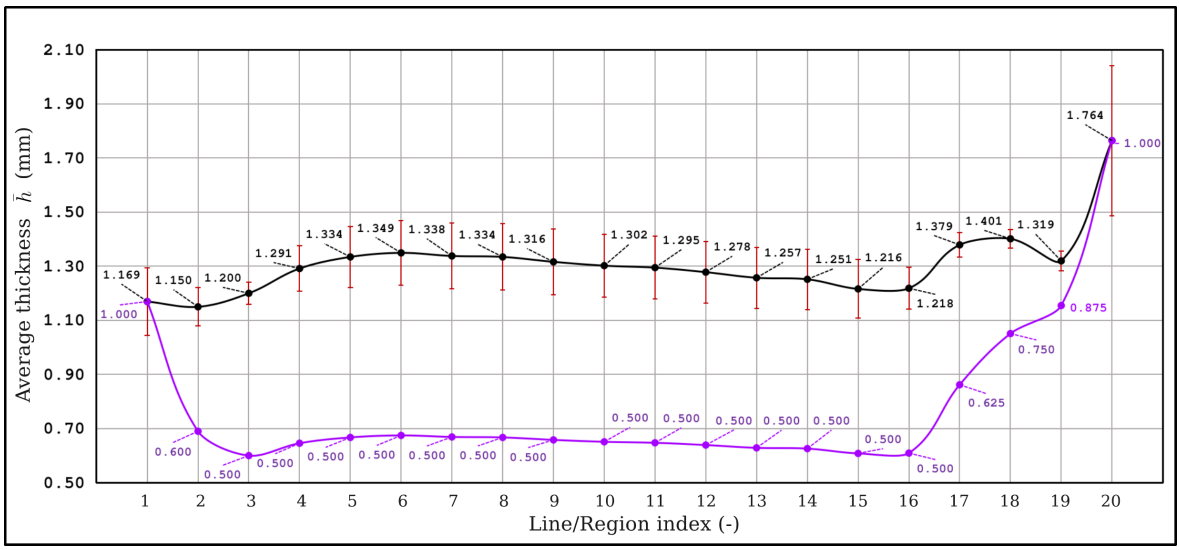


Figure 3.9: Definitions of regions for the optimisation study, and the black line is the final thickness profile for the experimental bottle obtained with a constant die gap opening.

This way, the target average thickness for each profiling line of a final optimised bottle, represented by the purple line, can be obtained by multiplying each factor (purple labels) by the average thickness value (black labels) of the uniform parison thickness bottle, and the resulting values are listed as h_T in Table 3.1. Additionally, it should be noted that the weighting factors for line indices 1 and 20 utilise unitary weighing factors, as they remain in the non-optimised regions, thus they were expected to maintain the thickness of the parison obtained without the programmed parison technique. Meanwhile, lines with indices 3 to 16 have weighting factors values of 0.5, as already mentioned, to reduce the optimised bottle weight to half. The factors of the transition regions, Lines 2 and 17 to 19, were linearly interpolated between the factor 1, that are imposed at the non-optimised extremes, and factor 0.5, imposed at the optimised region. All layer indices, ranges and target thicknesses attributed for the final part are listed in Table 3.1.

LI: Layer index - LR: Layer Range (mm) - h_T: target thickness (mm)

LI:	1	2	3	4	5	6	7	8	9	10
LR:	0.0 → 35.0	35.0 → 45.0	45.0 → 55.0	55.0 → 65.0	65.0 → 75.0	75.0 → 85.0	85.0 → 95.0	95.0 → 105.0	105.0 → 115.0	115.0 → 125.0
h_T:	1.169	0.690	0.600	0.646	0.667	0.675	0.669	0.667	0.658	0.651
LI:	11	12	13	14	15	16	17	18	19	20
LR:	125.0 → 135.0	135.0 → 145.0	145.0 → 155.0	155.0 → 165.0	165.0 → 175.0	175.0 → 185.0	185.0 → 195.0	195.0 → 205.0	205.0 → 214.5	214.5 → 305.0
h_T:	0.647	0.639	0.629	0.626	0.608	0.609	0.862	1.051	1.154	1.764

Table 3.1: Target thickness specifications used for the optimisation of the real bottle.

Since the optimised region consists of fourteen points, an equal number of optimisation groups, which were specifically oriented to capture a small portion of the clamped cells located at both the

bottom and neck regions of the bottle. These groups cover a total range of $210.00\,\mathrm{mm}$, with an offset of $30.00\,\mathrm{mm}$ from the lowest region of the parison (see Figure 3.10). The total length of the parison is $305.00\,\mathrm{mm}$.

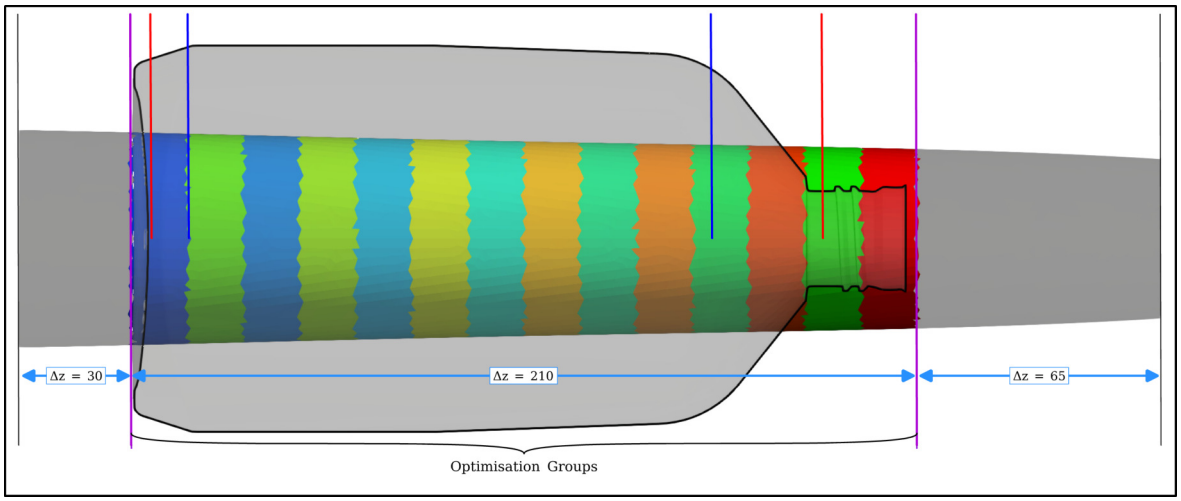


Figure 3.10: Parison optimisation groups definition, alongside with their relative position and lengths (dimensions in mm).

The approach and methodology used in [48] are also employed here, along with an initial uniform thickness distribution value of $h_0 = 1.774\,\mathrm{mm}$ for the entire parison. This value is calculated considering the mass conservation and correcting its corresponding volume at processing temperature conditions. Lastly, the experimental bottle was scanned by using an X-Ray microtomography from the RX Solutions, model Easytom S, where this technique allows obtaining the thickness distribution in cloud of points through the entire bottle surface. The final bottle dimensions an thicknesses were also corrected to the processing temperature conditions and considering the thermal expansion of the processing material.

3.4 Results and Discussion

This section explores the outcomes derived from the simulations, conducted as stated by previous case studies presented in Section 3.3, providing a comparative analysis to illustrate the evolution and effectiveness of the iterative optimisation technique employed.

The results from each of the three case studies are presented sequentially, offering different aspects of how the optimisation process influences the material distribution and overall quality of the final product.

The discussion aims to link the gap between theoretical predictions and practical outcomes, elucidating the intricacies and challenges encountered during the simulation process. By comparing the simulated results with each other, and against the set objectives and expected outcomes, these analysis seeks to validate the optimisation technique's reliability and applicability in real-world

manufacturing scenarios.

In addition to a direct comparison of results, this section also explores the implications of these findings, providing insight into the potential improvements in efficiency, product quality, and material usage that can be achieved through the adoption of the proposed optimisation strategies. Critical evaluations of the methodologies employed, including the effectiveness of different mesh refinements and the impact of varying thickness distributions, will also be discussed, extending the understanding of the optimisation in EBM process.

3.4.1 Cylindrical bottle with constant target thickness

This case study investigates the iterative optimisation process over four levels of mesh refinement, each encompassing ten individual simulation runs. Each subsequent run improves the optimisation based on the outcomes of its predecessor, as delineated in Section 3.2.3. Given that a perfect parison would be impractical in a real EBM process, thus deviations for the thicknesses profiles are anticipated and expected. However, the aim is for these deviations to diminish progressively throughout the optimisation iterations, aligning as close as possible with the target thickness profile.

The results obtained for this case study are covered as follows: An initial qualitative assessment of the thickness distribution of the entire bottle presented; A targeted quantitative analysis of critical areas is discussed; and lastly, an examination of how the optimisation of the controlling variables impact the results is performed.

The first stage presents the thickness distribution across the entire parison, before mould clamping as shown in Figure 3.11 and after being inflated, presented in Figure 3.12.

These distributions illustrate the progression across multiple runs (labelled as $Runi$, where i ranges from 1 to 10). The definition and positioning of these optimisation groups remain consistent throughout the optimisation iterations, making them similar for all simulations. Accordingly, they are only presented once on the left-hand side of Figure 3.11. The final positions of these groups changed during the optimisation process and are shown on the left-hand side of Figure 3.12. It is worth noting that the transparent areas in both Figures 3.11 and 3.12 indicate regions that were excluded from the optimisation calculations. This exclusion was due to either being outside the parison optimised region or forming the flash after mould clamping. The exclusion of these areas aligns with the strategy outlined in Section 3.2.3.

Significant changes are observed in both thickness maps, particularly between Runs 01 to 03. The upper and lower portion of the parison, mainly in Figure 3.11, shows a gradual modification up to Run 08, reflecting smooth adjustments to offset the extensive stretching experienced during inflation in these regions. This iterative adjustments are an indicative of the optimisation focus on achieving an improved final thickness distribution, correcting the non-homogeneous parison stretching that for the initial iterations was concentrated in the bottom region.

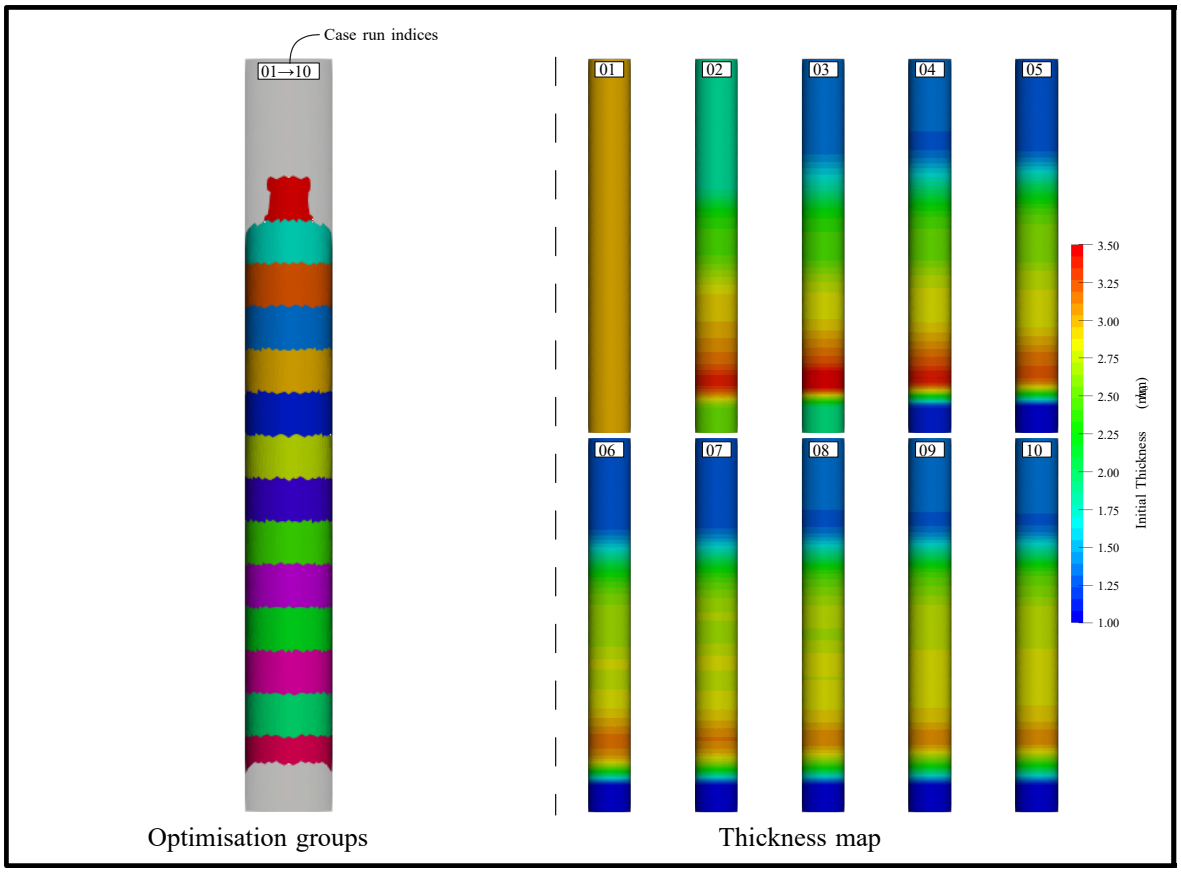


Figure 3.11: Parison optimisation groups and thickness map obtained with mesh M3, before mould clamping.

Figure 3.12 portrays the thickness map post-inflation, with a trend towards a more uniform thickness distribution (green colour) – a marker for alignment with the target thickness ($h_F = h_T = 1.0\,\mathrm{mm}$). It can be noticed, by the left-hand side of the Figure 3.12, that the final position of the optimisation groups slightly changed their final location as well. These optimisation groups are defined in the beginning of the mould clamping (Phase II) and, as mentioned before, they do not change through the optimisation process. Thus, modifying these layers' thicknesses, implies into modifying their stiffness as well, across the parison, with consequent impact in their final position. The last two layers of the inflated parison of Run 01 (pink and green), in the left-hand side of Figure 3.12, displaces towards the bottom of the bottle, during the optimisation between the Run 01 to the Run 05. In Run 05 the pink layer overtook the location partially occupied by the green layer in Run 01, and in Run 05 the green layer is at the bottle base region.

Subsequently, the quantitative analysis starts by presenting the parison's initial thickness profiles of all simulated cases, for meshes M1 and M2 is provided in Figures 3.13 a), and b), and meshes M3 and M4 in Figures 3.14 a), and b). The profiles illustrate the progression towards an optimised solution through ten iterative cases, encompassing various levels of mesh refinement. The last optimised profiles for each mesh exhibit similarities. Notably, Mesh M3 (Figure 3.14 a)) showed the most significant changes between each profile during the optimisation study. This was primarily because the initial corrections deviated more from the solution found in the last resulting profile. The

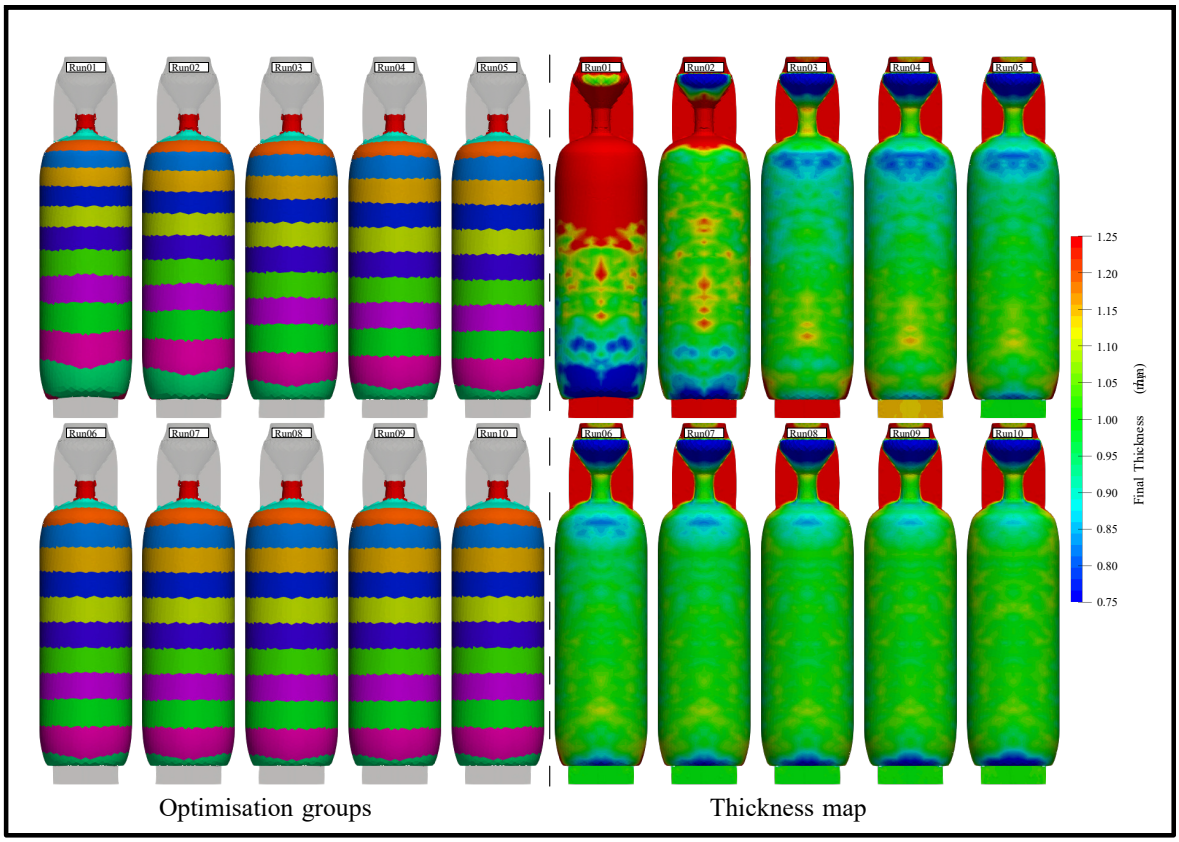


Figure 3.12: Parison optimisation groups and thickness map obtained with mesh M3, post-inflation.

iterations in between aimed to minimise these differences by making corrections. The main reason for this pattern is that the corrections consider achieving the target material distribution in the final inflated configuration. As a result, adjustments to the layer thickness affect their stiffness, which, in turn, influences the final positioning of the parison layers. All ten simulated cases were completed in 19.7 hours (PT19H42M25S) using a single core from the Intel® Core™- 12^{th} generation - i7-12700K processor [67].

The Analysis of the final thickness distribution for the inflated parison considers 33 axial profiling lines, all illustrated in Figure 3.15, while their defined coordinates considered for placing them are presented in Table 3.2. Some of the lines present radius values, since they were taken for a constant radius at specific regions of the bottle.

Considering any of these axial profiling lines, the frontal region of the bottle ($90°$ from the mould closure plane), is where the parison stretching is most pronounced, while the opposite occur for the perpendicular region (at the mould closure plane). The final thickness profiles are compared through their average thickness value ($\overline{h}_F$) and standard deviation, for each line, run and mesh, being the results depicted in Figures 3.16 a) and b), for meshes M1 and M2, and Figures 3.17 a) and b), for meshes M3 and M4, respectively. An overall analysis of these results reveals the optimisation's efficacy in disposing the final thickness closely with the desired target thickness outcomes, i.e. $h_F \approx h_T = 1.00\,\text{mm}$. Due to the minor variations observed in the profiles obtained between Runs 05

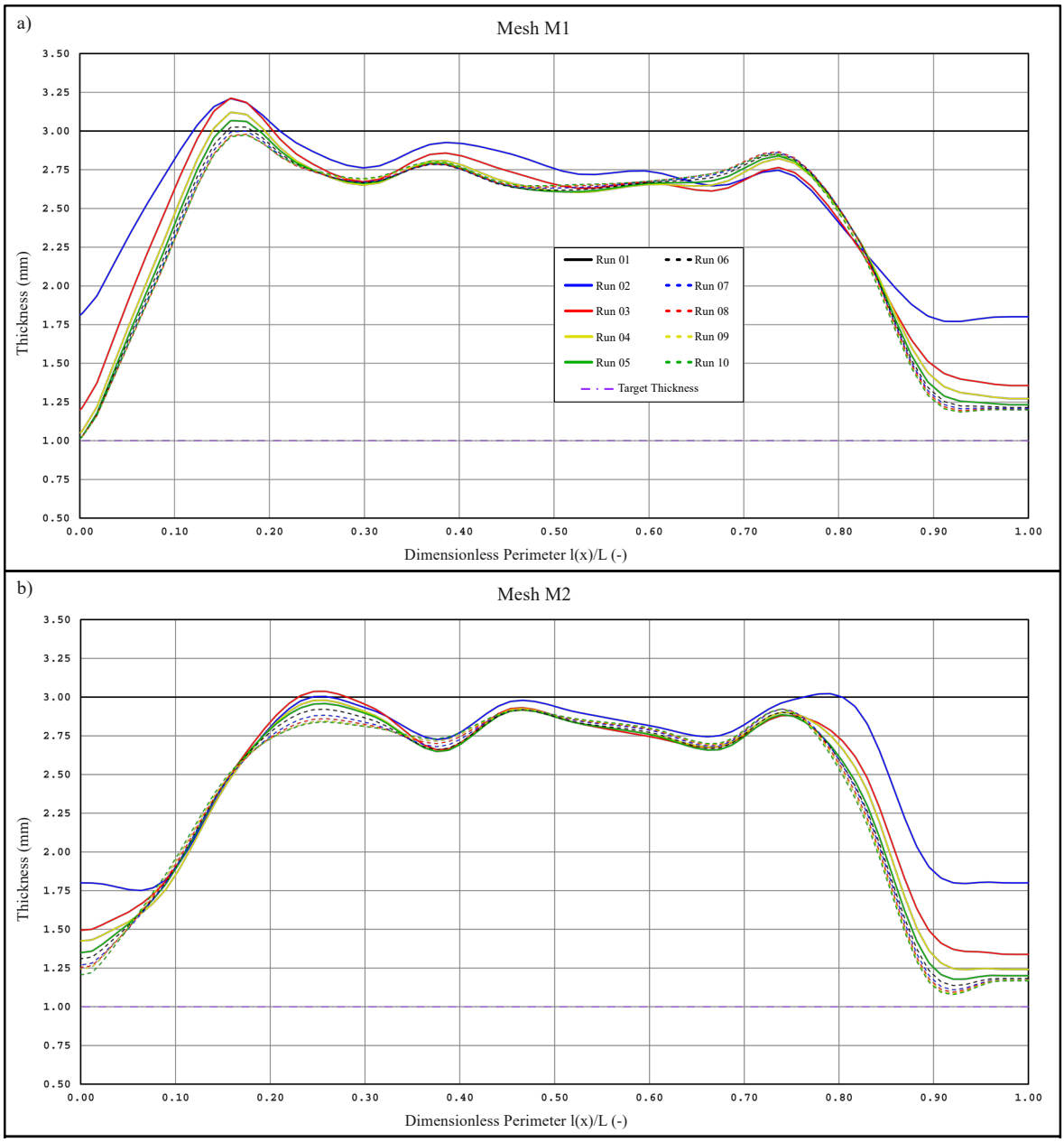


Figure 3.13: Variation of initial thickness profiles during the optimisation process across all simulated cases with coarser meshes, a) Mesh M1 and b) Mesh M2.

to 10, the intermediate results are not presented in Figures 3.16 and 3.17, to improve readability.

A profile similar of a sine function is observed in the beginning of the thickness profiles, between lines with indices 1 to 5, in Figures 3.16 and 3.17. Due to the higher initial thickness values set for the layers in this region to compensate for the pronounced stretching, the optimal profile found for all meshes oscillates around the desired target thickness, with their average value remaining approximately equal to the target.

The final results to assess is the relative variation in the controlling variables, which are the discrete thickness values definitions at the layers' axial midpoints h_0, across the optimisation layers

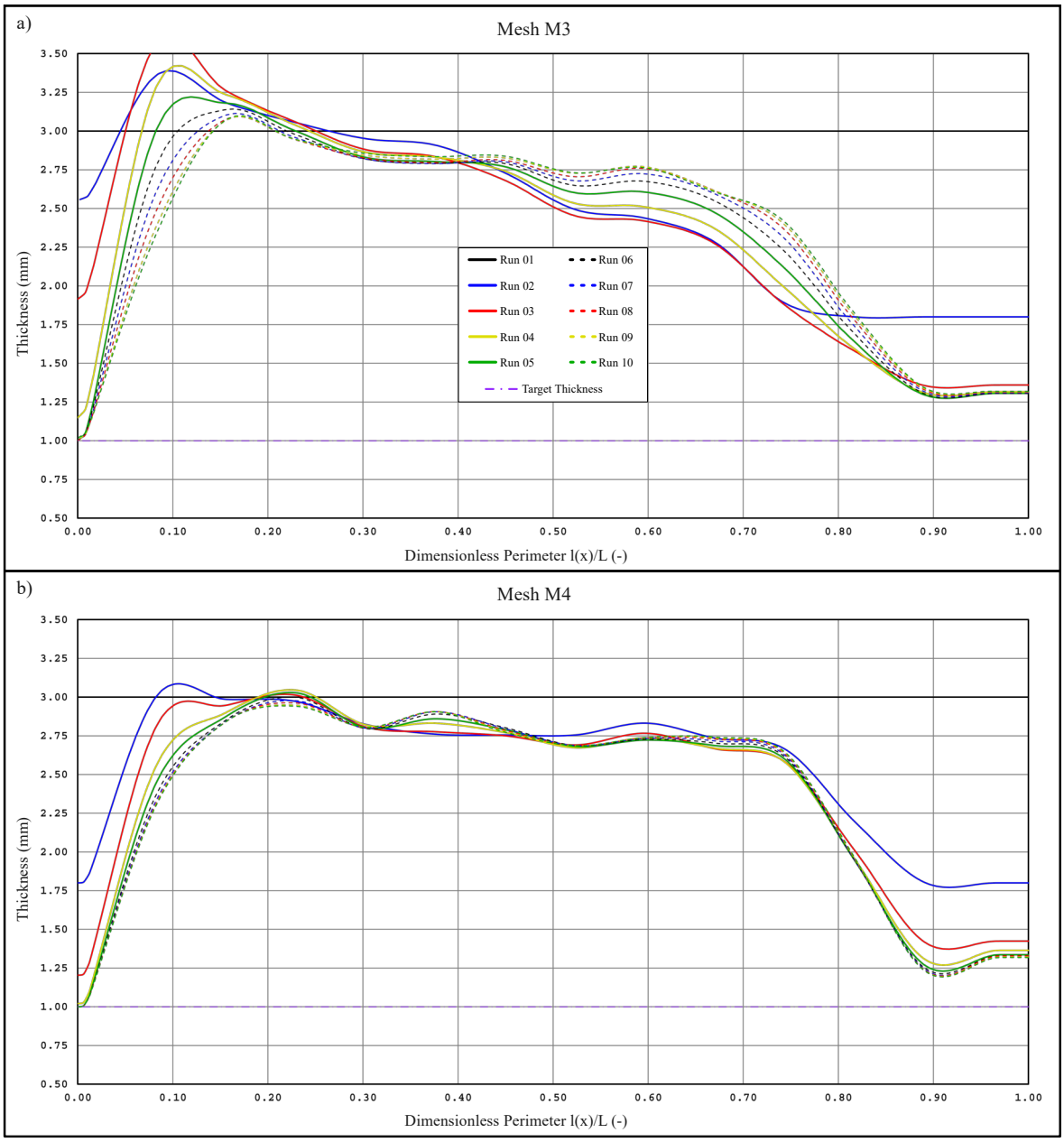


Figure 3.14: Variation of initial thickness profiles during the optimisation process across all simulated cases with finer meshes, a) Mesh M3 and b) Mesh M4.

for all meshes. The rate of change of thickness is calculated as follows:

$$h^{*}_{RC} = \frac{\| {}^{old}h_0 - {}^{new}h_0 \|}{{}^{old}h_0}, \tag{3.4}$$

where it quantifies the relative variation between the input values of initial thicknesses before the simulation, with the new optimised values obtained at the end of the simulation. These results are provided in Figures 3.18 a) and b), for meshes M1 and M2, and Figures 3.19 a) and b), for meshes M3 and M4, respectively. An overall analysis of these results reveals a trend towards stabilisation, with

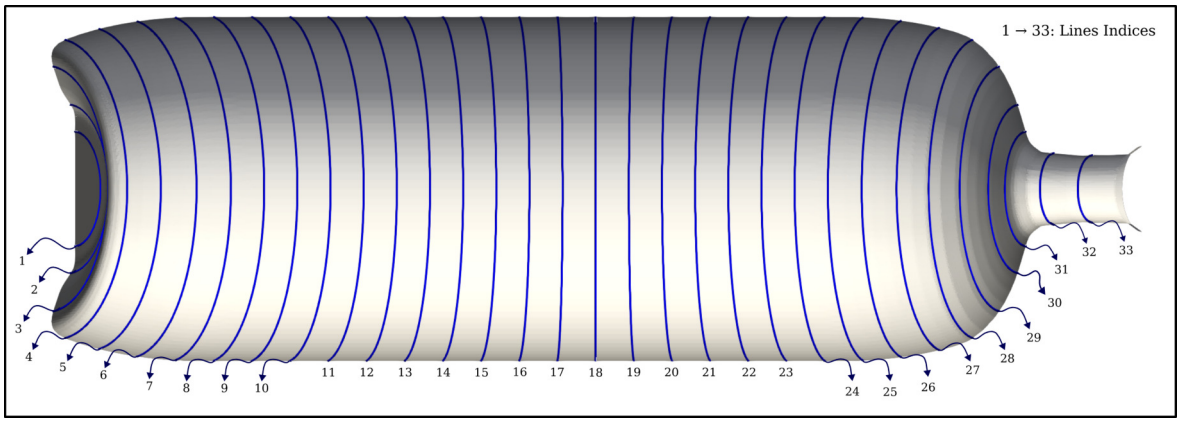


Figure 3.15: Lines taken from the bottle and their corresponding indices to analyse the final thickness profiles.

ID: Line index - **L:** Axial Length (mm) - **R:** Radius (mm)

ID:	1	2	3	4	5	6	7	8	9	10
L:	23.296	22.294	18.225	21.552	30.0	40.0	50.0	60.0	70.0	80.0
R:	14.0	22.0	32.0	39.0	-	-	-	-	-	-
ID:	11	12	13	14	15	16	17	18	19	20
L:	90.0	100.0	110.0	120.0	130.0	140.0	150.0	160.0	170.0	180.0
R:	-	-	-	-	-	-	-	-	-	-
ID:	21	22	23	24	25	26	27	28	29	30
L:	190.0	200.0	210.0	220.0	230.0	240.0	250.0	258.6	265.6	270.8
R:	-	-	-	-	-	-	-	39	32	22
ID:	31	32	33							
L:	273.136	280.0	290.0							
R:	14.0	-	-							

Table 3.2: Lines profiling indices and coordinates definitions.

initial changes being more pronounced but decreasing in magnitude as the process advances.

Typically, these differences drop to variations below 10% after the initial simulations, demonstrating the optimisation's convergence towards the desired target values. Furthermore, the extreme ends of the parison – corresponding to the bottom and neck of the bottle – exhibit the most significant adjustments due to the fact that the defined thickness of Run 01 were more different from the optimum value. The bottom part was subjected to the highest deformation, while the neck part was subjected to the lowest one, and the majority of the parison cells are clamped between the moulds composing the flash. Higher variations of initial thickness are observed for the mesh M3 (Figure 3.19 a)) for the layers between $155.0\,\mathrm{mm}$ to $255.0\,\mathrm{mm}$, which in the others they slightly changed, but, again, the final solution is similar for all meshes. Only the relative change for the runs 01 to 05 for all the meshes were placed in the Figures 3.18 and 3.19, because for runs 05 to 10 they were indistinguishable, with maximum changes bellow 3.1%, with the exception of mesh 3 which presented maximum values of 6.1%, 4.8%, 4.1%, 2.1% and 1.74% for runs 06 to 10, respectively.

3.4.2 Cylindrical bottle with variable target thickness

Similarly to the previous case study, this study also considered the four levels of mesh refinements and ten case runs for the iterative optimisation process. The peculiar aspect of this case

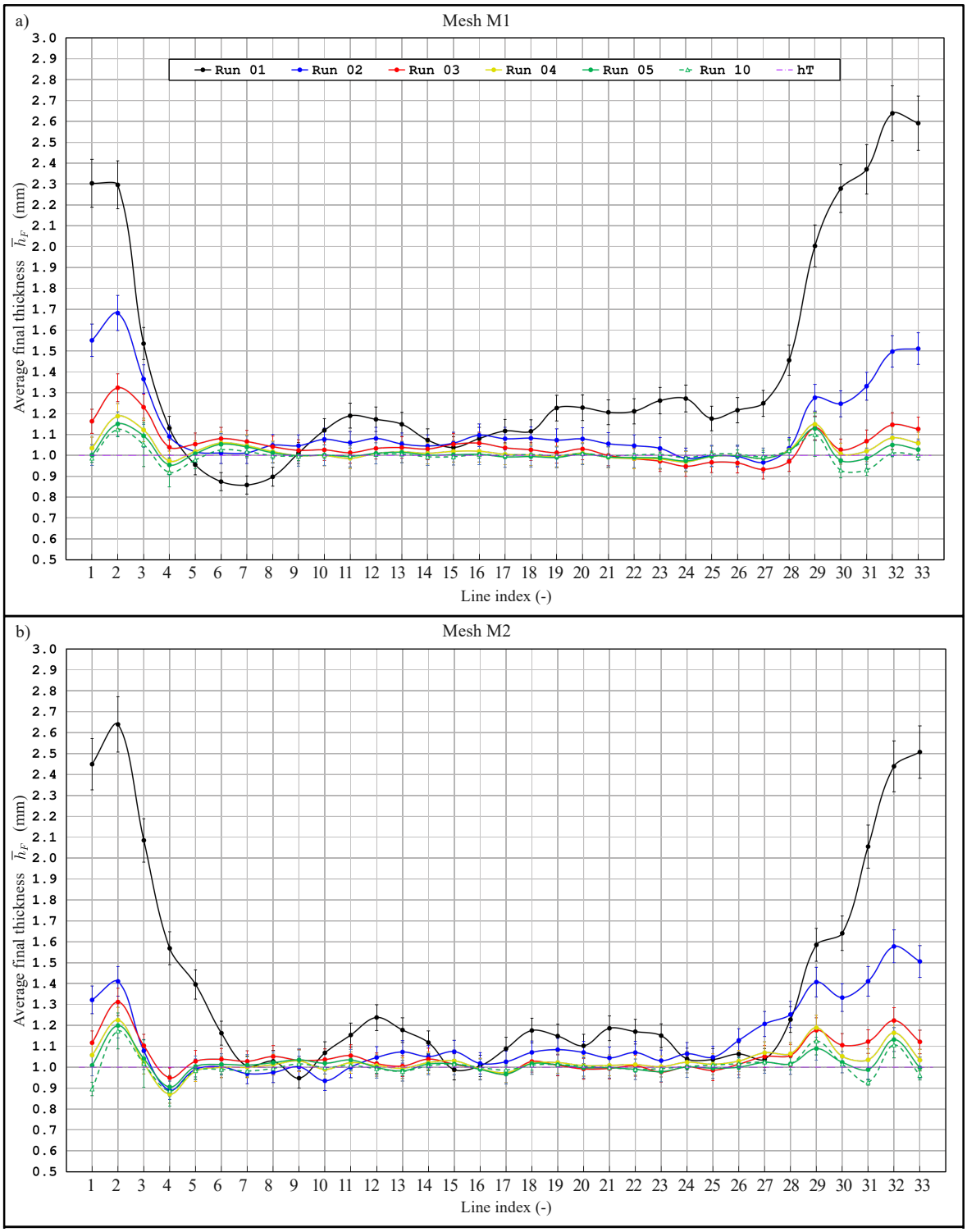


Figure 3.16: Final thickness profile evolution during the optimisation process for the simulated cases runs 1 to 5 and 10, using coarser meshes, a) Mesh M1 and b) Mesh M2.

study lies in the algorithm's ability to reach a non-uniform target thickness profile, examining the nuanced convergence behaviours under this more complex definition for the desired final part.

A quantitative analysis initiates this discussion, emphasising the transformation of the parison's thickness profiles from their initial to final states across all simulated cases for meshes M1 through

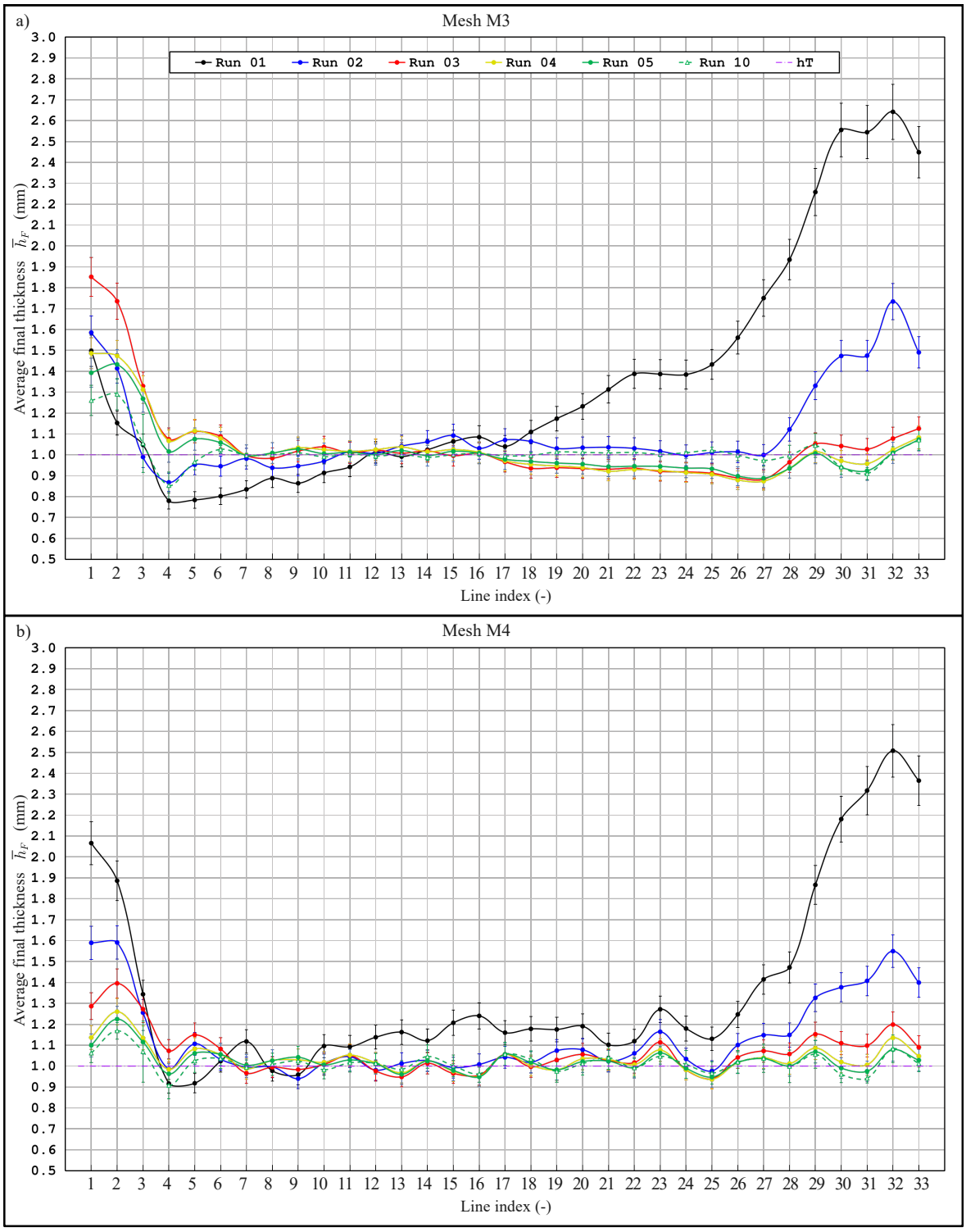


Figure 3.17: Final thickness profile evolution during the optimisation process for the simulated cases runs 1 to 5 and 10, using finer meshes, a) Mesh M3 and b) Mesh M4.

M4. These transformations are presented in Figures 3.20 a) and b), for meshes M1 and M2, and Figures 3.21 a) and b), for meshes M3 and M4, respectively.

In addition, simulated results for the final thickness profiles for the parison after being inflated are presented in Figures 3.22 a) and b), and Figures 3.23 a) and b), for meshes M1 to M4, respectively.

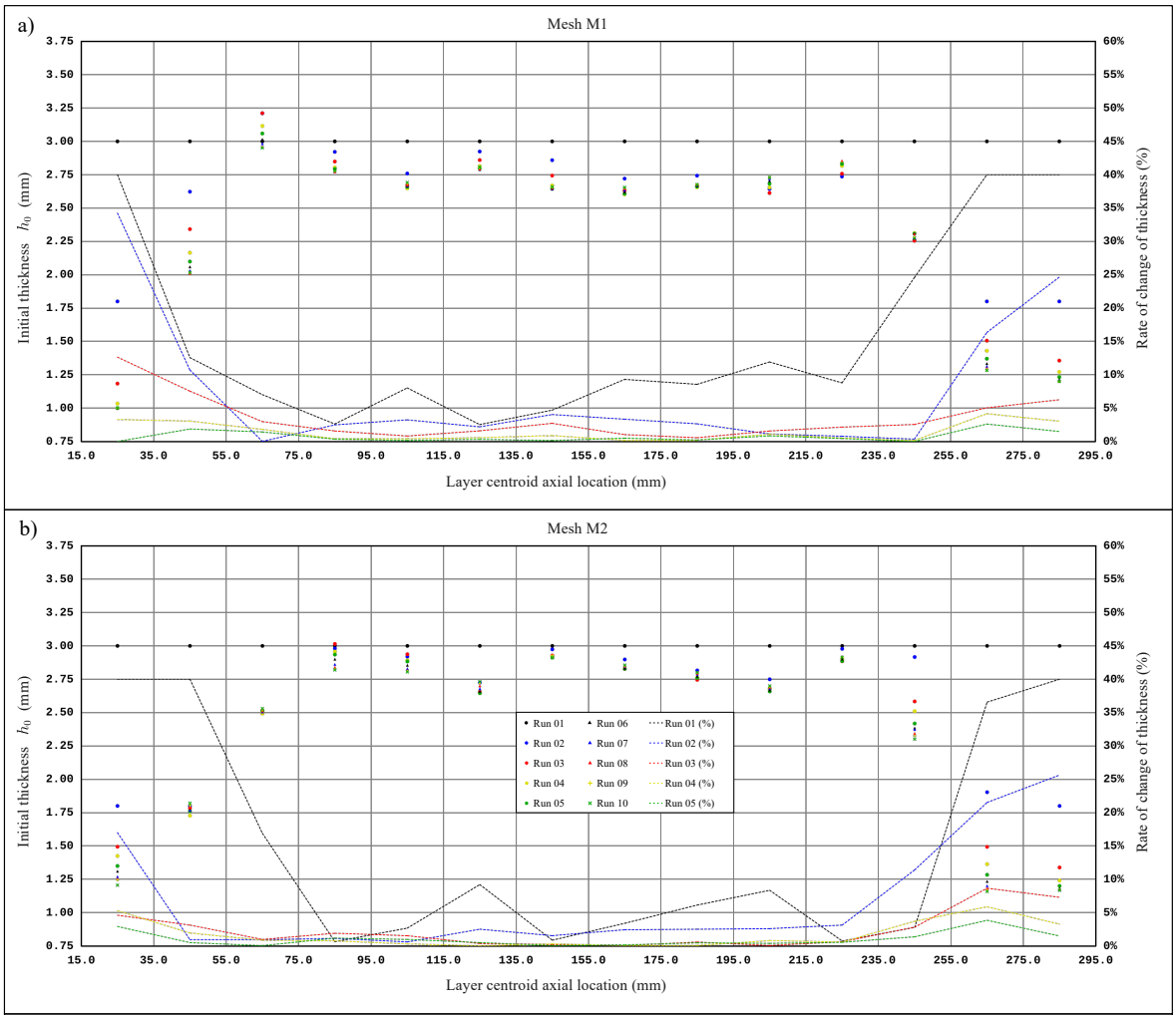


Figure 3.18: Variation of defined thicknesses in optimisation, at axial groups midpoints, through the optimisation process for all simulated cases with coarser meshes, a) Mesh M1 and b) Mesh M2.

To analyse the final thickness, profiling lines were taken across the entire height of the bottle, following identically the same procedure and definitions as described in the previous section and illustrated in Figure 3.15.

It should be noticed a higher increment of thicknesses in the beginning of the abscissa of the meshes M1, M3 and M4 in Figure 3.20 a), and Figure 3.21 a) and b), while the Mesh M2 (Figure 3.20 b)) presented also an increment but with lower values. These thicknesses increments were anticipated at referred regions, since they correspond to the highest stretched locations, i.e. the bottom corners after inflation. Therefore, these higher thicknesses at the parison, before mould clamp, were imposed by the algorithm to compensate the referred higher stretches. The initial profiles present different levels of change, with Mesh M2 exhibiting the least variation between runs. This suggests distinct optimisation challenges and accomplishments across various meshes.

The evolution of the final thicknesses profiles, detailed in Figures 3.22 and 3.23, confirms the optimisation algorithm's capability for improving initial thickness profiles that allow attaining a target variable final thickness distribution, illustrating the adaptive nature of the process even under non-trivial

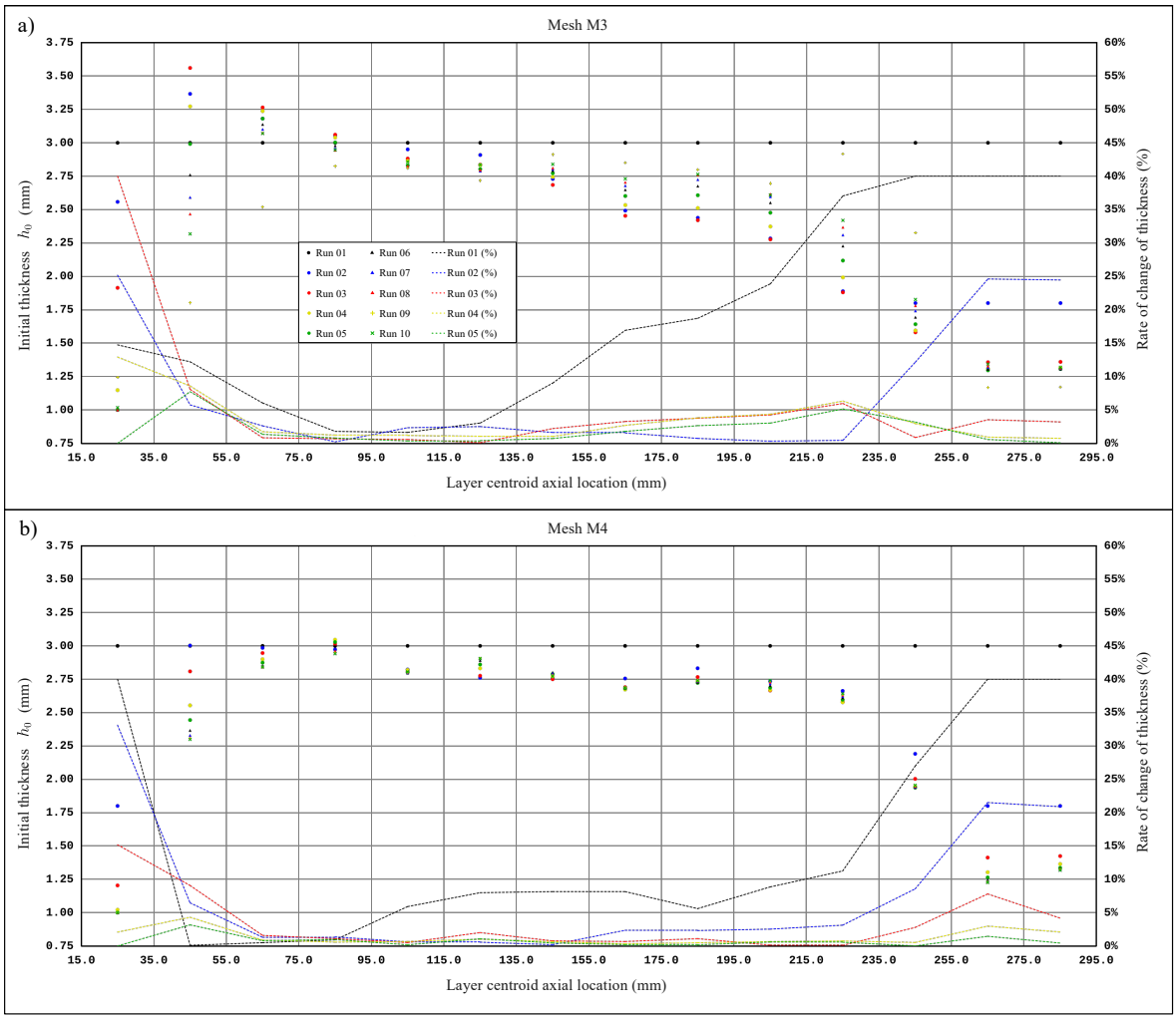


Figure 3.19: Variation of defined thicknesses in optimisation, at axial groups midpoints, through the optimisation process for all simulated cases with finer meshes, a) Mesh M3 and b) Mesh M4.

requirements.

A qualitative analysis of the method is illustrated in Figure 3.24, where Figure 3.24 a) presents the desired target thickness map, while Figure 3.24 b) shows the field of the absolute thickness deviation $|h_D|$ for all the runs used in the optimisation of Mesh M3.

The results for the colour maps of the absolute thickness deviations presented in Figure 3.24 b) reveals the improvements in the overall final thickness due to the fact that as the runs for the optimisation progresses, the colour map becomes more predominant of blue colour, meaning that the less the final thickness deviated from the desired thickness, the better the optimisation became, and an entire blue colour map would represent the perfect solution.

Computational time assessments reveal that finer meshes, while offering improved resolution and better corner capturing, demand higher computational resources. This is attributed to increased cell counts and the necessity for smaller time increments to reach converged solutions. Table 3.3 provides an overview of the relative computation times across all mesh refinements and their simulated

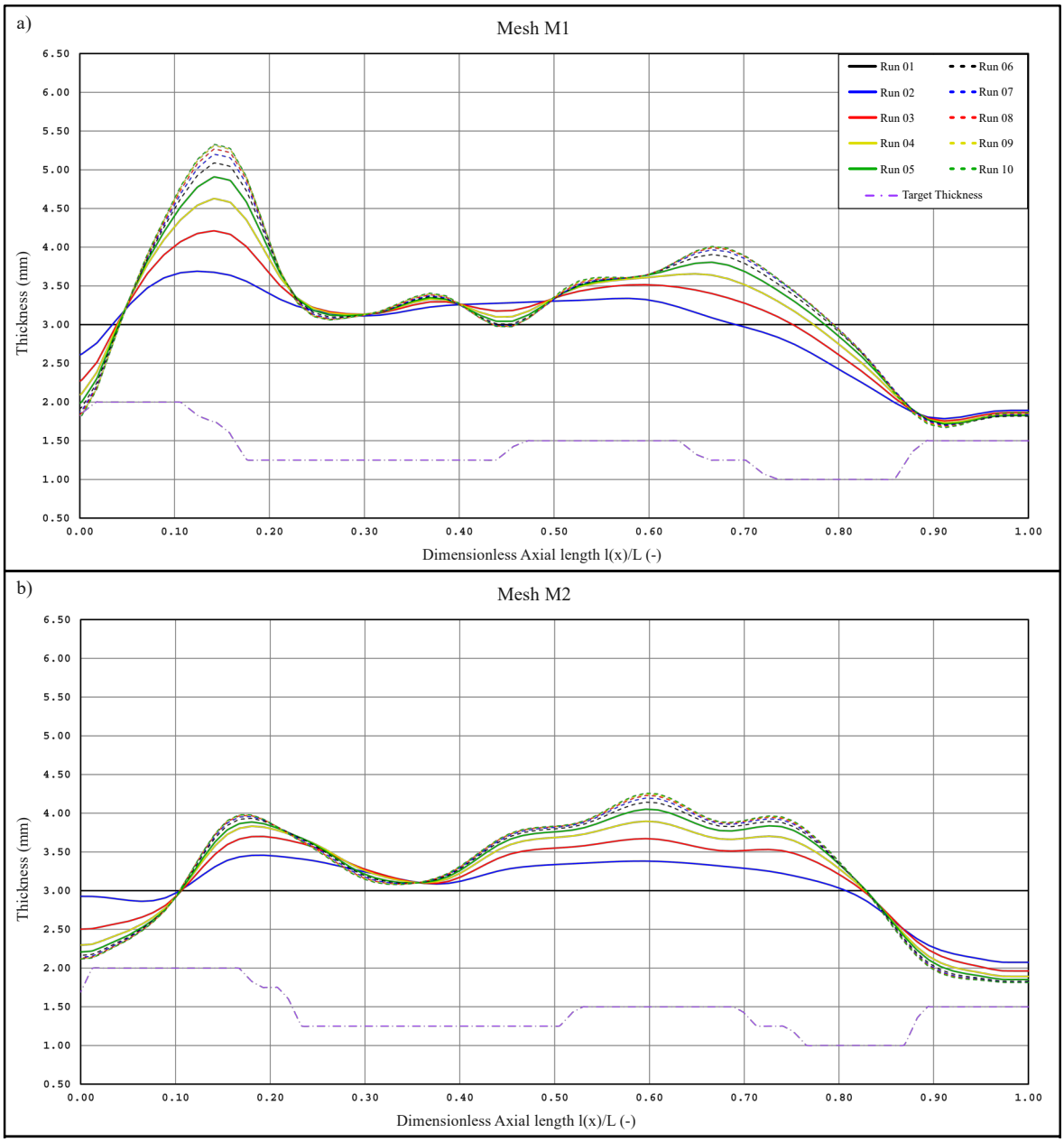


Figure 3.20: Evolution of the parison initial thickness profiles along the optimisation process for all cases with coarser meshes, a) Mesh M1 and b) Mesh M2.

cases.

Considering these findings, an investigation has been conducted using a multi-mesh approach, in which a gradual mesh refinement is considered. This method starts using coarser meshes, and their results are applied to inform subsequent simulations with finer meshes, thus aiming to optimise computational efficiency while maintaining accuracy.

The first two runs for this multi-mesh optimisation are done using mesh M1. Next runs are subsequently performed by using one simulation using Mesh M2 and one using Mesh M3. Finally, this multi-mesh optimisation ends with the last two runs by using Mesh M4. Results for this multi-mesh

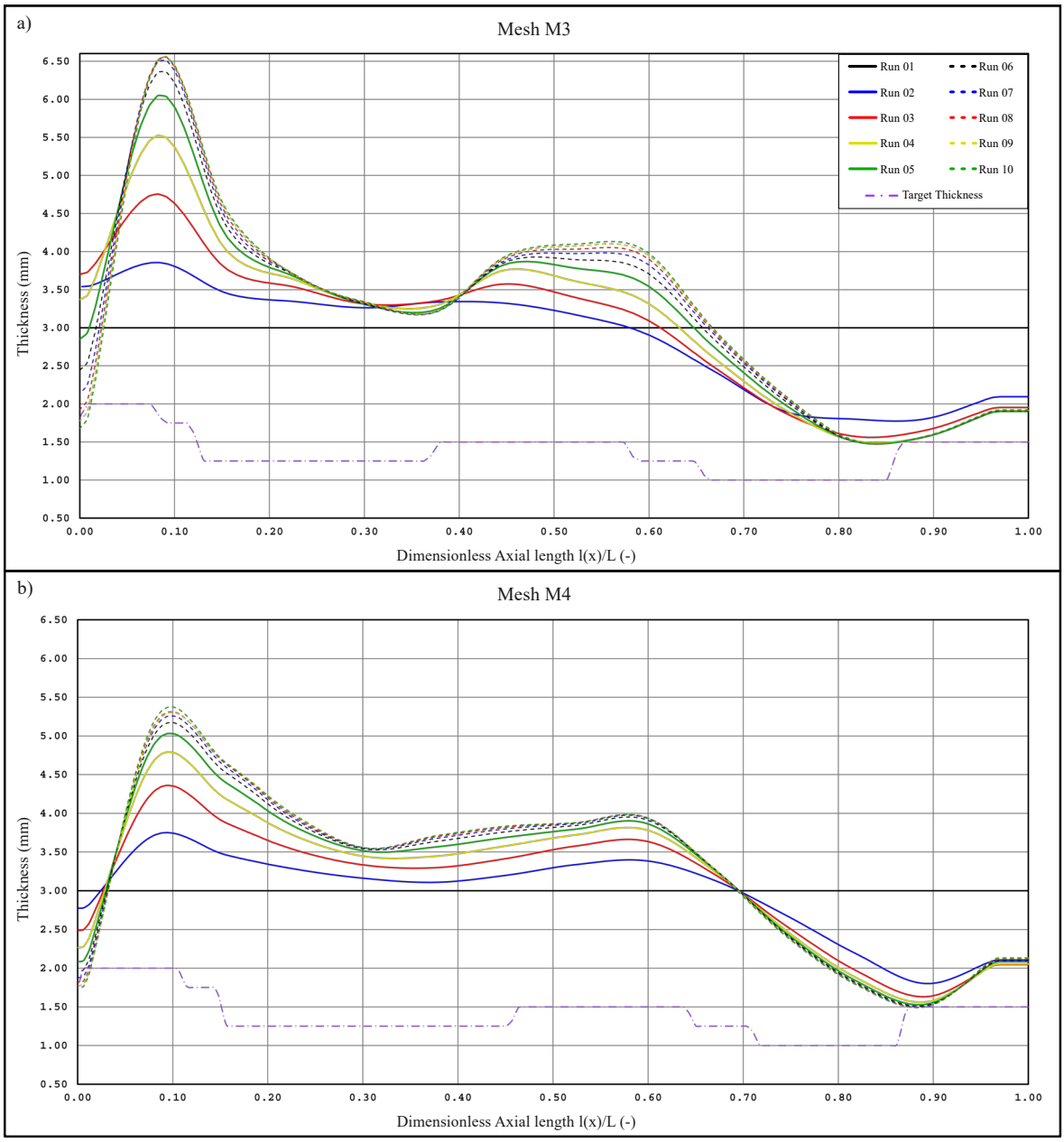


Figure 3.21: Evolution of the parison initial thickness profiles along the optimisation process for all cases with finer meshes, a) Mesh M3 and b) Mesh M4.

optimisation approach are depicted in Figure 3.25, highlighting a smoother transitions and enhanced final profiles achieved through this technique.

The analysis of initial thickness variations reveals smoother adjustments in optimised profiles, particularly noticeable when transitioning between mesh refinements. Notice that the Run 07 - M4 profile, exists only in Figure 3.25 a), this is because the optimised initial thickness profile of this run is obtained by doing the calculations using the data of previous run, i.e. Run 06. Results, presented in Figure 3.25 b), reveals that the variation of the final thickness profile during the optimisation using multi-mesh to be a faster way to optimise the final thickness distribution, since it also displaced the final profile closer to the target counterpart.

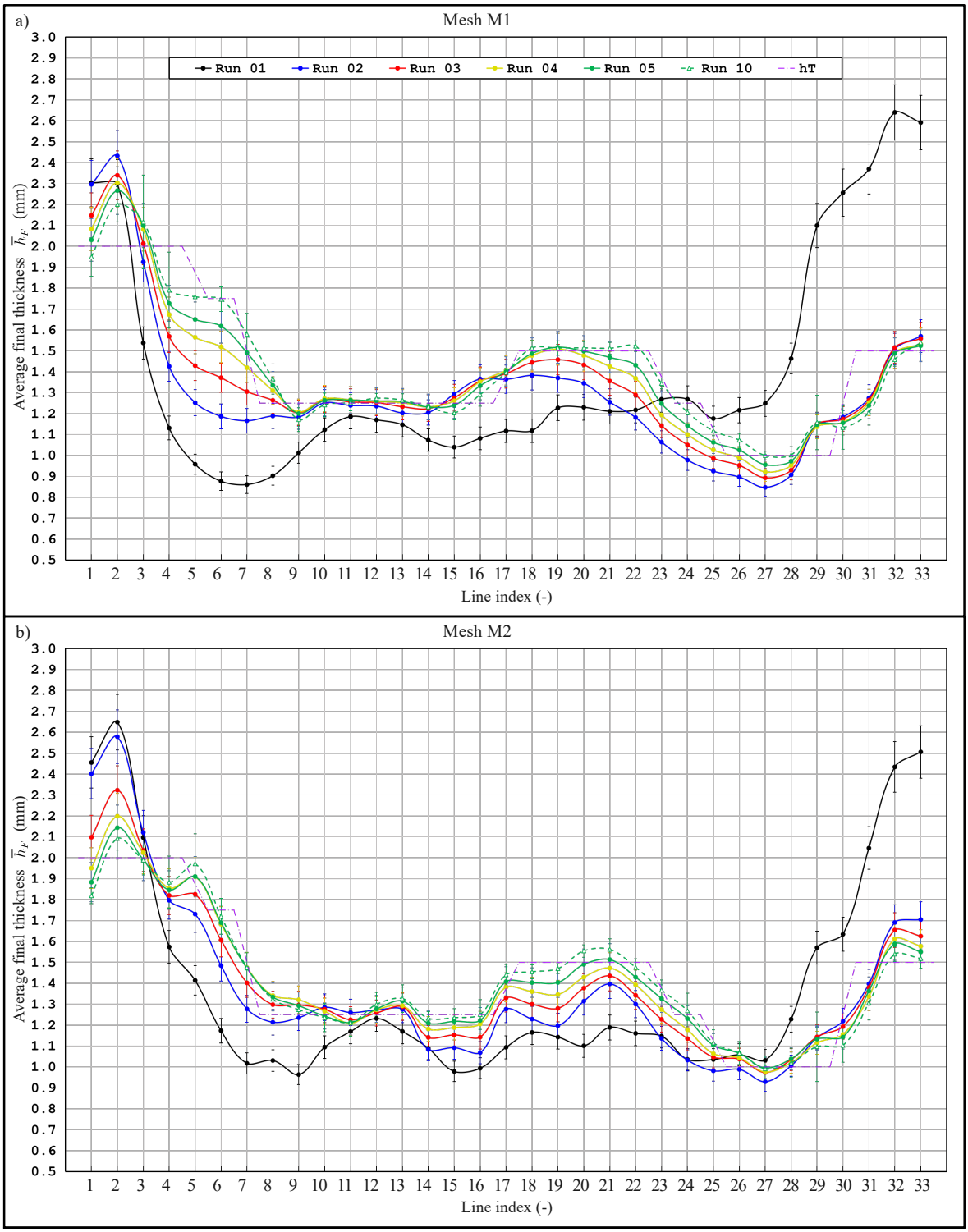


Figure 3.22: Evolution of the bottle thickness profiles along the optimisation process for all cases with coarser meshes, a) Mesh M1 and b) Mesh M2.

The comparative results of the multi-mesh approach are juxtaposed with the single-mesh of mesh M4, and this comparison is presented in Figure 3.26.

This comparison highlights the efficiency of the multi-mesh approach, as it achieves comparable thickness optimisation with a significantly reduced computational time, where the time elapsed for

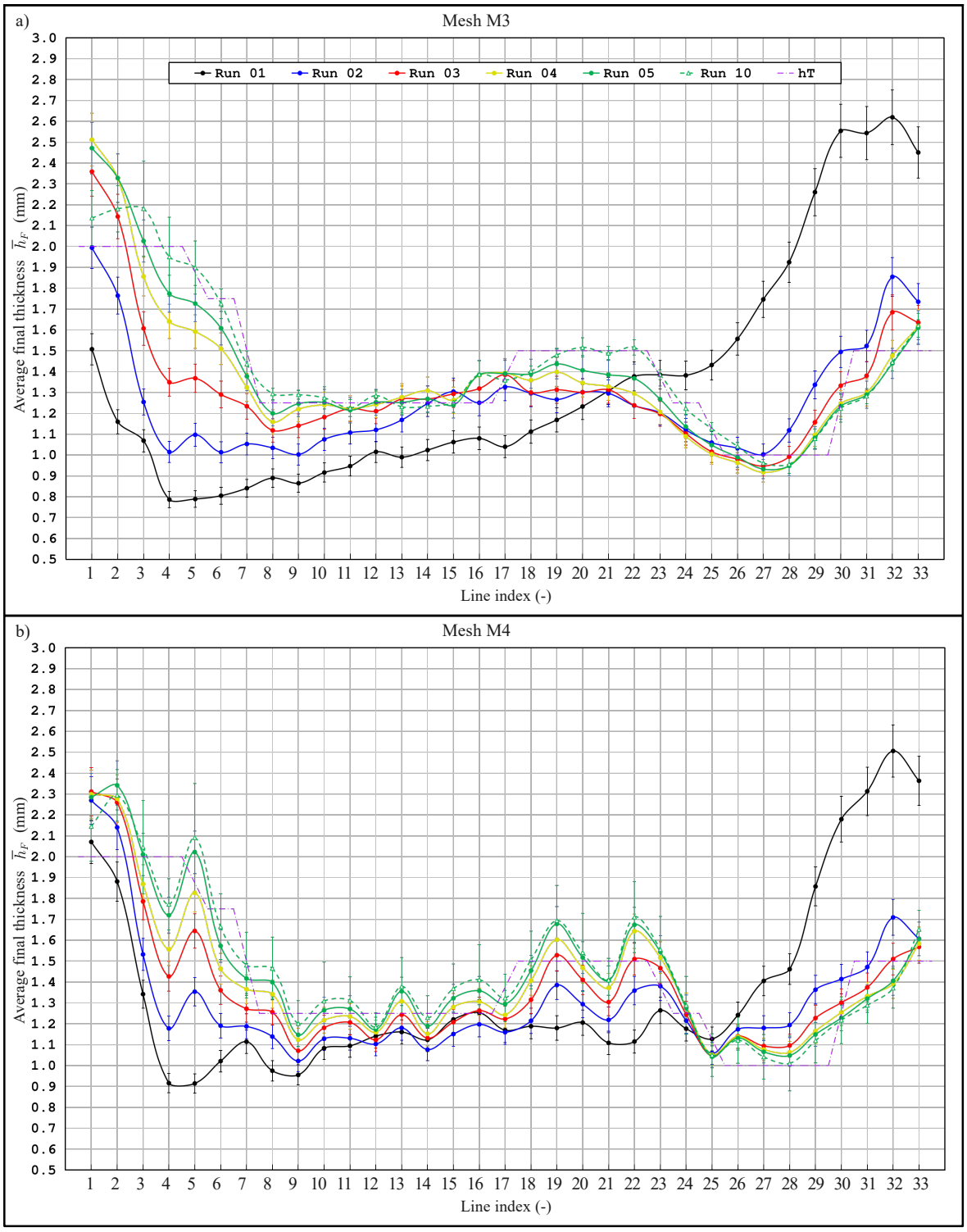


Figure 3.23: Evolution of the bottle thickness profiles along the optimisation process for all cases with finer meshes, a) Mesh M3 and b) Mesh M4.

the total calculation of the multi-mesh study required 41.22 hours of computing time while the mesh M4 this was of 61.49 hours, their relative times are illustrated in Table 3.4. The optimal profiles of the multi-mesh approach does not replicate the identical profile of the Run 05 - M4, mainly at the dimensionless perimeter of 0.10, although the resulting final thickness distribution were similar.

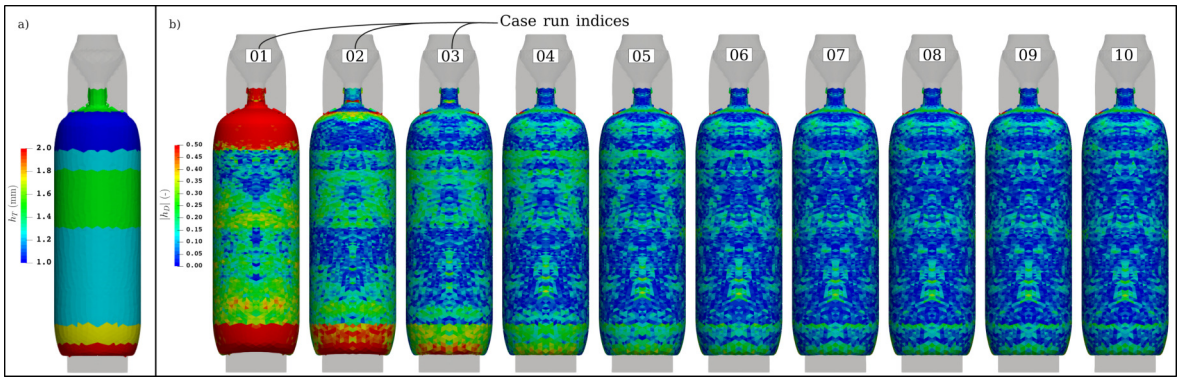


Figure 3.24: Colour map of distinct fields of the inflated parison, a) target thickness map and b) absolute value of the deviation thickness for all simulated cases using mesh M3.

	Mesh M1	Mesh M2	Mesh M3	Mesh M4
Run 01	8.5%	13.0%	24.8%	69.7%
Run 02	9.1%	13.8%	27.1%	66.8%
Run 03	9.1%	11.8%	28.0%	71.9%
Run 04	9.2%	11.8%	29.8%	82.4%
Run 05	10.2%	10.6%	30.2%	89.8%
Run 06	10.2%	10.7%	30.9%	97.7%
Run 07	9.2%	10.6%	31.6%	100.0%
Run 08	9.2%	10.8%	34.4%	98.5%
Run 09	9.2%	10.3%	35.2%	96.1%
Run 10	9.4%	10.3%	34.0%	94.8%
Total	**10.7%**	**13.1%**	**35.3%**	**100.0%**

Table 3.3: Relative simulation time for all simulated cases, demonstrating the computational requirements across mesh refinements. The real computational times for Run 07 of M4 and its total time, utilising a single core from the Intel® Core™- 12th generation - i7-12700K processor [67], correspond to 21.14 hours (PT21H8M37S) and 183.48 hours (P7DT15H29M16S), respectively.

The multi-mesh study explores various techniques for simultaneous thickness optimisation and mesh refinement. This study extends the potential for optimising the thickness of a part produced via EBM under more stringent requirements. This last study emphasises the adaptability and efficiency of the iterative process of optimisation, providing a robust framework for addressing these studies.

3.4.3 Oval-shaped bottle with variable target thickness

In this final case study, we aim to verify the developed computational optimisation framework in an industrial case study and compare the numerical predictions with data collected experimentally. The methodology for this study is outlined in Section 3.3.3, and the results are presented and discussed

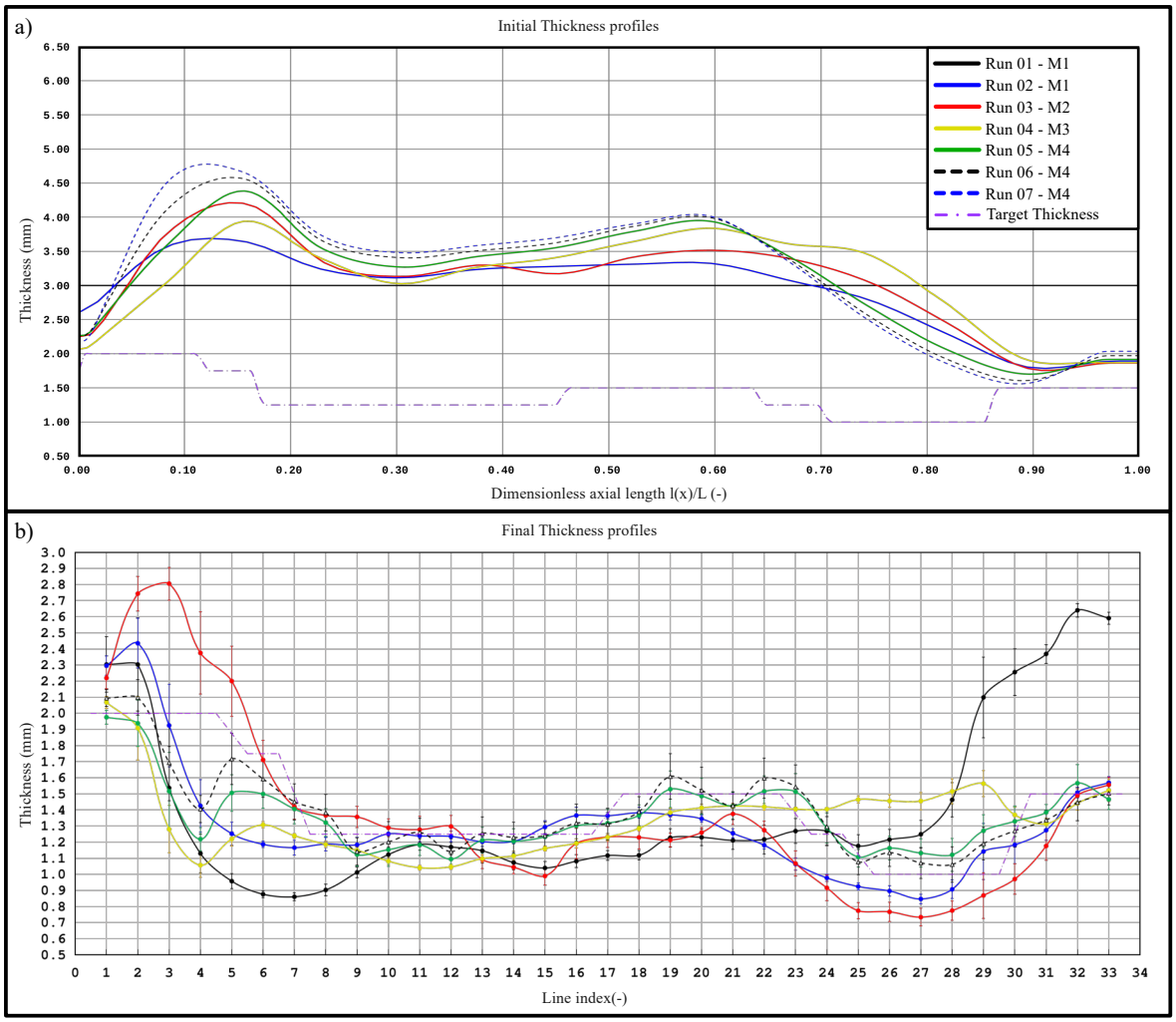


Figure 3.25: Thickness distributions for the two optimisation techniques addressed, a) Initial and b) final thickness profiles.

	Multi Mesh	Mesh M4
Run 01	3.7%	84.5%
Run 02	4.7%	81.0%
Run 03	8.9%	87.3%
Run 04	32.1%	100.0%
Run 05	94.9%	-
Run 06	92.3%	-
Total	**67.0%**	**100.0%**

Table 3.4: Relative calculation times for the optimisation studies using multi-mesh and single-mesh (with M4). The real computational time for Run 04 of M4, utilising a single core from the Intel® Core™- 12th generation - i7-12700K processor [67], correspond to 17.43 hours (PT17H25M34S).

hereafter.

First, a qualitative analysis is performed on the runs used in this optimisation, examining how the

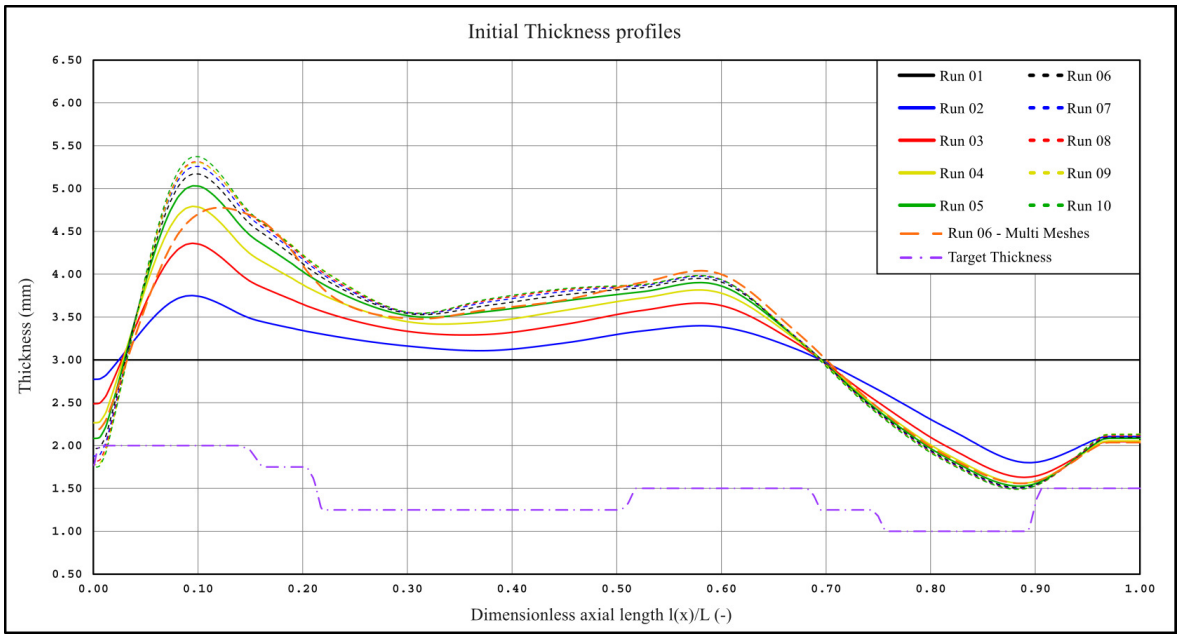


Figure 3.26: Comparison of initial and final thickness profiles between multi-mesh and single-mesh (M4) optimisation processes.

final thickness map varied throughout the optimisation steps. Next, a quantitative analysis is conducted by profiling the final thickness distribution. Subsequently, the numerical results are compared with experimentally obtained data. Lastly, the variations in shape and size of the outer surface of the real parison produced using both a constant die gap opening and a programmed parison are studied.

The Figure 3.27, shows all the thickness maps obtained for the two experimental bottles manufactures and the simulations results of the five optimisation runs. The Figure 3.27 a) shows the experimental thickness map of the bottle produced using a constant die gap opening, and Run 1 in Figure 3.27 b) the corresponding thickness distribution predicted by the numerical code. Runs 1 to 5 in Figure 3.27 b) show the thickness maps of the simulated bottles along the optimisation process, controlled by the developed code, being the last the one that provided the thickness distribution that better matches the target counterpart. The corresponding experimental thickness map, measured in a bottle produced with the optimised setup simulated in Run 5 is shown in Figure 3.27 c).

The results presented demonstrate the strong correlation of the thickness map between the actual manufactured bottles and their corresponding simulated versions. This holds true for both the initial trial, which was produced using a constant die gap, as well as the optimised bottles. While overall correlation is good for the former, there are some minor local deviations. However, these deviations are not noticeable in the latter case. These deviations were attributed to the simplification used in attributing a uniform thickness through the entire parison, while despite the die gap opening was set with a constant value, a thickness variation is expected through its axial length due to sagging (effect of gravity), thus promoting the formation of a parison that is thinner at the top and thicker at the bottom, as clearly seen in the measurements (Figure 3.27 a)).

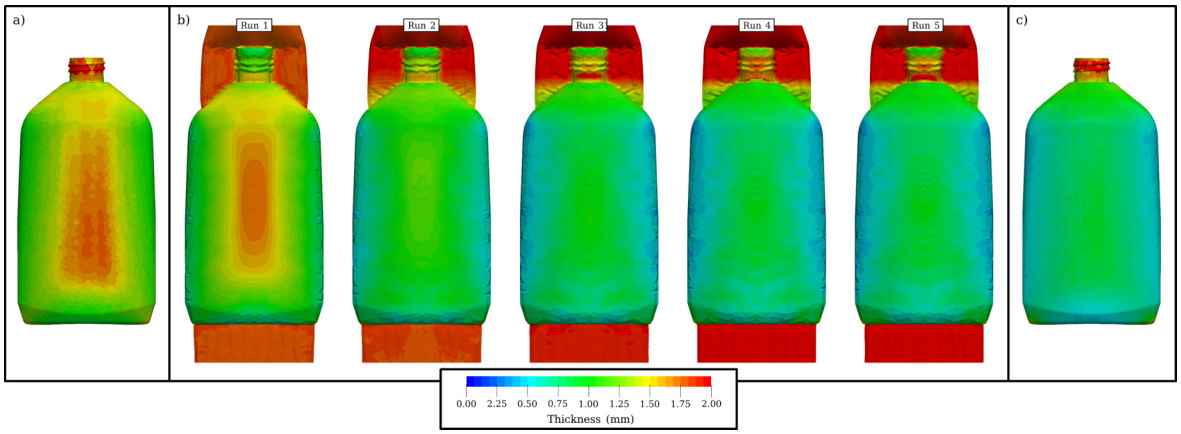


Figure 3.27: Final thickness maps for the oval-shaped bottle case study: a) Experimental data for the bottle produced with a constant die gap, b) Numerical data for Run 1 to 5 of the optimisation process and c) Experimental data for bottle produced with the optimised case study setup.

On the other hand, since the final thickness distribution of the bottle presented in Figure 3.27 a) was used to create the target thickness distribution, as shown previously in Figure 3.9, the effect of the sagging was included, and, thus, a better agreement is obtained between Run 5 of Figure 3.27 b) and Figure 3.27 c).

Figure 3.28 shows the thickness profiles for all the optimisation runs and for the two experimental bottles at the same profiling lines previously indicated in Figure 3.8. The evolution illustrated in Figure 3.28 a) shows that the developed algorithm was able to clearly improve the initial thickness distribution and achieve a setup that allows to obtain the target counterpart. Moreover, the good correlation between the numerical results and the data collected experimentally, shown in Figure 3.28 b), confirms the accuracy of the code predictions, and evidences the relevance of performing numerical studies prior start the experimental trials.

Aiming to clarify the effect of sagging, simulations were performed to identify the parison thickness distribution required to attain the experimental thickness distribution of the bottle produced with a constant die gap. The results obtained, not shown here, consisted in a parison with a gradual decrement of thickness from the bottom to the top regions. This finding corroborates the assumption that the small differences observed between the experimental and numerical thickness maps, Figure 3.28 a) and Run 1 of Figure 3.28 b), are related to the simplification of assuming a uniform parison thickness.

The final verification for this case, as well as for the entire paper, involves confirming the use of same parison geometry for the optimisation. This is accomplished by comparing the changes in the shape and size of the outer surface of the obtained parison using both a constant die gap opening and a programmed parison technique. Figure 3.29 illustrates that there are slight variations in their shapes when producing the parison using these different techniques. In Figure 3.29 a), a comparison between them is shown from a frontal view measurement, while in Figure 3.29 b), their measurements are compared from a lateral view. As long as these differences in size and shape fall within the range

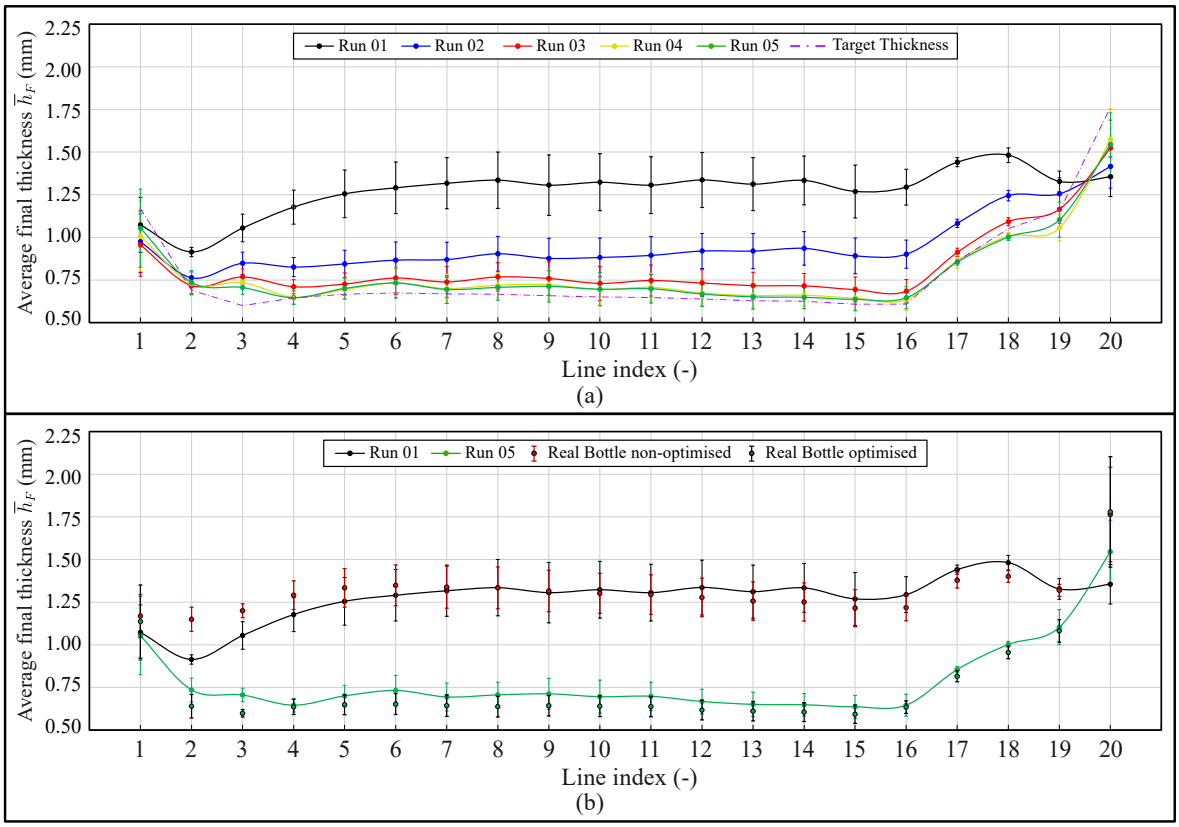


Figure 3.28: Final thickness profiles for the oval-shaped bottle case study: a) Optimisation process runs and b) First and last run of the optimisation process (dots linked with lines) and experimental data collected (non-linked dots). The dots mark the average values and the bars present the standard deviation

of measurement uncertainties, this simplification can be applied without compromising the final result. Higher deviations were observed for the frontal view bellow $270\,\mathrm{mm}$, which corresponds to a parison region that belongs to the flash and does not affect the final product. These regions present distinct tendencies due to the cutting process from the previous parison process. In practice, special attention is taken to ensure that this mentioned bottom region of the parison does not fall within the region of interest that forms the final part.

3.5 Conclusion

This research paper presents the development of an automated framework for optimising the material distribution in a part produced by the Extrusion Blow Moulding (EBM) process. The framework utilises tools developed within the OpenFOAM® computational library, which is the same framework employed for the computational numerical modelling code employed to perform the simulations [48]. The first utility developed aimed the creation of axial groups along the parison axial length to control the parison thickness profile. Another utility allows the definition of the target thickness map for the final part. A third utility uses the differences between the target and actual thickness to adjust the parison thickness control points and improve the final distribution.

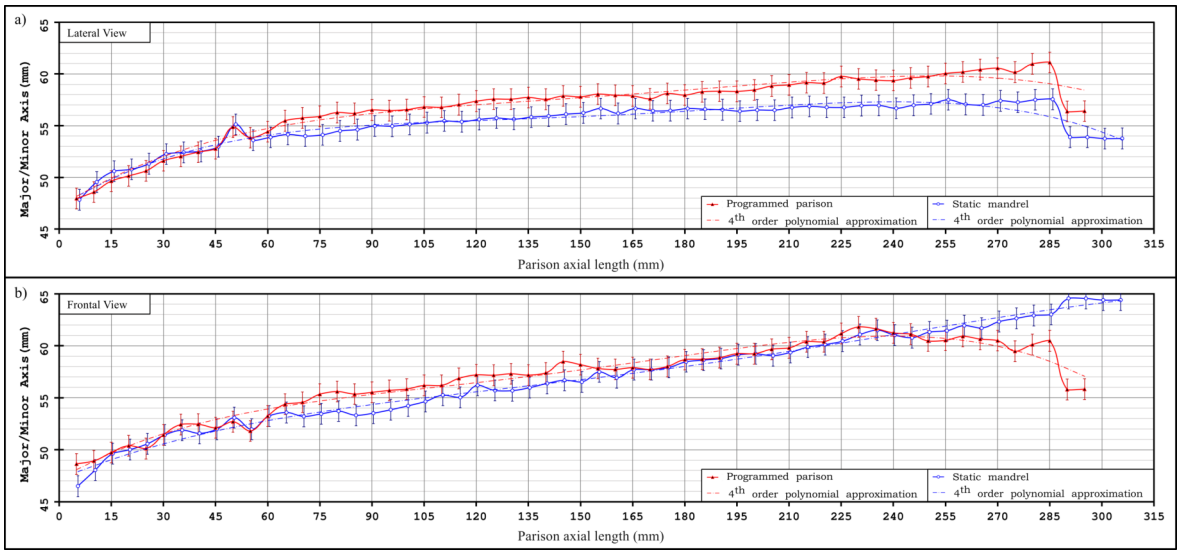


Figure 3.29: Real parison geometry dimensions measurements, obtained via constant die gap opening and via programmed parison technique, in a) lateral and b) frontal, perspectives.

The developed tools were tested with three case studies of increasing complexity. The first case study involved a cylindrical bottle with a constant target thickness. The algorithm successfully improved the initial solution and achieved a thickness distribution closer to the target value. Different mesh refinements yielded similar results. Next, the second case study, involved a non-uniform target thickness profile. The algorithm performed well in this more complex scenario, moving the final thickness distribution towards the target. A complementary study using multiple meshes proved also to be effective, and required less computational time to achieve similar results to the ones obtained with the most refined mesh.

A final case study considered the optimisation of an oval-shaped bottle, that was produced experimentally using two setups. The first setup employed a constant die gap during parison extrusion, resulting in a more uniform initial thickness distribution, while the second setup used a programmed parison technique that allowed for a variable initial thickness distribution using the optimised profile provided by the developed framework. In this last case study, it was verified that simulated results could accurately replicate the experimental measurements of both the initial trial and optimised bottles. The small deviations observed in the initial trial bottle were attributed to the simplification of assuming a uniformly distributed constant thickness for the initial parison, which neglected effects of sagging. The developed computational framework was able to significantly improve the thickness distribution of the initial trial, resulting in a final setup that produced a bottle with a thickness map very close to the target specifications. Additionally, this study confirmed that there were no significant deviations in the dimensions of the parison geometry, allowing the simplification of using the same initial geometry, during the optimisation study, without compromising the final results.

Based on these findings, results indicate that the proposed optimisation algorithm serves as an important tool for guiding the automatic optimisation of the EBM process design to attain the user

defined specifications. Therefore, the developments empower the packaging industry that resort to the EBM processes with a computational framework which, as the intended purposes, can contribute to further integrate it in the context of the industry 4.0. This framework enables digital manufacturing, where analysis of computational numerical simulation results can be utilised to define and determine the production setup, prior to manufacture the processing tools and spend resources in experimental trials.

References

[1] Eberhard Blümel. Global challenges and innovative technologies geared toward new markets: Prospects for virtual and augmented reality. Procedia Computer Science, 25:4–13, 2013. 2013 International Conference on Virtual and Augmented Reality in Education.

[2] Henning Kagermann. Change Through Digitization—Value Creation in the Age of Industry 4.0, chapter n/a, pages 23–45. Springer Fachmedien Wiesbaden, Wiesbaden, 2015.

[3] Achim Walter, Robert Finger, Robert Huber, and Nina Buchmann. Smart farming is key to developing sustainable agriculture. Proceedings of the National Academy of Sciences, 114(24):6148–6150, 2017.

[4] David Reinsel, John Gantz, and John Rydning. The digitization of the world from edge to core. Framingham: International Data Corporation, 16:1–28, 2018.

[5] Morteza Ghobakhloo. Industry 4.0, digitization, and opportunities for sustainability. Journal of Cleaner Production, 252:119869, 2020.

[6] Lorenzo Ardito, Antonio Messeni Petruzzelli, Umberto Panniello, and Achille Claudio Garavelli. Towards industry 4.0. Business Process Management Journal, 25(2):323–346, Jan 2019.

[7] Jan Ola Strandhagen Sven-Vegard Buer and Felix T. S. Chan. The link between industry 4.0 and lean manufacturing: mapping current research and establishing a research agenda. International Journal of Production Research, 56(8):2924–2940, 2018.

[8] Lucas Santos Dalenogare, Guilherme Brittes Benitez, Néstor Fabián Ayala, and Alejandro Germán Frank. The expected contribution of industry 4.0 technologies for industrial performance. International Journal of Production Economics, 204:383–394, 2018.

[9] Adam Schroeder, Brian Trease, and Alessandro Arsie. Balancing robot swarm cost and interference effects by varying robot quantity and size. Swarm Intelligence, 13(1):1–19, Mar 2019.

[10] Wing B. Lee, Benny C.F. Cheung, and Siu K. Kwok. Digital Manufacturing and RFID-Based Automation, chapter n/a, pages 859–879. Springer Berlin Heidelberg, Berlin, Heidelberg, 2009.

[11] Radhakisan Baheti and Helen Gill. Cyber-physical systems. The impact of control technology, 12(1):161–166, 2011.

[12] Dharmendra S Modha, Rajagopal Ananthanarayanan, Steven K Esser, Anthony Ndirango, Anthony J Sherbondy, and Raghavendra Singh. Cognitive computing. Communications of the ACM, 54(8):62–71, 2011.

[13] Javaid Butt. Exploring the interrelationship between additive manufacturing and industry 4.0. Designs, 4(2), 2020.

[14] Ahmad Barari, Marcos Tsuzuki, Yuval Cohen, and Marco Macchi. Editorial: intelligent manufacturing systems towards industry 4.0 era. Journal of Intelligent Manufacturing, 32(7):1793–1796, Oct 2021.

[15] Andrew Kusiak. Smart Manufacturing, chapter n/a, pages 973–985. Springer International Publishing, Cham, 2023.

[16] Ahmed Awouda, Emiliano Traini, Giulia Bruno, and Paolo Chiabert. Iot-based framework for digital twins in the industry 5.0 era. Sensors, 24(2), 2024.

[17] Andreja Rojko. Industry 4.0 concept: Background and overview. International Journal of Interactive Mobile Technologies (iJIM), 11(5):pp. 77–90, Jul. 2017.

[18] Judit Nagy, Judit Oláh, Edina Erdei, Domicián Máté, and József Popp. The role and impact of industry 4.0 and the internet of things on the business strategy of the value chain—the case of hungary. Sustainability, 10(10), 2018.

[19] Eric L. Xu Li Da Xu and Ling Li. Industry 4.0: state of the art and future trends. International Journal of Production Research, 56(8):2941–2962, 2018.

[20] Roland Geyer, Jenna R. Jambeck, and Kara Lavender Law. Production, use, and fate of all plastics ever made. Science Advances, 3:e1700782, 2017.

[21] Plastics Europe. The facts 2020. https://plasticseurope.org/knowledge-hub/plastics-the-facts-2020/, 2021. Accessed: 2023-Nov-25.

[22] Plastics Europe. The facts 2021. https://plasticseurope.org/knowledge-hub/plastics-the-facts-2021/, 2022. Accessed: 2023-Nov-25.

[23] Plastics Europe. The facts 2022. https://plasticseurope.org/knowledge-hub/plastics-the-facts-2022/, 2023. Accessed: 2023-Nov-25.

[24] Johann Schweighofer Harald Pilz and Evelin Kletzer. The contribution of plastic products to resource efficiency. https://www.teppfa.eu/wp-content/uploads/HSEGUAFinalreportplasticsressourceefficiencyupdateJan2005.pdf, 2005.

[25] European Commission. Single-use plastics. https://environment.ec.europa.eu/topics/plastics/single-use-plastics_en, 2021. Accessed: 2024-02-15.

[26] John Goff, Tony Whelan, and Don DeLaney. The dynisco extrusion processors handbook. Edition, 2:284, 2000.

[27] M. O. Ghafur, B. Koziey, and J. Vlachopoulos. Simulation of Thermoforming and Blowmolding — Theory and Experiments, chapter n/a, pages 321–383. Springer Netherlands, Dordrecht, 1995.

[28] G. H. Menary, C. W. Tan, M. Picard, N. Billon, C. G. Armstrong, and E. M. A. Harkin-Jones. Numerical Simulation of Injection Stretch Blow Moulding: Comparison with Experimental Free Blow Trials. AIP Conference Proceedings, 907(1):939–944, 04 2007.

[29] Ottmar Brandau. 1 - a short history of stretch blow molding. In Ottmar Brandau, editor, Stretch Blow Molding (Second Edition), Plastics Design Library, pages 1–4. William Andrew Publishing, Oxford, second edition edition, 2012.

[30] Benoit Cosson, Luc Chevalier, and Gilles Régnier. Simulation of the stretch blow moulding process: from the modelling of the microstructure evolution to the end-use elastic properties of polyethylene terephthalate bottles. International Journal of Material Forming, 5:39–53, 2012.

[31] Luis F. Ramos-De Valle. Principles of polymer processing, February 2013.

[32] Johannes Zimmer and Markus Stommel. Method for the evaluation of stretch blow molding simulations with free blow trials. In IOP Conference Series: Materials Science and Engineering, volume 48, page 012004. IOP Publishing, 2013.

[33] Samuel L. Belcher. 13 - blow molding. In Myer Kutz, editor, Applied Plastics Engineering Handbook (Second Edition), Plastics Design Library, pages 265–289. William Andrew Publishing, Moscow, Ohio, second edition edition, 2017.

[34] Market Research Future. Blow molding plastics market size, growth and analysis report 2030. https://www.marketresearchfuture.com/reports/blow-molding-plastics-market-4718, 2021. Accessed: [16/Jul/2024].

[35] A.D. Jayal, F. Badurdeen, O.W. Dillon, and I.S. Jawahir. Sustainable manufacturing: Modeling and optimization challenges at the product, process and system levels. CIRP Journal of Manufacturing Science and Technology, 2(3):144–152, 2010. Sustainable Development of Manufacturing Systems.

[36] Zhongfei Zhang, Ting Qu, Kuo Zhao, Kai Zhang, Yongheng Zhang, Lei Liu, Jun Wang, and George Q. Huang. Optimization model and strategy for dynamic material distribution scheduling based on digital twin: A step towards sustainable manufacturing. Sustainability, 15(23), 2023.

[37] Rohit Agrawal, Abhijit Majumdar, Anil Kumar, and Sunil Luthra. Integration of artificial intelligence in sustainable manufacturing: current status and future opportunities. Operations Management Research, 16(4):1720–1741, Dec 2023.

[38] M.F. Ashby. Overview no. 92: Materials and shape. Acta Metallurgica et Materialia, 39(6):1025–1039, 1991.

[39] Martin Philip Bendsoe and Ole Sigmund. Topology optimization. Springer, Berlin, Germany, 2 edition, July 2011.

[40] Javier Vera-Sorroche, Adrian Kelly, Elaine Brown, Phil Coates, Nayeem Karnachi, Eileen Harkin-Jones, Kang Li, and Jing Deng. Thermal optimisation of polymer extrusion using in-process monitoring techniques. Applied Thermal Engineering, 53(2):405–413, 2013. Includes Special Issue: PRO-TEM Special Issue.

[41] Jiyoung Jung, Kundo Park, Byungjin Cho, Jinkyoo Park, and Seunghwa Ryu. Optimization of injection molding process using multi-objective bayesian optimization and constrained generative inverse design networks. Journal of Intelligent Manufacturing, 34(8):3623–3636, Dec 2023.

[42] Renê S. Pinto, Hugo M. Silva, Fernando M. Duarte, João P. Nunes, and António Gaspar-Cunha. Neuroevolutionary Multiobjective Optimization of Injection Stretch Blow Molding Process in the Blowing Phase, chapter n/a, pages 307–318. Springer International Publishing, Cham, 2021.

[43] António Gaspar-Cunha, José A. Covas, and Janusz Sikora. Optimization of polymer processing: A review (part i—extrusion). Materials, 15(1), 2022.

[44] António Gaspar-Cunha, José A. Covas, and Janusz Sikora. Optimization of polymer processing: A review (part ii-molding technologies). Materials, 15(3), 2022.

[45] Erik Steinmetz, Seamus Scanlon, Tyler Schneider, and João Maia. Multi-layer co-extrusion blow molding. International Polymer Processing, 39(2):202–209, 2024.

[46] Samuel L Belcher. Practical guide to injection blow molding, volume 71. CRC Press, London, 2007.

[47] Michael Thielen. Extrusion Blow Molding. Carl Hanser Verlag GmbH & Company KG, 2021.

[48] Wagner de Campos Galuppo, Pedro Santana, Francisco Alves, and João Miguel Nóbrega. Extending the finite area method for enhanced simulation of deformable membranes and its application to extrusion blow moulding. Thin-Walled Structures, 203:112184, 2024.

[49] Blaž Rodič. Industry 4.0 and the new simulation modelling paradigm. Organizacija, 50(3):193–207, 2017.

[50] William de Paula Ferreira, Fabiano Armellini, and Luis Antonio De Santa-Eulalia. Simulation in industry 4.0: A state-of-the-art review. Computers & Industrial Engineering, 149:106868, 2020.

[51] D. Laroche, K. K. Kabanemi, L. Pecora, and R. W. Diraddo. Integrated numerical modeling of the blow molding process. Polymer Engineering & Science, 39(7):1223–1233, 1999.

[52] C. Gauvin, F. Thibault, and D. Laroche. Optimization of blow molded part performance through process simulation. Polymer Engineering & Science, 43(7):1407–1414, 2003.

[53] Y-L Hsu, T-C Liu, F Thibault, and B Lanctot. Design optimization of the blow moulding process using a fuzzy optimization algorithm. Proceedings of the Institution of Mechanical Engineers, Part B: Journal of Engineering Manufacture, 218(2):197–212, 2004.

[54] Jyh-Cheng Yu, Xiang-Xian Chen, Tsung-Ren Hung, and Francis Thibault. Optimization of extrusion blow molding processes using soft computing and taguchi's method. Journal of Intelligent Manufacturing, 15(5):625–634, Oct 2004.

[55] Geng-Qun Huang and Han-Xiong Huang. Optimizing parison thickness for extrusion blow molding by hybrid method. Journal of Materials Processing Technology, 182(1):512–518, 2007.

[56] J. A. W. M. Groot, C. G. Giannopapa, and R. M. M. Mattheij. Development of a Numerical Optimization Method for Blowing Glass Parison Shapes. Journal of Manufacturing Science and Engineering, 133(1):011010, 02 2011.

[57] Roman Denysiuk, Fernando M. Duarte, João P. Nunes, and António Gaspar-Cunha. Evolving Neural Networks to Optimize Material Usage in Blow Molded Containers, chapter n/a, pages 501–511. Springer International Publishing, Cham, 2019.

[58] Benoît Debbaut, Olivier Homerin, and Noor Jivraj. A comparison between experiments and predictions for the blow molding of an industrial part. Polymer Engineering & Science, 39(9):1812–1822, 1999.

[59] Gi Joon Nam, Jae Wook Lee, and Kyung Hyun Ahn. Three-dimensional simulation of thermoforming process and its comparison with experiments. Polymer Engineering & Science, 40(10):2232–2240, 2000.

[60] Noëlle Billon. New constitutive modeling for time-dependent mechanical behavior of polymers close to glass transition: Fundamentals and experimental validation. Journal of Applied Polymer Science, 125(6):4390–4401, 2012.

[61] Michael A. Kraus, Miriam Schuster, Johannes Kuntsche, Geralt Siebert, and Jens Schneider. Parameter identification methods for visco- and hyperelastic material models. Glass Structures & Engineering, 2(2):147–167, Oct 2017.

[62] Junuthula Narasimha Reddy. An introduction to continuum mechanics. Cambridge University Press, Cambridge, 2 edition, 2013.

[63] G.A. Holzapfel. Nonlinear Solid Mechanics: A Continuum Approach for Engineering. Wiley, Weinheim, 2000.

[64] Edwin Catmull and Raphael Rom. A class of local interpolating splines. In ROBERT E. BARNHILL and RICHARD F. RIESENFELD, editors, Computer Aided Geometric Design, pages 317–326. Academic Press, 1974.

[65] TotalEnergies SE. Technical datasheet 5502. https://polymers.totalenergies.com/5502, 2022. Accessed: 2024-Mar-07.

[66] Blender Online Community. Blender - a 3D modelling and rendering package. Blender Foundation, Stichting Blender Foundation, Amsterdam, 2018.

[67] Intel Corporation. Intel® core™ i7-12700k processor (25m cache, up to 5.00 ghz) specifications. https://www.intel.com/content/www/us/en/products/sku/134594/intel-core-i712700k-processor-25m-cache-up-to-5-00-ghz/specifications.html, 2021. Accessed: 2024-Jul-18.

CHAPTER 4

Extrusion Blow Moulding Process: Numerical Simulations of the Parison Extrusion Phase

Abstract: This work presents a comprehensive numerical and experimental study of the extrusion phase in extrusion blow moulding (EBM) process, a critical step that determines the geometry of the produced parison, including the associated material distribution, both essential to subsequent phases of the process and the performance of the final product. The material employed is the High-density polyethylene (HDPE), which was characterised considering a viscoelastic behaviour, which is expected to allow proper modelling of sagging and swelling phenomena. A new solver, rheoInterIsoFoam, has been developed within the RheoTool toolbox and based on OpenFOAM® [1] computational library, leveraging the geometric Volume-of-Fluid (GVoF) method to enhance the effectiveness of capturing the interface between the fluids, polymer and air, thereby solving the oscillations obtained with the original solver that follows an algebraic Volume-of-Fluid (AVoF) method. Simulations are conducted using the actual design of diverging extrusion die geometries and the relevant process conditions, predicting key outcomes such as diameter swell, thickness distribution, parison length, and the kinematics of this phase in the EBM process. The numerical simulation results are validated through experimental trials, demonstrating strong alignment, particularly regarding parison geometry and extrusion dynamics. This work contributes to advancing the understanding of the extrusion phase and provides a robust framework for simulating this process, while considering novel aspects in the simulations such as the effect of support air that is present in the real process. Furthermore, to enhance product quality, this numerical framework offers valuable insights and data that facilitate adjustments prior to the actual experimental processing, thereby supporting process efficiency and sustainability. The research also contributes to the broader field of polymer processing by providing advances in computational tool applicable to two-phase complex fluid flows, as well as advances for the simulation and optimisation of the EBM process for sustainable manufacturing practices.

Keywords: Extrusion Blow Moulding, Extrusion phase, Multi-phase Flow, Viscoelasticity, Numerical Simulation

This chapter was adapted from W. d. C. Galuppo, D. Nocita, P. Santana, F. Alves, and J.M. Nóbrega, Extrusion Blow Moulding Process: Numerical Simulations of the Parison Extrusion Phase, in preaparation (2024)

4.1 Introduction

Extrusion Blow Moulding (EBM) is an important manufacturing process in the plastics industry, enabling the production of a wide range of hollow parts, from small containers to large industrial components [2–9]. The process consists of sequential phases, all contributing to the final quality and performance of the product. The EBM cycle begins with the extrusion phase, where molten polymer is shaped into a tube-like form known as a parison. Subsequently, the parison is clamped by moulds, sealing it while leaving an opening region from which the air can be blown through by a nozzle during the subsequent inflation phase. Both during the mould clamping and as the parison inflates, it comes into contact with the mould surfaces, and it begins to cooling down. This process is accelerated by the mould's internal coolant circuits, which keeps it at a lower temperature. Once the polymer has reached a sufficient level of rigidity, it is demoulded, then the excess material is trimmed out, and the final product is obtained [9–13].

As industries increasingly focus on sustainability and resource efficiency, it has become crucial to analyse and optimise every phase of the EBM process [14–16]. Recent efforts have been made to simulate some phases from the EBM process, optimise material usage, and reduce waste, but there remains a significant need to accurately simulate the extrusion phase to enable a comprehensive understanding of the entire process [17]. While each phase of the EBM process is critical, the extrusion phase is fundamental, as it determines key properties of the parison—such as temperature, initial geometry, and material distribution—that directly affect subsequent phases. The outcomes of the extrusion phase are inherited by the subsequent phase in the EBM process, impacting the final product's quality and properties [9, 12, 13]. Therefore, understanding and accurately simulating the extrusion phase is essential for enhancing overall process efficiency, reducing material waste, and improving product quality.

The initial attempts to simulate the extrusion phase in the EBM process were reported by Dealy and Orbey [18]. Their approach involved developing a simple lumped-parameter analytical model to predict the length and shape of the parison without requiring extensive computations. This model utilised a few material properties, determined through laboratory tests based on experimental swell data and the storage modulus. Initially, they studied parison swell in the absence of sag, minimising the effects of gravity by extruding the parison directly into an oil bath with a density similar to that of the polymer. In a subsequent phase, they examined the combined effects of sag and swell. Comparing the experimental data with model predictions revealed that the proposed model, which assumed linear viscoelastic behaviour, consistently yielded highly inaccurate predictions for parison length. Consequently, the assumption of independence between swell and sag was found to be inaccurate. To improve the predictions, sag and swell effects were modelled as concurrent phenomena, requiring a more advanced discretisation technique than the previously described lumped-parameter model.

Garcia-Rejon et al. [19] expanded the understanding of the process by investigating the impact of various die design parameters, like the extrusion die inclination angle, die gap opening, die contraction

ratio, and diverging section length, on the swelling characteristics of an HDPE extrudate. The simulations were conducted using the Polyflow [20] software package with the Kaye-Bernstein, Kearsley, Zapas (K-BKZ) integral constitutive model to represent the polymer's viscoelastic behaviour [21]. Numerical predictions were compared to experimental data obtained from an industrial extrusion blow moulding machine. The findings revealed that thickness swell increases with higher die contraction ratios and decreases with greater die lengths and larger inclination angles from the vertical. Moreover, changes in die geometry were found to significantly affect diameter swell. In the absence of gravitational body forces, circumferential stresses caused the outer diameter of the parison to contract downstream of the die outlet in diverging die geometries. Conversely, extrudates emerging from converging annular dies exhibited pronounced expansion, attributed to the material's elasticity (memory) causing the extrudate to return to the upstream channel diameter of the annular die.

Tanoue et al. [22] built upon their previous study [23], which extended beyond analysing the time course of parison length and predicting parison area swell. The aim of their study was to calculate parison diameter and thickness swell. They examined three types of swell: outer diameter, thickness, and area swells, and obtained simulation predictions for annular extrudate swell using the Giesekus viscoelastic model. By analysing the results at low Weissenberg numbers ($Wi < 2.31$), they discovered a geometric relationship among these three types of swell using radius ratios. They used this relationship along with the area swell calculated in their previous study [23] to predict area, diameter, and thickness swell values for extruded parisons at high Wi, ranging from 50 to 300. The numerical results were within a 20% error margin when compared with experimental results in the parison creation process, including parison length, diameter, and thickness.

Another significant contribution, primarily related to the constitutive model, was made by Huang et al. [24], who compared experimental data to numerical predictions for parison extrusion conditions corresponding to industrial blow moulding. For their numerical investigation, they used the software Polyflow and the K-BKZ type constitutive equation associated with the Wagner-damping function. Six die geometries with converging, diverging, and straight configurations were examined to capture the effects of die geometry, particularly die inclination angle, on parison swell. The results showed that swells, especially thickness swell, increased with increasing axial and radial stresses or exit pressure. The dependency of melt stress distributions within the die on extrudate swell was noted, particularly, in dies with complex designs. The study demonstrated that predicted parison swelling is sensitive to the choice of material constants associated with the Wagner-damping function, which should be selected according to the die geometry to accurately reflect its contribution to the deformation history experienced by the polymer melt within the die.

Lastly, Tang et al. [25] reviewed and compared various viscoelastic models used for simulating polymer extrusion. The study examined the differential Phan–Thien–Tanner (PTT) model, the molecular-based Double-Convected POM–POM model (DCPP), and the integral K-BKZ model, along with their applicability in predicting swelling phenomena. These models were identified as promising for accurately capturing extrudate swell at high Weissenberg (Wi) numbers, particularly when combined

with suitable die designs for industrial applications.

The literature review confirms that the finite element method, particularly through the use of Polyflow, dominates the simulation studies of parison formation in the EBM process. However, an open-source alternative called RheoTool (version 5.0) was also made available. RheoTool is a toolbox based on OpenFOAM® [1] that utilises the finite volume method to simulate Generalised Newtonian Fluids (GNF) and viscoelastic fluids under pressure-driven conditions [26, 27]. Specifically, the rheoInterFoam solver, devised for multiphase flow simulations using the Eulerian Volume-of-Fluid (VoF) algebraic method, allows for the simulation of molten polymer and air. However, challenges such as viscoelastic stabilisation and accurately modelling the interface between the two fluids remain [28–30].

In this study, the focus is on simulating the extrusion phase of the EBM process and investigating its influence on parison formation as well as subsequent steps in the manufacturing cycle. The rheoInterFoam solver from the open-source software RheoTool [27] was used as a starting point, but preliminary studies shown that it predicts non-physical oscillatory pattern for the parison surface. Consequently, a new solver was developed, rheoInterIsoFoam, which employs a geometric method for capturing the interface location. Additionally, the viscoelastic differential PTT exponential model is adopted to describe the molten polymer and predict swelling and sagging phenomena. The main motivation of the work is to gain deeper insights into the dynamics of extrusion, enabling improved control and optimisation of the EBM process. This research contributes not only to the broader goal of sustainable manufacturing but also supports ongoing efforts to integrate advanced digital manufacturing technologies, such as digital twins and real-time process optimisation, into industrial practices. Furthermore, it provides valuable contributions to the simulation of complex flows.

The remaining part of this paper are organised as follows. Section 4.2 discusses the numerical tools used to simulate the extrusion phase, detailing both the VoF methods and algorithms employed. Section 4.3 elaborates on the theoretical background of the extrusion phase and outlines the geometries, conditions, and material characterisation used in this research. Section 4.4 presents the testing cases used for verification purposes and setups for the simulations. These comprise a simplified geometry and objective, followed by two more complex cases. The final testing case involves verifying numerical predictions against a real part produced via the EBM process. Section 4.5 showcases the main results and respective discussions for the employed case studies. Finally, in Section 4.6 this work summarises the findings and provides concluding remarks.

4.2 Mathematical Modelling

In this section, the mathematical modelling and formulations used for simulating the extrusion phase from the EBM process are covered in detail. The macroscopic length-scale level is considered for the matter in this work for its analysis, as stated by the continuum mechanics field. In EBM the molten polymer is subjected to a laminar pressure and stress driven complex fluid flow.

The governing equations that rule the extrusion phase in the EBM process are presented first. Then, the constitutive model that links stress and strain rates is given. Next, the Log-Conformation technique employed for the stabilisation of the viscoelastic stress tensor is over-viewed. Following, the two phase flows discretisation procedure is covered. Finally, the parison cut methodology is presented as the last topic of this section.

4.2.1 Governing Equations

The extrusion phase from the EBM process is governed by the following conservation equations, namely, continuity, Equation (4.1), and linear momentum balance, Equation (4.2) [31]. Due to the short duration of the stage, and low thermal diffusivity of polymer melts, an isothermal condition was assumed. Consequently, the heat generated by viscous dissipation within the flow channel of the extrusion die, as well as the heat transferred between the molten polymer and the surrounding air, after the extrusion die outlet, are neglected [32].

The incompressibility condition that applies to extruded polymers at the EBM processing conditions is suitable and assumed. Polymers largely deforms maintaining its volume constant, when subjected to the low pressure ranges typical of the EBM process. Under the above conditions, the continuity equation is given by:

$$\boldsymbol{\nabla} \cdot \mathbf{v} = 0 \,, \tag{4.1}$$

where $\mathbf{v}$ is the velocity vector.

The linear momentum equation is as follows:

$$\frac{\partial(\rho \mathbf{v})}{\partial t} + \boldsymbol{\nabla} \cdot (\rho \mathbf{v}\mathbf{v}) = -\boldsymbol{\nabla} p + \boldsymbol{\nabla} \cdot \boldsymbol{\tau} + \mathbf{f}_g + \mathbf{f}_{\Gamma_\sigma} \,, \tag{4.2}$$

where ρ is the specific mass, $\mathbf{v}$ is the velocity vector, t is the time, p is the pressure, $\boldsymbol{\tau}$ is the stress tensor, $\mathbf{f}_g$ is the gravitational body-force, and $\mathbf{f}_{\Gamma_\sigma}$ is the force per unit volume induced by surface tension at the interface between the two fluids [38].

The stress tensor is governed by a constitutive model, and several models have been deployed to represent distinct materials behaviours. Among these, the viscoelastic material behaviour is an appropriate choice to be used as constitutive model to simulate the polymer extrusion phase in EBM [25]. This is crucial to capture the elastic behaviour for the swelling that occurs to the molten polymer after leaving the extrusion the flow channel [31].

4.2.2 Constitutive Model

Constitutive models are mathematical formulations that describe the relationship between the stress tensor in the fluid and the rate-of-strain, and other fluid properties such as temperature, and material-specific characteristics. These models are typically classified into three primary categories: inviscid, Newtonian, and non-Newtonian fluids. The latter category can be further subdivided into inelastic fluids, modelled by GNF constitutive models, and elastic fluids, represented by linear and also by non-linear viscoelastic models.

Inviscid fluids are idealised as having no viscosity and governed by the Euler equations [33]. These equations describe fluid motion solely in terms of velocity, gravitational and pressure fields, neglecting viscous effects. Due to their simplicity, inviscid models are primarily applied to free-stream flow regions where viscous forces are negligible, such as regions far from the boundaries [33]. However, the inviscid assumption limits its applicability in many practical situations, particularly in non-thin boundary layers and where shear stresses are significant, because inviscid flows cannot satisfy the no-slip condition at the body surface [33].

The Newtonian fluid model is the most commonly applied constitutive equation, as it accurately describes the behaviour of many fluids, including air and water, which are prevalent in both nature and industrial applications. Newtonian fluids are characterised by a linear relationship between the stress tensor and the rate-of-strain tensor, as described by Newton's law of viscosity [34]. This model is particularly useful for capturing the behaviour of boundary layers, where viscosity plays a critical role in momentum transfer [33, 34].

Non-Newtonian fluids, on the other hand, exhibit a non-linear relationship between shear stress and the rate-of-strain. These fluids include shear-thinning fluids (e.g., polymer melts), shear-thickening fluids (e.g., cornstarch in water suspensions), and Bingham fluids (e.g., toothpaste), which require a yield stress to begin flowing [31, 35]. Non-Newtonian behaviour is more complex and requires specialised models to account for the varying responses under different flow conditions.

Viscoelastic fluids represent a subset of non-Newtonian fluids that exhibit both viscous and elastic characteristics, responding to deformation in two distinct ways: fluid-like (viscous) and solid-like (elastic). These models usually comprise two contributions for the stress tensor, the solvent and the polymeric, as follows [31, 36]:

$$\boldsymbol{\tau} = \boldsymbol{\tau}_s + \boldsymbol{\tau}_p \ , \tag{4.3}$$

where $\boldsymbol{\tau}_s$ and $\boldsymbol{\tau}_p$ are the solvent and polymeric contributions, respectively.

In order to close and solve the system of governing equations, one constitutive model is necessary for each term. These can be generically written in the forms of Equations (4.4) and (4.5)

for the solvent and polymeric parts, respectively.

$$\boldsymbol{\tau}_{\mathrm{s}} = \eta_{\mathrm{s}}\left(\boldsymbol{\nabla}\mathbf{v} + \boldsymbol{\nabla}\mathbf{v}^{\mathrm{T}}\right) \text{, and} \tag{4.4}$$

$$f\left(\boldsymbol{\tau}_{\mathrm{p}}\right)\boldsymbol{\tau}_{\mathrm{p}} + \lambda \overset{\nabla}{\boldsymbol{\tau}}_{\mathrm{p}} + \mathbf{h}\left(\boldsymbol{\tau}_{\mathrm{p}}\right) = \eta_{\mathrm{p}}(\dot{\gamma})\left(\boldsymbol{\nabla}\mathbf{v} + \boldsymbol{\nabla}\mathbf{v}^{\mathrm{T}}\right), \tag{4.5}$$

where η_{s} is the effective solvent viscosity, which can be a function of the rate-of-strain or shear rate, $\dot{\gamma}$, corresponding to the second invariant of the rate-of-strain tensor.

In Equation (4.5), the term $f\left(\boldsymbol{\tau}_{\mathrm{p}}\right)$ is a scalar-valued tensor function, that depends on the tensor $\boldsymbol{\tau}_{\mathrm{p}}$ invariants, λ is the relaxation time, $\overset{\nabla}{\boldsymbol{\tau}}_{\mathrm{p}}$ is the upper-convected time derivative term of the polymeric stress tensor, which assured the required frame-invariance, and the $\mathbf{h}\left(\boldsymbol{\tau}_{\mathrm{p}}\right)$ is a tensor-valued tensor function, that also depends on the polymeric tensor $\boldsymbol{\tau}_{\mathrm{p}}$. On the right-hand side of the same equation, $\eta_{\mathrm{p}}(\dot{\gamma})$ is the polymeric viscosity coefficient, which can be a function of the rate-of-strain $\dot{\gamma}$.

The term $\left(\boldsymbol{\nabla}\mathbf{v} + \boldsymbol{\nabla}\mathbf{v}^{\mathrm{T}}\right)$ in both equations is the symmetric rate-of-strain or rate-of-deformation tensor, i.e. $\dot{\boldsymbol{\gamma}} \equiv \nabla\mathbf{v} + (\nabla\mathbf{v})^{T}$ and it measures the rate which the fluid is deforming [31, 37, 38]. The rate-of-deformation tensor is defined as $\mathbf{d}$ and it is related to the previous tensor by a constant factor of two, i.e. $\mathbf{d} = \frac{1}{2}\dot{\boldsymbol{\gamma}} = \frac{1}{2}\left(\nabla\mathbf{v} + (\nabla\mathbf{v})^{T}\right)$ [39–41]. Notice that $\dot{\gamma}$ is a scalar, while $\dot{\boldsymbol{\gamma}}$ is a tensor, and they are also related to each other, where the former represents the second invariant of the later, which is equated as:

$$\dot{\gamma} = |\dot{\boldsymbol{\gamma}}| = +\sqrt{\frac{\dot{\boldsymbol{\gamma}} : \dot{\boldsymbol{\gamma}}}{2}} = +\sqrt{2(\mathbf{d} : \mathbf{d})} \ . \tag{4.6}$$

The upper-convected time derivative term of the polymeric stress tensor is given by [37, 39–41]:

$$\overset{\nabla}{\boldsymbol{\tau}}_{\mathrm{p}} = \frac{\partial \boldsymbol{\tau}_{\mathrm{p}}}{\partial t} + \mathbf{v} \cdot \boldsymbol{\nabla}\boldsymbol{\tau}_{\mathrm{p}} - \left(\boldsymbol{\tau}_{\mathrm{p}} \cdot \boldsymbol{\nabla}\mathbf{v} + \boldsymbol{\nabla}\mathbf{v}^{\mathrm{T}} \cdot \boldsymbol{\tau}_{\mathrm{p}}\right) \ . \tag{4.7}$$

Some models use the Gordon-Schowalter derivative, instead of the upper-convected derivative, to take non-affine deformation into account, and equated as follows [37, 42]:

$$\overset{\square}{\boldsymbol{\tau}}_{\mathrm{p}} = \overset{\nabla}{\boldsymbol{\tau}}_{\mathrm{p}} + \zeta\left(\boldsymbol{\tau}_{\mathrm{p}} \cdot \mathbf{d} + \mathbf{d} \cdot \boldsymbol{\tau}_{\mathrm{p}}\right), \tag{4.8}$$

where ζ ranging between 0 and 1, accounts for the slip between the molecular network and the continuous medium [43]. This Gordon-Schowalter derivative is used in the PTT model, which is the constitutive model chosen model to portray the viscoelastic materials in this study.

In the alternative formulations of the PTT model, the exponential form that describes the rate of

macromolecular network junctions destruction—caused by strong local attractions along the polymer chains—is adopted. Specifically, the term $f(\boldsymbol{\tau}_\mathrm{p})$ in Equation (4.5) is expressed as an exponential function. Accordingly, the constitutive equation for the PTT model, given by Equation (4.5), is as follows:

$$e^{\left[\frac{\epsilon\lambda}{\eta_\mathrm{p}}\mathrm{Tr}(\boldsymbol{\tau}_\mathrm{p})\right]}\boldsymbol{\tau}_\mathrm{p}+\lambda\overset{\square}{\boldsymbol{\tau}}_\mathrm{p}=\eta_\mathrm{p}\left(\boldsymbol{\nabla}\mathbf{v}+\boldsymbol{\nabla}\mathbf{v}^\mathsf{T}\right), \tag{4.9}$$

where ϵ represents the extensibility parameter, λ is the relaxation time and η_p is the zero-shear-rate polymer viscosity.

After a few numerical trials, in this work it was opt to follow the log-conformation formulation, in order to stabilise the calculation procedure [27, 29, 30]. The conformation tensor has an explicit relation with the polymeric component of the stress tensor, and represents the internal elastic strain of the fluid [44]. The relation between the polymeric extra-stress tensor and the conformation tensor for the PTT model is given by [27, 39, 43]:

$$\boldsymbol{\tau}_\mathrm{p}=\frac{\eta_\mathrm{p}}{\lambda(1-\zeta)}(\boldsymbol{A}-\boldsymbol{I}), \tag{4.10}$$

where $\boldsymbol{A}$ is the conformation tensor and $\boldsymbol{I}$ is the identity tensor.

The constitutive model presented in Equation (4.9), governs the behaviour of a single mode material, however, due to their nature, polymer melts present a behaviour that combines the effect of multiple modes, each governed by an equation similar to Equation (4.11), but with specific properties, given by:

$$e^{\left[\frac{\epsilon_i\lambda_i}{\eta_{\mathrm{p},i}}\mathrm{Tr}(\boldsymbol{\tau}_{\mathrm{p},i})\right]}\boldsymbol{\tau}_{\mathrm{p},i}+\lambda_i\overset{\square}{\boldsymbol{\tau}}_{\mathrm{p},i}=\eta_{\mathrm{p},i}\left(\boldsymbol{\nabla}\mathbf{v}+\boldsymbol{\nabla}\mathbf{v}^\mathsf{T}\right), \tag{4.11}$$

where the subscript i is used to identify a specific mode, which has its own set of values of material coefficients (λ_i, ϵ_i, $\eta_{\mathrm{p},i}$, ζ_i) that are obtained via the material characterisation. Accordingly, the polymeric stress tensor in a multi-mode material is given by:

$$\boldsymbol{\tau}_\mathrm{p}=\sum_{i=1}^{n}\boldsymbol{\tau}_{\mathrm{p},i}. \tag{4.12}$$

Similarly, the solvent contribution of a multi-mode material to the stress tensor is obtained:

$$\boldsymbol{\tau}_{\mathrm{s}} = \sum_{i=1}^{n} \boldsymbol{\tau}_{\mathrm{s,i}} \ , \tag{4.13}$$

Finally, the resulting stress tensor is the sum of both multi-mode resulting contributions, i.e. solvent and polymeric, as previously defined in Equation (4.3).

4.2.3 Two phase flow

In this study, two phases are simulated: one representing the air and the other the polymer melt. Among the techniques available for simulating multi-phase phenomena, the Eulerian Volume-of-Fluid (VoF) method [45] is employed. Unlike Lagrangian methods, the Eulerian approach is particularly effective for handling large interfacial deformations and complex shapes [46].

The VoF method is a numerical procedure used to follow the location of the interface between distinct fluids. It utilises an Eulerian framework in which the interface is implicitly accompanied as a field function. Specific advection solution are required to maintain the sharpness of the interface in two-phase flow simulations [47]. Following the VoF method a scalar value, denoted as α, designated by phase indicator, is used throughout all computational cells in the domain to distinguish the different fluids. In the context of two fluids, $\alpha = 1$ represents the molten polymer, designated with the subscript l, while $\alpha = 0$ represents the air surrounding the extruded parison, designated with the subscript g. Intermediate values of α correspond to computational cells where the interface between the two phases is located [48]. This method is schematically illustrated in Figure 4.1.

In conventional VoF method, the conservation equation for phase fraction, is solved along with the other conservation equations such as mass Equation (4.1) and linear momentum Equation (4.2), and calculated as follows,

$$\frac{\partial \alpha}{\partial t} + \boldsymbol{\nabla} \cdot (\boldsymbol{v}\alpha) = 0 \ , \tag{4.14}$$

where the first term is the rate of change of α in the domain, while the second term is the advection term, that calculated how α is convected through the domain [48].

The fluid properties of a discrete cell, such as specific mass and solvent and polymeric viscosities, are obtained by calculating weighted average values based on the volume fractions of the respective phases within that cell. Thus, for a cell containing the volume fractions of this binary fluid system, the resulting specific mass ρ and solvent viscosity η_s are calculated using the volume fraction α, as follows [49]:

$$\rho = \alpha\rho_l + (1-\alpha)\rho_g \ , \tag{4.15}$$

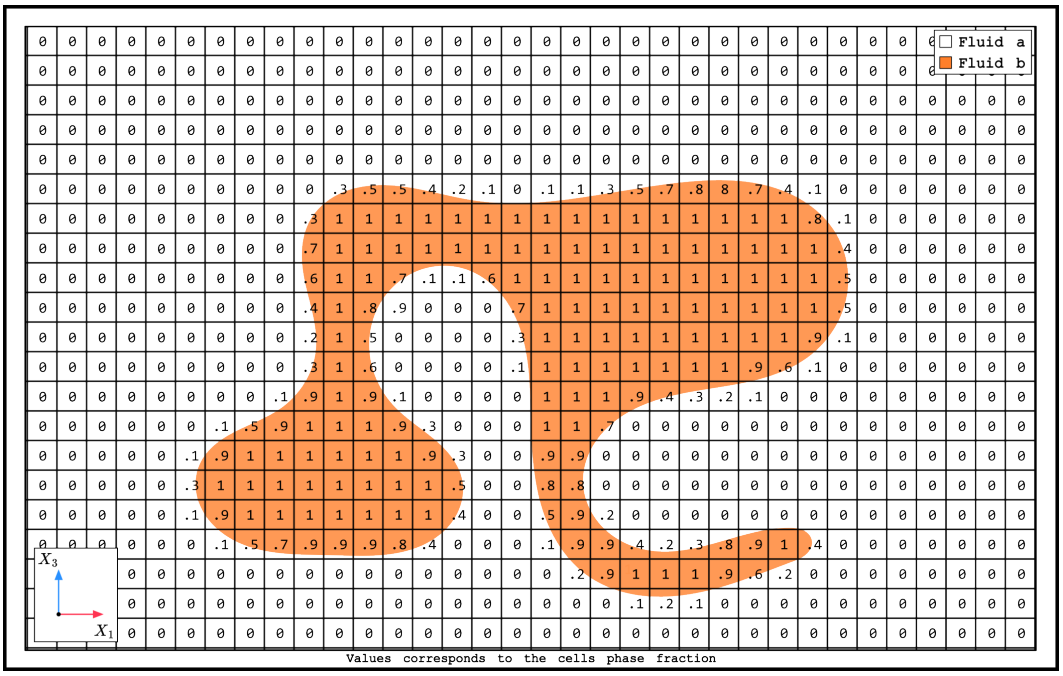


Figure 4.1: Illustrative representation of the phase indication, α, for a two-phase flow, solved by the Volume of Fluid method.

$$\eta_s = \alpha\eta_{s,l} + (1-\alpha)\eta_{s,g} \ . \tag{4.16}$$

This conventional VoF method is known for smearing the interface region over a few grid cells, making it very sensitive to grid resolution [50]. However, an accurate calculation of the phase fraction α distribution is essential for properly evaluating some flow characteristics, like the surface curvature. This evaluation is crucial for determining surface tension forces and the associated pressure gradient across the free surface [51].

Different VoF methods have been deployed so far, which are typically distinguished into two groups, namely, algebraic and geometric methods [46]. In the algebraic VoF (AVoF) method, the phase fraction α is represented by a the scalar function α, without any special concern regarding its distribution. In the geometric VoF (GVoF) method, a geometric representation for the interface is constructed to represent more accurately the distribution of the α field [46].

A shortcoming of VoF based methods is the abrupt changes in the volume fraction over interfacial regions. These induce inconsistent calculation of the surface tension force and the associated pressure jump, leading to interpolation and discretisation errors [46]. Therefore, such errors can result in an unrealistic representation of the interface, adversely affecting the accuracy and stability of the simulation.

A two-fluid Eulerian model for two-phase flow, where phase fraction equations are solved

separately, would decompose the velocity vector similarly to the approach used for the properties in Equations (4.15) and (4.16). Therefore, assuming that the contribution of each phase's velocity to the evolution of the free surface is proportional to the respective phase fractions, the velocity of the effective fluid in a VoF can be defined as a weighted average[51, 52]. Consequently, an additional term for the velocity emerges in the smeared interfacial region, known as the compression or relative velocity, denoted as $\mathbf{v}_r$ [51, 52].

The introduction of this relative velocity term is crucial for accurately capturing the interfacial dynamics and ensuring the stability and accuracy of the VoF method, This term is used in the calculations for the progression of the phase fraction field α [48], facilitating the simulation of complex fluid behaviours for precise modelling of the two-phase flow dynamics [51]. Consequently, the governing equation for the phase fraction α is rewritten as:

$$\frac{\partial \alpha}{\partial t} + \nabla \cdot (\alpha \mathbf{v}) + \nabla \cdot [\alpha(1-\alpha)\mathbf{v}_r] = 0 \,. \tag{4.17}$$

The third term on the left-hand side of the Equation (4.17) is non-zero only for $0 < \alpha < 1$, becoming zero when $\alpha = 0$ or $\alpha = 1$. This allows for the use of the single-fluid approach to solve both the continuity Equation (4.1) and the momentum balance Equation (4.2). Similarly, the stress tensor used in the second term of the right-hand side of Equation (4.2) is obtained for this AVoF method. A detailed explanation of this approach is provided in the work of Ubbink [49].

To minimise the numerical smearing of the interface, compressive numerical linear-solver are employed. These linear-solvers compute the interfacial flux based on the orientation of the interface normal for each computational cell [53].

The AVoF compressive numerical linear-solver used in this study is the one implemented in OpenFOAM® Computational library [1], known as the Multidimensional Universal Limiter with Explicit Solution (MULES) [54]. MULES is an advanced compressive numerical linear-solver that combines the AVoF method with additional sharpening, smoothing, and assures that the value fraction α remains bounded [55]. This combination helps to diminish non-physical spurious results within the VoF framework, aiming to ensure a more accurate and stable representation of the fluid interface [56].

On the other hand, GVoF methods use geometrical operations to approximate the solution of the phase fraction α in multi-phase flow simulations [57]. In general, these methods perform interface reconstruction and advection [46]. A prominent technique within GVoF methods is the Isoadvector linear-solver, which originally used the isoAlpha method for interface reconstruction [58]. However, another method, called Piecewise Linear Interface Calculation - Recursive Distance Function (PLIC-RDF), has shown even improved results in interface reconstruction [59]. The Isoadvector linear-solver, combined with PLIC-RDF method for interface reconstruction, was chosen because it is available in OpenFOAM® version 2206 [1], which, at the time of release was from the ESI Group, but

now belongs to Keysight Technologies, Inc.

4.2.4 Computational framework

RheoTool [27] is an open-source code that extends the capabilities of OpenFOAM® [1] computational fluid dynamics (CFD) toolbox, designed to model single-phase and multi-phase complex fluid flows, with complex rheological behaviour, such as GNF and viscoelastic. Moreover, RheoTool incorporates methods to enhance the stability of simulations as the log Conformation Approach.

RheoTool's solver designated as rheoInterFoam [27] is designed to handle the simulation of multiphase flows using the AVoF method involving complex rheological fluids, such as GNF and viscoelastic fluids. In the preliminary studies performed in this work the interface polymer-air presented intricacy results that lead to the development of a new solver, by modifying the original rheoInterFoam, to use the PLIC scheme for the GVoF method. This was undertaken by porting to RheoTool the interIsoFoam [60] solver available in OpenFOAM® [1]. The new solver was designated as rheoInterIsoFoam, where the Iso stands to the Isoadvector concept, a numerical method for passive advection of a surface.

4.2.5 Parison Cut

This paper aims to replicate the extrusion phase of a real EBM part while also assessing its transient behaviour. To replicate the real process, the developed simulation code was improved to incorporate a mechanism to cut the parison upon meeting a specified criterion, indicating the instant in the extrusion phase when the parison is formed. Hence cutting it and determining both the length of the extruded parison, based on the knife positioning, and the duration of the extrusion cycle in the EBM process involving continuous extrusion. However, it is important to note that the cut does not precisely define the start and end points of the extrusion cycle. At the moment the cut is executed, a portion of the parison intended for the subsequent cycle has already been extruded and is located between the extrusion die and the cutting plane. Consequently, the parison from the next cycle is partially extruded along with the uncut extrudate portion. Thus, the parison from the current cycle and the portion from the next cycle are separated by the cutting operation.

In this operation, the α field of the region corresponding to the parison to be cut is identified and the respective phase indicator, α, value is changed to 0. The numerical operation is illustrated in Figure 4.2. Accordingly, the region beneath the knife, which corresponds to the polymer phase, is replaced by air. This operation enables the developed code to simulate sequential cycles for parison extrusions effectively.

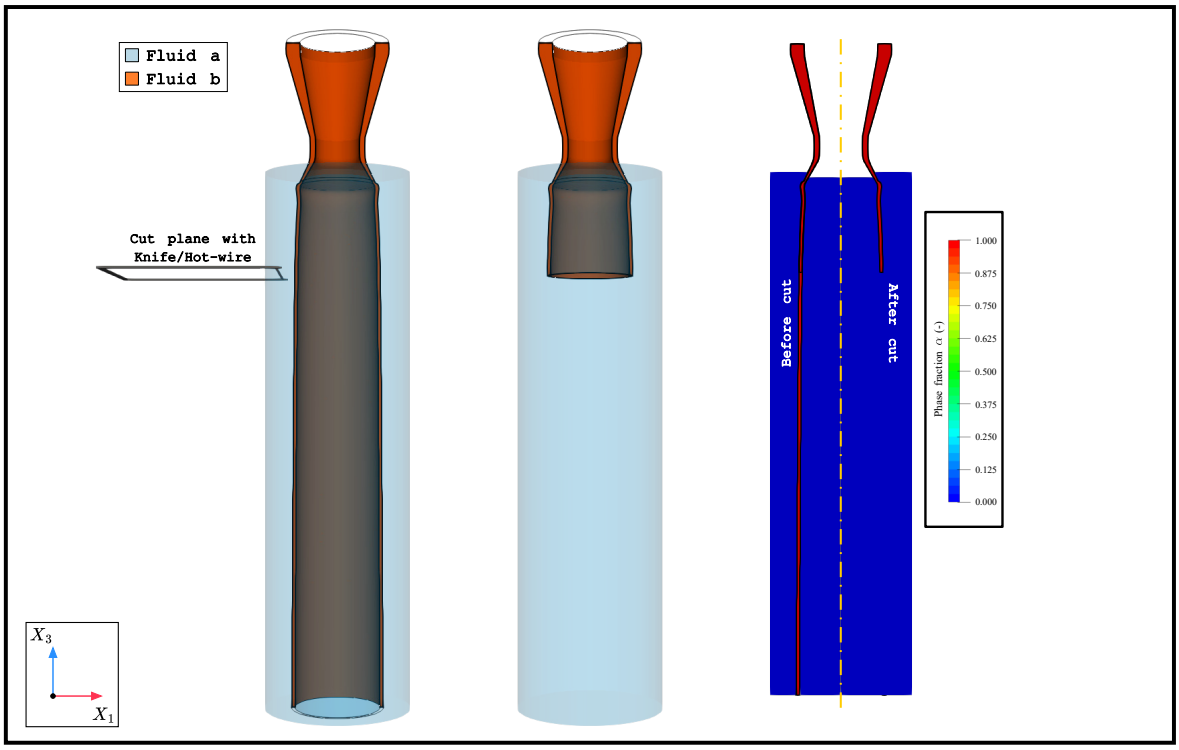


Figure 4.2: Extruded parison immediately before, and after cut. The illustration is with regard a full 360 degrees revolution parison, along with the phase fraction, field used to perform the cut.

4.3 Materials and Methods

In this section case studies used in this work are presented, which includes, for instance, the geometry type and its dimensions. In addition the discretisation and boundary conditions used for the simulations are also described. The overall process conditions defined for the extrusion phase, and the material characterisation process for the processed polymer melt is provided.

4.3.1 Extrusion Die Design

The extrusion set is typically classified in three categories depending on the geometry type channels in EBM process, namely, straight, converging or diverging die channels [12, 18]. The current study considers only the diverging die type. This type of die is used to obtain a parison with a larger diameter than the one of the extrusion die flow channel. In addition, parisons that are usually obtained with this type of die are generally of straightened shape format after leaving the die flow channel due to the gravitational effect. On the other hand, it causes the sagging effect, due to the parison own weight [61]. Thus, usually the parison extrusion direction is the same as the gravitational acceleration [19]. Moreover, during the extrusion there is a hole in the pin through which air is blown, to create a support air region that sustains and stretches the parison during this phase, as detailed in EBM technical guides [62].

The schematic representation of the extrusion channel used in the experimental work and simulations is shown in Figure 4.3, along with its main geometric parameters. For visual clarity, the geometry is presented only for one quarter of the full geometry. The design exhibits rotational symmetry, with the axisymmetric revolving line coinciding with the third principal direction (X_3) of the rectangular orthonormal basis, as depicted in Figure 4.3. The overall case study geometry is presented in Figure 4.3 a), while Figure 4.3 b) provides a zoomed-in view of the extrusion die flow channel to better showcase its parameters.

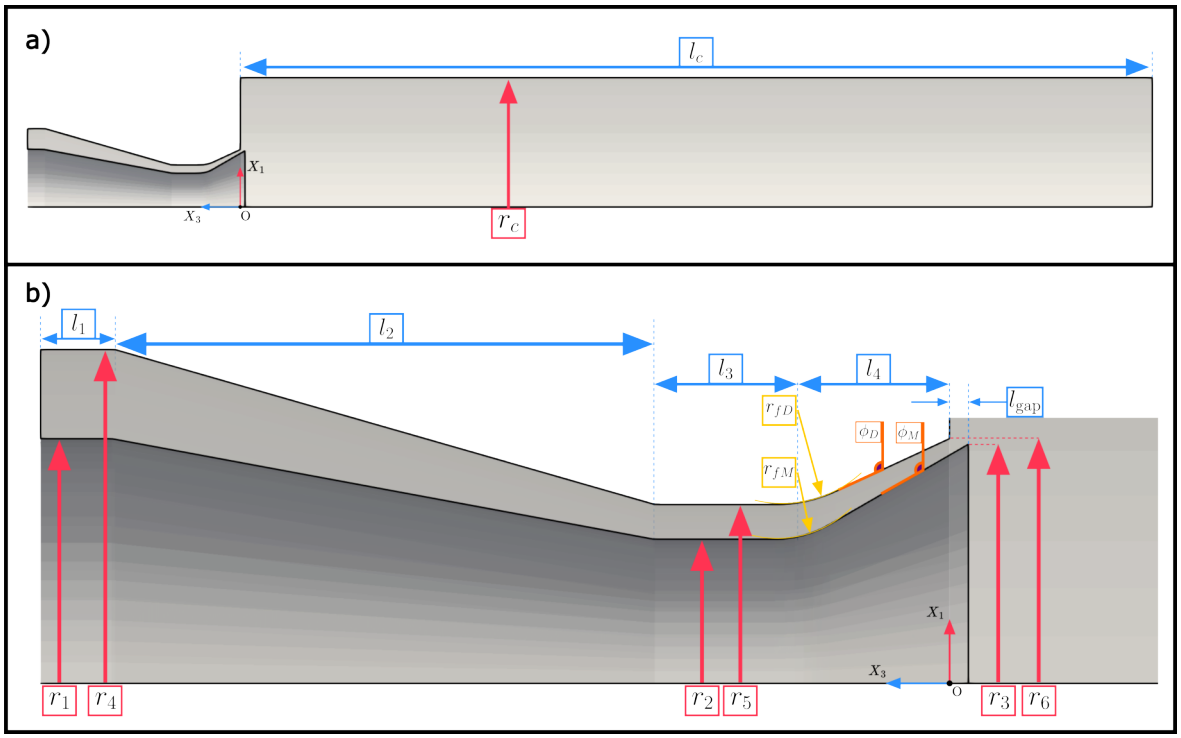


Figure 4.3: Extrusion geometry design with defined parameters: a) Overview of the extrusion chamber extension, and b) Extrusion channel view.

The values for all parameters illustrated in Figure 4.3 are listed in Table 4.1, for the cases studies employed in this work. An important parameter is the die diameter ($d_{\text{die}} = 2r_6$), which is used to calculate the dimensionless parameter for the parison, known by diameter swell, as follows, $d^*_{\text{swell}} = d_{\text{parison}}/d_{\text{die}}\,(-)$.

Variable	Value	Dimensions	Variable	Value	Dimensions	Variable	Value	Dimensions
r_1 :	21.50	mm	l_1 :	6.70	mm	r_c :	42.50	mm
r_2 :	13.00	mm	l_2 :	48.50	mm	r_{fD} :	12.50	mm
r_3 :	21.50	mm	l_3 :	35.70	mm	r_{fM} :	10.00	mm
r_4 :	30.00	mm	l_4 :	12.80	mm	ϕ_D :	115°	-
r_5 :	16.00	mm	l_{gap} :	1.70	mm	ϕ_M :	120°	-
r_6 :	22.00	mm	l_c :	307.00	mm	:		

Table 4.1: Defined values for the variables in the extrusion geometry design.

4.3.2 Extrusion Process Setup

The extrusion tool employed was the divergent configuration detailed in Section 4.3.1, using with a constant die gap opening, with a mass flow rate of $\dot{m} = 3.726 \pm 0.013\,\mathrm{g/s}$, at a processing temperature of $200 \pm 2.7\ ^{\circ}\mathrm{C}$.

The experimental EBM processing cycle lasted $19.39 \pm 0.15\ \mathrm{s}$ in average per parison cut for a run of 18 cycles. This is the total extrusion time, since the machine used a continuous extrusion process for the parison creation, while the subsequent phases from the process are undertaken in another place. Moreover, the full parison length is of $300.0 \pm 5.0\ \mathrm{mm}$, whether the knife is positioned at $54.0 \pm 1.0\ \mathrm{mm}$ downstream the extrusion die gap.

4.3.3 Material and Rheological Characterisation

The extrusion used raw virgin High-Density Polyethylene (HDPE) 5502, with melt index ($190\,^{\circ}\mathrm{C}/21.6\,\mathrm{kg}$) of $22\,\mathrm{g}/10\,\mathrm{min}$, is provided by TotalEnergies Petrochemicals [63].

The rheological analyses were carried out with a Physica MCR 501 rheometer from Anton Paar. It was equipped with a $25\,\mathrm{mm}$ diameter parallel plate geometry and a liquid cooled Peltier plate. Frequency sweep tests were conducted at the processing temperature of $200\ ^{\circ}\mathrm{C}$, 1% shear strain, which was previously verified to be in the linear viscoelastic region, and a logarithmic frequency ramp, ranging from 500 to $0.05\,\mathrm{rad/s}$.

The Storage Modulus (G'), Loss Modulus (G'') and Complex Viscosity (η^*) were obtained via direct rheological measurements, while the First Normal Stress Difference (N_1) was evaluated from the oscillatory test data using the Laun rule in Equation (4.18) [64], under the Cox-Merz assumption in Equation (4.19) [65]:

$$N_{1,\mathrm{Laun}}(\dot{\gamma})\,|_{\omega=\dot{\gamma}} \approx 2G'(\omega)\left\{1+\left(\frac{G'(\omega)}{G''(\omega)}\right)^{2}\right\}^{0.7}, \tag{4.18}$$

$$|\eta^*(\omega)| = |\eta(\dot{\gamma})|_{(\dot{\gamma})=(\omega)}\ . \tag{4.19}$$

The determination of N_1 is of particular importance when simulating complex flows of non-Newtonian fluids, as it has a relevant effect on the behaviour of free surfaces and extrudates. The normal stresses induced on molten polymer material during extrusion are thought to be caused by the entropic elasticity, in shear flows, characteristic of macro-molecules. This is thought to be the main reason for the elastic recovery of the melt, known as extrudate swell [66–68].

The rheological data analysis and fitting of a constitutive model were performed using TA Instruments TRIOS and Ansys® Academic Research Polymat, Release 22.1 software [69], respectively.

The data collected is illustrated in Figure 4.4.

The frequency response of the HDPE 5502 at the extrusion temperature $200\ °C$ is shown in the frequency sweep plots in Figure 4.4.

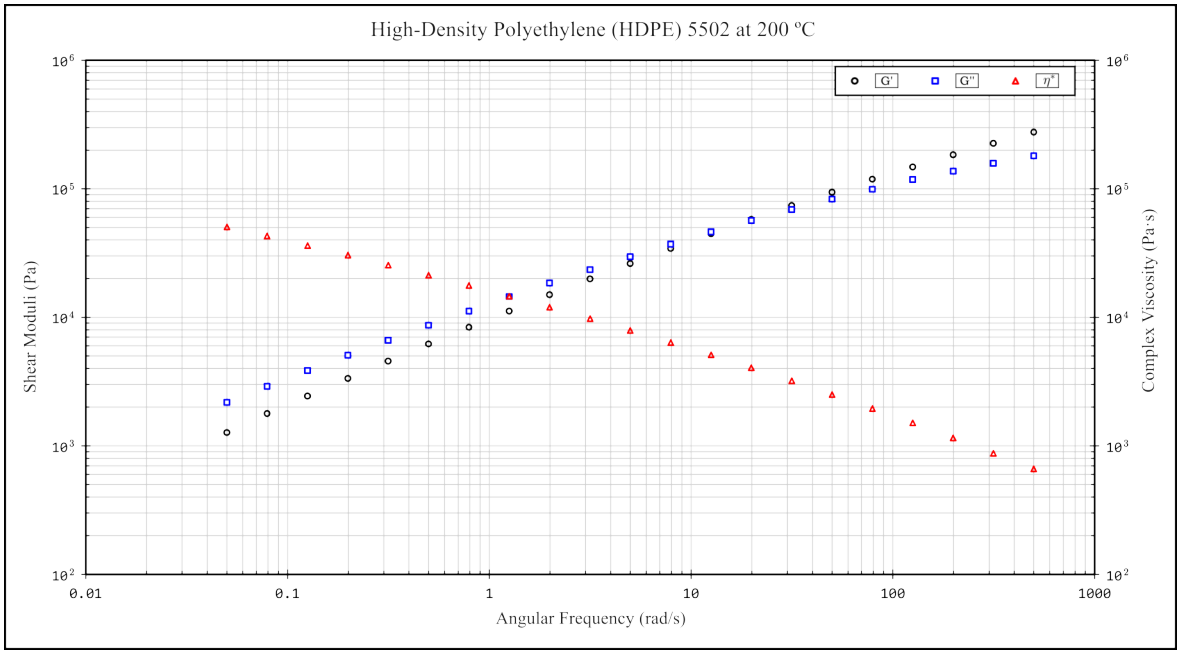


Figure 4.4: Results obtained on the frequency sweep tests of the HDPE 5502 at processing temperature of $200\ °C$.

The frequency sweep data, namely the Storage Modulus (G'), Loss Modulus (G''), were used for conducting a Discrete Relaxation Spectrum Analysis using the TA Trios software. This analysis yielded ten terms, with corresponding relative relaxation times and moduli, as detailed in Table 4.2.

Mode	1	2	3	4	5
Relaxation time (s)	2.00100E-04	1.59537E-03	6.43175E-03	2.31952E-02	7.93812E-02
Relaxation Modulus (Pa)	568721.0	188082.0	97436.0	52976.8	28366.7
Mode	6	7	8	9	10
Relaxation time (s)	0.26172	0.78804	2.65720	9.43741	45.55050
Relaxation Modulus (Pa)	13543.90	7157.90	3697.64	1629.06	1067.49

Table 4.2: Discrete relaxation spectrum for the HDPE 5502.

The tested range of relaxation times, which was presented in Table 4.2, along with the data from oscillatory tests (G', G'', η^*, and $\boldsymbol{N}_1$), were used in Ansys Polymat to conduct a rheological model fitting.

The best fit was achieved using an 8-mode PTT differential viscoelastic constitutive model [70], given by Equation 4.11. The fit curves generated by the software are presented in Figure 4.5, while the model parameters values are given in Table 4.3. The coefficients (λ_i, ϵ_i, $\eta_{p,i}$, ζ_i) for each mode correspond to the coefficients presented in Equation (4.9). It is worth highlighting that the total solvent viscosity obtained in the fitting is $\eta_s = 46.9189\,\text{Pa s}$, and the specific mass is $\rho = 938.219\,\text{kg/m}^3$.

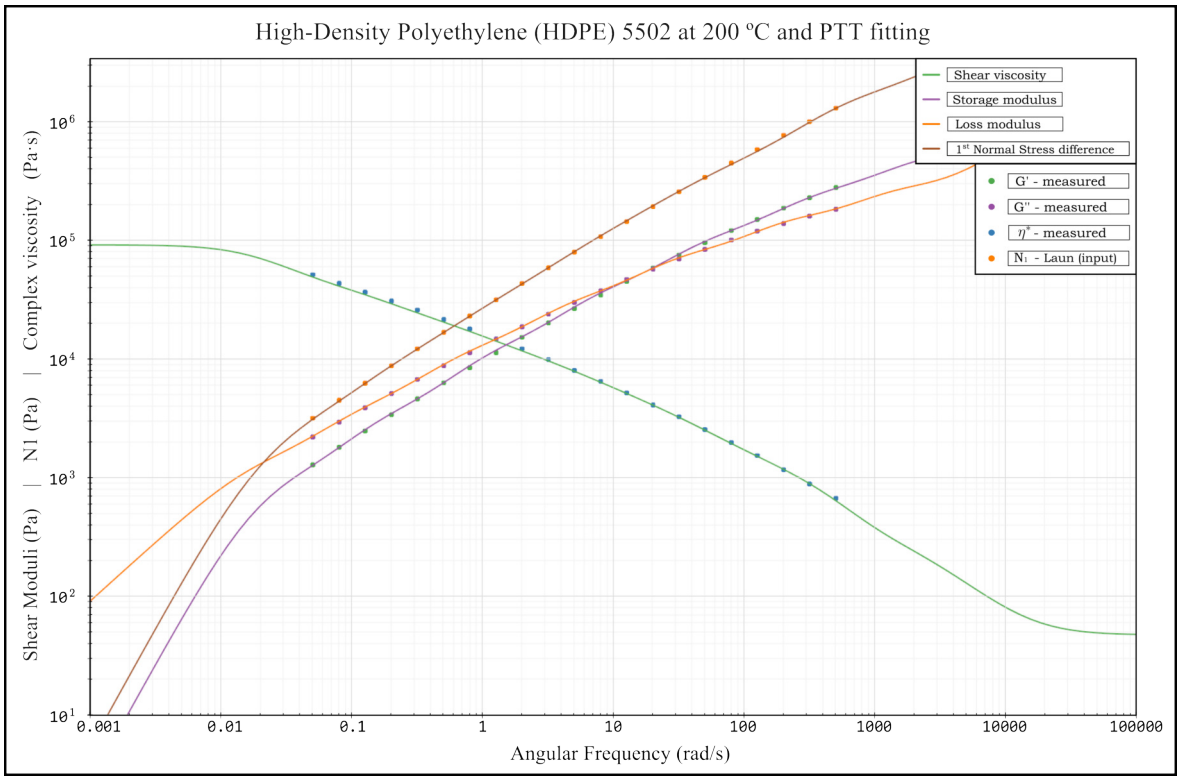


Figure 4.5: PTT 8 modes constitutive model fitting with HDPE 5502 rheological data at processing temperature of 200 °C.

Knowing that the a high ratio between the polymer melt and air viscosities, promote numerical instabilities, a study was also conducted to investigate the effect of the air phase viscosity in the flow. To streamline the study, the air phase viscosity was defined as a ratio of the total viscosity of the polymer, as follows:

$$\underbrace{\eta_{\mathrm{s}}}_{\text{air}} = f \underbrace{\left(\sum_{i=1}^{n} \eta_{\mathrm{s,i}} + \eta_{\mathrm{p},i} \right)}_{\text{polymer}} \tag{4.20}$$

It was concluded that a value of $f = 1 \times 10^{-3}$ for the air phase viscosity was sufficiently low to minimise the impact on the extrudate evolution, and sufficient high to assure numerical stability in the simulations. Furthermore, the specific mass for the air was $1.0\,\mathrm{kg/m^3}$, and a surface tension of $0.032\,\mathrm{kg/s^2}$ were considered.

Mode	1	2	3	4
λ:	1.00000E-04	6.51836E-04	4.24891E-03	2.76959E-02
η_p:	17.8018869	186.23760	667.601	2069.466
ϵ:	0.01517617	0.02990231	0.01889082	0.26987570
ζ:	0.5535601	0.1134860	0.1685369	0.1631256
Mode	5	6	7	8
λ:	0.18053	1.17677	7.67064	50.000
η_p:	5079.175	11280.04	20658.10	51091.26
ϵ:	0.213144	0.2419267	0.1728251	0.116263
ζ:	0.1585776	0.241768	0.3104443	0.4219211

Table 4.3: PTT 8 modes constitutive model equation parameters values for HDPE 5502 rheological data at processing temperature of $200\ ^{\circ}\mathrm{C}$. The dimensions for λ is $1/\mathrm{s}$, η_p is $\mathrm{Pa\ s}$, and the others are dimensionless.

4.4 Evaluation Cases

This section presents three distinct case studies to evaluate the capability of the numerical code for simulating the extrusion phase of the EBM process. The first analysis is regarding the mesh independence study, followed by the use of algebraic and geometric methods of VoF to assess their effect on the flow, in particular the interface geometry. Lastly, a study comparing simulated results and the experimental data collected is conducted.

All simulated cases considered the geometrical simplification of an axisymmetric condition by utilising a revolving angle of $0.011463°$. This was achieved using the wedge boundary condition available in OpenFOAM®. However, for visual clarity, the boundary faces naming is presented for a larger revolving angle and a shorter geometry in Figure 4.6.

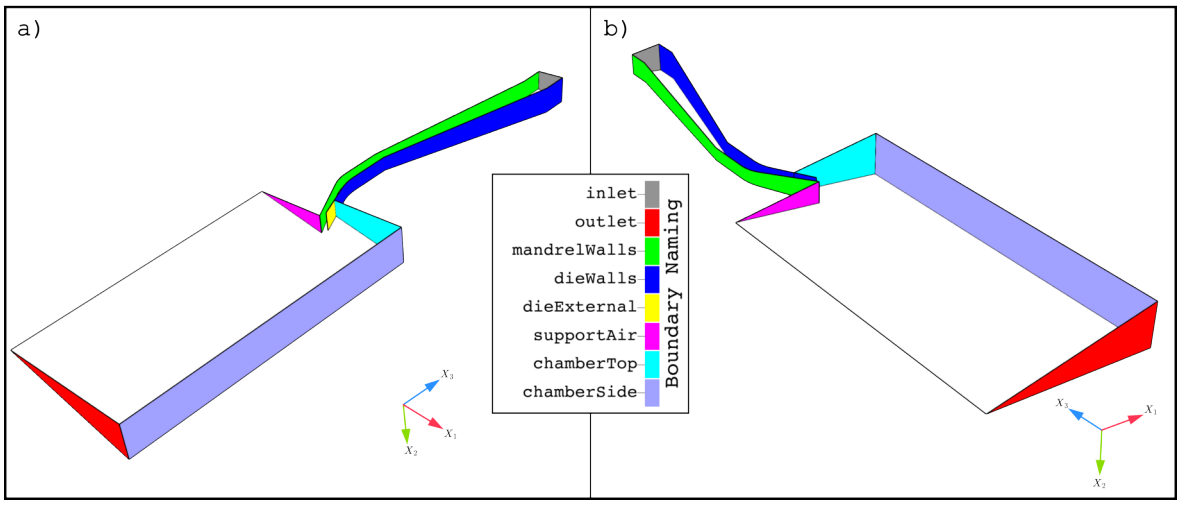


Figure 4.6: Naming used to distinguish the domain boundary regions used in the extrusion phase simulations, a) View from an outside perspective, and b) from an inside perspective.

Near the die gap in Figure 4.6 a), a yellow surface designated by dieExternal can be seen. This boundary face was inserted due to the need to displace the chamberTop planes $5.133\,\mathrm{mm}$ upwards

along the Z direction, to avoid the polymer from sticking in the region after getting out from the die flow channel. In practical processing, sometimes extrudate can accumulate in this region, and in the beginning of the extrusion as well, where the machine operator removes this excess material with a tool. Notice that the fluid flowing in the extrusion die flow channel does not interact with the fluid flowing in this additional region created. This interaction between them just happens in the neighbouring cells at their common edge, i.e. the edge formed between the dieWalls surface (blue) and dieExternal surface (yellow).

The boundary conditions applied to each region and each field are presented in Table 4.4. In this table, p' represents the alternative pressure, where $p' = p - \rho g h$, p is the pressure, and the term ($\rho g h$) is the hydrostatic pressure contribution. In addition, g is the the third component of gravitational acceleration vector that is aligned with the third principal direction X_3 of the rectangular orthonormal basis, i.e. $\mathbf{g} = (0.0 \;\; 0.0 \;\; 9.8)\,\mathrm{m/s^2}$ and $g = 9.8\,\mathrm{m/s^2}$. Also, $\mathbf{v}$ represents velocity, α represents phase fraction, τ represents the stress tensor, and $\ln(\boldsymbol{A})$ represents the log-conformation stabilisation of the conformation tensor $\boldsymbol{A}$. An additional boundary condition was defined for the central revolving axis as "empty", while the "wedge" boundary condition was applied to all planes normal to the revolving direction. It should be noted that the values shown in Table 4.4 for τ and $\ln(\boldsymbol{A})$ are denoted as $6(0)$, indicating that all six components of these symmetric tensors are zero.

	Fields				
Boundary region	p [Pa]	$\mathbf{v}$ [m/s]	α [-]	τ [Pa]	$ln(\boldsymbol{A})$ [-]
inlet	zero Gradient	fixed Value (0 0 -3.042e-3)	fixed Value 1	fixed Value 6(0)	fixed Value 6(0)
outlet	fixed Value 0	zero Gradient	fixed Value 0	zero Gradient	zero Gradient
mandrelWalls	zero Gradient	time Varying Partial Slip	zero Gradient	linear Extrapolation	zero Gradient
dieWalls	zero Gradient	time Varying Partial Slip	zero Gradient	linear Extrapolation	zero Gradient
dieExternal	zero Gradient	time Varying Partial Slip	fixed Value 0	zero Gradient	zero Gradient
supportAir	fixed Value 0	zero Gradient	fixed Value 0	fixed Value 6(0)	fixed Value 6(0)
chamberTop	fixed Value 0	zero Gradient	fixed Value 0	fixed Value 6(0)	fixed Value 6(0)
chamberSide	fixed Value 0	zero Gradient	fixed Value 0	zero Gradient	zero Gradient

Table 4.4: Boundary conditions defined for each plane for all the fields.

To initiate the simulation, the geometry was filled with a molten polymer at rest, starting from the inlet up to the mid-section of the straight region in the extrusion channel, $20\,\mathrm{mm}$ above the bush exit point. Additionally, the boundary condition implemented for the time-varying partial slip along the extrusion channel walls began with full slip for the first 6 seconds of extrusion, and then a linear transition to a no-slip condition is imposed until $t = 9\,\mathrm{s}$, which was maintained with the no-slip for the further simulated extrusion time. This procedure was identified after some numerical trials and was shown to be mandatory to assure stability of the numerical calculations. The dieExternal surface remained with the time-varying partial slip boundary condition at full slip throughout the entire simulation.

4.4.1 Mesh Sensitivity Analysis

This first study considers the diverging die design geometry as discussed in Section 4.3.1 with the boundary conditions as presented in the beginning of this section and the GVoF method. Moreover,

the mesh refinement study is conducted using a downstream chamber shorter than the real one, with a length of $l_c = 78.75\,\mathrm{mm}$.

The study investigates five levels of refinement, distinguished by the number of cells used within the extrusion die flow channel. The channel formed in the die, the cavity between the bush and concentric mandrel, is of great importance in this simulation as the stress history in this region will influence the behaviour of the extrudate after getting out from the extrusion die flow channel. These five meshes are labelled as M1 to M5, and due to the wedge condition, only a single cell is used along the angular direction. Consequently, the mesh refinements are performed only in the other directions, i.e. the radial (r) and z directions in a cylindrical coordinate system. Figure 4.7 a) presents all these meshes in their entirety, while Figure 4.7 b) provides a close-up view of the die gap for meshes M1 and M3.

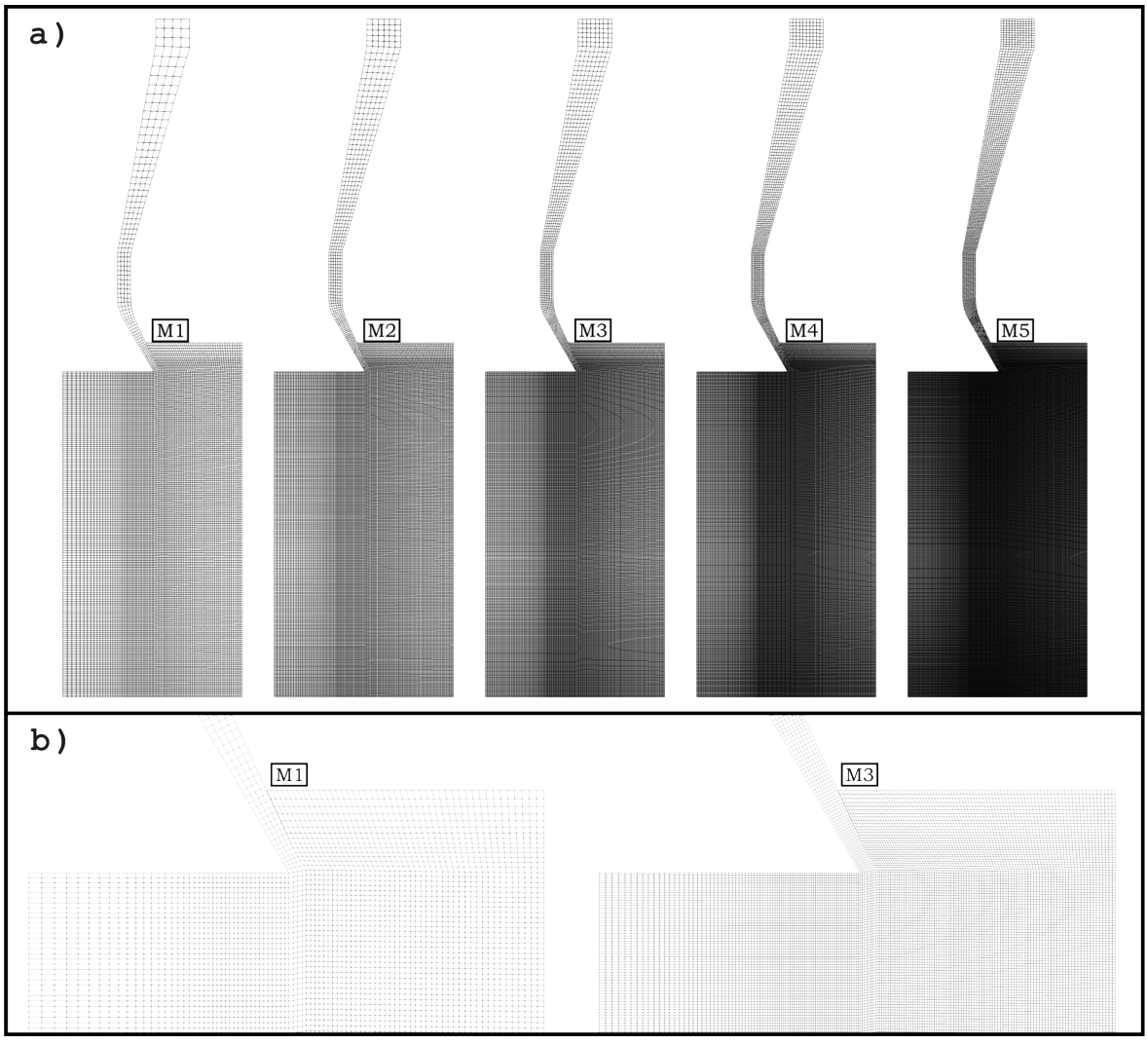


Figure 4.7: Mesh refinements for all the meshes, a) overall view of meshes M1 to M5, and b) zoomed view in the die gap opening for meshes M1 and M3 just.

Notice that meshes M1 to M5 consist of 4, 6, 8, 10, and 12 equally spaced cells, respectively, in the perpendicular direction from the flow direction within the channel. The ratio used for cell

expansion remains constant. Thus, the number of cells varies in the same proportion to maintain the same expansion ratio, and their non-orthogonality is kept at similar values.

The number of cells for all meshes, M1 to M5, is presented in Table 4.5, along with some relevant mesh metrics. It can be seen that max values of non-orthogonality are around $33°$, therefore the non-orthogonal corrections was set to 1 [71]. In addition, it was defined 3 inner corrections for the pressure-linked equations algorithm (PIMPLE).

Mesh	M1	M2	M3	M4	M5
number of cells	15,600	35,432	62,400	98,053	175,815
max non-orthogonality	32.753°	32.893°	32.960°	33.001°	33.037°
average non-orthogonality	3.6912°	3.709°	3.726°	3.730°	3.751°
Max aspect ratio	2.1855	2.2731	2.3766	2.4072	3.0696
Max skewness	0.7775	0.7877	0.7840	0.7888	0.6208

Table 4.5: Mesh metrics for all the five meshes used in the mesh sensitivity analysis.

4.4.2 Algebraic and Geometric VoF Methods

This second study envisages to analyse the different variants tested for the VoF methods, the algebraic and geometric methods. For this, the same approach, geometry and conditions as defined for the study in the previous section is also employed here. The main difference with this cases in analysis is regarding the employed method to capture the two phases interface. Furthermore, only the meshes M3, M4, and M5 were utilised in this study. Additionally, the boundary condition for the phase fraction field at the outlet and chamberSide was modified to zero gradient for the simulations of the AVoF, to ensure a convergent result when the interface phase fraction ($\alpha > 0$) gets into contact with these surfaces.

4.4.3 Experimental Assessment

The final study in this investigation involves conducting a simulation of a real extrusion experiment. The complete geometry, along with its dimensions presented in Table 4.1, was used in conjunction with mesh refinement M3. This refinement increased the number of cells while maintaining the same aspect ratio, as shown in Figure 4.7, in order to discretise the extended domain in this study. Moreover, only the GVoF method was utilised.

Similarly to the previous study, the boundary conditions remained the same as those presented in Table 4.4. The same initialisation procedure as those declared at the beginning of this section were considered. Then, the parison was allowed to extrude continuously for 70 seconds, after which a cyclic parison extrusion process was initiated, using periodically the parison cutting action described in 4.2.5 at the predefined knife plane position. During the initial 70 seconds of continuous extrusion, the parison reached the outlet surface of the domain. Due to the boundary condition defined as a fixed

value with the phase fraction for the air at the outlet surface, it acted as a destructor for the moving parison outside the domain.

Since the extrusion continued uninterrupted, the remaining parison above the knife cut plane started to displace downstream until its total length reached $305\,\mathrm{mm}$, measured from the bush. The parison was then cut off cyclically whenever it reached this predetermined length after the previous cutoff. This process was repeated for five complete parison extrusions. This study cover the dynamics of the extrusion considering the extrusion time for 8 full parisons each parison as this reference setup.

Finally, the analysis for the use of support air in conjunction with the extrusion process, focusing on four different scenarios, was also made. The reference case assumes no support air in the mandrel, establishing the boundary condition for this region as a fixed gradient value of zero, designated as case 1. Three additional cases were defined, namely case 2, case 3, and case 4, with support air velocities of $0.75\bar{v}_{\text{gap}}$, $1.00\bar{v}_{\text{gap}}$, and $1.25\bar{v}_{\text{gap}}$, respectively, where $\bar{v}_{\text{gap}}$ represents the mean scalar value of the velocity at which the polymer flows at the die gap.

It is important to note that the supportAir boundary face was positioned upward in the same manner as the chamberTop, as previously detailed and illustrated in Figure 4.6. The ratio of the upward displaced length to the mandrel radius for this boundary was 0.239. This boundary was reduced in size to ensure that it did not trespass nor intersect the inclined surface of the mandrel walls during its displacement. Additionally, the newly created boundary within the mandrel walls was designated as mandrelInternal, analogous to dieExternal, as also illustrated in Figure 4.6, and was assigned the same boundary conditions as the latter.

4.5 Results Analysis and Discussion

This section explores the outcomes obtained from the conducted simulations, as outlined in the previous Section 4.4. A comparative analysis is performed and presented to demonstrate the findings across various tested scenarios, to individually investigate the influences of different variables used to set up the simulations for the extrusion phase.

The results of each of the three case studies are presented sequentially, following the same order of their presentation in the previous section. The respective complexities of each case study are examined to provide insights that inform the variables and methods used in the final, more intricate, case setup encompassing the complete geometry. This approach provides an improvement in the quality of the final results for the extrudate configuration, thereby enhancing the overall result.

4.5.1 Mesh Sensitivity Analysis

The mesh sensitivity analysis was conducted to assure mesh independent results. It is expected that finer meshes result in better outcomes, especially when simulating viscous-dominated flows.

Initially, a qualitative analysis was performed by comparing results obtained from different meshes for the phase fraction field (α). This was followed by analyses of the pressure and stress fields. Finally, a quantitative analysis was carried out to compare the sharpness and positioning of the interface, as well as the magnitude of the polymeric extra-stress tensor profiles at the die gap.

The phase fraction (α) field is depicted in Figure 4.8, where it can be observed that the coarser the mesh, the more diffusive the interface becomes. Accordingly, mesh M1 shows the most diffusive interface. In terms of the final configuration, there are no significant differences among the meshes in relation to this α field. However, mesh M1 exhibits a slightly more curved profile immediately after the extrusion gap.

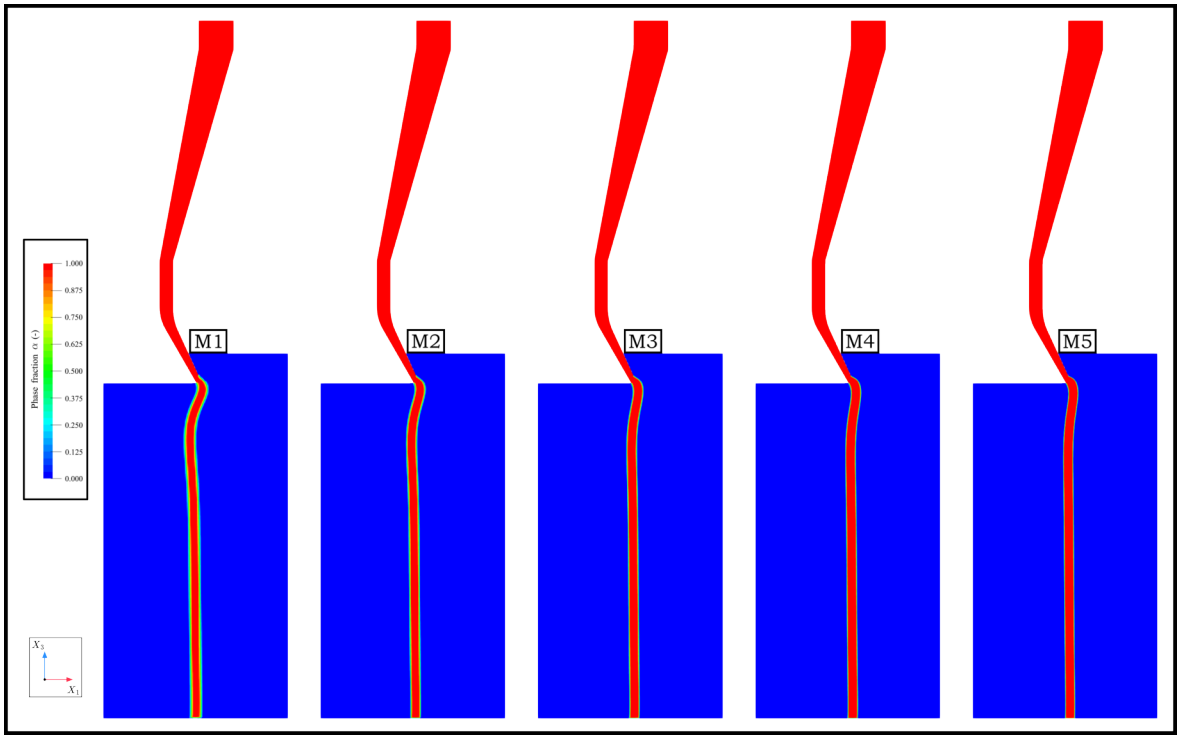


Figure 4.8: Mesh refinements effects in the phase fraction α field.

It is challenging to assert that meshes M2 to M5 exhibit a similar final configuration for the extrudate, considering the significant spacing between them in Figure 4.8. Therefore, a contour surface was created for all of them at a phase fraction of $\alpha = 0.5$. This value is considered to provide a reasonable estimate for a discrete interface between the two phases in AVoF simulations. Additionally, these contours were overlapped to enhance the visualisation of their differences, as depicted in Figure 4.9. It can be observed that there are minor deviations between meshes M3 to M5, and significant deviations between the results of meshes M1 and M2 compared to the others.

The results obtained for the pressure field distribution are schematically presented in Figure 4.10 to assess the effect of mesh refinement. It is important to note that the pressure (p) field is the sum of the alternative pressure (p') and the hydrostatic pressure contribution ($\rho\ g\ h$), thus, $p = p' + \rho\ g\ h$. However, the hydrostatic pressure contribution is much smaller than the other term, allowing for the

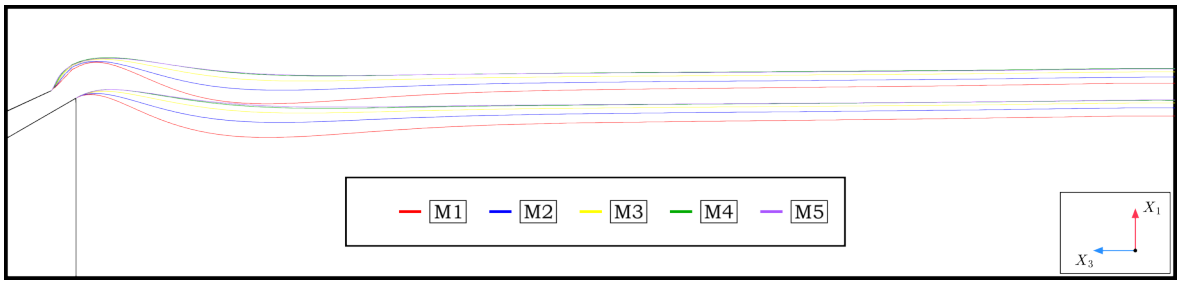


Figure 4.9: Mesh refinements effects in interface position between the two phases.

simplification $p \approx p'$. The scale range was chosen to make pressure variations visible in the air phase, as it is the least viscous phase and therefore more susceptible to variations. No differences were observed between meshes M4 and M5 for this field, while minor deviations were noticed between the results from mesh M3 and M4 within the air phase internally to the extrudate. However, major differences were observed between the results for mesh M1 and M2, both within the air phase, internally and externally to the extrudate. Another field of interest in the mesh refinement study is the

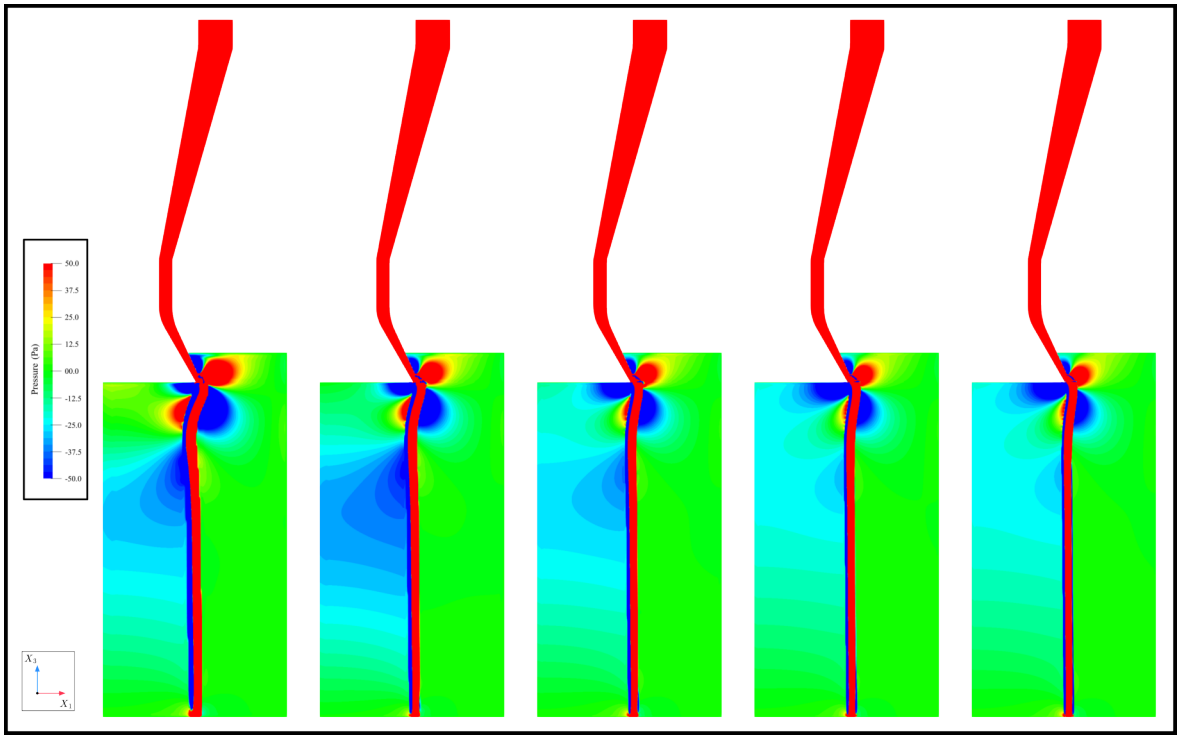


Figure 4.10: Mesh refinements effects in pressure field for the air phase fraction.

polymeric extra-stress tensor. However, since the numerical problem solution involves a constitutive equation for each phase, a different stress tensor field is calculated. This stress tensor, denoted as the polymeric extra-stress of mixture fraction ($\boldsymbol{\tau}_{\mathrm{MF}}$), is the weighted average of the polymeric extra-stress tensors from each phase, with the weighting determined by the volume fractions of each phase. This average field, which is the actual stress tensor field added to the momentum balance equation, allows for visualisation of the stress and its influence in all domain.

This polymeric extra-stress tensor magnitude of mixture fraction is presented schematically in Figure 4.11. As stress is a tensor, the magnitude was used to visualise as a single scalar field. This is achieved by calculating the magnitude of the tensor using the same equation as in Equation (4.6). Therefore, the scalar stress tensor (τ_{MF}) is calculated by using the stress tensor ($\boldsymbol{\tau}_{MF}$) in place of the rate-of-strain ($\dot{\boldsymbol{\gamma}}$), resulting in $\tau_{MF} = |\boldsymbol{\tau}_{MF}| = \sqrt{(\boldsymbol{\tau}_{MF} : \boldsymbol{\tau}_{MF})/\ 2}$.

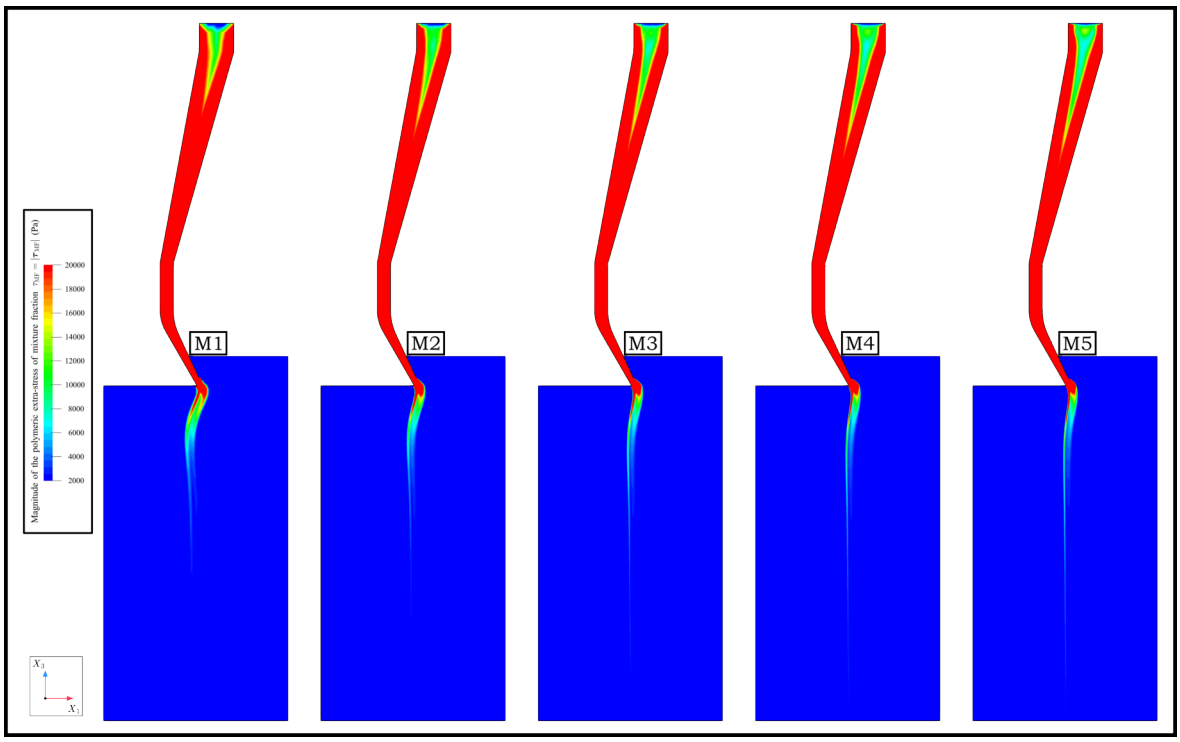


Figure 4.11: Mesh refinements effects in polymeric extra-stress tensor field for the mixture fraction.

From the analysis of the results plotted in Figure 4.11 it can be concluded that there are slight changes in the stress field for meshes M1 and M2, while the other meshes showed again similar results. Additionally, it is noticeable that higher stress values are dominant in the polymeric phase fraction, with the highest values found within the extrusion channel. This happens because the polymer experiences higher shear and elongational deformation rates in this region. Furthermore, it is observed that the stress starts to decrease downstream after the extrusion die gap.

To quantitatively compare the results obtained, the profile of the polymeric extra-stress of the mixture fraction was examined by considering the last layer of cells through which the polymer flows before getting out from the extrusion die flow channel. Since the simulations use the cell-centred approach for the finite volume method discretisation, the centroids of these cells were used to plot the stress profile. The layer of cells for each mesh refinement was selected, and a schematic representation of these cells, in on the region of interest, is shown in Figure 4.12 a). The points indicate the location of these cell centroids. Moreover, for better illustration, the actual cells from meshes M1 and M5 were shown in the same figure.

The profiles for the magnitude of the polymeric extra-stress for the mixture fraction using the

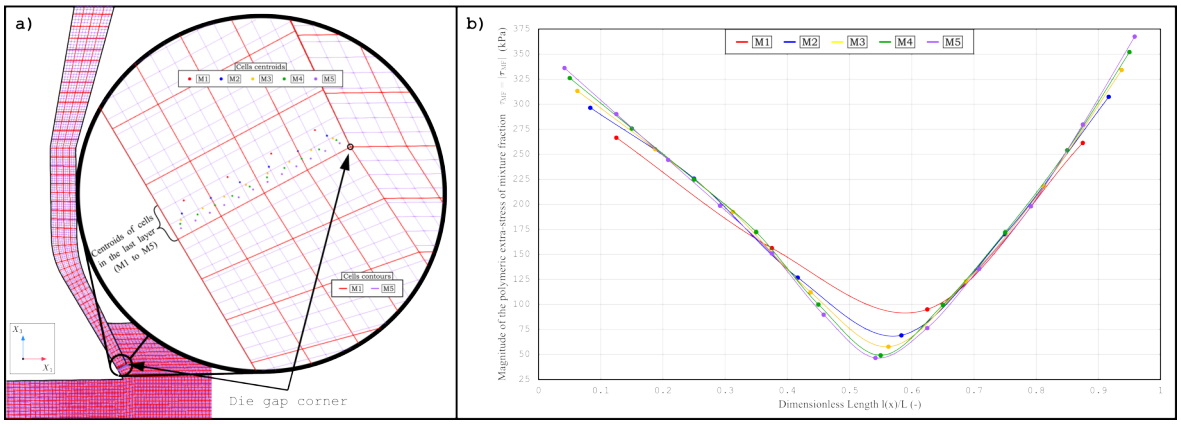


Figure 4.12: Mesh refinements effects in the polymeric extra-stress of mixture fraction, a) location of the centroids of the last cells in the channel and b) polymeric extra-stress variations in the the dimensionless length through the channel width.

last layers of each mesh are presented in Figure 4.12 b). The dimensionless length is calculated by taking the relative position of the cell centroid in the chord, where this length is divided by the total length of the chord. This chord starts perpendicularly from the mandrel wall ($l(x) = 0$) towards the die wall ($l(x) = L$), also perpendicularly, and passes through the cell centroids. It can be seen that the profiles deviate more, predicting the maximum location, around the dimensionless length value of $0.55\,\mathrm{mm}$. The profiles from meshes M4 and M5 present similar results, with a deviation of 5.6% for the lowest value of polymeric extra-stress, while the mesh M3 presents a deviation of 24.0% and the other meshes M1 and M2 show greater disparity. The inner part of the polymeric extra-stress profiles ($l(x)/L \lessapprox 0.58$) presents more differences between the mesh refinements compared to the same profile at the outer part ($l(x)/L \gtrapprox 0.58$).

The final quantitative analysis concerns the phase fraction field, where the interface between the two fluids is predicted. In Figure 4.13 a), the phase fraction (α) field is presented with the cut-plane used to compare the results. This profiling plane is positioned using the factor of $l(x_3)/r_3 = 3$, measured from the mandrel's lowest point downstream.

The profile in Figure 4.13 b) shows that the prediction of the interface location varied with the mesh refinement. Furthermore, these profiles show that the alpha field remained bounded, within the range or $0 \leq \alpha \leq 1$, for all meshes.

In Figure 4.13 c), the zoom in the transition between the two phases is presented, and it can be seen that the profiles for meshes M1 and M2 deviated more regarding the interface position, while keeping the extrudate thickness with the polymer phase with similar values. The extrudate thicknesses was measured as the length distance between the polymer-air outer interface with the polymer-air inner interface. Moreover, their positioning was measured regarding its mid-plane location, which was calculated by summing the inner interface with half of the thickness. These measurements are schematically presented in Table 4.6, where the extrudate mid-plane position was made dimensionless by dividing its position by the mandrel radius (r_3). These results show that meshes M1 and M2

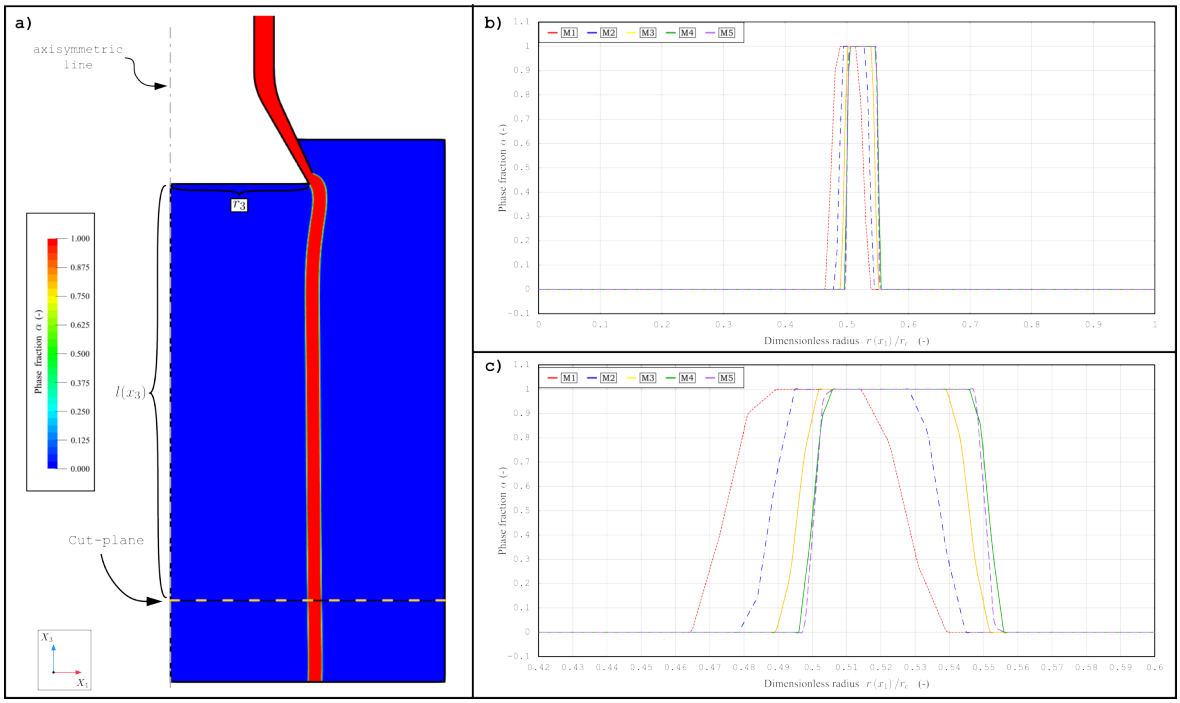


Figure 4.13: Mesh refinements effects in the phase fraction interface position, a) Location for the cutting plane used to take the profiles, b) Phase fraction full profile for all meshes refinement in the cut plane, and c) Phase fraction profile at the transition location between the air and polymer phases.

present greater inaccuracies, when compared with the M5 counterparts, while mesh M3 and M4 are more accurate.

Mesh	M1	M2	M3	M4	M5
Thicknees (mm)	2.2100	2.0825	2.0825	2.1250	2.0825
Thicknees deviation (%)	6.12%	<0.01%	<0.01%	2.04%	-
Dimensionless mid-plane position (-)	0.9903	1.0131	1.0289	1.0398	1.0388
Mid-plane position deviation (%)	4.66%	2.47%	0.95%	0.10%	-

Table 4.6: Extrudate dimensions measurements for all the meshes evaluated at cut-off profiling plane of $l(x_3)/r_6 = 3$.

The following calculation times represent the duration required to simulate 1 second of extrusion time. Consequently, meshes M1, M2, M3, and M4 require 0.448, 0.782, 1.281, and 2.181 hours per second of extrusion, respectively, and all simulations were conducted in parallel using 24 cores. The simulation for mesh M5 required 2.725 hours per second of extrusion, conducted in parallel with 36 cores. The computer utilised for the 24-core parallelisation comprised a rack with two processor units featuring Intel® Xeon® Processor E5-2695 v2 [72], while the computer used for the 36-core parallelisation consisted of a rack with two processor units containing Intel® Xeon® Processor E5-2683 v4 [73].

Through this analysis, the mesh M3 demonstrated to be a good choice due to the quality and lower deviations of the final results in comparison with the M5 results, as well as the lower calculating time in comparison with M4 and M5. Accordingly mesh M3 was the default level of refinement selected

for the subsequent studies.

4.5.2 Algebraic and Geometric Volume-of-Fluid (VoF) Methods

This case study aims to verify the differences in the final results obtained using the AVoF method with MULES linear-solver and the GVoF method with Isoadvector linear-solver and PLIC-RDF method for interface reconstruction. The definitions and methodologies are as presented in Section 4.4.2. Initial results were obtained with mesh M3; however, further investigations with finer meshes M4 and M5 were also conducted to evaluate possible improvements of the findings.

The first comparison is illustrated in Figure 4.14, where the differences in the interface shape between the two methods can be observed. When using the AVoF method (Figure 4.14 a, left), a nonphysical oscillatory pattern is evident at the downstream region of the extrudate. In contrast, results when using the GVoF method (Figure 4.14 a, right) were more realistic, smoother, interface in the same region.

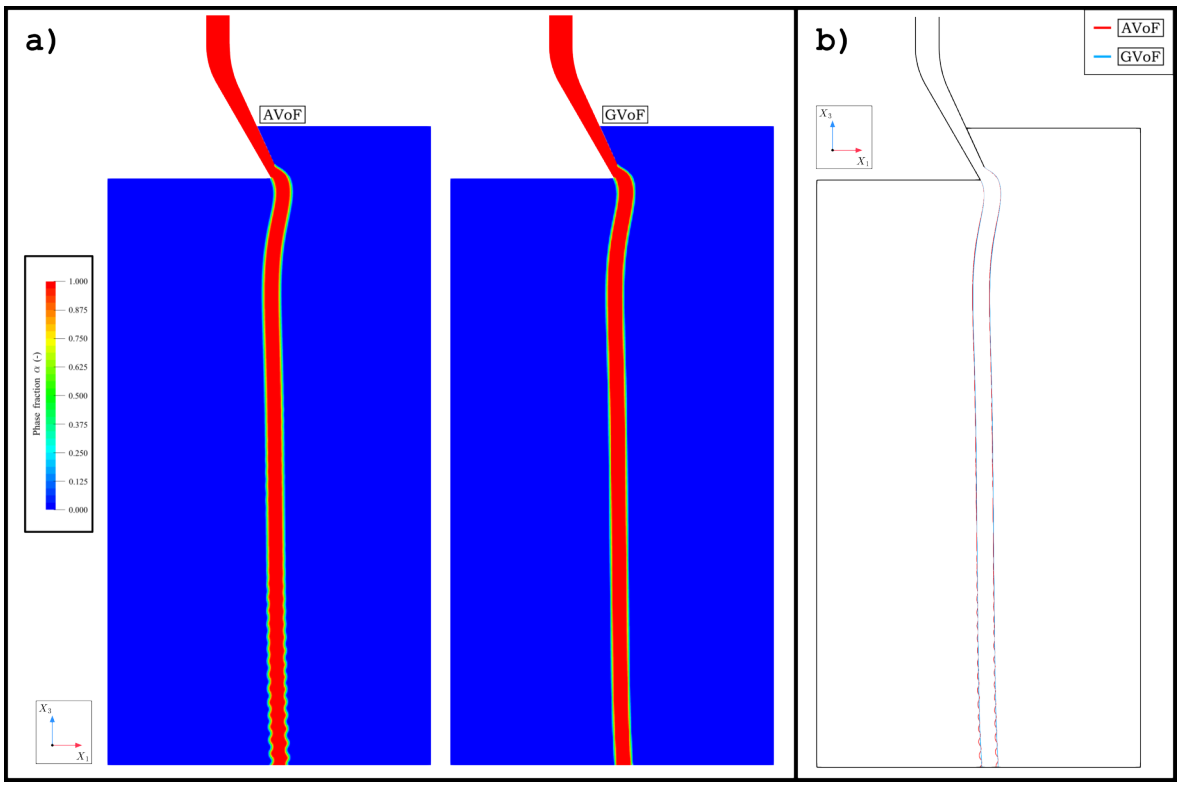


Figure 4.14: Comparison of the AVoF and GVoF methods for representing the interface of the phase fraction field. a) Visualization of the phase fraction fields for both methods using a collocated arrangement, showing the interface evolution, and b) Superimposed interfaces of the two methods for a direct comparison of their accuracy and behaviour.

To better understand these differences, the two simulation results were overlaid, as shown in Figure 4.14 b. Here, the discrete interfaces, defined by a phase fraction of $\alpha = 0.5$, are compared. It can be seen that the mid-plane positions of the interfaces coincide, indicating that the overall

positioning is consistent between the methods. However, the profile from the AVoF method oscillates around the straight profile of the GVoF method, suggesting that while the global interface location is similar, the local interface dynamics differ significantly.

Spurious velocity at the interface could be a reason for the oscillatory profile; however, this was not observed in the region. Furthermore, not even the artificial increase of the real air viscosity, as following Equation (4.20), was not able to suppress these non-physical oscillations. To confirm that this strange effect was not motivated by the level of mesh refinement, identical simulations were conducted using finer meshes, M4 and M5.

Figure 4.15 presents the results for simulations using the AVoF method and the GVoF method for meshes M3, M4, and M5. The results show that refining the mesh did not eliminate the oscillatory pattern at the interface for the AVoF method. In fact, in the AVoF simulation results for mesh M5, the oscillatory profile appeared throughout the extrudate, including regions immediately downstream of the mandrel-die gap, with an increased frequency of oscillations. Additionally, in the simulation using the AVoF method and mesh M4, the oscillatory pattern became more pronounced in the upstream regions of the extrudate. These results underscore the advantage of using the GVoF solver for the case study of interest, as the same oscillatory pattern was not observed in the real processing.

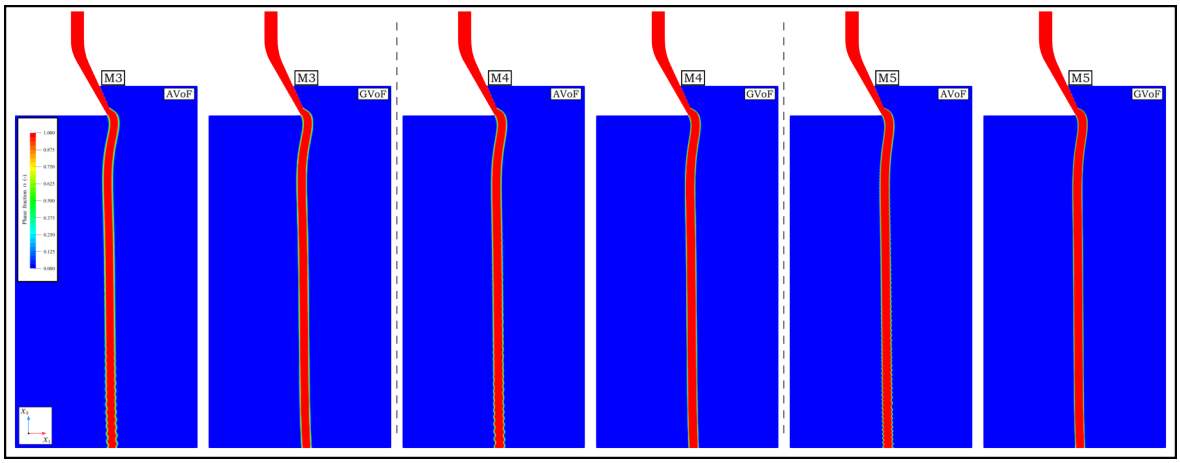


Figure 4.15: Comparison of the phase fraction (α) field between AVoF and GVoF methods for meshes M3, M4, and M5.

4.5.3 Experimental Assessment

The final investigation in this study involves analysing the dynamics of full parison extrusion, as described in Section 4.4.3. The first comparison addresses the differences in thickness under the same simulation conditions for both short and long chamber setups. As shown in Figure 4.16, increasing the chamber length results in a longer and heavier parison; however, the interface positions did not deviate significantly between the short and long chamber simulations. Thickness values were comparable, with the parison extruded in the short chamber showing $h = 2.083\,\mathrm{mm}$ and the long chamber parison measuring $h = 2.040\,\mathrm{mm}$. However, the diameter swell at the cutting plane,

$l_{\text{swell}}(x_3)/r_6 = 3.50$ (see Figure 4.16), differed, with values of $d^*_{\text{swell}} = 1.0567$ and $d_{\text{swell}} = 1.0239$ for the short and long chamber parisons, respectively.

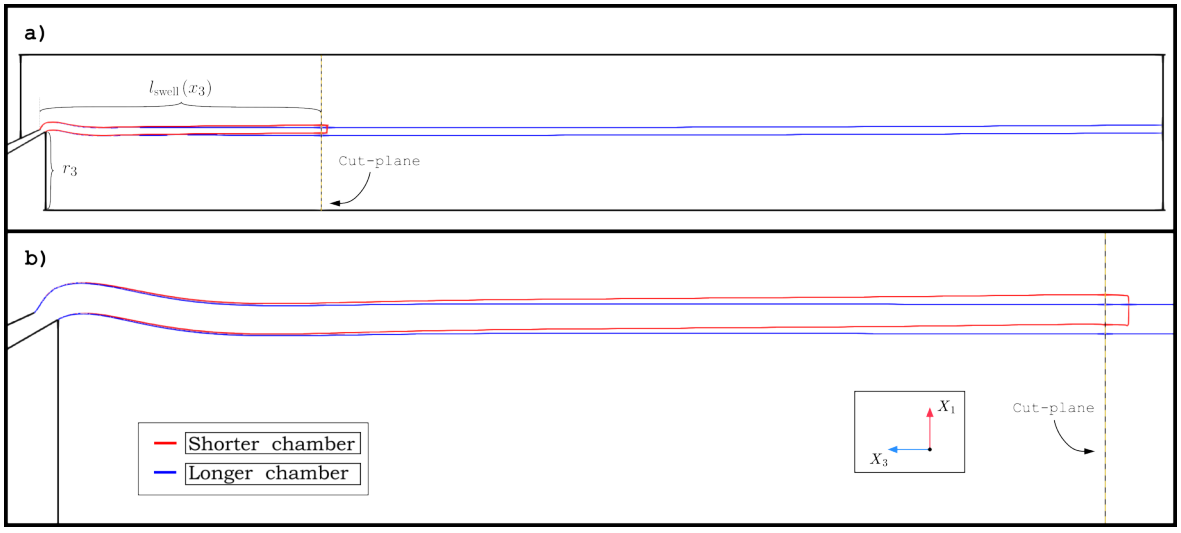


Figure 4.16: Comparison of interface positioning for the full parison extruded in a long chamber and the parison from M3 using a shorter chamber, a) Full geometry, and b) zoom in the cutting plane region.

Next, the process dynamics were assessed by performing eight sequential cuts on the extruded parison. After 70 seconds of extrusion, the parison was cut, and once it reached a length of 305 mm, it was cut again for eight subsequent cycles. The first parison extrusion lasted 24.37 seconds, while the subsequent extrusions lasted 18.90, 18.83, 18.90, 18.85, 18.87, 18.86, and 18.86 seconds, respectively. The first extrusion, being 28.9% longer than the second, deviated significantly, while the remaining cycles exhibited less than 0.5% deviation in extrusion time. The experimental trials for 18 full parisons yielded a duration of 19.389 ± 0.632 seconds. The last four simulation runs deviated by 2.73%—faster than the real processing time, yet within an acceptable range, given that the experimental uncertainty (3.26%) exceeded this difference.

An analogous simulation was performed, where the polymer phase was modeled as a GNF using the Carreau-Yasuda model [74], with the following parameters: zero shear-rate Newtonian plateau viscosity $\eta_0 = 91096.6, \text{Pa}$, infinite shear-rate Newtonian plateau viscosity $\eta_\infty = 0.0, \text{Pa}$, time-scale $k = 5, \text{s}$, flow behaviour index for shear rate dependent viscosity $n = 0.3$, and dimensionless parameter of the model $a = 2$. Therefore, yielded an extrusion time of 11.28 seconds, which is significantly lower than the real processing time. This portrays the importance of using the viscoelastic behaviour to properly capture the swelling and sagging effects of the parison during its extrusion.

The final assessment involved the use of support air, examining the four scenarios outlined in Section 4.4.3. The simulations demonstrated that introducing support air from the mandrel during extrusion caused the parison to slightly inflate, leading to an increase in diameter and a decrease in thickness. This technique is commonly employed in industrial EBM processes, with a similar outcome. However, due to the air phase's artificially increased viscosity in the simulation, the flow rate had to be significantly reduced to avoid rupturing the parison interface.

Figure 4.17 a) shows the interface variations between the parison and the air for the complete geometry. While all cases exhibited identical thickness and swelling immediately after the die gap, deviations became apparent downstream (see Figure 4.17 b)). The parison's diameter increased with the definitions of higher flow rate of the support air (Figure 4.17 c)). To better visualise the thickness variation, Figure 4.18 a) provides a chart showing the thickness along the parison length, highlighting that only case 4 exhibited the lowest thickness values at the midpoint. Diameter swell measurements, shown in Figure 4.18 b), compared simulated and experimental data, indicating that the setup for Case 4 yielded similar results between both, demonstrating strong correlation, as the parison was obtained using support air during extrusion. Despite variations in polymer distribution, extrusion time remained consistent, with times of 18.87, 19.66, 18.93, and 20.18 seconds for Cases 1 through 4, respectively.

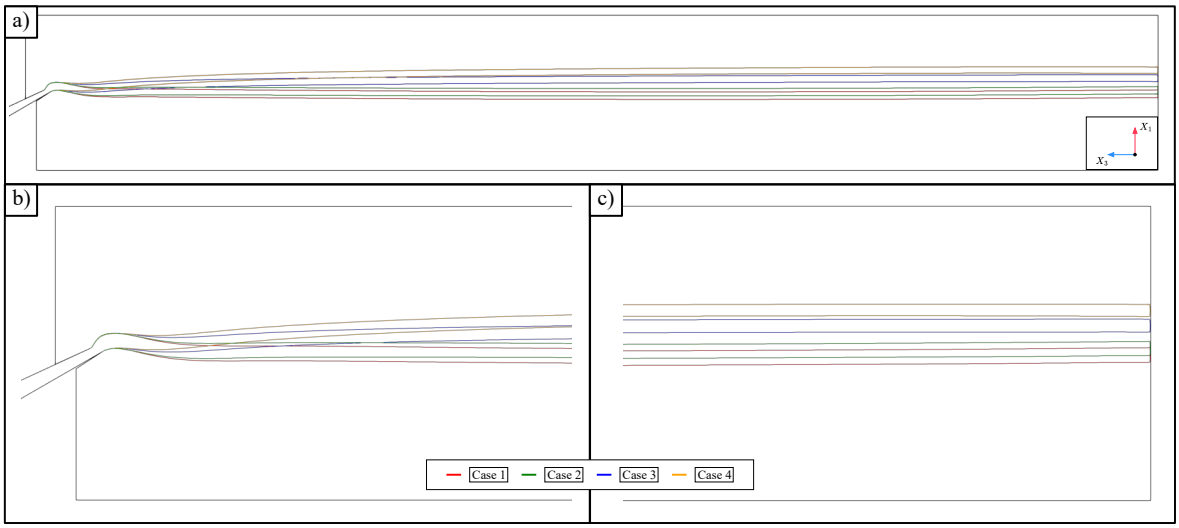


Figure 4.17: Interface location for different support air velocity conditions in the mandrel. a) Full geometry, b) zoomed-in view of the die gap, c) zoomed-in view of the outlet.

4.6 Conclusion

This work investigated the simulation of the Extrusion Blow Moulding (EBM) extrusion phase. Two distinct Volume-of-Fluid (VoF) methods for modelling the complex fluid flows were evaluated for the parison formation. The work included experimental processing, material characterisation, and rheological model fitting. The two VoF methods were assessed using the RheoTool open-source toolbox, based on OpenFOAM®. The simulations utilised the existing solver rheoInterFoam, which handles multiphase flows through an Algebraic VoF (AVoF) method, and a newly developed solver rheoInterIsoFoam, which employs a Geometric VoF (GVoF) method. The latter provided an improved interface profile between the two fluid phases, thereby enhancing the simulation's capability in capturing the dynamics of the EBM process.

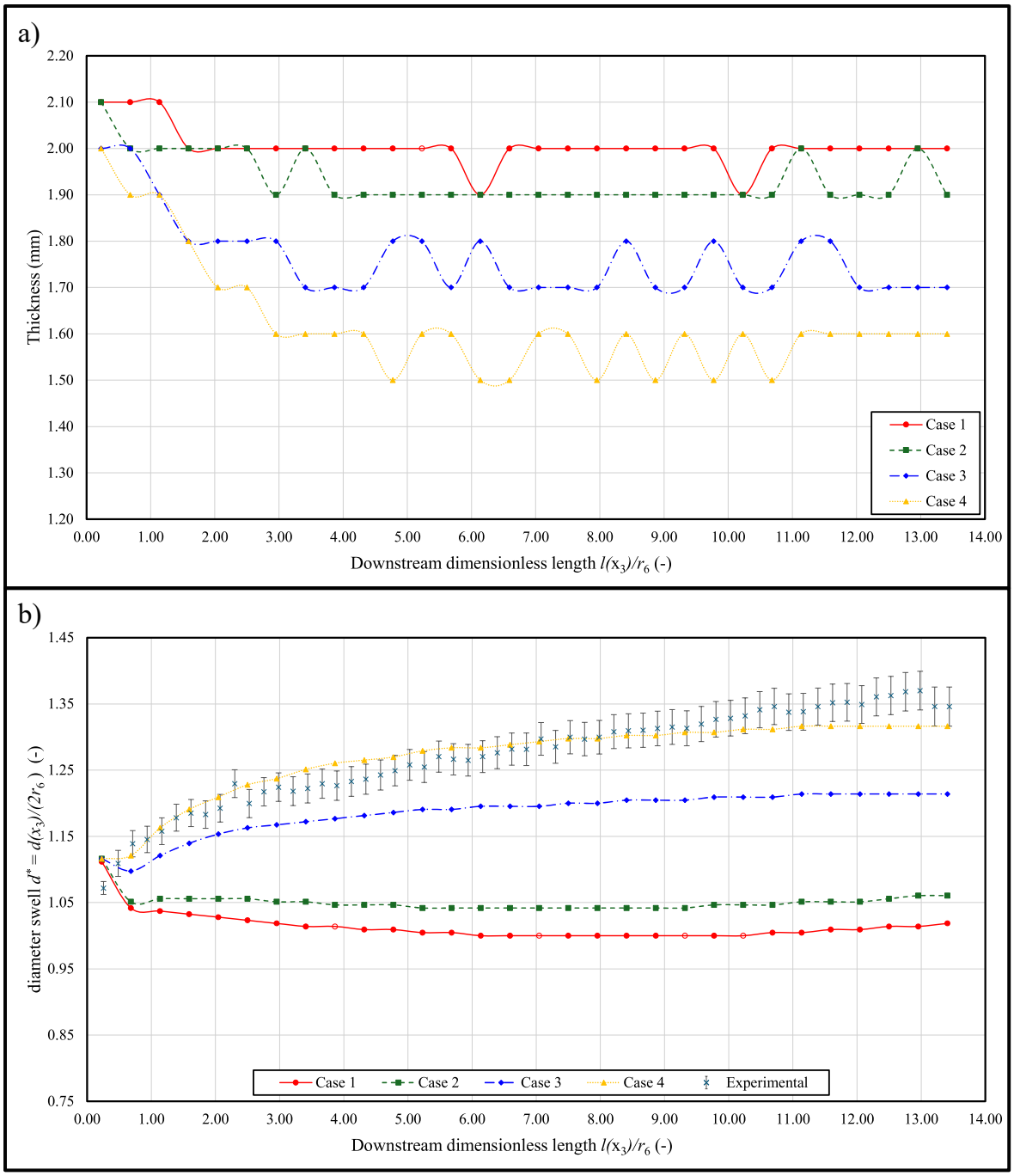


Figure 4.18: Measurements for the parison: a) thickness distribution and b) diameter swell.

The first investigation focused on the effect of mesh refinement on the accuracy for the simulations. Both qualitative and quantitative assessments of key fields and regions of interest were conducted. Mesh M3 was identified as the optimal choice, offering a balance between computational efficiency and result accuracy. The results obtained with this mesh exhibited minimal deviations, especially in the pressure field of the air phase and the mixture fraction tensor magnitude. The pressure field within the polymer phase showed consistently higher levels due to the significant shear rates experienced in the extrusion channel. Additionally, the stress magnitude was high inside the extrusion channel, extending slightly downstream after the polymer exited the gap, as the viscoelastic

material carried its stress-strain history. Over time, this stress relaxed downstream as expected for free flows of viscoelastic fluids. It was also possible to confirm that the phase fraction field remained bounded within the range $0 \leq \alpha \leq 1$, demonstrating the robustness of the solver.

The second study involved a comparison between the standard solver rheoInterFoam (AVoF method) and the newly developed rheoInterIsoFoam (GVoF method). The results highlighted significant differences in the interface quality between the two solvers. The GVoF method in rheoInterIsoFoam showed a marked improvement in capturing the fluid interface accurately, eliminating the oscillations that persisted in the AVoF method, even when using finer meshes. This confirmed the superior performance of the GVoF approach in simulating the two-phase flows for the extrusion phase of EBM process.

Finally, the third study simulated the full-length extrusion chamber, replicating the experimental data obtained from an industrial EBM machine. The simulation closely matched the experimental data, particularly in terms of the parison's geometry and extrusion dynamics. The results demonstrated the reliability of the computational framework developed in this study, enabling accurate predictions of the parison extrusion process in real-world conditions.

In conclusion, the proposed computational framework utilising the GVoF method with the rheoInterIsoFoam solver provides a robust tool for simulating the extrusion phase of the EBM process. This research advances the numerical simulation of the EBM process and contributes to the broader field of simulating complex fluid flows. The outcomes of this work offer the packaging industry a valuable resource for predicting potential issues and optimising process efficiency through advanced numerical simulations, significantly reducing the reliance on costly and time-consuming experimental trials. These developments strengthen the ability of manufacturers to improve process control fostering more efficient and sustainable production practices in the EBM process.

References

[1] Openfoam-v2206 - esi group. https://www.openfoam.com/news/main-news/openfoam-v2206, 2022. Accessed: 2024-Jul-13.

[2] John Goff, Tony Whelan, and Don DeLaney. The dynisco extrusion processors handbook. Edition, 2:284, 2000.

[3] M. O. Ghafur, B. Koziey, and J. Vlachopoulos. Simulation of Thermoforming and Blowmolding — Theory and Experiments, pages 321–383. Springer Netherlands, Dordrecht, 1995.

[4] G. H. Menary, C. W. Tan, M. Picard, N. Billon, C. G. Armstrong, and E. M. A. Harkin-Jones. Numerical Simulation of Injection Stretch Blow Moulding: Comparison with Experimental Free Blow Trials. AIP Conference Proceedings, 907(1):939–944, 04 2007.

[5] Ottmar Brandau. 1 - a short history of stretch blow molding. In Ottmar Brandau, editor, Stretch Blow Molding (Second Edition), Plastics Design Library, pages 1–4. William Andrew Publishing, Oxford, second edition edition, 2012.

[6] Benoit Cosson, Luc Chevalier, and Gilles Régnier. Simulation of the stretch blow moulding process: from the modelling of the microstructure evolution to the end-use elastic properties of polyethylene terephthalate bottles. International Journal of Material Forming, 5:39–53, 2012.

[7] Luis F. Ramos-De Valle. Principles of polymer processing, February 2013.

[8] Johannes Zimmer and Markus Stommel. Method for the evaluation of stretch blow molding simulations with free blow trials. In IOP Conference Series: Materials Science and Engineering, volume 48, page 012004. IOP Publishing, 2013.

[9] Samuel L. Belcher. 13 - blow molding. In Myer Kutz, editor, Applied Plastics Engineering Handbook (Second Edition), Plastics Design Library, pages 265–289. William Andrew Publishing, Moscow, Ohio, second edition edition, 2017.

[10] Norman C Lee. Understanding blow molding. Hanser Publishers, 2000.

[11] Samuel L Belcher. Practical guide to injection blow molding, volume 71. CRC Press, London, 2007.

[12] John Vlachopoulos and Nickolas D Polychronopoulos. Chapter 3 - viscoelasticity, 2019.

[13] Michael Thielen. Extrusion Blow Molding. Carl Hanser Verlag GmbH & Company KG, 2021.

[14] A.D. Jayal, F. Badurdeen, O.W. Dillon, and I.S. Jawahir. Sustainable manufacturing: Modeling and optimization challenges at the product, process and system levels. CIRP Journal of Manufacturing Science and Technology, 2(3):144–152, 2010. Sustainable Development of Manufacturing Systems.

[15] The circular economy for plastics – a european analysis 2024. https://plasticseurope.org/knowledge-hub/the-circular-economy-for-plastics-a-european-analysis-2024/, 2024. Accessed: 2024-Aug-09.

[16] Rohit Agrawal, Abhijit Majumdar, Anil Kumar, and Sunil Luthra. Integration of artificial intelligence in sustainable manufacturing: current status and future opportunities. Operations Management Research, 16(4):1720–1741, Dec 2023.

[17] Wagner de Campos Galuppo, Pedro Santana, Francisco Alves, and João Miguel Nóbrega. Extending the finite area method for enhanced simulation of deformable membranes and its application to extrusion blow moulding. Thin-Walled Structures, 203:112184, 2024.

[18] JM Dealy and Nese Orbey. A model for parison behavior in the extrusion blow molding process. AIChE journal, 31(5):807–811, 1985.

[19] A Garcia-Rejon, R.W DiRaddo, and M.E Ryan. Effect of die geometry and flow characteristics on viscoelastic annular swell. Journal of Non-Newtonian Fluid Mechanics, 60(2):107–128, 1995.

[20] ANSYS Inc. Polyflow, 1995. Software.

[21] B. Bernstein, E. A. Kearsley, and L. J. Zapas. A Study of Stress Relaxation with Finite Strain. Transactions of The Society of Rheology, 7(1):391–410, 03 1963.

[22] Shuichi Tanoue, Toshihisa Kajiwara, Kazumori Funatsu, Kousuke Terada, and Masashi Yamabe. Numerical simulation of blow molding—prediction of parison diameter and thickness distributions in the parison formation process. Polymer Engineering & Science, 36(15):2008–2017, 1996.

[23] Shuichi Tanoue, Yoshifumi Kuwano, Toshihisa Kajiwara, Kazumori Funatsu, Kousuke Terada, and Masashi Yamabe. Numerical simulation of blow molding—viscoelastic flow analysis of parison formation. Polymer Engineering & Science, 35(19):1546–1554, 1995.

[24] Han-Xiong Huang, Yan-Sheng Miao, and Dong Li. Numerical prediction and experimental validation of viscoelastic annular swell. Advances in Polymer Technology, 25(4):259–269, 2006.

[25] Dahang Tang, Flavio H. Marchesini, Ludwig Cardon, and Dagmar R. D'hooge. State of the-art for extrudate swell of molten polymers: From fundamental understanding at molecular scale toward optimal die design at final product scale. Macromolecular Materials and Engineering, 305(11):2000340, 2020.

[26] F. Pimenta and M.A. Alves. Stabilization of an open-source finite-volume solver for viscoelastic fluid flows. Journal of Non-Newtonian Fluid Mechanics, 239:85–104, 2017.

[27] Manuel A. Alves Francisco Pimenta. GitHub Repository - fppimenta/rheoTool: Toolbox to simulate GNF and viscoelastic fluid flows in OpenFOAM® - version 5.0. https://github.com/fppimenta/rheoTool, 2022. [Accessed 09-08-2024].

[28] Raphaël Comminal, Jon Spangenberg, and Jesper Henri Hattel. Robust simulations of viscoelastic flows at high weissenberg numbers with the streamfunction/log-conformation formulation. Journal of Non-Newtonian Fluid Mechanics, 223:37–61, 2015.

[29] Raanan Fattal and Raz Kupferman. Constitutive laws for the matrix-logarithm of the conformation tensor. Journal of Non-Newtonian Fluid Mechanics, 123(2):281–285, 2004.

[30] Raanan Fattal and Raz Kupferman. Time-dependent simulation of viscoelastic flows at high weissenberg number using the log-conformation representation. Journal of Non-Newtonian Fluid Mechanics, 126(1):23–37, 2005.

[31] Robert Byron Bird, Charles F. Curtiss, Robert C. Armstrong, and Ole Hassager. Dynamics of Polymeric Liquids, Volume 2: Kinetic Theory, 2nd Edition. Wiley, New York, 2nd edition, 1987.

[32] Dahang Tang, Flávio H. Marchesini, Dagmar R. D'hooge, and Ludwig Cardon. Isothermal flow of neat polypropylene through a slit die and its die swell: Bridging experiments and 3d numerical simulations. Journal of Non-Newtonian Fluid Mechanics, 266:33–45, 2019.

[33] Pijush K Kundu, Ira M Cohen, and David R Dowling. Fluid mechanics. Academic press, 2015.

[34] George Keith Batchelor. An introduction to fluid dynamics. Cambridge university press, 2000.

[35] Ronald G Larson. The structure and rheology of complex fluids, volume 150. Oxford university press New York, 1999.

[36] Christopher W Macosko. Chapter 4 - Nonlinear Viscoelasticity. Wiley-VCH, Weinheim, 1994.

[37] Faith A Morrison et al. Understanding rheology, volume 1. Oxford University Press, New York, 2001.

[38] Junuthula Narasimha Reddy. An introduction to continuum mechanics. Cambridge University Press, Cambridge, 2 edition, 2013.

[39] A. Afonso, P.J. Oliveira, F.T. Pinho, and M.A. Alves. The log-conformation tensor approach in the finite-volume method framework. Journal of Non-Newtonian Fluid Mechanics, 157(1):55–65, 2009.

[40] Yue Mu, Guoqun Zhao, Xianghong Wu, and Jiqiang Zhai. Modeling and simulation of three-dimensional planar contraction flow of viscoelastic fluids with ptt, giesekus and fene-p constitutive models. Applied Mathematics and Computation, 218(17):8429–8443, 2012.

[41] MA Alves, PJ Oliveira, and FT Pinho. Numerical methods for viscoelastic fluid flows. Annual Review of Fluid Mechanics, 53(1):509–541, 2021.

[42] Manuel A. Alves, Fernando T. Pinho, and Paulo J. Oliveira. Study of steady pipe and channel flows of a single-mode phan-thien–tanner fluid. Journal of Non-Newtonian Fluid Mechanics, 101(1):55–76, 2001.

[43] L.L. Ferrás, M.L. Morgado, M. Rebelo, Gareth H. McKinley, and A.M. Afonso. A generalised phan–thien—tanner model. Journal of Non-Newtonian Fluid Mechanics, 269:88–99, 2019.

[44] P.A. Dashner and W.E. Vanarsdale. A phenomenological theory for elastic fluids. Journal of Non-Newtonian Fluid Mechanics, 8(1):59–67, 1981.

[45] Henrik Rusche. Computational fluid dynamics of dispersed two-phase flow at high phase fractions. PhD thesis, University of London, 2002.

[46] Christian Mulbah, Can Kang, Ning Mao, Wei Zhang, Ali Raza Shaikh, and Shuang Teng. A review of vof methods for simulating bubble dynamics. Progress in Nuclear Energy, 154:104478, 2022.

[47] Gregor Černe, Stojan Petelin, and Iztok Tiselj. Coupling of the interface tracking and the two-fluid models for the simulation of incompressible two-phase flow. Journal of Computational Physics, 171(2):776–804, 2001.

[48] C.W Hirt and B.D Nichols. Volume of fluid (vof) method for the dynamics of free boundaries. Journal of Computational Physics, 39(1):201–225, 1981.

[49] Onno Ubbink. Numerical prediction of two fluid systems with sharp interfaces. PhD thesis, University of London & Imperial College, 1997.

[50] P. Cifani, W.R. Michalek, G.J.M. Priems, J.G.M. Kuerten, C.W.M. van der Geld, and B.J. Geurts. A comparison between the surface compression method and an interface reconstruction method for the vof approach. Computers & Fluids, 136:421–435, 2016.

[51] Edin Berberović, Nils P van Hinsberg, Suad Jakirlić, Ilia V Roisman, and Cameron Tropea. Drop impact onto a liquid layer of finite thickness: Dynamics of the cavity evolution. Physical Review E—Statistical, Nonlinear, and Soft Matter Physics, 79(3):036306, 2009.

[52] Henrik Rusche. Computational fluid dynamics of dispersed two-phase flows at high phase fractions. PhD thesis, University of London & Imperial College, 2003.

[53] Johan A Heyns, AG Malan, TM Harms, and Oliver F Oxtoby. Development of a compressive surface capturing formulation for modelling free-surface flow by using the volume-of-fluid approach. International Journal for Numerical Methods in Fluids, 71(6):788–804, 2013.

[54] Henry G Weller. A new approach to vof-based interface capturing methods for incompressible and compressible flow. OpenCFD Ltd., Report TR/HGW, 4:35, 2008.

[55] Openfoam 2.3.0: Multiphase modelling - predictor-corrector semi-implicit mules. https://openfoam.org/release/2-3-0/multiphase/, 2014. Accessed: 2024-Jul-18.

[56] T. Abadie, J. Aubin, and D. Legendre. On the combined effects of surface tension force calculation and interface advection on spurious currents within volume of fluid and level set frameworks. Journal of Computational Physics, 297:611–636, 2015.

[57] Johan Roenby, Henrik Bredmose, and Hrvoje Jasak. IsoAdvector: Geometric VOF on General Meshes, pages 281–296. Springer International Publishing, Cham, 2019.

[58] Johan Roenby, Henrik Bredmose, and Hrvoje Jasak. A computational method for sharp interface advection. Royal Society open science, 3(11):160405, 2016.

[59] Henning Scheufler and Johan Roenby. Accurate and efficient surface reconstruction from volume fraction data on general meshes. Journal of Computational Physics, 383:1–23, 2019.

[60] Openfoam-v2206 - esi group. https://www.openfoam.com/documentation/guides/latest/api/interIsoFoam_8C.html, 2022. Accessed: 2024-Jul-13.

[61] D. Laroche, K. K. Kabanemi, L. Pecora, and R. W. Diraddo. Integrated numerical modeling of the blow molding process. Polymer Engineering & Science, 39(7):1223–1233, 1999.

[62] Quenos. Quenos polyethylene blow moulding – 08 technical guide. https://www.qenos.com/internet/home.nsf/2aca3dffefaad4efca257f9300044af6/5966cbbda306caa4ca2582330013ac17/$FILE/TechGuideBlowMolding.pdf, 2022. Accessed: 2024-Jul-14.

[63] Technical datasheet 5502. https://polymers.totalenergies.com/5502, 2022. Accessed: 2024-Jul-19.

[64] H. M. Laun. Prediction of Elastic Strains of Polymer Melts in Shear and Elongation. Journal of Rheology, 30(3):459–501, 06 1986.

[65] W. P. Cox and E. H. Merz. Correlation of dynamic and steady flow viscosities. Journal of Polymer Science, 28(118):619–622, 1958.

[66] RI Tanner. A theory of die-swell. Journal of Polymer Science Part A-2: Polymer Physics, 8(12):2067–2078, 1970.

[67] Ji-Zhao Liang. Predictions of normal stress difference during circular duct flow of polymer melts. Polymer Testing, 21(6):619–622, 2002.

[68] Christopher W Macosko. Chapter 6 - shear rheometry: Pressure–driven flows. In Rheology: Principles, Measurements, and Applications, pages 237–284. Wiley-VCH, Weinheim, 1994.

[69] Ansys. Polymat User's Guide - Release 2022 R1. Ansys inc., Canonsburg, PA 15317, United States, 2022.

[70] Nhan Phan Thien and Roger I. Tanner. A new constitutive equation derived from network theory. Journal of Non-Newtonian Fluid Mechanics, 2(4):353–365, 1977.

[71] Masahiro Ishigaki, Satoshi Abe, Yasuteru Sibamoto, and Taisuke Yonomoto. Influence of mesh non-orthogonality on numerical simulation of buoyant jet flows. Nuclear Engineering and Design, 314:326–337, 2017.

[72] Intel Corporation. Intel® xeon® processor e5-2695 v2 (30m cache, 2.40 ghz) specifications. https://ark.intel.com/content/www/us/en/ark/products/75281/intel-xeon-processor-e5-2695-v2-30m-cache-2-40-ghz.html, 2019. Accessed: 2024-Jul-18.

[73] Intel Corporation. Intel® xeon® processor e5-2683 v4 (40m cache, 2.10 ghz) specifications. https://www.intel.com/content/www/us/en/products/sku/91766/intel-xeon-processor-e52683-v4-40m-cache-2-10-ghz/specifications.html, 2021. Accessed: 2024-Jul-18.

[74] K. Yasuda, R. C. Armstrong, and R. E. Cohen. Shear flow properties of concentrated solutions of linear and star branched polystyrenes. Rheologica Acta, 20(2):163–178, Mar 1981.

CHAPTER 5 Conclusion

This final chapter includes the general conclusion and future perspectives for further research. The research presented in this thesis has made significant contributions to the advancement of computational modelling and optimisation techniques in the context of the Extrusion Blow Moulding (EBM) process. The study comprised the development, implementation and assessment of a formulation to simulate the parison extrusion, mould clamping and parison inflation phases and a framework to optimise controlling parameters such as material distribution. The following sections cover an overview of the key findings of this research work, its main contributions to the field, proposals for possible future work and some final closing remarks.

5.1 Summary of Key Findings

The first major contribution of this thesis, discussed in Chapter 2, was the development and implementation of a membrane formulation that uses the finite area class and methods available in the OpenFOAM® computational library. This model was specifically designed to address the challenges of simulating thin structures as membranes. It was successfully applied to simulate key phases of the EBM process, namely mould clamping and parison inflation. The model was validated extensively using a combination of analytical solutions and comparison with experimental data. The validation process confirmed the applicability, accuracy, and robustness of the model in simulating these EBM process phases. The computational framework developed in this thesis is, therefore, shown to be a valuable tool for simulating the mechanical behaviour of membranes under different loading conditions and can inform decision-making based on its results.

In Chapter 3, the focus shifted towards developing a comprehensive computational framework aimed at automating the optimisation of material distribution for parts produced through the EBM process. This framework integrated the membrane modelling, developed in Chapter 2, and extended its application to optimising the EBM process, in the context of replicating the programmed parison technique employed in practise. Simulation results were utilised to optimise specific input controlling variables that are feasible in the actual EBM process. The framework was designed with a strong emphasis on aligning with Industry 4.0 principles, integrating the packaging industry with digital

manufacturing. This integration aimed at enhancing material use efficiency and reduce waste. The efficacy of the framework was demonstrated through simulated case studies, which were further validated by producing optimised and non-optimised bottles in a real-world setting. The results showed a significant improvement in material distribution and overall product quality, highlighting the potential of this framework in industrial applications, as well as its capability to replicate the major features observed in the real process.

Chapter 4 provided a detailed investigation into the extrusion phase of the EBM process, specifically focusing on parison formation in the extrusion phase. The study utilises the open-source RheoTool to model the flow of viscoelastic materials using a log conformation approach, which is also based on OpenFOAM®, along with a newly developed solver called rheoInterIsoFoam, that follows a geometric volume-of-fluid approach to model the two phase flow inherent to this process phase. By considering various aspects that affect the parison formation, such as viscoelasticity and the interactions between the two phases, the research highlights the importance of accurately simulating the complex fluid flow dynamics during this phase. The simulation results are validated through comparison with experimental data, demonstrating a strong correlation and confirming the effectiveness of the approach, along with the influence of the support air used during the extrusion to assist the parison formation. Moreover, the new solver, employing a geometric scheme to capture the fluid interface location, was shown to significantly improve the quality of the numerical results for this specific process phase. This contribution not only enhances understanding of the extrusion phase but also provides additional practical insights into the resulting parison obtained in EBM processes.

These developments enable the study of EBM process phases in an isolated and independent manner, although they can also be sequentially performed to replicate the real process. Since the extrusion phase requires a different formulation, where the modelled parison result in a solid volume, an additional tool was developed to transform the volumetric solid into a membrane, considering its external surface, while accurately assigning its corresponding thickness and conserving its volume.

5.2 Contributions to the Field

This thesis allowed significant contributions to the fields of finite area with membranes, computational fluid dynamics, and advanced manufacturing.

1. Methodological Advancements: The development of a membrane model within the finite area framework represents a significant methodological advancement. This model enhances the capabilities of OpenFOAM® for simulating thin-walled structures in the context of finite strain, accounting for geometric, material, and contact non-linearities. Consequently, it provides a powerful tool for both academic research and industrial applications in the context of EBM and similar processes, such as thermoforming. The newly developed solver, rheoInterIsoFoam, which employs a geometric Volume-of-Fluid method, demonstrated a significant improvement in accurately capturing the fluid

interface location. This advancement eliminated the non-physical oscillations that were present in the interface when using algebraic Volume-of-Fluid method, that appeared even in other regions when utilising finer meshes. These findings confirm the superior performance of the geometric Volume-of-Fluid method in simulating multiphase complex fluid flows within the EBM process.

2. Framework for Optimisation: The creation of a computational framework for optimising material distribution in EBM aligns with the objectives of Industry 4.0. By improving material efficiency and reducing waste, this framework addresses key challenges in modern manufacturing and offers a practical solution for designers aiming to enhance the EBM processes. The framework demonstrates its capability to support the real process design by optimising the wide number of the input variables.

3. Process Understanding: The detailed simulation and analysis of the extrusion phase in EBM make valuable contributions on the understanding of parison formation. The insights gained from this research are crucial for improving control over the EBM process, leading to higher product quality and more efficient manufacturing practices. Furthermore, this research captures not only the complexity of this phase, including viscoelastic phenomena that result in more intricate geometric variations due to sag and swell, but also its dynamics.

5.3 Future Research Directions

While this thesis has made significant progress, there are a number of areas for future research that are worth exploring, which are described in this section.

- Enhanced Materials and Models: The current work primarily focused on the isothermal viscoelastic material behaviour of polymers for the extrusion phase and the hyperelastic behaviour for the clamp and inflation phases. Future research could investigate temperature-dependent properties for these models and expand the membrane model to include viscoelastic material behaviour for applications, where the hyperelastic simplification is not applicable. It would be also useful to simulate the rise of residual stresses, that occurs during the cooling phase, and the consequent warpage effects on the final part. Additionally, further development of material models that account for complex behaviours such as anisotropy or multilayered membrane formulations are also envisaged as beneficial. Evaluating different materials during the extrusion process to produce multilayered parisons using the co-extrusion technique could also be explored. Furthermore, the formulation of shells, where the bending contribution plays a role in the mechanics of the mechanical element, which allows to deal with thicker parisons, which could not be properly modelled using the membrane approximation, would be valuable. These enhancements would improve the accuracy and a range of applications of the developed computational framework for a wider range of industrial settings.

- Optimisation of Other Parameters: Extending the current code to perform die design optimisation, including ovalization for the die to redistribute the material in the produced parison, an approach often employed in industry, would allow for greater control over more complex part formats.

- Broader Experimental Validation: While the thesis includes a significant validation of the developed tools through experimental comparisons, conducting further validation under a wider range of operational conditions would be valuable. Expanding the scope of experimental validation to include different materials, die geometries, and processing conditions would help refine the computational models and ensure their robustness in various industrial applications.

5.4 Final Remarks

In conclusion, this thesis has successfully contributed to advancing the computational modelling and optimisation of the EBM process. The development of a robust membrane model, the creation of an optimisation framework, and the detailed analysis of the extrusion phase collectively contribute to a deeper understanding of the main phases of the EBM process and its optimisation. These contributions not only advance the academic understanding of the process but also provide practical tools for improving manufacturing efficiency and product quality in industrial environments. The methodologies and insights developed in this research lay a strong foundation for future innovations in advanced manufacturing, particularly as the industry continues to evolve and society places increasing emphasis on sustainability and performance in a world that relies on plastic products, while grappling with the challenge of reducing plastic consumption.